

Manipulation of the Two-Dimensional States at Titanates Surfaces studied by ARPES

THÈSE N° 7995 (2017)

PRÉSENTÉE LE 20 SEPTEMBRE 2017
À LA FACULTÉ DES SCIENCES DE BASE
GROUPE DIL
PROGRAMME DOCTORAL EN PHYSIQUE

ÉCOLE POLYTECHNIQUE FÉDÉRALE DE LAUSANNE

POUR L'OBTENTION DU GRADE DE DOCTEUR ÈS SCIENCES

PAR

Stefan Peter MUFF

acceptée sur proposition du jury:

Prof. M. Grioni, président du jury
Prof. J. H. Dil, directeur de thèse
Prof. K. Hricovini, rapporteur
Prof. N. Pryds, rapporteur
Dr U. Staub, rapporteur



ÉCOLE POLYTECHNIQUE
FÉDÉRALE DE LAUSANNE

Suisse
2017

Abstract

The transition metal oxides are known for their versatile physical properties and are therefore an active field of research towards possible new functionalities and applications. This thesis focuses on the subgroup of titanates with perovskite structure that shows a wide range of interesting bulk properties, ranging from para-, ferro-, and antiferroelectric orders to superconductivity. Since the finding of a two-dimensional electron gas (2DEG) at the interface and surface of titanates, the interaction of the bulk properties with the 2DEG is of particular interest. In this thesis, ways to manipulate the 2DEG formation at the surface of titanates by ferro- and paraelectric bulk properties and the surface crystal structure are investigated by the help of angle-resolved photoelectron spectroscopy (ARPES). Measured are films of CaTiO_3 , BaTiO_3 , SrTiO_3 , and $\text{Ba}_x\text{Sr}_{1-x}\text{TiO}_3$ grown on different substrates by pulsed laser deposition (PLD), as well as vicinal SrTiO_3 substrates.

The investigated quantum paraelectric CaTiO_3 hosts a 2DEG at its surface with d_{xy} orbital character that is the only metallic state of the system. The 2DEG shows indications of a Rashba-type spin splitting and has a band bottom at approximately 400 meV. Therefore the TiO_6 octahedrons at the film surface are likely strong tetragonally distorted. The symmetry of the grown films is given by the pseudo-cubic unit cell of CaTiO_3 with a $c(4\times 2)$ reconstruction. Under irradiation with ultra-violet light, the reconstruction is changed to a $p(2\times 2)$ symmetry with folded Fermi surfaces according to the reconstruction. The affinity of the 2DEG at the CaTiO_3 surface to arrange with the surface reconstruction makes it feasible to further manipulate the system with different surface terminations and formations, with the goal to tailor its two-dimensional transport properties.

BaTiO_3 is a well known ferroelectric material. In this thesis, 20 unit cell thick films of BaTiO_3 grown on SrTiO_3 and KTaO_3 substrates are studied. The films exhibit ferroelectric properties, measured by piezo-response force microscopy (PFM) and show indications of domains that are locked in in-plane directions. The strong in-plane electric field is responsible for a Wannier-Stark localization (WSL) of the conduction electrons, resulting in a smearing of the observed two-dimensional states in reciprocal space. These effects are also observable in small overlayers of SrTiO_3 grown on top, and fade with increasing SrTiO_3 film thickness.

The 2DEG observed at the vacuum surface of SrTiO_3 can be directly affected by the crystalline properties of the surface. On vicinal SrTiO_3 surfaces, the surface relaxation is altered by the terrace width. This affects the tetragonal distortion of the TiO_6 octahedron and results in changes of the energy splitting of the surface localized bands. Apart from this, the surface band bending is altered due to the electron affinity of the vicinal substrates and the dielectric

properties of the surface region. This is responsible for the presence of only the d_{xy} bands at the surface of SrTiO₃ thin films grown on SrTiO₃. At the surface of Ba doped SrTiO₃ films the 2DEG forms similar as on the SrTiO₃ thin films. For the different dopings investigated, the ARPES signature of the 2DEG vanishes at different temperatures, likely due to the altered behavior of the dielectric properties with temperature.

Keywords: titanates
perovskites
angle-resolved photoelectron spectroscopy (ARPES)
pulsed laser deposition (PLD)
piezo-response force microscopy (PFM)
two-dimensional electron gas (2DEG)
ferroelectricity
Wannier-Stark localization
vicinal surfaces
thin films

Zusammenfassung

Die Übergangsmetalloxide sind bekannt für ihre unzähligen physikalischen Eigenschaften und sind deshalb ein aktives Forschungsgebiet zur Entdeckung neuer Funktionalitäten und Anwendungen. In dieser Doktorarbeit steht die Untergruppe der Titanate mit Perovskitstruktur mit ihren interessanten Eigenschaften, die von Para-, Ferro- und Antiferroelektrizität bis zu Supraleitung reichen, im Fokus. Seit der Entdeckung eines zweidimensionalen Elektronengases (2DEG) an der Grenz- und Oberfläche von Titanaten ist die Wechselwirkung dieses 2DEGs mit den Materialeigenschaften von besonderem Interesse. In dieser Doktorarbeit werden Möglichkeiten zur Manipulation des 2DEG durch ferro- und paraelektrische Materialeigenschaften und durch die Oberflächenstruktur mittels winkelaufgelöster Photoelektronenspektroskopie (ARPES) untersucht. Gemessen wurden mit Laserstrahlverdampfen gewachsene Filme von CaTiO_3 , BaTiO_3 , SrTiO_3 und $\text{Ba}_x\text{Sr}_{1-x}\text{TiO}_3$ auf verschiedenen Substraten, sowie gestufte SrTiO_3 Substrate.

Das untersuchte, quanten-paraelektrische CaTiO_3 hat ein 2DEG an seiner Oberfläche mit d_{xy} orbitalem Charakter, welches der einzige metallische Zustand ist. Das 2DEG hat Anzeichen für eine Rashba-artige Aufspaltung und reicht bis zu einer Bindungsenergie von 400 meV. Deshalb lässt sich folgern, dass das TiO_6 Oktaeder an der Oberfläche stark tetragonal verformt ist. Die Symmetrie der gewachsenen Filme stimmt mit der pseudokubischen Einheitszelle von CaTiO_3 überein und zeigt ausserdem eine $c(4\times 2)$ Oberflächenrekonstruktion. Durch Bestrahlung mit ultra-violeten Photonen ändert sich die Rekonstruktion zu einer $p(2\times 2)$ Symmetrie, die in gefalteten Fermi-Flächen sichtbar ist. Die Eigenschaft des 2DEG von CaTiO_3 , sich mit der Oberflächensymmetrie zu arrangieren eröffnet Möglichkeiten die Oberfläche mittels anderen Terminierungen und Strukturen zu manipulieren, mit dem Ziel seine zweidimensionalen Transporteigenschaften zu bestimmen.

BaTiO_3 ist ein bekanntes ferroelektrisches Material. In dieser Doktorarbeit werden 20 Einheitszellen dicke Filme, gewachsen auf SrTiO_3 und KTaO_3 Substraten, untersucht. In Piezobewegungskraftmikroskopie (PFM) zeigen die gewachsenen Filme ferroelektrische Eigenschaften und Anzeichen für starre Domänen, die entlang der Oberfläche polarisiert sind. Das resultierende starke elektrische Feld, parallel zur Probenoberfläche, führt zu einer Wannier-Stark-Lokalisierung der Leitungsbandelektronen, sichtbar als eine verschmierte Struktur der zweidimensionalen Zustände im reziproken Raum. Diese Effekte lassen sich auch in dünnen Filmen von SrTiO_3 , gewachsen auf den BaTiO_3 Filmen beobachten und klingen mit wachsender Filmdicke ab.

Das 2DEG an der Vakuumoberfläche von SrTiO_3 kann durch Oberflächeneigenschaften manipuliert werden. Auf gestuften SrTiO_3 Oberflächen ist die Oberflächenrelaxierung abhängig

von der Stufenweite. Das beeinflusst die tetragonale Verformung vom TiO_6 Oktaeder und führt zur beobachteten Veränderung in der Aufspaltung der oberflächenlokalisierten Bänder. Zusätzlich ist die Oberflächenbandverbiegung durch die Elektronenaffinität der gestuften Oberfläche sowie durch die dielektrischen Eigenschaften der Oberflächenregion verändert. Dies ist vermutlich dafür verantwortlich, dass an der Oberfläche von dünnen SrTiO_3 Filmen nur ein Band mit d_{xy} Charakter messbar ist. Das 2DEG an der Oberfläche von Ba dotiertem SrTiO_3 ist vergleichbar mit dem 2DEG an den Oberflächen der dünnen SrTiO_3 Filme. Mit steigender Temperatur verschwindet die ARPES-Signatur der zweidimensionalen Zustände. Dabei ist das Verhalten mit steigender Temperatur abhängig von der Dotierungsmenge und erklärbar mit dem veränderten Temperaturverhalten der dielektrischen Eigenschaften.

Stichwörter: Titanate
Perovskite
Winkelaufgelöste Photoelektronenspektroskopie (ARPES)
Laserstrahlverdampfen (PLD)
Piezobewegungs-Kraftmikroskopie (PFM)
Zweidimensionales Elektronengas (2DEG)
Ferroelektrizität
Wannier-Stark lokalisierung
Gestufte Oberflächen
Dünne Filme

List of Acronyms

2D	two-dimensional
2DEG	two-dimensional electron gas
3D	three-dimensional
ADRESS-beamline	advanced resonant spectroscopies beamline
AFM	atomic force microscopy
ARPES	angle-resolved photoelectron spectroscopy
BTO	bariumtitanate (BaTiO_3)
CTO	calciumtitanate (CaTiO_3)
EDC	energy distribution curve
HRPES	high-resolution photoemission spectroscopy
LAO	lanthanumaluminate (LaAlO_3)
LEED	low-energy electron diffraction
MDC	momentum distribution curve
PFM	piezo-response force microscopy
PLD	pulsed laser deposition
RHEED	reflective high-energy electron diffraction
SIS-beamline	surface and interface spectroscopy beamline
SLS	swiss light source
STO	strontiumtitanate (SrTiO_3)
SX	soft X-ray
SX-ARPES	soft X-ray angle-resolved photoelectron spectroscopy
uc	unit cell
UHV	ultra-high vacuum
UV	ultra violet
UV-ARPES	ultra violet angle-resolved photoelectron spectroscopy
WSL	Wannier-Stark localization
XPS	X-ray photoelectron spectroscopy

Contents

Abstract (English/Deutsch)	i
Introduction	1
1 Basic background	5
1.1 The $\text{LaAlO}_3/\text{SrTiO}_3$ interface	5
1.2 Anatase TiO_2	7
1.3 $\text{SrTiO}_3(001)$ surface states	8
1.3.1 Rashba-like spin splitting	11
1.4 Surface states of other SrTiO_3 terminations and KTaO_3	13
1.5 Influence of an electric field on electrons in solids	14
2 Bulk properties of titanates	19
2.1 Orbital ordering in titanates	19
2.2 Structural phase transitions in titanates	23
2.2.1 Parent perovskite CaTiO_3	23
2.2.2 Ferroelectric BaTiO_3	24
2.2.3 Properties of SrTiO_3	26
2.2.4 CaTiO_3 - BaTiO_3 - SrTiO_3 intermixtures	28
3 Experimental methods	31
3.1 Angle-resolved photoelectron spectroscopy	31
3.1.1 High-resolution angle-resolved photoelectron spectroscopy	36
3.1.2 Soft X-ray angle-resolved photoelectron spectroscopy	37
3.2 Thin film growth	38
3.2.1 Pulsed laser deposition	38
3.2.2 Reflection high-energy electron diffraction and low-energy electron diffraction	41
3.3 Piezo-response force microscopy	43
4 The parent perovskite CaTiO_3	45
4.1 Observation of a two-dimensional electron gas at CaTiO_3 film surfaces	45
4.2 Rashba-like splitting of the CaTiO_3 surface states	52
4.3 Doping approach by Rb-deposition	53

Contents

4.4	Conclusion	55
5	Interaction of ferroelectricity with the 2D states at the BaTiO₃ surface	57
5.1	Direct observation of Wannier-Stark localization at the surface of BaTiO ₃ films	57
5.2	Piezo-response force microscopy	64
5.3	Estimation of the electric field	65
5.4	Additional ARPES measurements of BaTiO ₃	68
5.4.1	Measurements along $\overline{\Gamma M}$	68
5.4.2	Photon energy dependency	68
5.4.3	Light polarizations	69
5.4.4	Time dependent behavior	71
5.4.5	Temperature dependent measurements	72
5.5	Further characterization of SrTiO ₃ thin films on BaTiO ₃	73
5.5.1	RHEED pattern and oscillations	73
5.5.2	XPS measurements	74
5.5.3	ARPES measurements	75
5.6	SX-ARPES measurements of BaTiO ₃	76
5.7	Conclusion	79
6	Manipulation of the SrTiO₃ surface states	81
6.1	Altered octahedral distortion by vicinal surfaces	82
6.1.1	Sample preparation	82
6.1.2	Changes in the band structure	84
6.1.3	Temperature dependent behavior	88
6.2	Ba _x Sr _{1-x} TiO ₃ Thin Films	91
6.2.1	Film preparation	91
6.2.2	Band dispersion of thin SrTiO ₃ films	92
6.2.3	Altering of the band structure by Ba doping	97
6.3	Conclusion	103
7	Conclusion and Outlook	105
	Acknowledgements	109
	Bibliography	132
	Curriculum Vitae	133

Introduction

A key working principle of semiconductor electronics is the control of the charge carrier densities and therefore the conducting properties by electric fields. An exemplary building block of modern integrated circuits are silicon based metal-oxide-semiconductor field effect transistors (MOSFET) where an insulating metal oxide layer separates the gate electrode from the main current carrying, doped semiconductor. By applying a potential to the gate electrode, the confinement of the two-dimensional electron gas (2DEG) at the insulator semiconductor interface is altered. This directly affects the charge carrier density of the 2DEG and therefore gives a control of the conducting properties in this device. Apart from the technical success of MOSFETs they also lead to the discovery of the integer and fractional quantum Hall effect originating from the response of the 2DEG to magnetic fields [1]. In 1965, Gordon Moore formulated his law that predicts a doubling of the complexity of low cost integrated circuits every year, which is, with some corrections, still describing today's developments [2]. By now the increase in complexity is realized by a continuous down scaling of the devices in the past years to a size of 10 nm of recent transistor structures. Apart from the economical and industrial challenges, the shrinking size also demands an increasing charge carrier density of the structures in use. The charge carrier density is in the order of 10^{12} cm^{-2} in silicon based devices and has to be higher than 10^{13} cm^{-2} for atomic-scale transistors [3]. To further increase the complexity of the building blocks in integrated circuits in the future, there are two possibilities; a further down-scaling, demanding higher carrier densities of the materials in use or, for the long term, the search and implementation of new working principles.

A promising way to find new working principles for possible future applications are systems with a strong interaction between their order parameters and a responsive behavior to external physical constraints. Transition metal oxides (TMOs) have a wide variety of exotic properties and are therefore promising candidates for new electronics and possible other new applications in science and technology. The properties found in TMOs range from ferroelectric, ferromagnetic, quantum paraelectric, multiferroic phases, and high-temperature superconductivity to physical phenomena like colossal magneto resistance, wide-range magnetic ordering and metal to insulator transitions [3–6]. Due to these properties, TMOs are already today an integral part of electronic devices used for example as dielectric ceramics in thin film capacitors or as piezoelectric materials in sensors and actuators. The variety of phenomena observed for TMOs are linked to the electron correlations of the transition metal

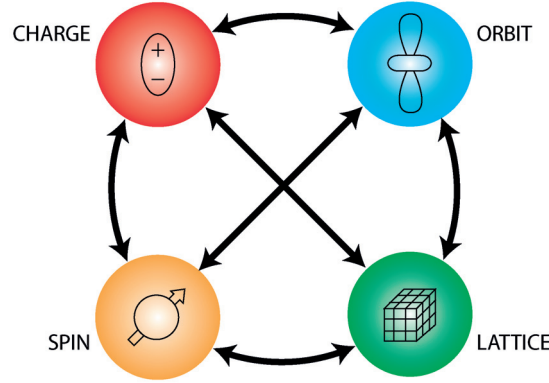


Figure 1 – The entanglement of the spin, orbit, charge and lattice degree of freedom responsible for the variety of properties of transition metal oxides (TMOs). (adapted from Ref. [5])

d orbitals, coupled with the interplay, ordering, and entanglement of the spin, charge, lattice, and orbital degree of freedom in these systems.

A vast contribution to the success of III-V semiconductors that are widely used in today's electronic devices is the matching lattice constant of compounds with different band gap energies. By this, a large palette of matching materials is available that enables the production of epitaxial grown interfaces with tailored energetic properties for specific applications. The lattice parameters of TMOs are also similar among each other and in the range of the lattice parameters of III-V semiconductors. Therefore by adding the TMOs to the available building blocks for semiconductor superstructures, the available possible functionalities are massively enhanced due to their various physical properties. This variety of properties is even richer by considering the phase diagram accessible by the intermixing and doping of TMOs. The fabrication of such structures with dedicated properties could serve a basis for the development of new electronic and spintronic devices. To make the properties of TMOs available for such future applications it is the challenge of today's condensed matter physics to explore the complex behavior of TMOs and find ways to manipulate their properties in a controlled way.

The solid-solid and solid-vacuum interfaces as well as heterostructures of TMOs open a platform to explore and disentangle the contributing factors responsible for the rich behavior of TMOs. The model concept of a TMO interface and the initial point of the emerged studies on these class of materials is the $\text{LaAlO}_3/\text{SrTiO}_3$ interface. At this interface of two insulating materials a 2DEG was discovered, showing carrier densities of up to $3 \cdot 10^{13} \text{ cm}^{-2}$ [7]. As a consequence of this finding, research on other oxide interfaces was triggered, for example the $\text{GdTiO}_3/\text{SrTiO}_3$ interface where also two-dimensional states were found, supporting even higher charge carrier densities [8]. Therefore TMOs, apart from providing numerous physical properties for novel working principles, are also prospective candidates to further down-scale electronic devices. The existence of a 2DEG at the interface of TMOs gives an opportunity to directly manipulate the system by external means as dimensionality, lattice strain or doping and therefore explore the interplay of the spin, charge, lattice and orbital degree of freedoms.

Soon after the discovery of a low-dimensional conducting channel at the $\text{LaAlO}_3/\text{SrTiO}_3$ interface and at the interfaces of other TMOs, the finding of a 2DEG at the vacuum surface of SrTiO_3 underlines the crucial role of SrTiO_3 in the formation of the interface 2DEG [9, 10]. The location of the 2DEG at the vacuum interface of the system further makes it approachable by surface sensitive experimental techniques giving new insight from different perspectives. SrTiO_3 is a TMO of the perovskite family and exhibits various of the properties found in other TMOs. It is a quantum paraelectric with high permittivity [11–13] and can exhibit ferroelectric phases under strain or by isotopic substitution [14–16]. It has superconducting properties under doping [17–19] and significantly increases the superconductive transition temperature of a FeSe monolayer grown on top [20, 21]. With these variety of properties present in SrTiO_3 , the two dimensional states at the vacuum interface of SrTiO_3 and related materials can serve as a model system to study the effects responsible for the formation of a 2DEG. It furthermore provides a playground to explore the interplay of the 2DEG with the various physical properties of TMOs.

In the first two chapters of this thesis, the relevant background regarding the two-dimensional electron gas (2DEG) at titanates surfaces and the titanate bulk properties is introduced. Chapter 1 is dedicated to the published findings regarding the two-dimensional states at titanates surfaces and gives an introduction to the interaction of strong electric fields with electrons in solids. Chapter 2 presents an overview of the basic properties of the materials studied. The chapter discusses the orbital ordering of the Ti $3d$ derived conduction band and the observed phases of CaTiO_3 , BaTiO_3 , and SrTiO_3 and their intermixtures with regard to their para- and ferroelectric properties. Chapter 3 is an overview of the experimental methods used in this thesis. The basic concept of angle-photoelectron spectroscopy (ARPES) is presented, followed by a description of the principle of pulsed laser deposition (PLD) growth and surface sensitive electron diffraction techniques; reflective high-energy electron diffraction (RHEED) and low-energy electron diffraction (LEED). Piezo-response force microscopy (PFM) as a method to investigate ferroelectric properties is reviewed in the last part of this chapter.

In the following chapters 4-6 the experimental results obtained during this thesis are presented. First, the results of the parent perovskite CaTiO_3 are discussed in chapter 4. The presented findings show a 2DEG at the surface of PLD grown CaTiO_3 films, that have a symmetry of the pseud-cubic unit cell of the orthorhombic CTO with folded band according to a $p(2\times 2)$ reconstruction. These results are accepted for publication in the manuscript "*Observation of a two-dimensional electron gas at CaTiO_3 film surfaces*" at *Applied Surface Science* [22].

Chapter 5 is dedicated to the findings at the surface of ferroelectric BaTiO_3 films, that are currently under review at *Physical Review Letters*. In BTO the ferroelectric properties are responsible for a Wannier-Stark localization of the electrons, leading to smeared states in reciprocal space. The strength of the intrinsic electric field of BTO is demonstrated by the observation of these effects in thin STO layers grown on top of BTO.

Contents

In chapter 6, different approaches to manipulate the formation of the 2DEG at the STO surface are shown. In a first attempt, vicinal surfaces are used to give a direct access to the surface structure of STO that result in a altered crystal field splitting. In STO thin films, as well as Ba doped STO films, the effect of altered dielectric and possibly ferroelectric properties on the STO 2DEG are investigated. By altering the 2DEG at the STO surface these results give an insight in the mechanisms responsible for its formation.

1 Basic background

This chapter gives an overview of the basic background and relevant literature for this thesis. The first part from Sec. 1.1 to 1.4 is dedicated to the 2DEG found at oxide interfaces and vacuum surfaces. The LAO/STO system is introduced as the emerging point of the in-dept study of the perovskite interface states in the past years. As a model system for the observed properties, the closely related 2DEG found at the surface of anatase TiO_2 is discussed in Sec. 1.2. Of central relevance to explain and compare the results of this thesis are the findings at the STO (001) surface that are elaborated in Sec. 1.3. In the last section of this chapter (Sec. 1.5) the concepts of the interaction of electrons in solids with strong electric fields, resulting in Bloch oscillations and Wannier-Stark localization is discussed. These concepts explain the results of BTO, presented in Chapter 5, where high intrinsic electric fields are present due to the ferroelectric properties of BTO.

1.1 The $\text{LaAlO}_3/\text{SrTiO}_3$ interface

The observation of a two-dimensional conduction channel at the interface between the two bulk isolators LaAlO_3 and SrTiO_3 by Ohtomo and Hwang [7] initiated the research on the electronic surface and interface properties of related oxides [23, 24]. For the 2DEG confined at the LAO/STO interface to exist, at least 4 uc of LAO are necessary, grown on TiO_2 terminated STO [7, 25]. The origin of the charge carriers that lead to the formation of the 2DEG is still under debate. One of the first hypothesis was that the polar stacking of LAO along the (001) direction is responsible for a charge accumulation at the interface and explains the critical thickness of 4 uc for the observation of the 2DEG [26]. However, this scenario contradicts with the finding of interface states at the (111) and (110) LAO/STO interface that exhibit different interface polarity [27] and also the predicted charge carrier density is not found in experiments [25, 28]. Therefore other effects as oxygen vacancies [29, 30] and interface intermixing leading to a La doping in STO [31] likely also play a role in the formation of the 2DEG. The interface strain could also give rise to an octahedral rotation in the STO interface layers, making the structure of the interface another possible factor, responsible for the 2DEG formation [32, 33].

The confined 2DEG at the LAO/STO interface exhibits, apart from its conductivity other interesting physical properties as superconductivity, ferromagnetism, magnetoresistance and a tunable Rashba splitting. 2D superconductive properties of the LAO/STO interface were reported below a temperature of 200 mK that can be tuned by a gate voltage [34–36]. Furthermore the interface shows ferromagnetic properties that seems to coexist with the superconducting properties [37–39]. The interface 2DEG further shows a linear magnetoresistance at high temperature and a negative magnetoresistance at low temperature [37, 40]. Responsible for the negative magnetoresistance is a Rashba-type splitting of the 2DEG that can be modulated by an external electric field [41].

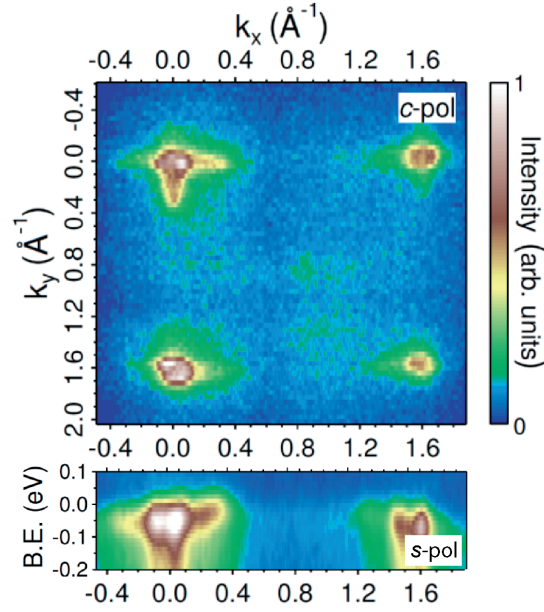


Figure 1.1 – Measured soft x-ray ARPES Fermi surface and band structure of the 2DEG at the LAO/STO surface at $h\nu = 460.5$ eV, corresponding to the Ti L-edge (from [28]).

The bands forming the 2DEG originate from the Ti 3d states. The orbital configuration is given by a tetragonal distortion of the TiO_6 octahedron, responsible for a splitting of the t_{2g} manifold in the low effective mass d_{xy} band at higher binding energy, and the d_{xz}/d_{yz} bands at lower binding energy with a heavier effective mass [42, 43]. Despite the location of the 2DEG below at least 4 uc of LAO, ARPES measurements can be obtained by the use of light in the soft X-ray range (see Sec. 3.1.2). This is possible due to the increased probing depth and the resonant enhancement at the Ti L-edge [28, 33, 44]. The Fermi surface shows a clear signal of the two heavy bands, elongated in $\overline{\Gamma X}$ direction and indications of the light d_{xy} bands in the band structure. The size of the Fermi surface further corresponds with the charge carrier density obtained in transport measurements (see Fig. 1.1) [28]. The 2DEG at the LAO/STO interface is confined asymmetrically in the STO side of the interface decaying within 2 nm, with a tail of up to 11 nm [45, 46]. Therefore, the electronic properties of the interface state are expected to be related to the electronic structure of the TiO_2 terminated STO to vacuum interface.

1.2 Anatase TiO₂

The TiO₂ surface is a famous material due to its photocatalytic properties that are brought to application for example in purification systems and can assist to decompose water with visible light [47–49]. With its similarities regarding the crystal structure and orbital ordering, anatase TiO₂ can serve, to a certain extend, as a model system to understand the electronic properties of the titanate perovskites with a TiO₂ vacuum termination. In TiO₂ the building block of the unit cell is the TiO₆ octahedron [see Fig. 1.2 (a)]. The conduction band of TiO₂ is therefore formed by the Ti 3d band with an ordering given by the distortion of the octahedron and the respective bonding angles between them (see also Chapter 2.1). Band structure calculations reveal that the bottom of the conduction band has primary d_{xy} character.

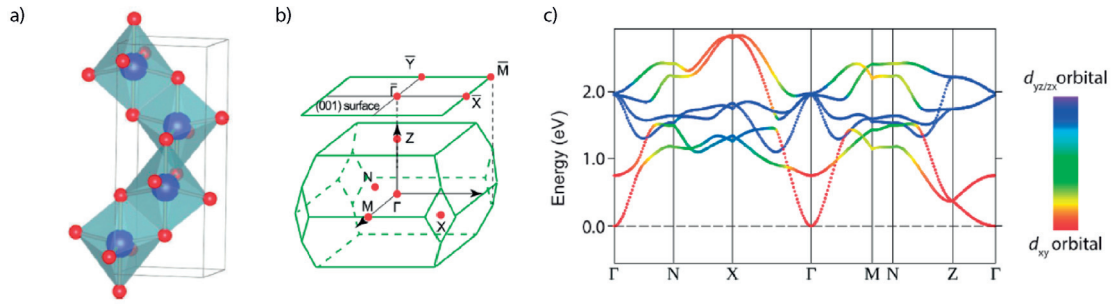


Figure 1.2 – (a) Crystal structure of anatase TiO₂ with its Brillouin zone (b). (c) Calculated band structure of the Ti 3d conduction band with denoted orbital character (from [50]).

The anatase TiO₂ (001) surface is highly reactive and energetically less stable than other surface terminations [51, 52]. Therefore oxygen vacancies can be created by UV irradiation of the surface [53] and are responsible for the availability of excess electrons. These electrons are strongly coupled to the lattice by Coulomb interaction that leads to the formation of mobile, large polarons at low charge carrier densities, contributing to the metallic properties of the system [54, 55]. The metallic state exhibits a 3D dispersion of d_{xy} character, with shifted replicas at higher binding energies (see Fig. 1.3). These replica bands are separated by the energy of an optical phonon and indicate the existence of polarons [54]. The origin of the charge carriers in the oxygen vacancies created by light irradiation allows a control of the charge carrier density by oxygen dosing [54].

Later ARPES studies of anatase TiO₂ films show a more 2D nature of the d_{xy} bands, due to the stronger 2D confinement in the films [50]. The d_{xy} band is furthermore split into two subbands and is also observed at the (101) surface and the (4×1) reconstructed surface. At the (101) surface, the anisotropy of the surface is reflected by an anisotropic mass of the d_{xy} electrons resulting in an ellipsoidal Fermi surface [56]. At the reconstructed (4×1) surface, the folding of the Fermi surfaces is responsible for a gap opening at the overlap of the Fermi surfaces [50]. Metallic states have only been observed at the surface of anatase TiO₂ and not for the closely related rutile TiO₂, although light induced oxygen vacancies are also known to be created at both surfaces. However, the different crystal structure leads to the formation of

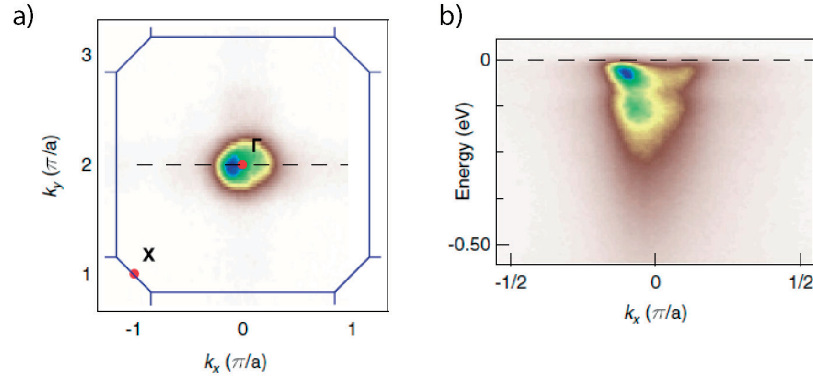


Figure 1.3 – (a) ARPES Fermi surface and (b) band structure of anatase TiO₂ with a charge carrier concentration of $n_{e^-} \approx 3.5 \times 10^{19} \text{ cm}^{-3}$, measured with $h\nu = 85 \text{ eV}$ (from [54]).

more localized polarons with no metallic properties, demonstrating the importance of the surface crystal arrangement for the formation of 2D states [54–56].

1.3 SrTiO₃(001) surface states

In early 2011, two studies were published, presenting results of a 2D metallic state at the surface of SrTiO₃(001) (see Fig. 1.4) [9, 10]. Santander-Syro et al. [9] published results of vacuum cleaved, undoped STO and samples with oxygen vacancies created by annealing. The metallic states measured with photonenergies of 45 and 47 eV and different light polarizations, consist of a concentric pair of bands with a light effective mass and a band bottom around 220 meV. Additionally there is a more shallow band with a higher effective mass observed close to the Fermi energy. None of the bands are altered with the induced bulk oxygen vacancies by annealing and show a charge carrier density of $n_{e^-} = 2 \times 10^{14} \text{ cm}^{-2}$. Santander-Syro et al. [9] attribute the existence of the 2D states to a surface band bending caused by oxygen vacancies, located at the surface as an effect of the cleaving.

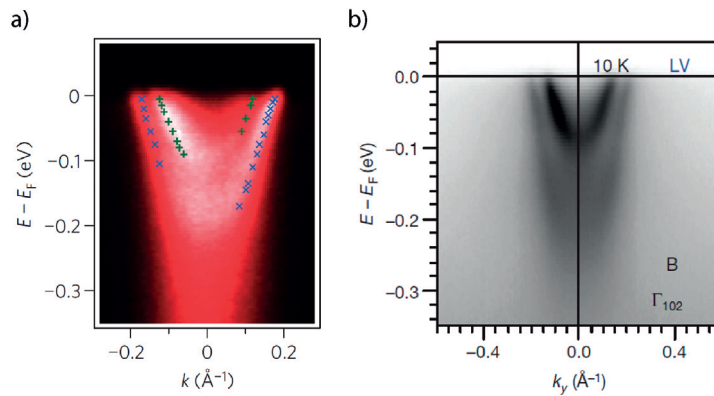


Figure 1.4 – ARPES measurements of the 2D electron gas (2DEG) at the surface of STO. (a) Results of Meevasana et al. [10] and (b) results of Santander-Syro et al. [9].

Meevasana et al. [10] published result of lightly La-doped STO cleaved crystal surfaces. The observed Fermi surface, measured with a photon energy of $h\nu = 55$ eV, consist of two concentric rings with a band bottom similar to the results of Santander-Syro et al. [9]. No dispersion of the states was observed at photon energies between 45-65 eV, suggesting a two-dimensional nature. The surface charge carrier density of the 2D state was found to increase under synchrotron irradiation and to saturate at a value of $n_{e^-} = 8 \times 10^{13} \text{ cm}^{-2}$. The presence of the 2D states is accompanied by the formation of an in-gap state at a binding energy of 1.3 eV that shows an increasing photoemission intensity with irradiation. Therefore the authors suggested the creation of oxygen vacancies by UV irradiation to be responsible for a downwards band bending at the STO surface leading to the occupation of the 2D electronic states at the surface.

Indications for the existence of metallic states at the STO surface can already been found in earlier works. In angle integrated photoemission data, a clear signature of the in-gap state at approximately 1.3 eV with intensity close to the Fermi energy was observed [57, 58]. The work of Aiura et al. [59] showed a clear, sharp peak at the Fermi level additionally to the in-gap states in the angle-integrated photoemission intensity. This peak can be suppressed by oxygen dosing of very small amounts, suggesting that the appearance of the state is directly related to the surface properties of STO. Similar bands as found at the STO surface in [9, 10] were already reported by Meevasana et al. [60] in 2010 on lightly La doped, oxygen deficient STO. The reported bands consist of states with a heavy effective mass, that disperse with photon energy and states with low effective mass that do not disperse with photon energy, indicating their 2D nature [60].

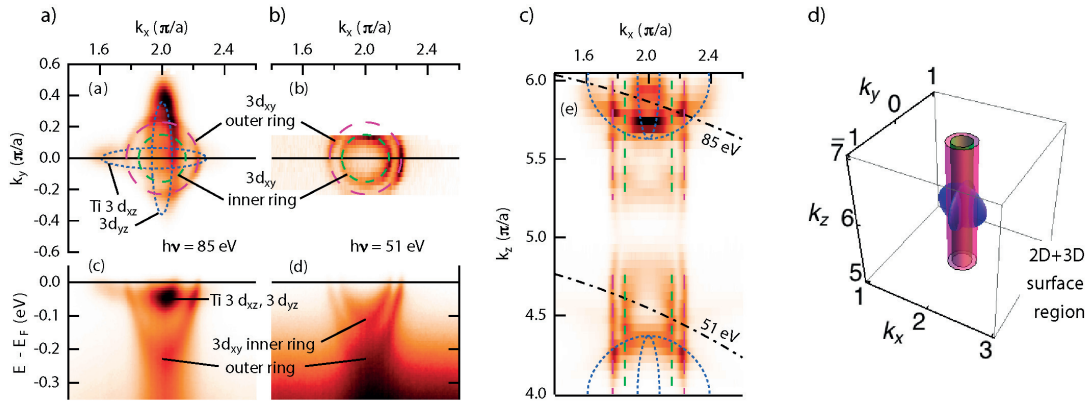


Figure 1.5 – (a) ARPES Fermi surface and band structure measured with $h\nu = 85$ eV close to the Γ point. (b) ARPES Fermi surface and band structure between two Γ points at $h\nu = 51$ eV. (c) Dispersion along k_z of the second Brillouin zone, obtained by scanning the photon energy from $h\nu = 35$ eV to 95 eV. (d) Representation of the 2D and 3D bands in reciprocal space (from [61]).

The findings of Santander-Syro et al. [9] and Meevasana et al. [10] both show two concentric bands, with similar charge carrier densities and comparable band bottoms that are likely 2D. However, one difference is the appearance of a third band in the measurements of Santander-

Syro et al. [9] at a photon energy of $h\nu = 47$ eV, that is absent in the measurements of Meevasana et al. [10]. This resulted also in a different interpretation of the orbital origin of the observed states. Later studies of Plumb et al. [61] addressed this issue by studying the states at the surface of TiO₂ terminated STO crystals, with in-situ preparation instead of cleaving, over a larger photon energy range. The states are found to consist on one hand of two sheets of 2D bands showing no dispersion with photon energy and on the other hand 3D dispersing bands, located in the vicinity of the Γ points (see Fig. 1.5). These findings explain the different observations of the previous papers at different photon energies.

In measurements with different light polarizations, the orbital origin of the 2D and 3D band can be clearly identified [62]. The two concentric light bands with a 2D dispersion originate from the Ti $3d_{xy}$ orbitals probed with s -polarized light. The 3D bands with larger effective mass have character of the Ti $3d_{yz}$ and Ti $3d_{xz}$ orbitals, probed with s - and p -polarized light respectively (see Fig. 1.6 and Sec. 3.1). The d_{xy} , d_{xz} and d_{yz} bands of the t_{2g} manifold are split in energy due to a distortion of the TiO₆ octahedron (compare Sec. 2.1). The 2D nature of the d_{xy} orbitals indicates their surface localization. The disk shape of the 3D d_{xz}/d_{yz} bands in reciprocal space (see Fig. 1.5) is distorted from the ellipsoidal shape of the d_{xz}/d_{yz} expected in the bulk (see Sec. 2.1). Therefore, although they are dispersing with photon energy, they are not completely bulk like, but confined in a larger volume close to the surface than the d_{xy} bands [61, 63]. The measured dispersion of the metallic state at the STO surface with 2D d_{xy} and 3D d_{xz}/d_{yz} bands is accordingly similar to the dispersion observed at the LAO/STO interface (see Sec. 1.1).

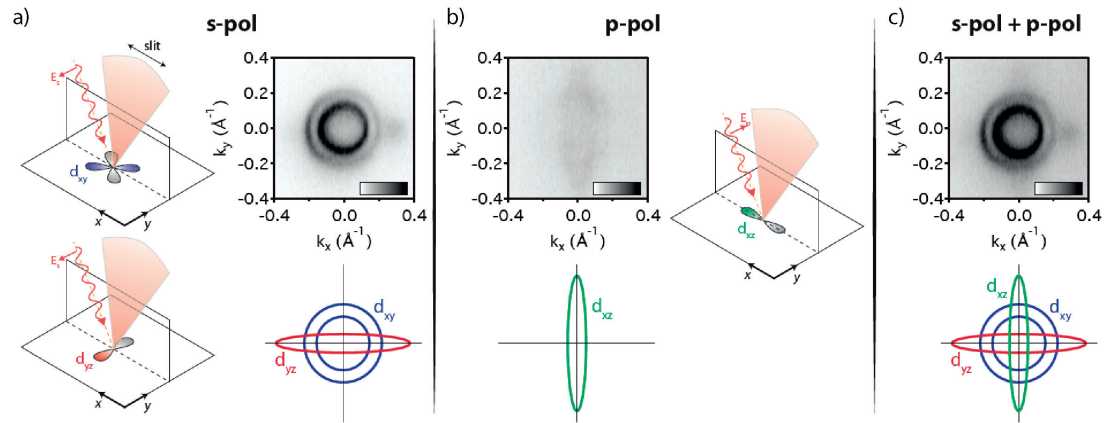


Figure 1.6 – (a) Measured Fermi surface with s -polarized light, probing the d_{xy} and d_{yz} orbitals. (b) ARPES Fermi surface with s -polarized light probing the d_{xz} orbital. (c) Composed Fermi surface, exhibiting all three orbital contributions. (from [62])

In both of the first papers, light-induced oxygen vacancies were assigned to be the main driving force for the formation of the metallic states at the STO surface [9, 10]. However, the formation of the states is observed on a range of differently prepared samples, with and without oxygen bulk defects and different dopings [61] and can even be suppressed by a high amount of bulk oxygen vacancies induced by high-temperature annealing [64]. Plumb et al.

[61] further investigated the UV-induced changes by time dependent measurements of the angle integrated photoemission intensity. Under UV-irradiation, the carrier density of the metallic states saturates very quickly to a similar value in all the reported experiments on STO surfaces regardless of the preparation method. After the saturation of the charge carrier density is reached, the photoemission intensity of the metallic states is observed to increase further. This change is accompanied by an increase of the intensity of the in-gap state, a decrease of the valence band intensity, and a weight shift to shoulders of the O, Ti and Sr core levels (see Fig. 1.7). The changes in the O 1s level, as well as the creation of a shoulder in the Ti 2p corelevel, attributed to Ti 3⁺, can be associated with the creation of oxygen vacancies. The decrease of the O 2p valence band intensity, however, is much larger than the observed changes in the O 1s corelevel, indicating a change of the hybridization and therefore of the structural arrangement in the surface region. The observed change in the intensity of the Sr 3d corelevel also points in this direction and could be due to excess Sr or SrO at the surface. Therefore it is likely that light induces changes of the surface lattice arrangement contributing to the formation of the surface metallicity of STO. This rearrangement is stable after the first irradiation, defining the charge carrier density, but will extend over a larger portion of the sample surface with time, responsible for the continuous increase of photoemission intensity [65].

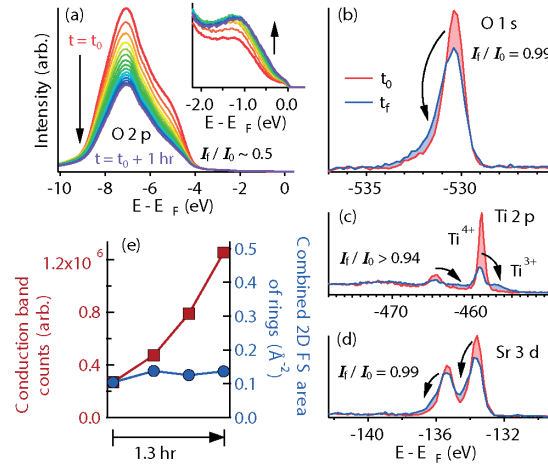


Figure 1.7 – (a) Angle-integrated photoemission intensity of the STO valence band and in-gap state (inset) under UV-irradiation as a function of time. (b-d) Intensity changes of the O 1s corelevel (b), the Ti 2p corelevel (c) and the Sr 3d corelevel (d). (e) Development of the conduction band photoemission intensity and charge carrier concentration with time. (from [66])

1.3.1 Rashba-like spin splitting

Spin-resolved ARPES measurements reveal a strong spin polarization of the two d_{xy} bands forming the 2DEG at the STO surface (see Fig. 1.8) [66]. The two concentric parabola show a helical spin texture with opposite winding directions for the inner and the outer band. The

magnitude of the spin polarization is 100% at the Fermi energy and is decreasing towards the bottom of the inner as well as the outer band. At the Γ -point the degeneracy of the bands is lifted with no noticeable spin polarization. The obtained measurements are consistent for different light polarization (s -, p - and circularly polarized light) and photon energies of $h\nu = 47$ eV and 52 eV. The observed spin texture of the two d_{xy} band therefore matches with a Rashba-like splitting.

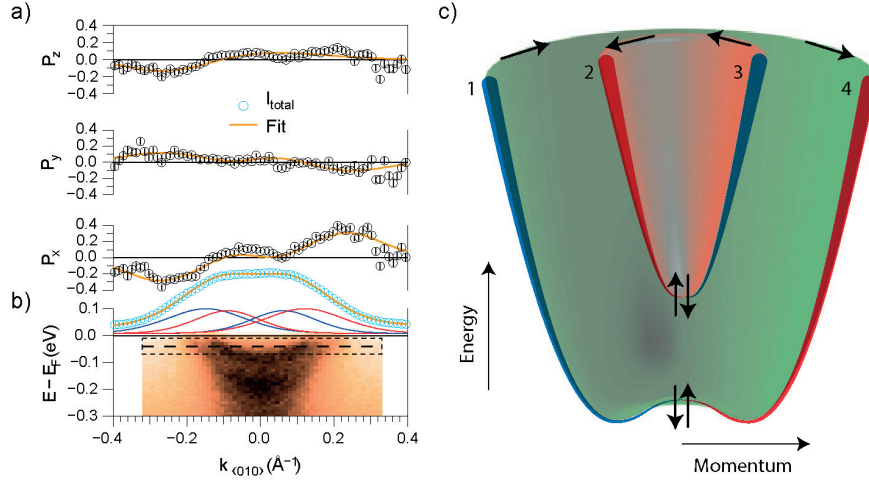


Figure 1.8 – (a) Spin polarization with respect to the three spatial coordinates obtained from spin-resolved ARPES at the Fermi energy. (b) Total intensity of the spin-resolved measurements with fitted peak intensities of the four peaks visible in the ARPES bandmap. (c) Schematic picture of the spin polarization of the STO 2DEG with arrows denoting the direction of the spin polarization and the thickness the magnitude of the polarization. (from [66])

A Rashba-type spin splitting occurs from the asymmetric potential due to the inversion symmetry breaking at the crystals vacuum termination [67, 68]. By Lorentz transformation, the electric field gradient at the surface results in a magnetic field in the rest frame of the electron and therefore lifts the spin degeneracy. The momentum and the spin direction of the degenerate bands are locked orthogonally to each other, resulting in a helical spin texture. A Rashba-like spin splitting is observed at the surface of a variety of system [69–74]. However, the magnitude of the splitting of 100 meV, reported for STO is significantly larger than expected. In order for a splitting of this size to exist, the local potential gradient at the surface has to be enhanced. This could possibly be explained by a polar buckling of the surface, resulting in an increased Rashba splitting [75, 76]. Possible ferroelectric properties enhance the Rashba splitting even further [77]. A Rashba-type splitting was also reported to exist at the LAO/STO interface [41]. Although the splitting at the LAO/STO interface is considerably smaller than the splitting at the STO surface, it is also highly sensitive to an applied gate voltage and therefore likely also to changes of the potential gradient at the STO surface [65].

Furthermore to explain the lifted degeneracy at the Γ -point, the time-reversal symmetry at the surface needs to be broken by local magnetic properties of the STO surface. The type of these properties and their origin is unknown, but experimental evidence of magnetic properties

of the STO surface exist [78, 79] (see also Sec. 2.2.3). The absence of an out-of-plane spin polarization at the Γ point matches with the presence of oppositely polarized ferromagnetic domains. Therefore the existence of a splitting of the observed size can be explained by the local surface properties of STO [80–82].

Nevertheless, the spin-texture of the STO 2DEG and its origin is still under debate. A publication of Walker et al. [83] found a different spin-polarization of the STO 2DEG, with no indication of a helical spin texture of the two d_{xy} band. They suggest a rather small Rashba-like splitting that splits the two d_{xy} band each into sub bands. These measurements were taken at photonenergies of $h\nu = 80$ eV and 100 eV and therefore closer to the Γ -point with contributions from the heavy d_{xz}/d_{yz} bands (see Fig. 1.5). Additionally the higher photonenergies also results in a different coupling to the final states in the photoemission process. Further measurements will have to clarify whether the differences in the observed spin texture are of intrinsic nature or related to the experimental conditions.

1.4 Surface states of other SrTiO₃ terminations and KTaO₃

Apart from the well studied 2DEG at the STO(001) surface, metallic states were also found at other STO surface terminations. At the STO(111) surface, three bands, derived from the d_{xy} , d_{xz} and d_{yz} orbitals, form a sixfold symmetric Fermi surface [see Fig. 1.9(a,b)] [84, 85]. The STO (110) surface also exhibits metallic states, consisting of the d_{xy} derived band and d_{xz}/d_{yz} band with anisotropic masses due to the given hopping probabilities of the orbitals at the (110) surface termination [see Fig. 1.9(c-e)] [84, 86].

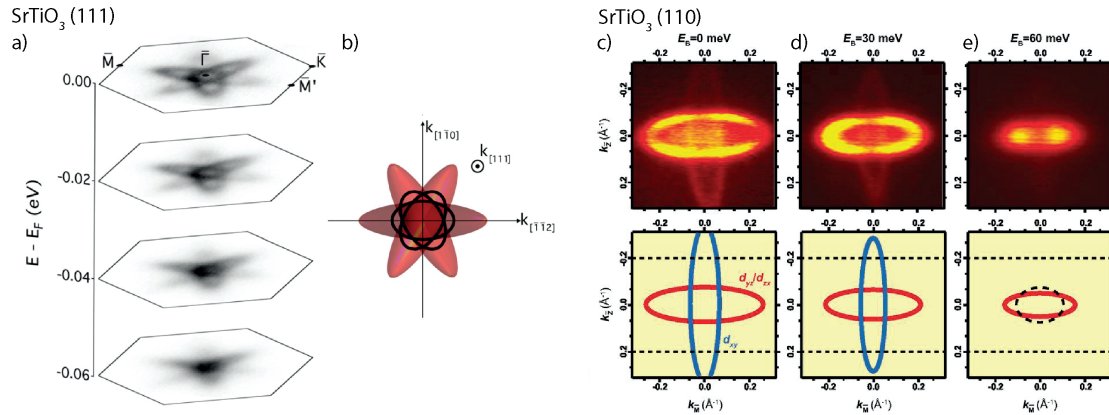


Figure 1.9 – (a) Constant energy surfaces of STO (111) at different binding energies measured with $h\nu = 108$ eV, circularly polarized light. (b) Top view of the schematic representation of the bulk Fermi surface of STO viewed from the $\langle 111 \rangle$ direction. Black lines indicate a cut through the Γ -point. (from [85]). (c) Constant energy surfaces of STO(110) at the Fermi energy, $E_B = 30$ meV and $E_B = 60$ meV with schematic representations of the constant energy surface. (from [86])

The findings of a 2DEG at the STO surface also initiated investigations on other perovskites and lead to the discovery of confined bands at the surface of KTaO_3 . KTaO_3 is a $5d^0$ oxide and has similar properties as STO regarding its dielectric properties and quantum paraelectric behaviour (compare Sec. 2.2.3). Due to the increased mass of tantalum the spin-orbit coupling effects are expected to be higher, compared to STO. For KTaO_3 metallic states are reported to exist at its (001) and (111) surface. The KTaO_3 (001) surface shows a strong splitting between the d_{xy} , d_{xz} and d_{yz} bands [63, 87]. The KTaO_3 (111) surface also shows metallic bands with a sixfold symmetric structure [88].

The finding of metallic states at different surface termination of SrTiO_3 and KTaO_3 implies that also other perovskites are likely to host a 2DEG at their surface. In this thesis results of the perovskites BaTiO_3 (Chap. 5) with its well known ferroelectric properties and of CaTiO_3 also exhibiting dielectric and quantum paraelectric properties similar as STO and KTaO_3 are presented (Chap. 4).

1.5 Influence of an electric field on electrons in solids

In ferroelectric materials like BaTiO_3 (Chapter 5), the intrinsic electric field acts on the electrons in the crystal. The effects of an electric field on the electrons in a solid are the basis of electric transport in crystals. One of the first descriptions of electronic transport in a solid is given in the Drude model. This model is based on the assumption that electrons in a solid act like a gas without interaction between the electrons. However, collisions with the positively charged ions of the crystal are possible. The acceleration of the electrons (mass m_e , charge $-e$) in an applied electric field $\vec{\mathcal{E}}$ is therefore described as the acceleration of a free electron, damped by a frictional force [89].

$$m_e \dot{\vec{v}} = -e\vec{\mathcal{E}} - m_e \frac{\vec{v}}{\tau} \quad (1.1)$$

The damping depends on the so-called relaxation time τ that gives the scatter probability of the electrons on the ions per time as $1/\tau$. The relaxation time is therefore the time the electron can be freely accelerated in the solid, which results in a average drift velocity of the electrons given by the electric field as

$$\vec{v} = \frac{-e\vec{\mathcal{E}}\tau}{m_e} \quad (1.2)$$

that is opposite to the applied electric field. The picture of the Drude model with scattering of the electrons on the ions does not agree with the observation of an increasing relaxation time at lower temperatures. In a quantum mechanical description of the electron as a Bloch Wave no scattering of the electrons with the ions is possible. The reason for a finite relaxation time

1.5. Influence of an electric field on electrons in solids

is the scattering of the Bloch Wave on lattice imperfections and electron-phonon interactions [90]. The relaxation time is typically in the order of $\tau = 10^{-14}$ s and is linked to the mean free path λ of the electron in the crystal and the Fermi velocity v_F of the electrons as $\tau = \lambda / v_F$ [89, 90].

In a semi classical picture, the effect of the electric field on an electron is described by Bloch's acceleration theorem as an equation of motion in reciprocal space [89–91].

$$\hbar \frac{d\vec{k}}{dt} = -e\vec{\mathcal{E}} \quad (1.3)$$

This implies a continuous change of k of the electrons with time, if an electric field is present. However, the acceleration is stopped by the inelastic scattering of the electrons on the lattice defects. The size of the momentum dislocation δk of the electrons is therefore given by the relaxation time τ responsible for a finite resistance in the electron transport. In a band structure picture (see Fig1.10) the electrons of a partially filled metallic band are dislocated by δk after a time δt opposite to the electric field \mathcal{E} . The probability to scatter from $+k_F$ to $-k_F$ depends on the relaxation time and is given by $1/\tau$ [92].

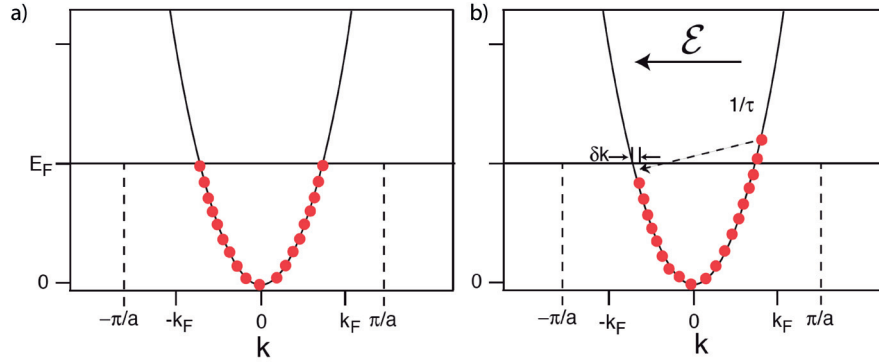


Figure 1.10 – Illustration of the effect of an electric field on the band structure and therefore the transport properties of a metal. (a) Partially filled band without external electric field. (b) Band after turning on an electric field \mathcal{E} . Electrons get dislocated by δk . The probability of an electron with $+k_F$ to scatter back to $-k_F$ is given by $1/\tau$. (from [92])

The finite value of the relaxation time therefore sets a limit to the electron movement in a solid. We now consider the behavior of electrons that do not experience any scattering, so with infinite τ . According to the acceleration theorem in eq. 1.3 the electrons experience a displacement in k as a function of time t . In a periodic energy dispersion as shown in Fig.

Chapter 1. Basic background

1.11(a), the electrons are displaced until they reach the energy maximum of the band at the zone boundary. The group velocity v_g of the electrons during this movement

$$v_g = \frac{1}{\hbar} \frac{\partial E(k)}{\partial k} \quad (1.4)$$

will reach a maximal value on the maximal slope of the energy dispersion $E(k)$ and then go to zero at the zone boundary [point A in Fig. 1.11(a)]. Due to the periodicity of the dispersion, the electron is scattered to the equivalent point A'. With the negative slope, the group velocity becomes negative until the zone center is reached (Fig. 1.11) [93]. This motion of the electron in the periodic band structure is called Bloch oscillation.

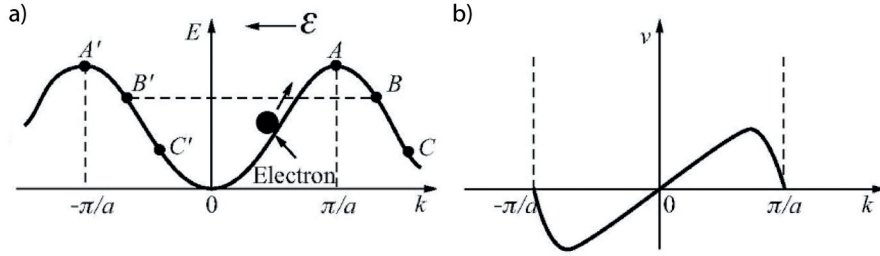


Figure 1.11 – (a) Movement of the electron in a periodic dispersion with applied electric field. (b) Group velocity of the electrons during the movement in (a). (from [93])

With the periodic change in group velocity, Bloch oscillations also exhibit an oscillating motion of the electrons in real space that should result in an AC current when a DC voltage is applied to the sample. The frequency ω_B of the AC current is related to the applied electric field and the lattice constant of the system a [92].

$$\omega_B = \frac{e\mathcal{E}a}{\hbar} \quad (1.5)$$

Therefore the time for one oscillation cycle is given as

$$\tau_B = \frac{h}{e\mathcal{E}a} \quad (1.6)$$

The initial consideration was an infinite relaxation time of the system. This explains, why the AC current of Bloch oscillations cannot be measured in real world crystals. The effect could only be observed if the electron can finish one or more oscillation cycles before being scattered at lattice defects. This means, the oscillation time τ_B would have to be smaller than the relaxation time τ of the system. With a typical relaxation time of $\tau = 10^{-14}$ s and a

1.5. Influence of an electric field on electrons in solids

lattice constant of $a = 4 \text{ \AA}$ an electric field of $1 \times 10^9 \text{ V/m}$ would be necessary to observe Bloch oscillations, that is above the break down voltage of known isolators.

Whereas in Bloch oscillations the effect of the electric field on the electrons in a solid is discussed in the time domain, the Wannier-Stark ladder is a description of the same effect in the energy domain [94]. Wannier solved the Schrödinger equation for a periodic potential with an applied electric field, considering the altered kinetic and potential energy of the system. For a system with periodic potentials, given for example by a crystal lattice, without an electric field applied, the electron wavefunctions are delocalized over the whole system. If the electric field is turned on, the periodic potential becomes asymmetric and the electrons start to be localized in the potential wells (see Fig. 1.12) [95]. The higher the electric field, the more localized are the electrons in the periodic potential. This effect of the localization of the electrons in a periodic potential by an applied field is called a Wannier-Stark localization.

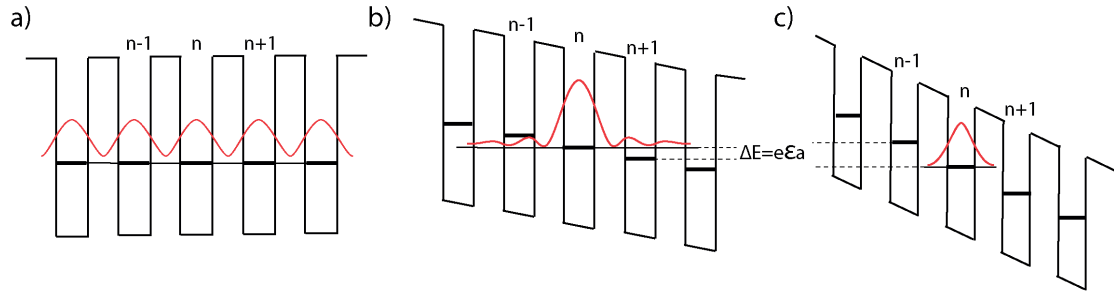


Figure 1.12 – (a) Delocalized electron wavefunction in a periodic potential. (b) Wannier-Stark localization in a periodic potential by applied electric field. (c) Stronger localization by increased electric field. (adapted from [95])

The localization of the electrons in the potential wells results in an energy spectrum that is no longer continuous, but separated in discrete energy levels with a separation proportional to the electric field. The electron wave functions are therefore separated in space by the periodic wells and in energy by the electric field and form a so-called Wannier-Stark ladder [93, 95, 96]. The energy separation between two adjacent energy levels is given as:

$$\Delta E = e\mathcal{E}a = \frac{h}{\tau_B} \quad (1.7)$$

Like in the picture of the Bloch oscillations, the localization of the electrons can also be seen as an oscillating motion in the unit cell and is therefore also restricted by the scattering events [89]. In the energy picture the formation of a Wannier-Stark ladder takes place when the scattering induced broadening of the states is smaller than the energy separation [94].

The experimental restrictions regarding the magnitude of an external applied field were overcome by the fabrication of high quality layered superlattices. In superlattices the size of

the periodic potential a can be increased and the low defect density increases the relaxation time τ of these systems. By this, the necessary electric field to observe Bloch oscillations is significantly reduced. This was successfully demonstrated for the first time by Mendez et al. [97] in a GaAs/GaAlAs superlattice with a periodicity of 65 Å. The stronger localization of the valence band electrons due to their heavier mass allows optical absorption between the localized states in the valence band and still delocalized states in the conduction band. The absorption peaks shift with applied electric field from the $n = 0$ transition (see Fig.1.13). At high electric fields, the levels disappear due to the localization of the wavefunction in the conduction band.

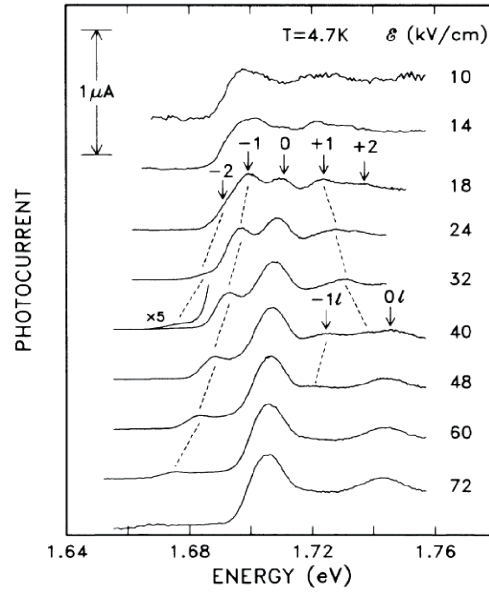


Figure 1.13 – Results of Mendez et al. [97] showing the photocurrent of a GaAs/GaAlAs superstructure with different applied electric fields.

The existence of Bloch oscillations and Wannier-Stark ladders in crystalline structure opens various possible applications. Bloch oscillations could serve as a source for electromagnetic radiation with variable frequency controlled by the electric field. This is one of the attempts to produce emitters with frequencies in the THz gap [98–100]. The tunable energy gap in the Wannier-Stark ladder could for example be used for lasers with a tunable wavelength [101].

The occurrence of Wannier-Stark localization in single crystals is limited by the external electric field that can be applied. Apart from changing the periodicity as it is done in superlattices, this problem can also be addressed by utilizing intrinsic electric fields of ferroelectric material. In chapter 5 the effect of the intrinsic electric field of ferroelectric BaTiO₃ on the conduction band electrons is presented. The high fields are responsible for a localization of the electrons in real space, and consequently for a delocalization in reciprocal space.

2 Bulk properties of titanates

The aim of this chapter is to give a general overview of the properties of the titanates CaTiO_3 , BaTiO_3 and SrTiO_3 studied in this thesis. In the first part, the perovskite lattice with its atomic arrangement and the implications on the Ti $3d$ conduction band are discussed. Of central importance for the orbital arrangement of the conduction band is the octahedral field of the TiO_6 octahedron, energetically splitting the t_{2g} and e_g manifolds. The effects of a distortion of the TiO_6 octahedron on the orbital ordering are pointed out. In the second part the phases, with special regard to the para- and ferroelectric properties of CTO, BTO and STO are discussed. Apart from the bulk properties, effects related to the vacuum termination as well as effects related to the film growth are reviewed. The last part focuses on the properties of intermixtures between the three materials giving rise to para-, ferro- and antiferroelectric properties.

2.1 Orbital ordering in titanates

The general composition of titanates and perovskites is described with ABO_3 . The A-site placed in the center of the unit cell, is usually occupied by a alkaline earth or rare earth metal. The B stands for the transition metal oxide, sitting on each of the eight corners of the unit cell. Each B-site then forms together with the surrounding six oxygen atoms an octahedron (see Fig. 2.1). In the case of the titanates, the transition metal oxide at the B-site is titanium and the A-site, in the materials presented in this thesis, either strontium, calcium or barium. In this structure the A- and B-site are electron donors, donating 2 and 4 electrons respectively to the three oxygen atoms which results in two additional electrons per oxygen atom. The material can also be seen as charge neutral layers of $\text{A}^{2+}\text{O}_2^{2-}$ and $\text{Ti}^{4+}\text{O}_2^{2-}$ stacked in the $\langle 001 \rangle$ direction.

The band ordering of the titanates in the proximity of the Fermi energy is determined by the O $2s$, the O $2p$ and the Ti $3d$ and Ti $4sp$ bands. In the formation of the octahedron, the octahedron crystal field leads to a splitting of the Ti $3d$ state energetically separating the 3-fold degenerate t_{2g} consisting of the d_{xy} , d_{yz} and d_{zx} orbitals from the 2-fold degenerate e_g orbitals $d_{x^2-y^2}$ and d_{z^2} [see (1) in Fig.2.2(a)]. The t_{2g} orbitals are lower in energy due to their alignment between the Ti-O bond axis in the TiO_6 octahedron while the e_g orbital are

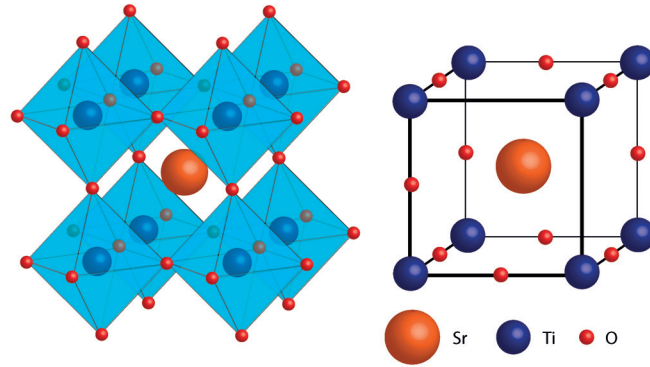


Figure 2.1 – Crystal structure of the ABO_3 perovskites illustrated on the example of cubic $SrTiO_3$.

aligned along the bond axis. The O $2p$ states are also split into the P_σ and the P_π orbitals in the octahedral crystal field. The resulting states are on one hand the valence band, formed by the O $2p$ bands, hybridized with the Ti $4sp$ and Ti $3d$ states and on the other hand the unoccupied conduction band formed by the Ti $3d$ bands, partially hybridized with the O $2s$ and O $2p$ bands. This results in the band structures of bulk titanates, showing an indirect bulk band gap between the O $2p$ and Ti $3d$ states of several electron volts for the studied $SrTiO_3$, $BaTiO_3$ and $CaTiO_3$ (see Fig. 2.2(c) for the calculated band structure of $SrTiO_3$).

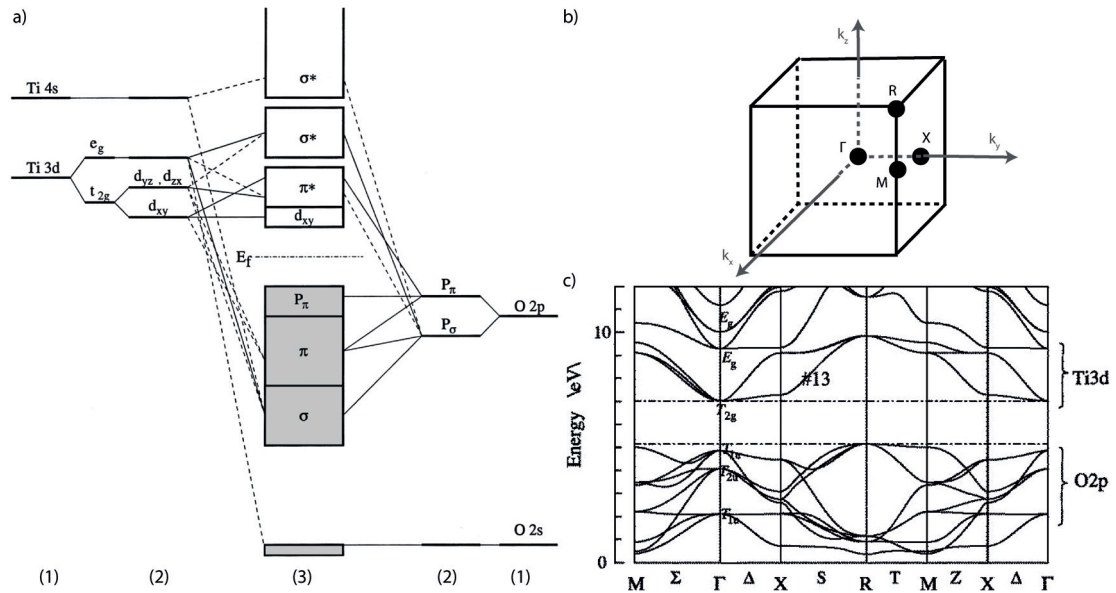


Figure 2.2 – (a) Orbital bond structure of titanates by the example of TiO_2 anatase (from [102]). (1) Atomic levels, (2) crystal-field split levels and (c) final, hybridized states. (b) Brillouin zone of a cubic simple lattice with marked symmetry points. (c) Calculated band structure of cubic STO (from [103]).

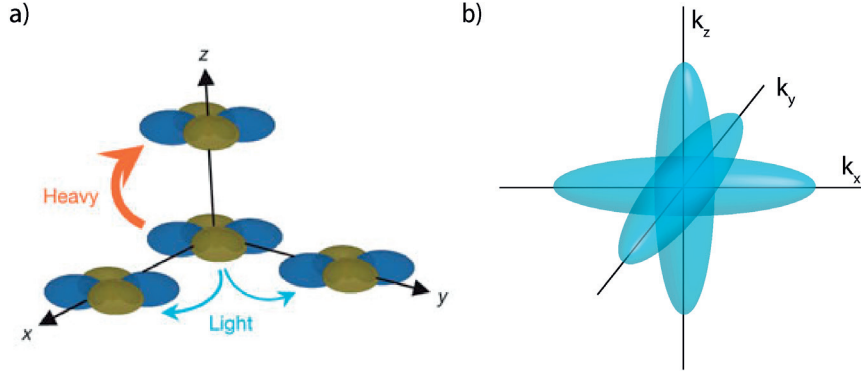


Figure 2.3 – (a) Geometry of the orbitals of the t_{2g} manifold in real space on the example of the d_{xy} orbital (from [9]). (b) Band dispersion of the Fermi surface in reciprocal space of the d_{xy} , d_{xz} and d_{yz} orbitals.

The band dispersion of the t_{2g} manifold that forms the conduction band bottom, after the splitting in the octahedral field is given by the hopping probabilities. The situation is exemplary shown for the d_{xy} orbital in Fig. 2.3(a). Due to the location of the d_{xy} band in the xy-plane, the hopping probability to the neighboring orbital in the plane is higher than in the z-direction to the next layer. With the increased hopping probability in the x- and y-direction, the electron mass is low in these directions and high in z-direction. This results in a Fermi surface contribution of the d_{xy} orbital in form of a band with the shape of an ellipsoid, elongated in z-direction [see Fig. 2.3(b)]. The same principle applies for the d_{xz} and d_{yz} orbital with Fermi surfaces elongated in the y- and z-direction respectively. The Fermi surface of the t_{2g} orbitals in the octahedral field without distortion therefore consist of three ellipsoidal shaped band from the contribution of the three orbitals [see Fig. 2.3(b)].

The octahedral field, responsible for the splitting of the Ti 3d bands can further be responsible for a energy splitting of the e_g and t_{2g} manifolds into their orbitals upon distortion of the octahedron (see Fig. 2.4). By a tetrahedral distortion, the mostly affected orbitals are the ones in the xz- or yz-plane. These are the d_{z^2} and the d_{xz} and d_{yz} orbitals. With increasing length of the bonds in the z-axis, the electrostatic repulsion between the electrons in the orbitals and the negative oxygen at the octahedron corners decrease. Therefore the energy of the d_{z^2} , d_{xz} and d_{yz} orbitals decrease. In the reversed case, with decreasing of the bond lengths along the z-axis, the electrostatic repulsion increases and therefore the energy of the bands are shifted upwards. The same principle applies for the distortion in a rhombic shape inducing a further splitting between the d_{xz} and d_{yz} bands due to the distorted symmetry of the xy-plane. When one oxygen atom of the octahedron is removed, the changed electrostatic interaction will increase the attraction between the remaining oxygens and the titanium and is responsible for a shrinking of the remaining bonds. In the case of a square planar deformation, this increases the interaction of the $d_{x^2-y^2}$ and d_{xy} with the other orbitals and increases their energy.

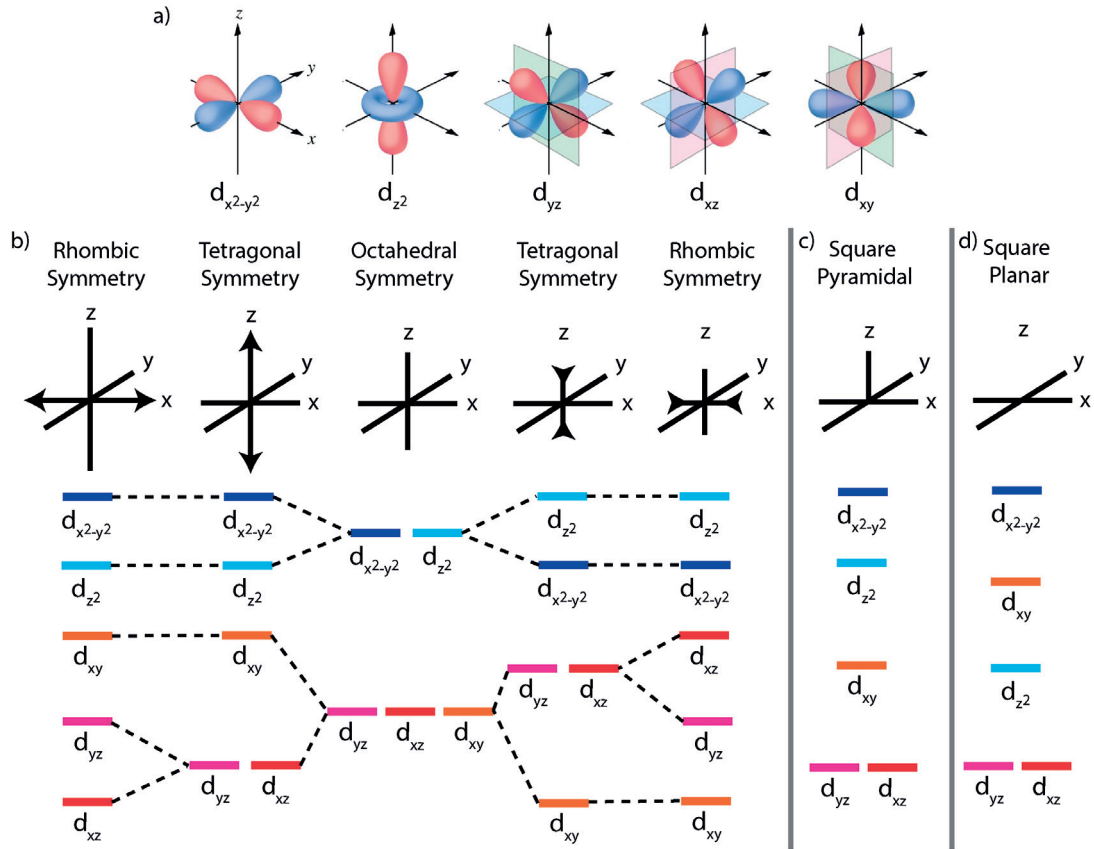


Figure 2.4 – (a) Orbitals of the 3 d states with their symmetries (from [104]). (b) Different distortions of the TiO_6 octahedron and their effect on the band ordering of the Ti 3d t_{2g} and e_g bands. (c) Splitting of the Ti 3d bands in a square pyramidal and (d) square planar crystal field. (adapted from [105]).

Consequently the band structure of the perovskites are very sensitive to altered lattice arrangements, affecting the distortion of the TiO_6 octahedron by any means. In the initial cubic lattice the octahedron can be considered undistorted. However, the perovskites show a variety of different structural phases with tetragonal, orthorhombic and rhombohedral symmetries (see Fig. 2.5). Under these structural changes, the lattice either arranges by altering the Ti-O-Ti bond angles between two neighboring octahedrons or by a distortion of the octahedron. The changes in Ti-O-Ti bond angle change the hopping probabilities between the orbitals and affect therefore the bandwidth. This effect is stronger for the e_g orbitals due to their alignment in the bond direction [106]. The two mechanisms, distortion of the octahedron and altering of the binding angle can also occur due to stress, externally applied or by growth conditions and lattice defects, as well as due to relaxation of the crystal lattice in the surface region of the crystal. In this thesis, different ways to manipulate the Ti 3d derived conduction band through the surface crystal structure are examined.

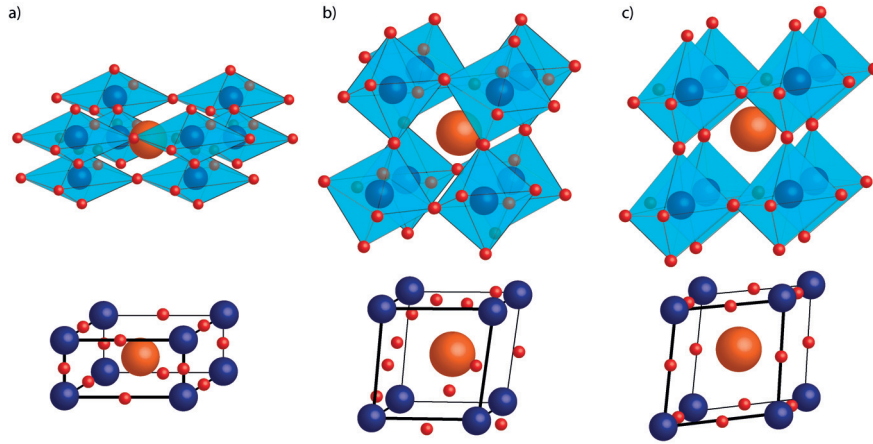


Figure 2.5 – (a) Tetragonal, (b) orthorhombic and (c) rhombohedral unit cell of the ABO_3 perovskites (adapted from [107]).

2.2 Structural phase transitions in titanates

2.2.1 Parent perovskite $CaTiO_3$

$CaTiO_3$ is the first discovered material of the perovskite family, named after L. A. Perovski, a Russian mineralogist [108]. Bulk CTO is in an orthorhombic structure at room temperature, with tilted TiO_6 octahedrons [see Fig. 2.5(b) for pseudo-cubic unit cell]. There have been numerous publications investigating the phase transitions of CTO at higher temperatures [109–118]. The most accepted version is the existence of two phase transitions at higher temperatures; from cubic to tetragonal at a temperature of 1635 K and from tetragonal to orthorhombic at 1523 K [119]. The tetragonal as well as the orthorhombic phase exhibit a change of the tilting angle of the TiO_6 octahedron with temperature (see Fig. 2.6). In all the three phases, CTO is insulating with a band gap of 2.4 eV in the orthorhombic phase according to band structure calculations [100].

CTO is not ferroelectric in any of his phases but it shows an increase of its dielectric constant at low temperatures (see Fig. 2.6) [120]. Therefore CTO is like STO and KTO classified as an incipient ferroelectric or quantum paraelectric material. In these type of materials, quantum fluctuations stabilize the system at low temperatures and prevent the instability of the polar soft-phonon mode, necessary for the formation of a ferroelectric phase [12, 120–122]. Due to its proximity to a ferroelectric phase, ferroelectric properties can be induced into the system by epitaxial strain in film growth [123, 124].

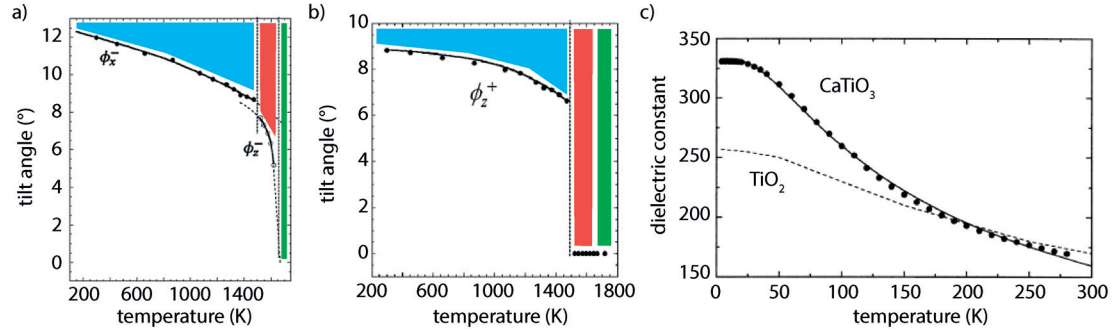


Figure 2.6 – (a) Out-of-phase change of the tilt Φ_u^- of the respective octahedron axis u with temperature and (b) in-phase change of the tilt Φ_u^+ (from Ref. [119]). Temperature ranges of the three phases are marked; orthorhombic (blue), tetragonal (red), cubic (green). (c) Behaviour of the dielectric constant at low temperatures (solid line and measurement points) with the dielectric constant of TiO₂ as a reference (dashed) (from Ref. [120]).

2.2.2 Ferroelectric BaTiO₃

BaTiO₃ is a well known ferroelectric material with a spontaneous polarization of up to 25 $\mu\text{C}/\text{cm}^2$ [125] and is already an integral part of electronic devices. Due to its high dielectric constant of up to 15'000 [126] it is widely used as a dielectric material in capacitors. Its pyroelectric behavior finds applications in PCT thermistors and its ferroelectric properties are demanded in microphones and other transducers [127]. It is insulator with a band gap of 3.9 eV in its tetragonal phase at room temperature [128]. Upon cooling, BTO undergoes three different ferroelectric phases below the paraelectric to ferroelectric phase transition at 400 K. These are the tetragonal phase, existing at room temperature and exhibiting 6 possible polarization directions, the orthorhombic phase, below 280 K with 12 different polarization directions and the rhombohedral phase below temperatures of 190 K hosting 8 different polarization directions (see Fig. 2.7).

Compared to the paraelectric CTO and STO the barium ion in BTO is larger in size, enabling new arrangements of the perovskite unit cell. Whereas in CTO, the phase transitions exhibit foremost a rotation of the TiO₆ octahedron and therefore a change in bonding angle between neighboring TiO₆ octahedron, the larger ion size of barium rather promotes a distortion of the octahedron [131]. As a result the position of the titanium atom in the octahedron center is not energetically favorable anymore. Therefore the titanium moves to an off center position forming, together with the charge of the oxygen atoms unpaired by barium, a dipole moment in the unit cell. The dipole results in a macroscopic polarization of the crystal lattice depending on the displacement of the titanium ion. This explanation of a displacement-type phase transition, responsible for the ferroelectric properties of BTO is in agreement with the Landau theory of phase transitions. The Landau theory describes the phase transition as a polynomial change in free energy responsible for new energetically stable lattice configurations. The displacement-type phase transition also agrees with a softening of a soft-phonon mode at the phase transition, changing the symmetry [131–133].

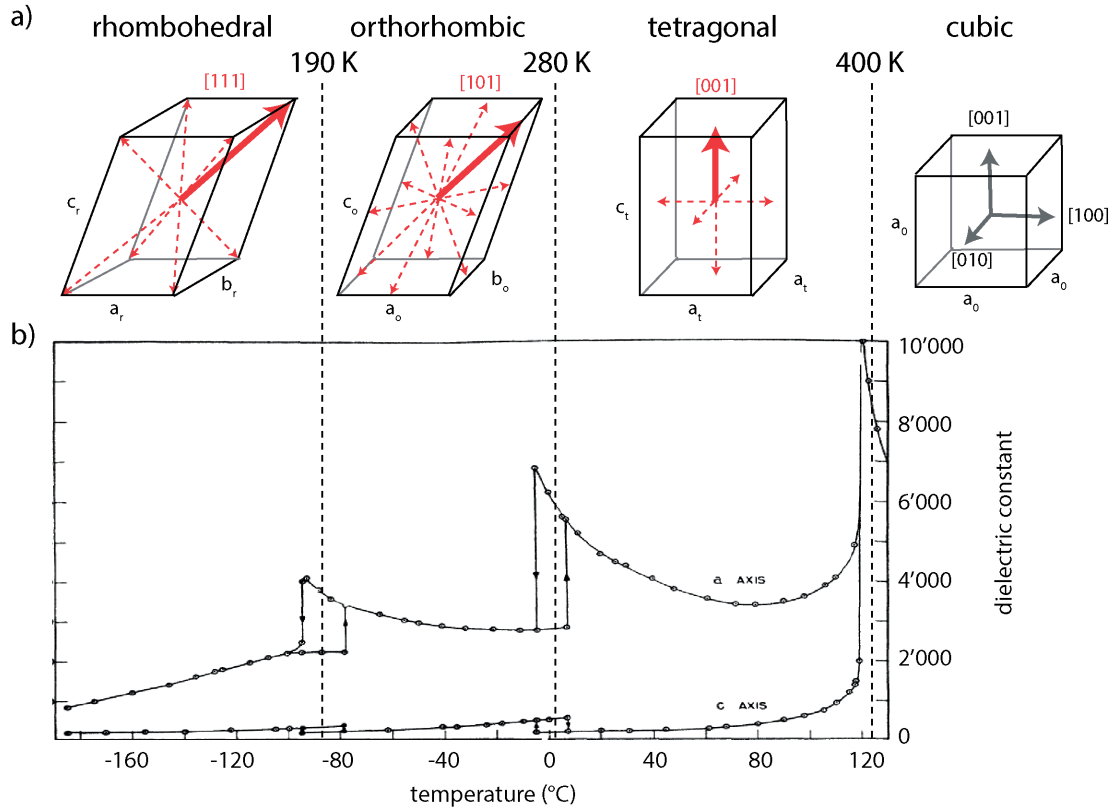


Figure 2.7 – (a) Phases of BTO with the possible ferroelectric polarization directions. Rhombohedral phase below 190 K with 8 different polarization directions, orthorhombic phase between 190 K and 280 K with 12 possible polarization directions, tetragonal phase with 6 polarization directions between 280 K and 400 K and the non ferroelectric cubic phase above 400 K (after [129]). (b) Dielectric constant along the a- and c-axis of the four phases as a function of temperature measured by W.J. Merz [130].

However, the displacement model does not seem to fully explain the formation of the ferroelectric phases in BTO. In fact the paraelectric, cubic phase above 400 K already shows indication of a displacement of the titanium ion from its center position in the TiO₆ octahedron and a rhombohedral distortion of the octahedron is present all the four phases [136–139]. A model explaining the formation of the ferroelectric phases with their polarization directions in agreement with the observations of non-zero displacement in the cubic phase is a deviation of the titanium ion from its center position towards one of the octahedron faces. In the cubic phase the random statistical distribution between the 8 possible displacement sites leads to zero macroscopic polarization. In the ferroelectric phases the distribution between the 8 sites is altered, responsible for a macroscopic polarization of the material [131, 137, 140, 141]. This order-disorder model and the mechanism responsible for the formation of the ferroelectric domains in BTO is still under debate and also models based on a mixture of displacement and order-disorder type phase transitions are discussed [142].

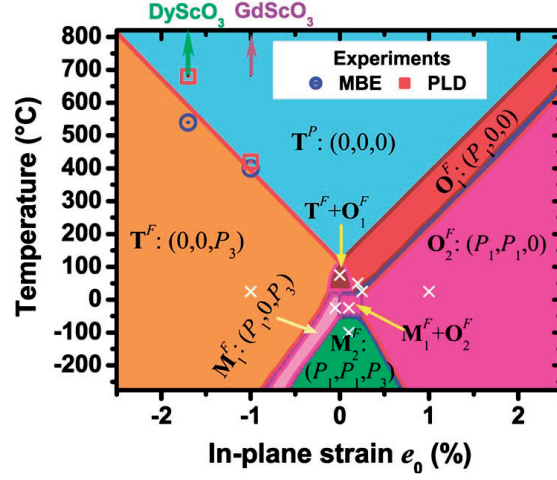


Figure 2.8 – Phases of BTO as a function of in-plane epitaxial strain and temperature. Circles and boxes mark transition temperatures obtained by measurements (from [134]). Phases are indicated as **T** for cubic/tetragonal, **O** for orthorhombic and **M** for monoclinic/rhombohedral. Each phase is marked with his polarization vectors (P_x, P_y, P_z). Index *P* and *F* indicate para- or ferroelectric properties respectively (from [135]).

The undoubted link between the structural phase of BTO and the possible ferroelectric polarization directions are responsible for a sensitivity of the ferroelectric properties to strain. Films grown on substrates with mismatching lattice parameters, that result in an interface strain, are shown to have an altered transition temperature [134]. Theoretical studies predict the existence of tetragonal phases for compressive, and orthorhombic phases for tensile strain even at low temperatures [135, 143–145]. The phase diagram of BTO films as a function of in-plane stress and temperature suggested by *Li et al.* [135] is shown in Fig. 2.8. With increasing thickness of the BTO films, relaxation of the interface strain can be responsible for different domain configurations and phases at the surface [146]. Therefore, the growth of BTO film with variable thickness on selected substrates allows to tailor the ferroelectric properties [146–150].

2.2.3 Properties of SrTiO₃

STO is a bulk insulator with a band gap of 3.25 eV in its room temperature cubic phase (see Fig. 2.1) [151]. At low temperatures, STO undergoes a phase transition to a tetragonal unit cell at 110 K with a ratio of its lattice parameters a/c of 1.00056 [152, 153]. Surface sensitive studies show that the surface undergoes the phase transition to a tetragonal unit cell above the transition temperature of the bulk [154–156]. Below the tetragonal phase transition, STO shows indication of a slight orthorhombic distortion around 65 K and there is also some indication of a low temperature phase transition below 10 K that could be a rhombohedral distortion [152, 157, 158]. At low temperatures, with a Curie temperature of around 300 mK a superconducting phase was found in metallic, electron-doped STO [17–19]. The transition temperature of the superconducting phase in STO depends on the carrier density that has to

be around $n = 10^{20} \text{ cm}^{-3}$. In the BCS theory this is a very low carrier density for the observed transition temperature and suggest strong pairing interaction at low temperatures for the superconductivity to exist [159].

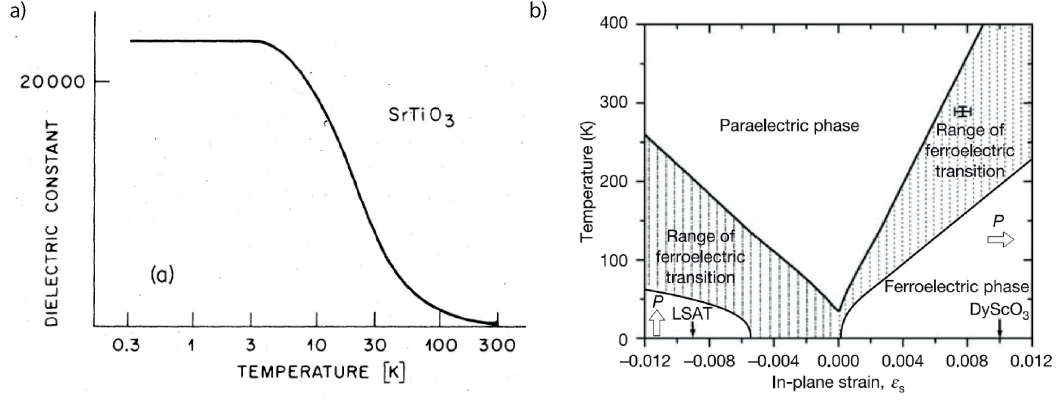


Figure 2.9 – (a) Dielectric constant of STO as a function of temperature (from [12]). (b) Ferroelectric phase transition temperature of STO films as a function of in-plane strain (from [15]).

Similar to CTO, STO shows an anomaly of its dielectric constant at low temperature. The dielectric constant begins to rise at approximately 35 K and saturates below 4 K [see Fig. 2.9(a)] [11–13]. Müller et al. [12] therefore suggested a quantum paraelectric phase or an incipient ferroelectric phase to exist in STO at low temperatures. The name quantum paraelectric refers to a quantum mechanical stabilization of the soft-phonon modes below the transition temperature, preventing a ferroelectric phase. Due to the incipient ferroelectric phase, STO can exhibit ferroelectric properties upon small distortion of its lattice. For example exchange doping of the A-site strontium can induce a ferroelectric phase at low temperatures (see below). A ferroelectric phase is also found below 23 K when O^{16} is replaced with its isotope O^{18} [13, 14]. In film growth a ferroelectric phase can be induced by interface strain with a tunable transition temperature up to room temperature as a function of in-plane strain [see Fig. 2.9(b)] [15, 16]. At the surface of STO films the topmost, charge neutral TiO_2 and SrO layers can exhibit a buckling due to the vacuum termination as confirmed by experiments and calculations [160–164]. In this buckling the oxygen atom of the TiO_2 layer is dislocated by approximately 0.1 Å above the titanium atoms. This results in local dipoles at the surface and may give rise to ferroelectric properties of the STO surface.

Experimentally it is shown that STO, nominally non-magnetic, can show magnetic properties under certain circumstances. In Nb doped STO, ferromagnetic properties at room temperature measured with superconducting quantum interference device (SQUID) measurements are reported by Liu et al. [165]. These properties can be suppressed by annealing in air and recovered by annealing in vacuum conditions. Their existence is therefore likely linked to free carriers in the system, induced by oxygen vacancies. Experiments by Rice et al. [78] and Rao et al. [79] show that local magnetic moments can also be induced in a controlled way by

photon irradiation. In the experiments of Rice et al. [78] magnetic properties were found below 18 K, upon irradiation of visible light on oxygen deficient samples. Rao et al. [79] created magnetic properties present up to 400 K by irradiation with UV light that can be suppressed by annealing in oxygen. All these experiments suggest that magnetic moments are related to excess electrons that come from oxygen vacancies that are either created by light or are preexisting in the bulk due to vacancies or doping. These excess electrons lead to unpaired spins that are responsible for a magnetic moment [81]. It is under debate, however, if the magnetism is bulk or surface related [78, 79, 165].

2.2.4 CaTiO_3 - BaTiO_3 - SrTiO_3 intermixtures

The three perovskites CTO, BTO and STO exhibit very similar phases in their phase diagrams although at different temperatures. Since they are all isovalent to each other, doping and mixture of the three titanates is possible. The incipient ferroelectric STO and CTO are, due to their proximity to a ferroelectric phase, very sensitive to doping. Therefore in the intermixture and mutual doping of CTO, BTO and STO a multitude of phases are observed.

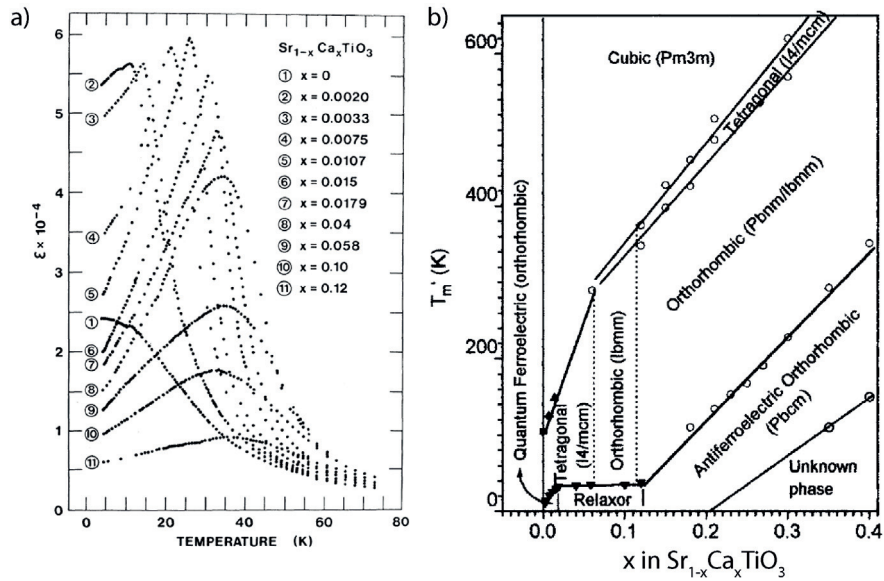


Figure 2.10 – (a) Dielectric constant of different calcium concentrations in $\text{Sr}_{1-x}\text{Ca}_x\text{TiO}_3$ at low temperatures (from [166]). (b) Phase diagram of $\text{Sr}_{1-x}\text{Ca}_x\text{TiO}_3$ for $x < 0.4$ versus temperature with labeled phases (from [167]).

The instability of the STO quantum paraelectric phase was shown in 1978 by Uwe and Sakudo [168]. By applying external stress, they induced a ferroelectric phase in STO at low temperatures. Bednorz and Müller [166] demonstrated with their measurements on calcium doped STO, the formation of a ferroelectric phase in STO by lattice stress. This ferroelectric phase already exists at a doping of 0.2% calcium and is visible as a peak in the dielectric constant versus temperature plot [see Fig. 2.10(a)]. The ferroelectric phase at these low temperatures

can exist due to the quantum mechanical zero-point motion and are therefore named quantum ferroelectric phases [169]. At higher dopings, above 1.8% the transition temperature stabilizes and the peak in dielectric constant broadens [see Fig. 2.10(a,b)]. This broadening is suggested to be an effect of frustration, introduced by the crossover from the low calcium doped ferroelectric to the higher calcium doped antiferroelectric phase and was denoted as a random or relaxator phase [170]. The structural phase diagram of $\text{Sr}_{1-x}\text{Ca}_x\text{TiO}_3$ by Ranjan et al. [167] suggest a variety of phases to exist in STO under calcium doping [see Fig. 2.10(b)].

Due to the incipient ferroelectricity of STO, ferroelectric properties can also be induced upon small amounts of barium doping. At dopings above $x=0.07$ in $\text{Sr}_{1-x}\text{Ba}_x\text{TiO}_3$, a ferroelectric phase transition takes place at increasing transition temperature with barium doping [see Fig. 2.11(a)] [120, 171]. Whereas at low doping, the ferroelectric phase is of rhombohedral symmetry, all three ferroelectric phases observed for BTO start to emerge at doping above $x=0.15$. At low dopings, below $x=0.03$ and low temperatures, Lemanov et al. [120] suggested a glasslike phase to exist. This glasslike phase, an intermixture of ferroelectric and antiferroelectric properties shows similar experimental footprints as the relaxator phase in $\text{Sr}_{1-x}\text{Ca}_x\text{TiO}_3$.

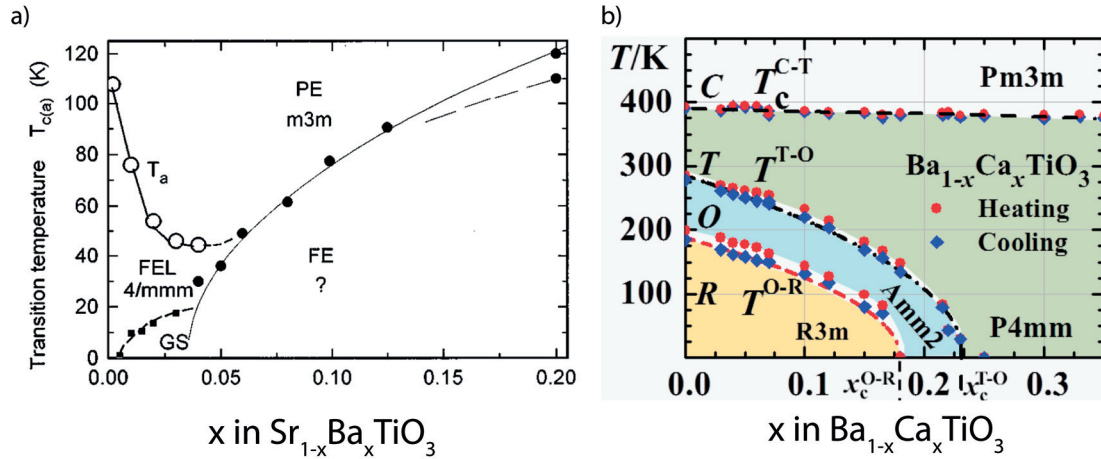


Figure 2.11 – (a) Phase diagram of $\text{Sr}_{1-x}\text{Ba}_x\text{TiO}_3$ for low barium doping, showing paraelectric (PE), ferroelectric (FE), ferroelastic (FEL) (that corresponds to the STO tetragonal phase) and glasslike (GS) phases (from [172]). (b) Phase diagram of $\text{Ba}_{1-x}\text{Ca}_x\text{TiO}_3$ showing $x < 0.3$ for 0 K till 500 K. Phases are denoted as C cubic, T tetragonal, O orthorhombic and R rhombohedral (from [173])

Doping of calcium in BTO also shows a direct effect on the phase formation [173, 174]. The cubic to tetragonal, corresponding to the para- to ferroelectric phase transition at 400 K is only slightly lowered under calcium doping. The ferroelectric properties are likely maintained with a shift of the calcium ion from the barium sites [173]. This off-centering of the calcium ions is likely also responsible for the strong dependence of the formation of the orthorhombic as well as the rhombohedral phase on calcium doping [see Fig. 2.11(b)]. At a doping of $x=0.175$ the rhombohedral and at a doping of $x=0.23$ the orthorhombic phase are suppressed. The behavior of the dielectric constant at these two phase transitions suggest a ferroelectric to

quantum ferroelectric transition, indicating the importance of quantum fluctuations for the formation of the orthorhombic as well as rhombohedral phase [173].

There is a variety of phases accessible in the intermixture of CTO, BTO and STO with para-, ferro-, antiferroelectric and other properties. There are still white spots in this phase diagram suggesting the existence of other, undisclosed properties to be accessible. Apart from the intermixture of two of the three materials, compositions of all the three are possible. In $\text{Sr}_{0.7-x}\text{Ca}_{0.3}\text{Ba}_x\text{TiO}_3$ it is for example possible to change the antiferroelectric phase of $\text{Sr}_{0.7}\text{Ca}_{0.3}\text{TiO}_3$ to a ferroelectric phase under barium doping [175]. Furthermore the phase space can also be extended into defects where the calcium doping can rise the superconducting transition temperature of $\text{SrTiO}_{x-\delta}$ [176]. The properties of the three compounds and their intermixtures can also be combined in films and multilayer structure due to their similar lattice parameters. This thesis takes use of these variety of phases, to investigate the effect of the different bulk phases of the three titanates CTO, BTO and STO and their intermixtures on the two-dimensional surface states.

3 Experimental methods

In this chapter an overview and introduction to the experimental methods used in this thesis is given. The majority of the results presented in this thesis are angle-resolved photoelectron spectroscopy (ARPES) measurements to determine the electronic band structure of the 2D states of the titanates surfaces. The studied film samples of BTO, CTO and STO were grown by pulsed laser deposition (PLD) with real time reflection high-energy electron diffraction (RHEED). Low-energy electron diffraction (LEED) was used to control the surface quality and the formation of reconstructions. Atomic force microscopy (AFM) and piezo-response force microscopy (PFM) gave information on the topography of the samples as well as on their ferroelectric properties.

3.1 Angle-resolved photoelectron spectroscopy

Angle-resolved photoelectron spectroscopy (ARPES) is based on the photoelectric effect that was discovered by Heinrich Hertz in 1887 [177] experimentally and theoretically described by Albert Einstein in 1905 [178]. The photoelectric effect describes the emission of electrons from a material by light, implying a transfer of energy from the light quanta (photon) on the electron. ARPES makes use of the photoelectric effect by measuring the intensity of the emitted electrons as a function of their kinetic energy and the emission angle to retrieve information about the binding energy and momentum of the electrons in the solid. ARPES is therefore a well established technique to determine the electronic band structure of solids. This chapter recaps the most important points of the ARPES process. For a more detailed discussion, the reader is referred to the literature of this techniques [179, 180].

The photoelectric effect is directly used in X-ray photoelectron spectroscopy (XPS) measurements, to probe the electronic density of states as a function of the electron binding energy. In XPS, the bound electrons in the solid are emitted to the vacuum by the energy of the photons. The process follows the energy conservation law, that determines the kinetic energy E_{kin} of

Chapter 3. Experimental methods

the emitted electron based on the binding energy of the electron in the solid E_{bin} and the work function Φ_S of the material.

$$E_{kin} = h\nu - \Phi_S - E_{bin} \quad (3.1)$$

Using this relation, the electron binding energy can be distinguished by using a monochromatic light source and measuring the kinetic energy of the emitted electrons. For measurements with an electrostatic analyzer, the kinetic energy is determined by the work function of the analyzer Φ_A and not the sample (see below). XPS can especially be used to determine the chemical composition of materials by measuring the intensity of the atomic core levels. The probing depth of the photoemission process is given by the mean free path of the emitted electron (see also Fig. 3.2). This can be used to obtain information on the location of the atoms with respect to the surface by measurements with different emission angles.

The photoemission process is described in the framework of the *one-step model* as the photo excited transition from an initial state of a system with N possible electron eigenstates into a final state consisting of $(N - 1)$ possible eigenstates. The final state additionally needs to include a propagating plane-wave in vacuum with a finite extension in the solid [180]. A simplified model widely used in the ARPES community to describe the photoemission process is the *three-step model* dividing the process into three separately treated processes:

- i The excitation of the electron in the bulk by absorption of a photon
- ii The travel of the electron through the solid to the surface
- iii The escape of the electron into the vacuum and its detection

The first of the three steps, the excitation of the electron by a photon, is responsible for the measurable photoemission intensity at a given energy E and momentum \mathbf{k} . A general expression of the photoemission intensity

$$I(\mathbf{k}, E) \sim |M_{f,i}|^2 f(E) A(\mathbf{k}, E) \quad (3.2)$$

depends on the photoemission matrix element $M_{f,i}$, the spectral function $A(\mathbf{k}, E)$ and the Fermi-Dirac distribution $f(E)$ that accounts for the fact that photoemission intensity can only be obtained from occupied electronic states [180, 181]. The spectral function $A(\mathbf{k}, E)$ represents the excited $(N - 1)$ body system after the photoemission process. It describes the band structure $\epsilon(\mathbf{k})$ of the system, modified by many-body interaction like electron-electron, electron-spin or electron-phonon interactions. These many body effects are considered by the

introduction of a complex electron self-energy $\Sigma(\mathbf{k}, E) = \Sigma(\mathbf{k}, E)' + i\Sigma(\mathbf{k}, E)''$ [179, 180]. The spectral function can be written as

$$A(\mathbf{k}, E) = -\frac{1}{\pi} \frac{\Sigma(\mathbf{k}, E)''}{[E - \epsilon(\mathbf{k}) - \Sigma(\mathbf{k}, E)']^2 + [\Sigma(\mathbf{k}, E)']^2} \quad (3.3)$$

For system with no interactions, the self-energy becomes zero and the spectral function becomes a delta function, with peak maximum at the energy and momentum of the initial band structure $\epsilon(E)$. In interacting systems with a finite self-energy, the initial band-structure is broadened by the imaginary part of the self-energy $\Sigma(\mathbf{k}, E)''$ and shifted by the real part $\Sigma(\mathbf{k}, E)'$. The measured band structure therefore also contains information of the many-body interaction of the system, present for example as shifted replicas or kinks of the band structure.

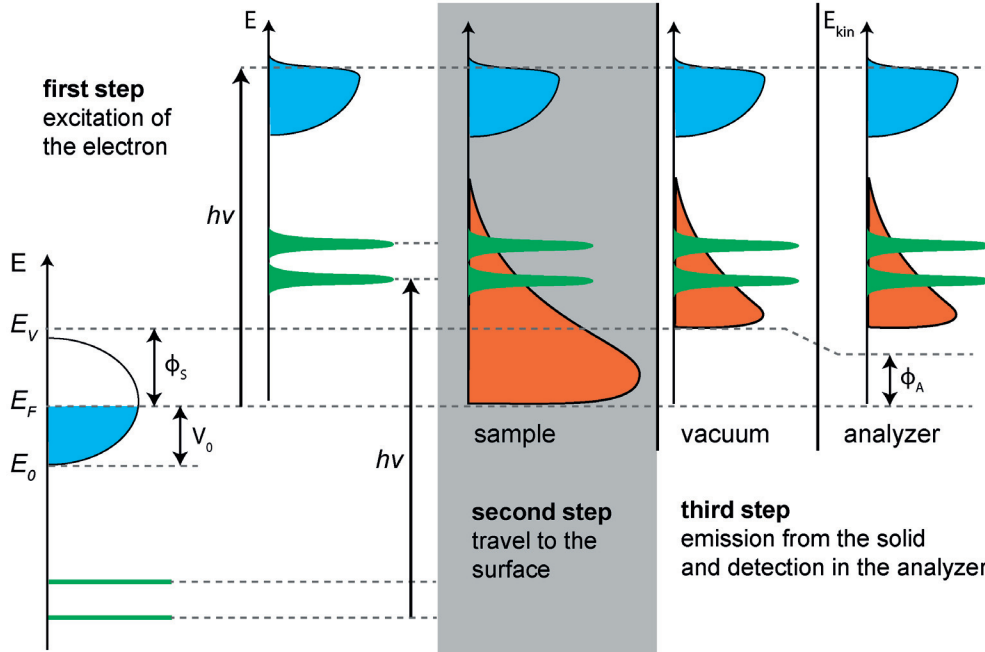


Figure 3.1 – Illustration of the three step model of the photoemission process. First step, excitation of the electrons from the core levels (green) and valence band (blue) in the solid. Second step, travel to the surface with the creation of secondary electrons (orange). Third step, emission from the solid and detection in the analyzer. (adapted from [179, 180])

The matrix element $M_{f,i}$ describes the excitation of the photo electron from the solid and therefore contributes the electron-photon interaction to the photoemission intensity. It can be described in the simplified frame work of the *sudden-approximation*. In the *sudden-approximation* the many-body interactions of the system and relaxation processes are not considered. Therefore the initial system can be described as a $N - 1$ body state with a single

electron state with wavefunction ϕ_i and the final system consisting of $N - 1$ particles and a electron final state with wavefunction ϕ_f . The matrix element $M_{f,i}$ can be expressed as

$$M_{f,i} = |\langle \phi_f | \mathbf{A} \cdot \mathbf{p} | \phi_i \rangle| \quad (3.4)$$

where \mathbf{p} stands for the electron momentum operator and \mathbf{A} for the electromagnetic vector potential of the photon radiation that depends on the light polarization and the photon energy [180]. The photoemission intensity is therefore sensible to the experimental geometry regarding the sample orientation and light polarization. With appropriate choice of these parameters, information on the orbital composition of the initial state wave function can be obtained. The results obtained from ARPES measurements are commonly referred to as band structure or Fermi surface although the measured intensity is not directly the band dispersion of the electrons in the solid but modified by many-body and matrix element effects also depending on the experimental conditions.

In the second step of the three step model, the electrons travel through the solid to the vacuum surface of the crystal. Within this process, a part of the emitted electrons are inelastically scattered and therefore lose energy and momentum. Due to the loss of energy, these so called secondary electron contribute as a background, increasing with decreasing kinetic energy, to the ARPES intensity. The scattering probability and therefore the mean free path of the electron in the solid depends on its kinetic energy. This relation is described by the so-called universal curve and also indicates the surface sensitivity of the ARPES measurements (see Fig. 3.2). In UV-ARPES, the mean free path of the electrons, excited by photons of $h\nu = 20$ eV to $h\nu = 100$ eV is between 5-7 Å resulting in a sensitivity to the surface layers of the probed material. With photons in the SX-energies from $h\nu = 300$ eV to $h\nu = 1000$ eV the mean free path is in the range of 8-20 Å. Therefore it is possible to probe electronic states at interfaces or below a capping layer with increased photon energies.

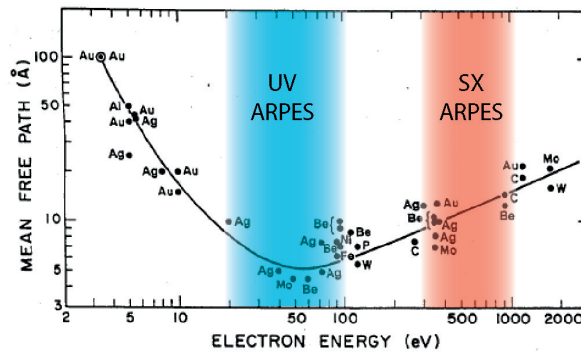


Figure 3.2 – Universal curve describing the relation of mean free path and electron energy with marked energy region of the UV-ARPES and SX-ARPES photon energies (adapted from [182, 183]).

3.1. Angle-resolved photoelectron spectroscopy

In the last step, the electron escapes the solid into the vacuum, where it is detected by an electron analyzer. Experimentally the photoemission intensity as a function of the kinetic energy E_{kin} and the emission angle ϑ is measured. The kinetic energy of the emitted electron in the vacuum is determined by the electron binding energy E_{bin} with respect to the Fermi energy E_F in the material, the work function of the material Φ_S and the energy of the incident light $h\nu$.

$$E_{kin}^{vac} = h\nu - E_{bin} - \Phi_S \quad (3.5)$$

This implies that an electron has at least a kinetic energy larger than the sample work function in order to be emitted into the vacuum. In the electron analyzer the electron kinetic energy is measured with respect to the vacuum level E_V of the analyzer. Therefore in ARPES data the binding energy of the electron is determined depending on the work function of the analyzer Φ_A and is independent of the sample work function Φ_S .

$$E_{bin} = h\nu - E_{kin} - \Phi_A \quad (3.6)$$

The modulo of the total momentum of the electron in vacuum by approximation of a free electron final state is given by its kinetic energy as

$$p = \hbar k = \sqrt{2m_e E_{kin}} \quad (3.7)$$

where \hbar is the reduced Planck constant and m_e the free electron mass. The momentum can be divided into a component parallel and a component orthogonal to the surface $\mathbf{k} = k_{\parallel} + k_{\perp}$. Due to translation symmetry along the surface, the momentum component parallel to the surface is conserved analog to Snell's law in optics. It is therefore given by [179, 180]

$$k_{\parallel} = \sqrt{\frac{2m_e}{\hbar^2} E_{kin}} \sin \vartheta \quad (3.8)$$

The momentum component orthogonal to the sample surface k_{\perp} , also often referred to as k_z is, due to the broken inversion symmetry along the crystal normal, not conserved in the

emission process. The out-of-plane momentum can be obtained by the assumption of a free electron final state in the vacuum, with a dispersion

$$E_f(\mathbf{k}) = \frac{\hbar^2(k_{\parallel}^2 + k_{\perp}^2)}{2m_e} - E_0 \quad (3.9)$$

The bottom of the free electron parabola E_0 is considered to roughly correspond to the bottom of the valence band (see Fig. 3.1). With $E_f = E_{kin} + \phi_A$ and the expression 3.8 for the in-plane momentum, the out-of-plane momentum is given as [180]

$$k_{\perp} = \frac{1}{\hbar} \sqrt{2m_e(E_{kin} \cos^2 \vartheta + V_0 + \Phi_A)} \quad (3.10)$$

Where V_0 is the inner potential that accounts for the potential step along the surface normal direction. In practice the dispersion with k_{\perp} is obtained by scanning the photon energy. For 2D state no dispersion with k_{\perp} is measurable due to the finite extension of the states in out-of-plane direction. 3D states however, show a distinct dispersion with k_{\perp} . In this case, the unknown inner potential V_0 can be determined experimentally, based on the periodicity of the 3D states with the out-of-plane momentum according to the Brillouin zone size of the material. Therefore in ARPES based on the photoemission intensity of the emitted electrons the in three-dimensional reciprocal space as a function of electron binding energy

3.1.1 High-resolution angle-resolved photoelectron spectroscopy

The majority of the data presented in this thesis was measured at the high-resolution angle-resolved photoemission spectroscopy (HRPES) endstation at Surface and Interface Spectroscopy (SIS) beamline of the SLS. The photoelectron analyzer in use is a Scienta R4000 hemispherical analyzer. The angular acceptance of the analyzer is adjustable and set to 30° for the presented experiments. The sample can be moved by a CARVING manipulator that allows a rotation around three axis and a linear movement along three axis (see Fig. 3.3(a) for the setup geometries). The sample is cooled by a liquid Helium cryostat which allows measurements at temperatures as low as 15 K. The SIS beamline provides photons in an energy range between 20 eV to 800 eV with best working conditions regarding the intensity in the range from 20 eV to approximately 120 eV. The polarization of the light can be selected between s- and p- linearly polarized light and C+ and C- circularly polarized light.

3.1. Angle-resolved photoelectron spectroscopy

The transformation from the emission angle θ and ψ in the geometry of the HRPES setup to the momentum of the electron is given according to eq. 3.8 and eq. 3.10.

$$\begin{aligned} k_{\parallel}^x &= \sqrt{\frac{2m_e}{\hbar^2} E_{kin}} \sin\theta \cos\psi \\ k_{\parallel}^y &= \sqrt{\frac{2m_e}{\hbar^2} E_{kin}} \sin\theta \sin\psi \\ k_{\perp}^z &= \sqrt{\frac{2m_e}{\hbar^2} (E_{kin} \cos^2\theta + V_0 + \Phi_A)} \end{aligned} \quad (3.11)$$

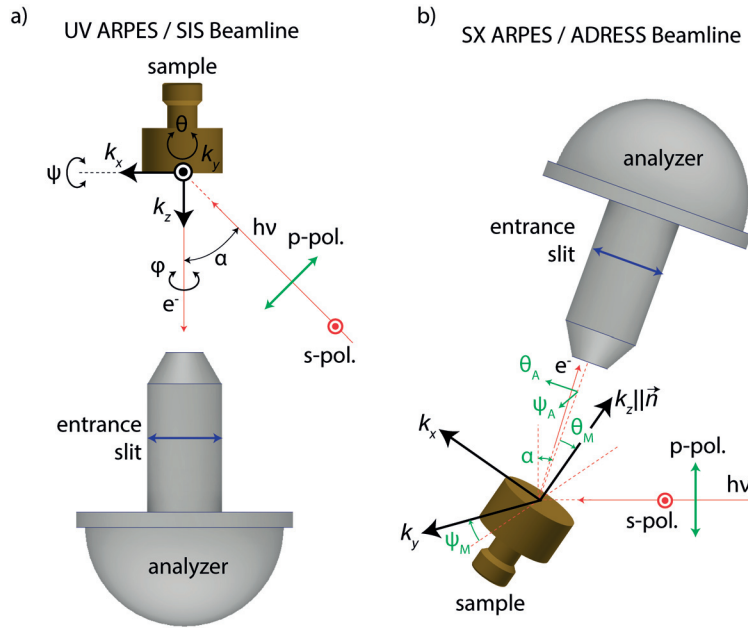


Figure 3.3 – (a) Setup of the UV-ARPES endstation at the SIS beamline with the relevant experimental parameters marked ($\alpha = 45^\circ$). (b) SX-ARPES setup at the ADDRESS beamline with marked analyzer angles θ_A , ψ_A and manipulator angles θ_M , ψ_M ($\alpha = 20^\circ$). (adapted from [184, 185])

3.1.2 Soft X-ray angle-resolved photoelectron spectroscopy

In chapter 5.6, data is discussed that was measured at the soft X-ray ARPES (SXARPES) endstation at the ADvanced RESonant Spectroscopies (ADDRESS) beamline of SLS. At this beamline the photon energy range is tunable between 300 eV to 1600 eV with s-, p-, C+ and C- polarized light. The endstation is equipped with a PHOIBOS 150 hemispherical electron analyzer that was set to an angular acceptance of $\pm 8^\circ$ for the performed experiments. Due to the dependence of the in-plane momentum k_{\parallel} on the kinetic energy, the momentum resolution is lower at the higher photon energies of SXARPES compared to HRPES. Furthermore, the photoemission

cross section of the core levels as well as the valence band are reduced at the higher photon energies. To compensate for this, a higher pass energy of the analyzer is chosen, reducing the energy resolution compared the UV-ARPES [184, 185]. Apart from these complications there are several advantages of SX ARPES due to the increased kinetic energy of the electrons and the accessible photon energy range (see [184] for more details). Of special interest for the study of oxides is the possibility to measure resonant photoemission at the titanium resonances to get information on the hybridizations of the valence and conduction band.

In the photoemission in the UV range, the momentum of the photon is neglectable and does not have to be considered to distinguish the electron moment (eq. 3.8, 3.10). In the SX range however, the contribution of the photon momentum to the moment of the photoelectron is comparable to the size of the Brillouin zone. Therefore a correction of the expressions for eq. 3.8 and 3.10 is necessary. The correction depends on the exact geometry of the setup [see Fig. 3.3(b)]. For the SX ARPES endstation the expression for the in- and out-of-plane moment writes as [185, 186]

$$\begin{aligned} k_{\parallel}^x &= +\sqrt{\frac{2m_e}{\hbar^2} E_{kin}} \sin(\theta_M + \theta_A) - \frac{h\nu}{\hbar c} \sin(\alpha - \theta_M) \\ k_{\parallel}^y &= -\sqrt{\frac{2m_e}{\hbar^2} E_{kin}} \sin(\psi_M + \psi_A) - \frac{h\nu}{\hbar c} \cos(\alpha - \theta_M) \sin(\psi_M) \\ k_{\perp}^z &= \sqrt{\frac{2m_e}{\hbar^2} (E_{kin} + V_0 + \Phi_A) - k_{\parallel}^2} - \frac{h\nu}{\hbar c} \cos(\alpha - \theta_M) \end{aligned} \quad (3.12)$$

These expressions depend on θ_A and ψ_A that are the angles between the electron momentum and the analyzer and on θ_M and ψ_M , the manipulator rotation angles parallel and perpendicular to the slit respectively [see Fig. 3.3(b)]. Due to the incident angle of 20° between the photons and the sample surface in the scattering plane, the photon momentum correction mainly applies to the k_{\parallel}^x component [185, 186].

3.2 Thin film growth

3.2.1 Pulsed laser deposition

Pulsed Laser Deposition has proven to be a valuable technique to grow high quality oxide materials and hetero structures [187–189]. The basic principle of this form of physical vapor deposition is as follows; A target made of the substance to be evaporated is hit by a laser beam. The laser beam vaporizes the material, leading to the formation of a plasma plume. This plume is deposited on a substrate forming a thin film of the evaporated material. In the evaporation and growth process the stoichiometry of the target material is maintained. Furthermore the possibility to induce oxygen as a background gas during the growth helps to avoid oxygen deficiency in the grown oxide films. There is a large amount of adjustable

variables in PLD growth process. These are the laser power and repetition rate, the oxygen background pressure, the geometry of the setup especially the target-substrate distance and the substrate temperature and surface structure. However, once the correct parameters for a type of material is found, a high-quality growth is possible.

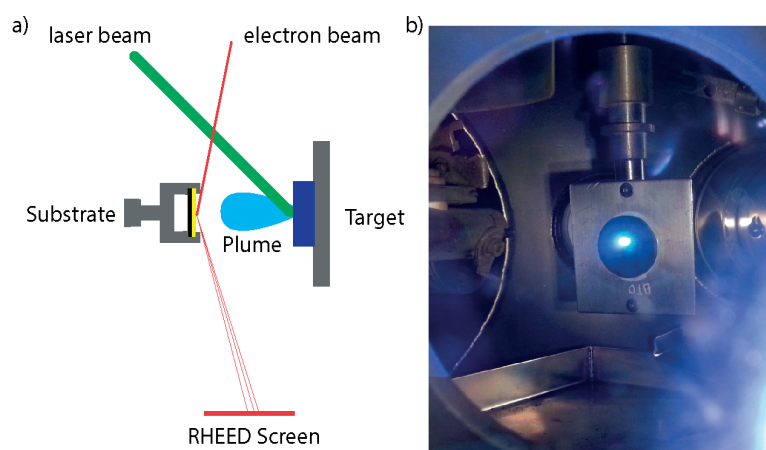


Figure 3.4 – (a) Sketch of the PLD setup with the relevant components. (b) Plume plasma is emitted from the target during ablation.

The first step of the PLD process is the interaction of the laser pulse with the target. The laser pulse is first absorbed in the target material. The absorption length is typically around 100 nm for oxides [189] and depends on the wavelength of the laser and the properties of the target material. The electric field of the laser pulse excites the electrons and therefore the lattice of the target, resulting in a melting of the material and finally vaporizing it. The electric field is also responsible for an ionization of the bulk material and the creation of a plasma. The oscillating electric field of the laser further excites the plasma leading to further ionization. Important in this process is a controlled heating of the surface layers of the target without affecting deeper layers. If the lower layers of the target are heated, splashing of the target material can occur, leading to droplets in the plume. Furthermore, the power of the laser has to be high enough to avoid an element specific evaporation. The power can be controlled through the wavelength or through the repetition rate of the laser.

Once the target material is evaporated, a plume of the material vapor forms. The plume expands away from the target due to recoil and Coulomb repulsion from the surface. Apart from the expansion away from the target, Coulomb repulsion is also responsible for a 3D expansion of the plume. The velocity of the plume and therefore the speed of the evaporation process can be further moderated by the gas pressure in the chamber.

Upon impact on the substrate, conditions have to be met to enable a layer-by-layer growth to get high quality film surfaces. This growth mode occurs if the sum of the film and the interface free energy is smaller than the surface free energy. This growth mode can be enhanced by

Chapter 3. Experimental methods

sufficient substrate temperature, to guarantee a high mobility of the deposited material and by the choice of a substrate with step edges to provide a starting point for the growth.

For the growth of the oxide films used in this thesis, well established parameters for the PLD growth were used. These parameters were obtained for other, related projects and are not distinguished in the framework of this thesis.

The PLD system used for the growth of the film studied in this thesis is equipped with a Quantel-Brilliant Nd:YAG laser. It is set to provide a laser beam in the UV range with a wavelength of 266 nm and an energy of approximately 85 mJ. The pulses have a repetition rate of 2 Hz and a length of 5 ns. As target, commercially available, pressed powder target with the desired stoichiometry are used. The substrate has a size of $0.5 \times 5 \times 10 \text{ mm}^3$ and is clamped on top of a doped silicon substrate. For heating a voltage is applied to the silicon substrate, leading to a resistive heating of the silicon substrate as well as the insulating substrate of choice on top. The temperature is measured with an external pyrometer. For the systems grown in this thesis, a temperature of approximately 680° was chosen. The substrates used for film growth had a miscut of $0.1\text{-}0.2^\circ$ to the (001) surface to enhance a layer-by-layer growth condition. The sample as well as the target are mounted on manipulators for a precise alignment. The PLD system is furthermore equipped with a RHEED setup to monitor the growth (see Fig. 3.4). After the growth, the sample can be *in-situ* transferred from the PLD growth chamber to the HRPES end station to do ARPES experiments (see Fig. 3.5).

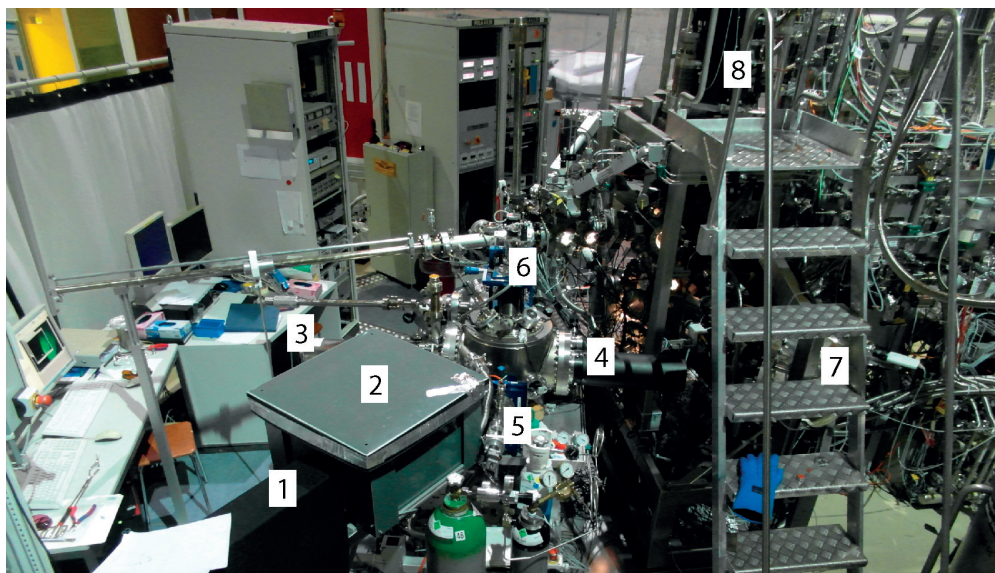


Figure 3.5 – Picture of the PLD setup at the SIS beamline connected to the HRPES endstation. Marked components are: (1) Laser, (2) laser optics, (3) RHEED electron gun, (4) RHEED screen and camera, (5) substrate manipulator, (6) target manipulator (7) ARPES analyzer, (8) ARPES manipulator.

3.2.2 Reflection high-energy electron diffraction and low-energy electron diffraction

The two electron diffraction techniques, reflection high-energy electron diffraction (RHEED) and low-energy electron diffraction (LEED) were used in this thesis to characterize the sample surface regarding its quality and to identify possible reconstructions. Both techniques are based on the same principles, but are different in geometry and energies. The techniques are based on constructive interference between the incoming electron wave with wavevector \mathbf{k}_{in} and the out-going inelastically scattered electron wave with wave vector \mathbf{k}_{out} . This is satisfied if the difference between the two wave vectors is equal to the reciprocal lattice vector \mathbf{G} , expressed by the Laue condition [90].

$$\mathbf{G} = \mathbf{k}_{out} - \mathbf{k}_{in} \quad (3.13)$$

This condition can be illustrated by the so-called Ewald sphere of radius \mathbf{k}_{in} centered in the origin of the reciprocal lattice. Constructive interference is met at the intersection of the sphere with the reciprocal lattice (see Fig. 3.6).

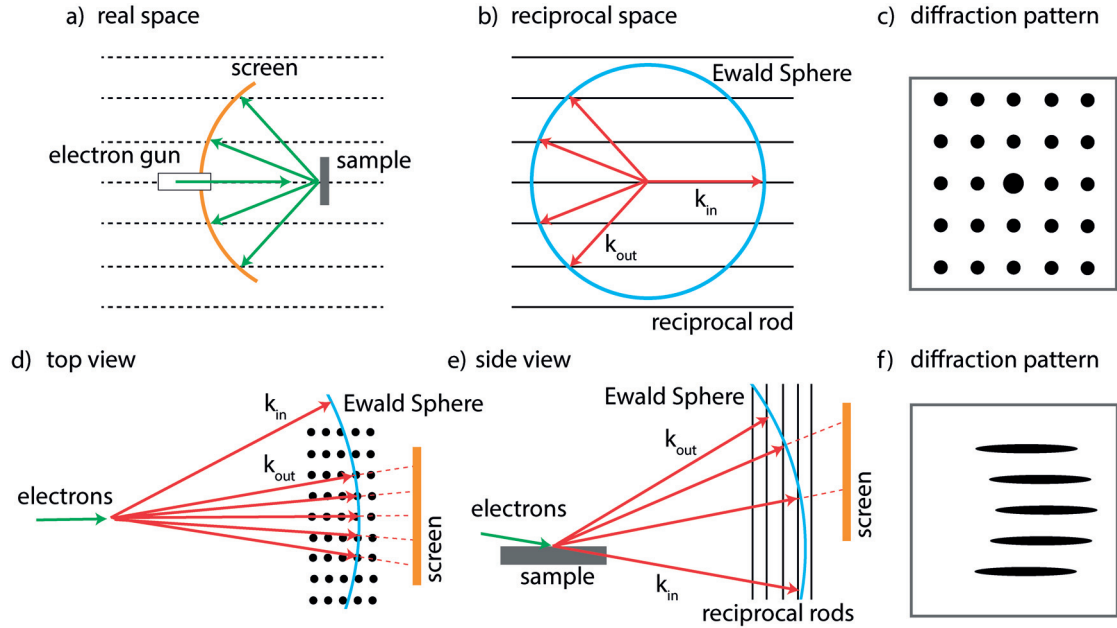


Figure 3.6 – (a-c) Illustration of the LEED process with (a) setup in real space (b) Ewald sphere construction in reciprocal space and (c) resulting diffraction pattern (adapted from [190]). (d-f) Ewald sphere construction in the RHEED process in (d) top-view and (e) side view with (f) resulting diffraction pattern (adapted from [191]).

In the case of LEED, electrons accelerated to an energy of 20-300 eV impinge the sample at normal incidence. With to the low energies of these electrons, only the first few layers of the

material are probed. Due to the surface termination at the vacuum interface of the probed crystals, the reciprocal lattice consists of elongated rods perpendicular to the crystal surface. The conditions for constructive interference are therefore given at the intersection of the Ewald sphere with this rods [see Fig. 3.6(a-c)]. The scattered electrons are displayed on a phosphor screen, providing a diffraction pattern. LEED is therefore very sensitive to the 2D periodicities of the sample surface.

In RHEED, the electrons used are in an energy range of 5-40 keV. Due to this higher energy a gracing incidence angle of the electrons to the surface is chosen. This geometry results in a similar probing depth as LEED. The phosphor screen to detect the diffraction pattern is placed opposite to the electron source, measuring the forward scattered electrons [see Fig. 3.6(d-f)]. The larger energies lead to a larger Ewald sphere in RHEED and therefore in a smaller intersection angle between the lattice rods and the sphere. As a result the diffraction spots are elongated in out-of-plane direction. At higher temperatures this elongation is enhanced due to the thermal excitation resulting in a broadening of the lattice rods. A RHEED pattern with elongated spots therefore indicates a well ordered, two dimensional surface [see Fig. 3.6(f)].

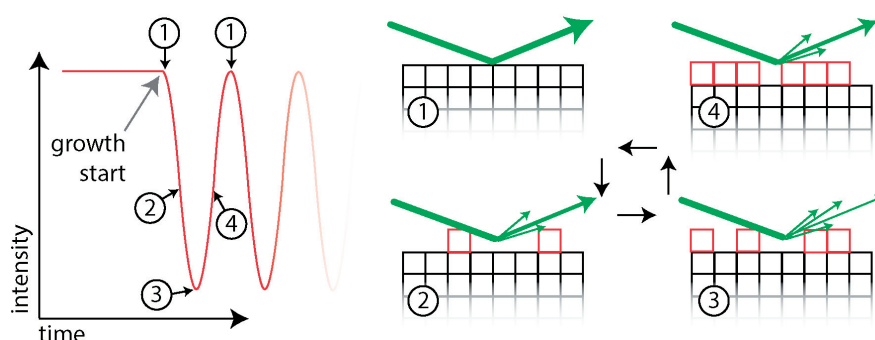


Figure 3.7 – Principle of the RHEED oscillations during the film growth. The diffracted electron beam (green) gets weaker due to ad-atoms at the surface. Maximal intensity is reached at the complete formation of a layer.

RHEED is often a method of choice for *in-situ* film growth analysis. Due to the gracing incidence of the electron beam, it is possible to obtain a RHEED pattern during the deposition process. The intensity of the RHEED pattern gives information on the roughness of the surface and can therefore give real time information of the film growth. The intensity variation during the growth is called RHEED oscillations (see Fig. 3.7). For a perfect, well ordered surface the RHEED intensity is high. When the deposition process starts, a partial coverage leads to a weakening of the RHEED intensity. Finally, full intensity is recovered when a complete layer is formed. Based on the RHEED oscillations the thickness of the film as well as the moment to stop the deposition at the complete coverage can be determined.

3.3 Piezo-response force microscopy

The piezo-response force microscopy (PFM) is a surface sensitive technique, that allows the mapping as well as writing of ferroelectric domains at the surface of a material. PFM measurements are based on the working principle of atomic force microscopy (AFM) [192, 193]. In AFM a probe tip, mounted on a cantilever, is brought to the proximity of the sample surface. The atomic forces between the tip and the sample surface are responsible for a bending of the cantilever. The atomic forces are long range Van-der-Waals and capillary forces, chemical bonding, electrostatic and magnetic forces and others. This bending is detected by the help of a laser, reflected from the cantilever and a photo sensitive device (PSD) detecting any movement of the reflected beam and therefore the movement of the probe tip [see Fig. 3.8(a)]. By this, the movement of the cantilever normal to the surface as well as sideways, lateral movement can be detected. The sample is mounted on a piezoelectric stage, that allows a positioning of the sample surface under the tip. By recording the sample position and the normal deflection of the AFM tip a topographic image of the sample surface can be obtained. The lateral deflection at the same time, gives indication of the friction coefficient of the surface. AFM topography can be obtained in two main different modes; tapping mode, where the tip is brought to oscillate near its resonance frequency and contact mode, where the tip is directly moved along the surface. The AFM data presented in this thesis are obtained by contact mode with a platinum tip of 10-20 nm tip size. This results in a resolution of approximately 40 nm.

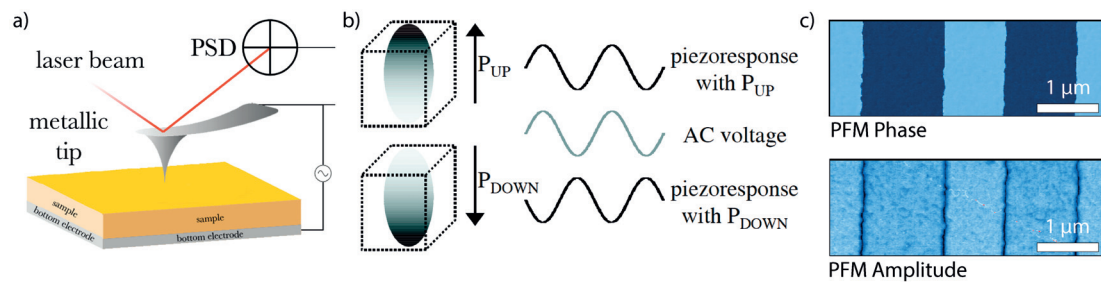


Figure 3.8 – (a) Setup for AFM and PFM measurements. (b) Principle of PFM, the ferroelectric unit cell either oscillates in-phase or out-of-phases with the AC voltage applied to the tip. (b) Resulting phase and amplitude signal of a ferroelectric material polarized in alternating stripes. (from [194])

The PFM measurements are based on the converse piezoelectric effect that describes the lattice deformation of a piezoelectric material in an electric field. Since ferroelectrics also exhibit piezoelectric properties, this effect can be used to measure ferroelectric polarizations via small lattice deformations. In PFM measurements an oscillating voltage is applied between a metallic tip and the sample surface or a back electrode. Due to the applied voltage, an electric field is present between the tip and the sample. This field is responsible for a deformation of the local lattice and results in a movement of the cantilever. If the dipole moment of the unit cell is aligned with the applied electric field, the deformation of the lattice is in phase with the applied oscillating voltage. If the dipole moment is opposite to the electric field, the

deformation of the lattice is opposite and the phase therefore shifted by 180° [see Fig. 3.8(b)]. Since the deformation of the lattice in the electric field is in the pm range, a lock-in amplifier between the applied voltage and the tip position detecting the oscillation of the unit cell is used to detect it.

The PFM data is shown as an amplitude signal and a phase signal of the sample surface. For a sample surface that is polarized in domains with out-of-plane direction and into the plane direction a 180° phase difference is measured [see Fig. 3.8(c)]. In the PFM amplitude signal the domains show both a maximal amplitude regardless if they are polarized in into the plane or out of the plane direction. At the domain boundary however, the unit cell is not polarized and therefore shows no response to the electric field of the tip resulting in a dip of the PFM amplitude.

The PFM measurements on BTO presented in this thesis were done by Nicolas Pilet at the NanoXAS beamline of the SLS. The samples are *ex-situ* transferred to the PFM setup, where the measurements are performed in UHV conditions at room temperature without further sample treatment. Since the BTO samples exhibit intrinsically no large domains, the sample surface was first polarized by writing the surface with a constant potential applied to the probe tip. Like this, a ferroelectric response and a contrast between oppositely polarized areas can be measured in the PFM signal (see Sec. 5.1 and Sec. 5.2).

4 The parent perovskite CaTiO_3

The parent compound of the transition metal oxides with perovskite structure CaTiO_3 was discovered as the first material of his kind by Gustav Rose in 1839 [108]. In this chapter results of films of CaTiO_3 , grown on SrTiO_3 substrates by pulsed laser deposition are presented and discussed. The films show a symmetry given by its pseudo cubic unit cell, with a $c(4\times 2)$ surface reconstruction, present after the growth. This reconstruction is altered to a $p(2\times 2)$ reconstruction under UV-light. At the CaTiO_3 film surface, a two-dimensional electron gas (2DEG) is found with an occupied band width of 400 meV and indication of a Rashba-like splitting of the band. With the presented findings CaTiO_3 is added to the group of oxides with a 2DEG at their surface. Based on these results the phase space is widened to investigate strontium and barium doped CaTiO_3 and the interplay of ferroelectric properties with the 2DEG at oxide surfaces. This could open up new paths to tailor two-dimensional transport properties of these systems towards possible applications.

The first section of this chapter (Sec. 4.1) is published in Applied Surface Science [22]. Coauthors of this publication are Mauro Fanciulli, Andrew Weber, Nicolas Pilet, Zoran Ristić, Zhiming Wang, Nicholas Plumb, Milan Radović and Hugo Dil. The author of this thesis performed the film growth, conducted the photoemission experiments, analyzed all the data and wrote the manuscript.

4.1 Observation of a two-dimensional electron gas at CaTiO_3 film surfaces

Introduction

The discovery of a two-dimensional electronic state at the interface of LaAlO_3 and SrTiO_3 [7] triggered research on other oxide interfaces where similar states were found [149, 195–197]. These two-dimensional states at interfaces of complex oxides give rise to different phenomena such as superconductivity [34, 198], metal-insulator transitions [199, 200] or magnetism [37]. More recently, a two-dimensional electron gas (2DEG) was also found on clean SrTiO_3 and

KTaO_3 (001) surfaces [9, 10, 61, 63, 87]. These states at the vacuum interface can, in contrast to the buried interface states, be more easily probed by angular-resolved photoelectron spectroscopy (ARPES) in the UV-range, revealing their band structure in reciprocal space. It was shown by spin-resolved ARPES, that the 2DEG at the surface of SrTiO_3 exhibits a Rashba-like spin splitting of approximately 100 meV, likely enhanced due to the presence of (anti)ferroelectricity and magnetic order at the sample surface [66]. The strong electron-phonon coupling of the TiO_2 surface [54, 201], which depends on carrier density, is most likely responsible for a drastic rise of the superconducting transition temperature of a monolayer FeSe deposited on top [20, 21]. The variety of observed properties makes these oxide-based two-dimensional states an ideal platform to explore new functionalities and possible ways towards device application in the future.

CaTiO_3 is the very first discovered perovskite of the transition metal oxide (TMO) family and is thus closely related to the members recent studies focus on. Like SrTiO_3 , KTaO_3 and TiO_2 (all compounds shown to host a 2DEG at their surface) CaTiO_3 is classified as an incipient ferroelectric or quantum paraelectric material, meaning that it is very close to a ferroelectric phase [120]. Intermixtures of SrTiO_3 , BaTiO_3 and CaTiO_3 form a rich phase diagram, especially regarding the ferroelectric properties, exhibiting para-, ferro- and antiferro-electric phases [166, 167, 202]. Pure, crystalline CaTiO_3 undergoes two phase transitions at elevated temperatures; from orthorhombic to tetragonal at 1512 K and from tetragonal to cubic at 1635 K [119]. According to band structure calculations for the orthorhombic and cubic crystal lattice the band gap is 2.43 eV or 2.0 eV, respectively [100, 203]. In today's electronics, CaTiO_3 is widely used as a ceramic and as rare-earth doped phosphor with excellent luminescence properties.

In this work, films of 20 unit cells CaTiO_3 grown by pulsed laser deposition (PLD) on Nb:SrTiO_3 substrates were studied by UV-ARPES and X-ray photoelectron spectroscopy (XPS). Our low-energy electron diffraction (LEED) measurements show that the surface of the CaTiO_3 films reconstruct while XPS indicates a TiO_2 terminated surface. In addition, observed surface plasmon loss features in the region of the Ti 2*p* core levels suggest the presence of metallic states at the surface of the films. Using ARPES, we found that these metallic states show a purely two-dimensional dispersion with a band width of ≈ 400 meV. Folded bands are visible as an effect of the surface reconstruction. In contrast to SrTiO_3 where the mixture of two- and three-dimensional states is observed [61], this 2DEG is the only metallic state present at the surface. Therefore the CaTiO_3 surface states yield easy access to directly manipulate the two-dimensional transport properties of this system by surface structure or gating. Furthermore, with the ferroelectricity introduced in $\text{Sr}_x\text{Ca}_{1-x}\text{TiO}_3$ this is a promising material to investigate the influence of ferroelectricity and the connected electric fields on the 2DEG at the surface of perovskites.

Materials and experimental method

The CaTiO_3 films of 20 unit cell thickness used for this study were grown by PLD on commercial TiO_2 terminated SrTiO_3 (001) substrates with a niobium doping of 0.5 wt% (Twente Solid State Technology BV). The growth was performed at a substrate temperature of 680°C in partial oxygen pressure of 5×10^{-5} mbar. The growth process and film thickness was monitored by reflection high-energy electron diffraction. The prepared films were *in-situ* transferred to the experimental station at the Surface and Interface Spectroscopy beam line of the Swiss Light Source at the Paul Scherrer Institut under ultra high vacuum (UHV) conditions and measured without further treatment. The sample was held at a temperature of 20 K in pressures better than 8×10^{-11} mbar during the measurements. Photoemission spectra (XPS and ARPES) were taken using a Scienta R4000 hemispherical electron analyzer and circular polarized synchrotron light. LEED patterns were obtained at 20 K before the ARPES measurements. The atomic force microscopy (AFM) topography was measured at the NanoXAS beam line of the Swiss Light Source at the Paul Scherrer Institut with the sample at room temperature in UHV environment.

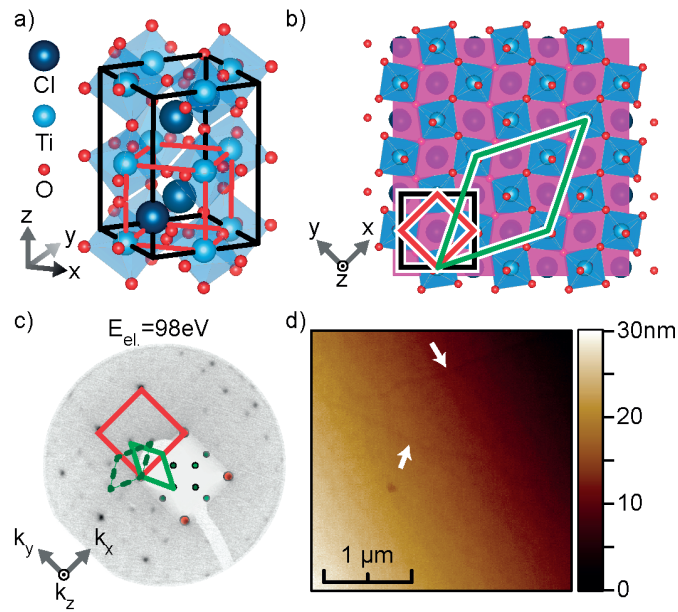


Figure 4.1 – a) Orthorhombic unit cell of bulk CaTiO_3 (black) with the simplified pseudo-cubic unit cell (red). b) Crystal surface of TiO_2 terminated bulk CaTiO_3 in (001) direction with the orthorhombic (black) and pseudo-cubic (red) surface unit cell and the observed $c(4 \times 2)$ reconstruction with respect to the pseudo-cubic lattice (green). c) LEED image with the marked pseudo-cubic Brillouin zone (red) and $c(4 \times 2)$ reconstruction (green) and the 90° rotated domain (green dashed). White square inset shows an overlay with the calculated LEED spots for a $c(4 \times 2)$ reconstructed surface. d) AFM topography of the surface. Arrows indicate the domain walls.

The orthorhombic unit cell of bulk crystalline CaTiO_3 has lattice parameters of $a = 5.367 \text{ \AA}$, $b = 7.644 \text{ \AA}$ and $c = 5.444 \text{ \AA}$ [204]. An approximate representation of the orthorhombic unit cell can be made by a pseudo-cubic unit cell as marked in Fig. 4.1(a). The lattice parameters of the pseudo-cubic unit cell $a/\sqrt{2} \approx b/2 \approx c/\sqrt{2} \approx 3.822 \text{ \AA}$ are similar to cubic SrTiO_3 with a lattice mismatch of approximately 2%.

In LEED we can identify the primary diffraction spots corresponding to the pseudo-cubic unit cell. Further we observe spots indicating a $c(4 \times 2)$ surface reconstruction of the pseudo-cubic lattice with domains rotated 90° with respect to each other [see Fig. 4.1(b,c)]. The (1×1) TiO_2 terminated surface at the vacuum interface of TMO perovskites might be unstable due to the unshared oxygen atom of the TiO_6 octahedron sticking out of the surface. Of the surface reconstructions reported for the closely related SrTiO_3 system, $c(4 \times 2)$ reconstruction has also been observed [205–208].

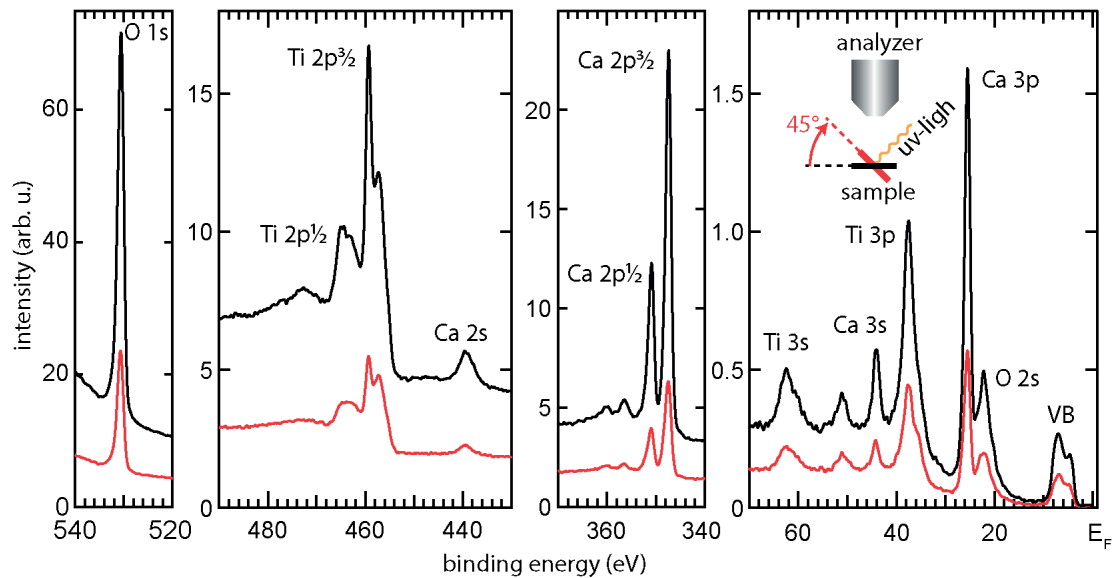


Figure 4.2 – Photoemission intensity of the core levels obtained with $h\nu = 600 \text{ eV}$ at normal emission (black) and 45° rotated (red) as illustrated in the setup sketch.

The AFM topography in Fig. 4.1(d) shows that the films are of low roughness and follow the substrate steps with a terrace size of approximately 200 nm. However, the AFM measurements do not have the resolution required to observe the surface reconstruction. The observed presence of domain walls is a further indication of the existence of multiple rotated domains corroborating the LEED data.

Results and discussion

The XPS spectrum of the films in Fig. 4.2, measured with a photon energy of $h\nu = 600 \text{ eV}$, shows clear signatures of the expected calcium, titanium and oxygen core levels with no detectable contamination. Comparing the spectra taken with the sample surface normal to

4.1. Observation of a two-dimensional electron gas at CaTiO₃ film surfaces

the analyzer to the more surface sensitive measurement taken at an angle of 45° between the sample normal and the analyzer axis (see sketch inset in Fig. 4.2) we can confirm the TiO₂ termination of the grown films. This termination of the film surface is expected due to the TiO₂ termination of the SrTiO₃ substrate [209]. When comparing the peak areas (A_i) after background subtraction the ratio $A_{Ca\ 2p}/A_{Ti\ 2p}$ of 0.75 at normal emission is significantly higher than the ratio of 0.65 measured at an emission angle of 45°.

All the titanium peaks show a shoulder towards lower binding energy, indicating the existence of titanium atoms with different valency. The increase of the surface located Ti 3⁺ shoulder is a light induced effect commonly observed in this class of materials [61]. The appearance of Ti 3⁺ ions is likely linked to a distortion of the TiO₆ octahedron, for example due to the creation of oxygen vacancies in the surface region and/or a structural rearrangement and buckling of the surface layers.

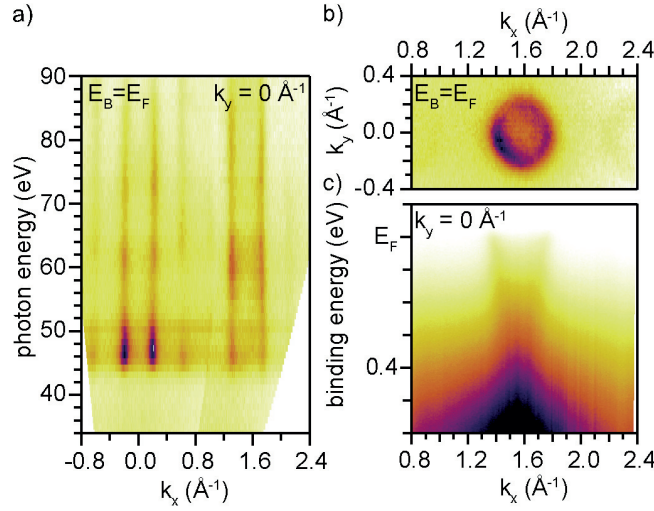


Figure 4.3 – a) Measured dispersion at the Fermi energy as a function of photon energy and k_x . b) Fermi surface measured at $h\nu = 60$ eV and c) band structure along the high symmetry direction $\overline{\Gamma X}$.

The Ti 2*p* as well as the Ca 2*p* core levels show plasmon loss peaks in their shake-up tail with an energy loss of 13.2 eV for titanium and 9 eV for calcium. Plasmon loss peaks with this loss energy of the Ti 2*p* core levels have been observed in other perovskites. The measured plasmon energy corresponds to surface plasmons present in TiO₂ where the plasmons are trapped at the interface of the metallic surface and the dielectric bulk due to the sudden change in dielectric constant. [210–213]

Consequently, we also expect metallic states to be present at the surface of our CaTiO₃ films. Indeed, the ARPES measurements in Fig. 4.3 show an electron-like surface state. The scan over a wide range of photon energies in Fig. 4.3(a) shows no dispersion of these states with out-of-plane momentum, verifying their two-dimensional nature. In contrast to the well-studied metallic states present at the surface of SrTiO₃ (001) and KTaO₃ (001) [9, 10, 61, 63, 87] we have

no indication of three-dimensional features, making the 2DEG the only states contributing to the metallicity. Similar to the other perovskites the spectral intensity of the 2DEG at the CaTiO_3 surface increases under UV-irradiation. This is attributed to light induced surface rearrangements and induced carriers [61].

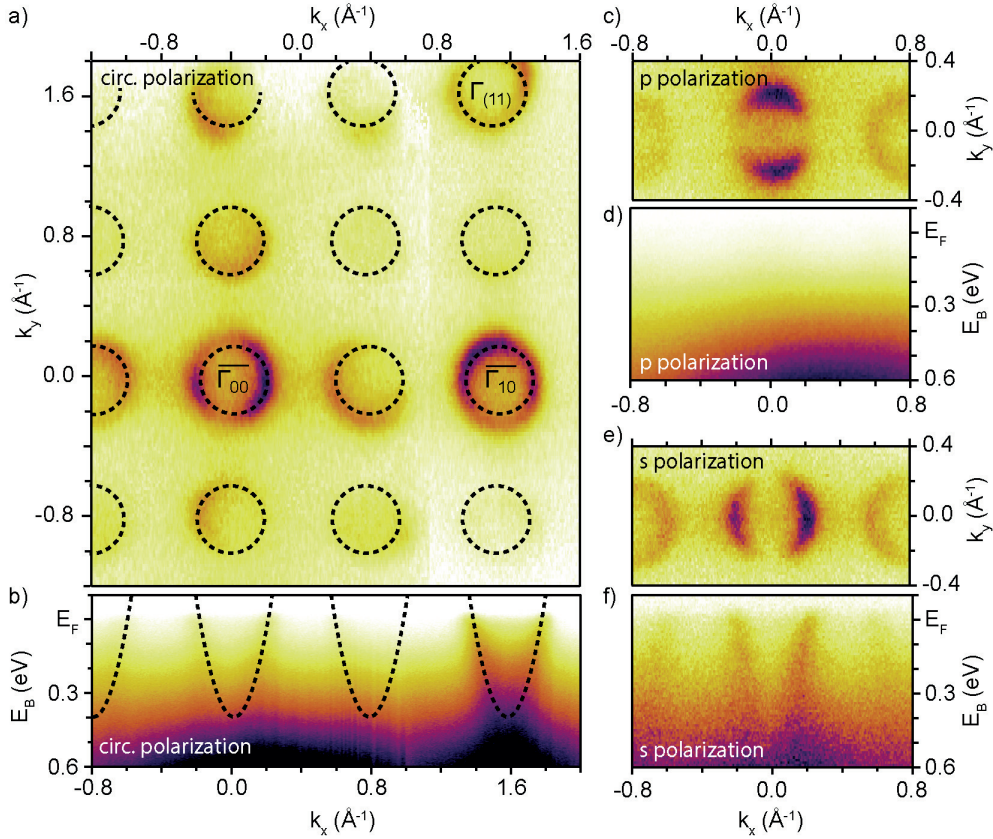


Figure 4.4 – a) ARPES Fermi surface at $h\nu = 80\text{eV}$ for circular polarized light. Dashed black circles mark the expected Fermi surface due to the $p(2\times 2)$ reconstruction. b) Measured band dispersion along the $\overline{\Gamma X}$ direction with indicated positions of the free electron like parabolas. c) ARPES Fermi surface and d) band structure for p-polarized light of $\overline{\Gamma_{00}}$. e) Fermi surface and f) band structure for s-polarized light.

The circular Fermi surface of $\Gamma_{(100)}$ is depicted in Fig. 4.3(b) and the corresponding clear free-electron-like parabolic band along the high symmetry direction $\overline{\Gamma X}$ in Fig. 4.3(c). The in-plane momentum $g \approx 1.57 \text{ \AA}^{-1}$ at the ring center, corresponding to the momentum of $\Gamma_{(100)}$, is equal to a lattice parameter of $a \approx 4 \text{ \AA}$. This is in good agreement with the lattice parameter of the pseudo-cubic unit cell of CaTiO_3 and the SrTiO_3 substrate. Also clearly visible in Fig. 4.3(a) is the intensity at the Fermi energy of an additional, folded parabola between $\Gamma_{(000)}$ and $\Gamma_{(100)}$ due to the surface reconstruction observed also in LEED as described in section 4.1. Similar band folding has been observed for the (1×4) reconstructed anatase TiO_2 films [50].

4.1. Observation of a two-dimensional electron gas at CaTiO₃ film surfaces

The band structure of the 2DEG in Fig. 4.3(c) and Fig. 4.4(b) can be fitted with a free-electron-like parabola yielding an effective mass of $m^* \approx 0.39m_e$, a Fermi momentum of $k_F \approx 0.20 \text{ \AA}^{-1}$, a Fermi velocity of $v_F \approx 6.3 \times 10^5 \text{ m/s}$, and a band minimum at a binding energy of $E_b \approx 400 \text{ meV}$. This corresponds to a charge carrier density per parabola of $6.4 \times 10^{13} \text{ cm}^{-2}$ or $0.1 e^-/a^2$ with $a = 3.822 \text{ \AA}$. This charge carrier density is similar to SrTiO₃ [10, 61] while the band width is significantly higher and the effective mass much lower than for SrTiO₃ and KTaO₃. The ARPES measurements with s- and p-polarized light in Fig. 4.4(c-f) confirm the xy -symmetry of the 2DEG with no indications of bands with xz - or yz -symmetry. The 2DEG thus consists of the Ti $3d_{xy}$ bands splitted from d_{xz}/d_{yz} by crystal field splitting and partially filled due to surface band bending and light induced carriers.

With the absence of the Ti $3d_{xz}$ and $3d_{yz}$ bands and the two-dimensional Ti $3d_{xy}$ bands at relatively high binding energies, the splitting between the d_{xy} and d_{xz}/d_{yz} -bands has to be large, at least of the size of the observed bandwidth of $\approx 400 \text{ meV}$. This splitting is considerably larger than the 190 meV measured for SrTiO₃ [61] but smaller than for TiO₂ anatase where 1 eV is reported [54, 201]. For the orthorhombic oxide LaAlO₃ a comparable noncubic crystal field splitting of 120 meV to 300 meV for the t_{2g} sub shell is reported [214]. However, there is no detectable additional splitting of the Ti $3d_{xy}$ band as observed for SrTiO₃ [66]. Comparing SrTiO₃ to CaTiO₃ the increased rotation of the TiO₆ octahedron in the later due to the orthorhombicity will likely reduce the local electric fields as observed in other perovskites [215]. The resulting weak polarization field at the surface could be the reason that the splitting is too small to be observed in our data.

The results of the fitting are indicated in Fig. 4.4(a,b) showing the circular Fermi surface composed by parabolic bands for the primary Γ -points as well as for the reconstructed Γ -points. Along the $\overline{\Gamma X}$ direction, the Fermi surfaces and parabolic bands corresponding to the folded Γ -points, which are present as a result of the reconstruction, are clearly visible in the data. However their intensity is weaker than the signal of the 2DEG at the primary Γ -points. In contrast to the folding along the high-symmetry direction, the Γ -points offset by $1/4 \cdot g$ in k_y direction are not present in the data. A possible reason for this is a change of the reconstruction from $c(4 \times 2)$ either to a combination of (2×1) and $c(2 \times 2)$ or more likely to $p(2 \times 2)$ under irradiation with UV-light. Since we observe an increasing intensity of the 2DEG as well as the described formation of a low binding energy shoulder on the titanium core levels under UV-light, a change of reconstruction under light due to the deposited energy is plausible.

Summary

In conclusion, we have revealed the existence of metallic states at the surface of CaTiO₃ films consisting solely of a 2DEG. The 2DEG has a band width of $\approx 400 \text{ meV}$, indicating a large splitting between the unoccupied Ti $3d_{xz}/d_{yz}$ bands and the two-dimensional $3d_{xy}$ bands. Due to its metallicity, the surface also hosts plasmons visible as loss peaks in the XPS data. The bands are folded according to the surface reconstruction that is likely changed from

$c(4 \times 2)$ to $p(2 \times 2)$ under UV irradiation. Due to the lack of higher-dimensional conducting channels and the affinity of the system to adapt to its surface structure, various paths open up to directly manipulate the surface states. This manipulation may give direct access to the transport properties of the system and its coupling to overlayers. With the possibility to induce ferroelectricity into the quantum paraelectric materials CaTiO_3 and SrTiO_3 by mutual doping, the phase space is open to probe the effect of ferroelectricity on the 2DEG hosted by both of these materials.

4.2 Rashba-like splitting of the CaTiO_3 surface states

As mentioned above, a Rashba-like splitting of the 2DEG at the surface of CTO films is possible. The fitting parameters for the 2DEG presented in chapter 4.1, are based on a free electron like parabola. In Fig. 4.5(a), the obtained free electron like parabola is indicated. However, the energy distribution curves at different binding energies [Fig. 4.5(b)] indicate the presence of two parabolas that would agree with a Rashba-like dispersion (compare Sec. 1.3.1). The peak fitting of the EDC's in Fig. 4.5(b) was performed with two pairs of Lorentz distributions. The inner two bands are weaker in intensity closer to the Fermi energy while towards higher binding energy the peak intensity of the two doublets matches. The position of the peak maxima are indicated in the band dispersion depicted in Fig. 4.5(a). The found peak positions can be matched with a Rashba-split, free-electron-like parabola as shown.

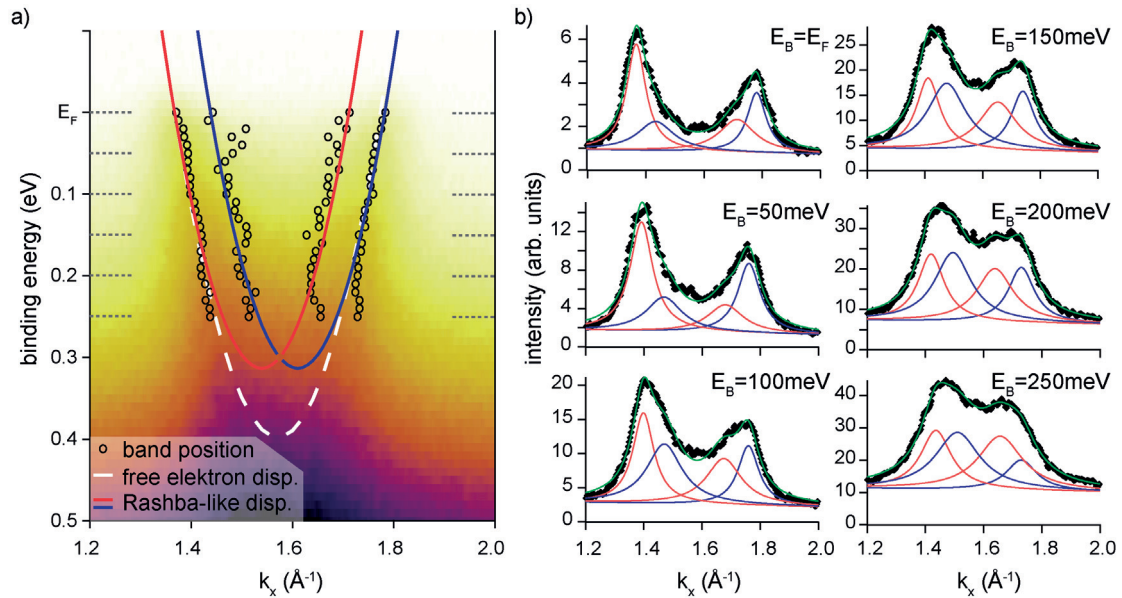


Figure 4.5 – (a) ARPES band structure at Γ_{10} for $h\nu = 80$ eV with fitted band positions and fitted dispersion of a free electron like parabola or Rashba-like splitted parabola. (b) Energy distribution curves of (a) at different binding energies with peak fitting of the band positions.

The Rashba parameter is with $\alpha \approx 7.5 \cdot 10^{-11}$ eVm slightly larger than for STO [66]. The mass with $m^* \approx 0.36 \cdot m_e$ and the bottom of the band with $E_b \approx 0.32$ eV are smaller than the results

obtained with the free-electron-like fit without Rashba splitting. Compared to STO [66], the band bottom is still at higher binding energy and the mass lower. There is also the possibility of a Zeeman splitting, lifting the spin-degeneracy at the Γ -points as observed for STO [66]. With the current data presented here, no conclusion on its existence or size is possible. Also in order to get a reliable fit of the Rashba-like dispersion, data of better quality and higher resolution is necessary. Furthermore the existence of a Rashba-like spin splitting should be confirmed by the help of spin-resolved ARPES measurements, revealing the spin texture of these states.

4.3 Doping approach by Rb-deposition

Since the 2DEG observed at the surface of bulk insulating CTO is the only state contributing to its surface conductivity, the 2DEG gives direct access to the transport properties of this system. A direct way to manipulate the transport properties is electron doping. The expected rigid bandshift to higher binding energies of the 2DEG with n-type doping would eventually cause an overlap of the band dispersion around neighboring Γ points. This overlap could give rise to more exotic states and possible hybridization, especially if a Rashba-like splitting with spin polarized bands is present.

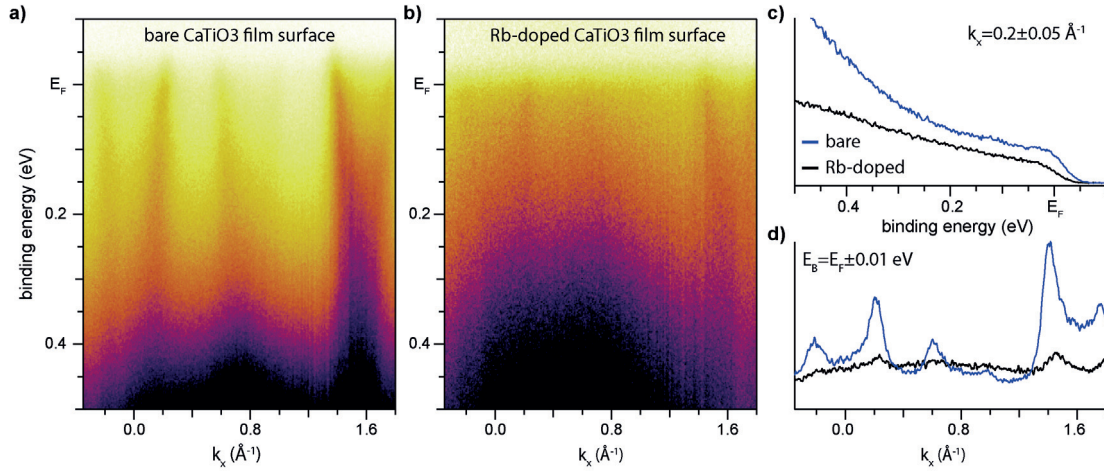


Figure 4.6 – Measured band dispersion at $h\nu = 80$ eV, showing $\overline{\Gamma_{00}}$ and $\overline{\Gamma_{10}}$ before (a) and after (b) Rb deposition. (c) Energy distribution curves at k_F and (d) momentum distribution curves at the Fermi energy before and after Rb deposition.

Apart from gating with an external potential applied, n-type doping can be achieved by deposition of alkali metals on the surface demonstrated for various compounds [216–218]. Due to their half filled s-orbitals alkali metals act as an electron donor. In Fig. 4.6 the band structure before and after Rb-deposition to the cold film surface are shown. The exact Rb coverage after the deposition is unknown due to the uncalibrated evaporation source but is expected to be below one monolayer. However, the band dispersion observed after the deposition show no signs of a rigid bandshift as an effect of electron doping. Moreover, the

band structure after Rb deposition in Fig. 4.6(b) shows a significant reduction of the 2DEG ARPES intensity. With the deposition of less than a monolayer of Rb this reduction can not be solely due to the limited escape depth of the photoelectrons. A likely explanation of this change in the ARPES signal is that the deposition of adatoms to the grown film alters its surface structure and is therefore affecting the formation of the 2DEG. This implies that the 2DEG formation is related to the surface structure and relaxations.

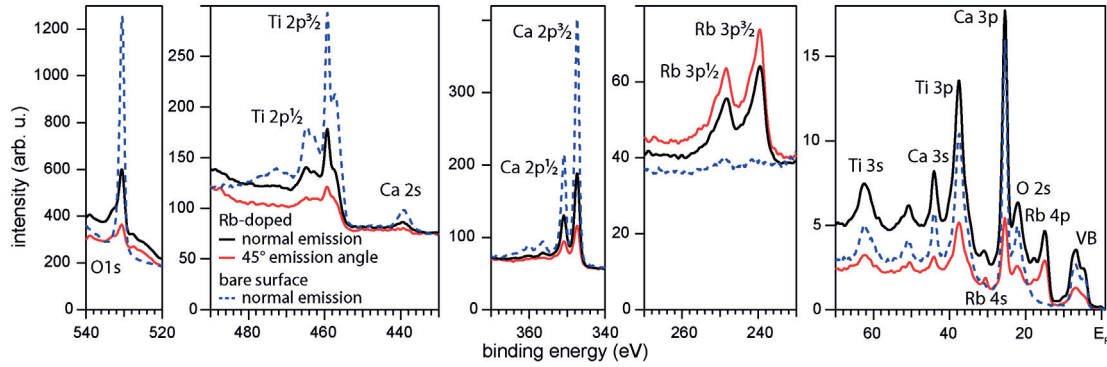


Figure 4.7 – Measured core level intensity of 20 uc CTO on STO with Rb deposited on the cold surface. The measurements are taken with $h\nu = 600$ eV at normal emission (black) and 45° to it. Data of the sample before Rb deposition (blue dashed) are plotted as a reference.

The XPS data in Fig. 4.7 are obtained under the same experimental conditions as the data presented in Fig. 4.2 for the as-grown sample. The core levels of Ca, as well as Ti are unaffected in shape by the Rb deposition but lower in intensity. Apart from the appearance of clearly surface localized Rb core levels as expected, a change of the O 1s line shape can be observed. After Rb deposition additional intensity at higher as well as lower binding energy are present shifted each by approximately 2 eV from the O 1s at $E_B = 530.6$ eV. The lower binding energy peak can be assigned to the MMN Auger process of Rb, the additional peak at a binding energy of $E_B = 532.6$ eV is an indication of the formation of rubidium oxide or rubidium dioxide at the surface. This is in agreement with a low intensity shoulder visible at the higher binding energy side of the Rb 3p core levels. The oxygen for this formation has to be supplied by the CTO, thus creating oxygen vacancies in the surface layers. This creation of this oxygen vacancies seemingly does not alter the band structure in terms of doping.

4.4 Conclusion

In this chapter the ARPES results of the parent perovskite CaTiO_3 were presented. The PLD grown films show a 2DEG at their surface, consisting of the occupied Ti $3d$ bands with xy -symmetry. In comparison with STO, in CTO there is no signal of the 3D d_{xz}/d_{yz} bands present at the CTO film surface. This suggest a splitting between the d_{xy} and d_{xz}/d_{yz} of 400 meV or larger. This indicates an stronger tetragonal distortion of the TiO_6 octahedron compared to STO. The symmetry of the film is in agreement with the pseudo-cubic unit cell of CTO and shows a $c(4\times 2)$ reconstruction after the growth that is changed to a $p(2\times 2)$ reconstruction under UV-light. The Fermi surface therefore consists of the circular contributions from the 2DEG at the primary $\bar{\Gamma}$ -points and at the folded $\bar{\Gamma}'$ -points according to the reconstruction. The 2DEG itself shows indication of a Rashba-like splitting as it is observed for STO. However, further experiments exploring their spin polarization are necessary to decide on the nature of the splitting. Under Rb-deposition the filling of the 2DEG is not altered but the quality of the ARPES signal is significantly reduced due to the ad-atoms deposition on the surface. These results add CTO to the group of perovskites shown to host a 2DEG at their surface. This makes it feasible to further explore the phasediagram of Ca doped STO or BTO with its para- ferro- and antiferroelectric phases [166, 167, 174, 202]. Furthermore the affinity of the CTO 2DEG to adapt to reconstructions with the formation of stable, folded bands as well as the absence of 3D bands at the Fermi energy yield various possibilities to alter the 2DEG formation and therefore the conduction properties of the system. With the growth of CTO films on different substrates or substrates with different surface symmetries other reconstructions could be induced.

5 Interaction of ferroelectricity with the 2D states at the BaTiO₃ surface

This chapter focuses on the ferroelectric material BaTiO₃ that is closely related to the previously discussed CaTiO₃ and the well studied SrTiO₃. The presented results show the existence of 2D states at the BaTiO₃ surface and a Wannier-Stark localization of these states. Observation of Bloch oscillations and Wannier-Stark localization of charge carriers is typically impossible in single-crystals, because an electric field higher than the breakdown voltage is required. In BaTiO₃ however, high intrinsic electric fields are present due to its ferroelectric properties. With angle-resolved photoemission we directly probe the Wannier-Stark localized surface states of the BaTiO₃ film-vacuum interface and show that this effect extends to thin SrTiO₃ overlayers. The electrons are found to be localized along the in-plane polarization direction of the BaTiO₃ film. This agrees with a low-temperature, strain induced tetragonal phase of the BaTiO₃ films.

The majority of the content of this chapter is written as a manuscript (Sec. 5.1) and its supplemental material (Sec. 5.2, 5.3, 5.4 and 5.5) that is currently under review. Coauthors of this future publication are Nicolas Pilet, Mauro Fanciulli, Andrew Weber, Zoran Ristić, Zhiming Wang, Nicholas Plumb, Milan Radović and Hugo Dil. The author of this thesis did grow the investigated BaTiO₃ and SrTiO₃ films, performed the photoemission experiments, analyzed the data and wrote the manuscript.

5.1 Direct observation of Wannier-Stark localization at the surface of BaTiO₃ films

Electric fields are the driving force of electric transport and a variety of electronic properties of semiconductor systems. The ultimate limiting mechanism of conductance in crystals is defect scattering, which prevents ballistic transport. However, in an ideal system, without defect scattering, electrons would perform an oscillating motion for large enough electric fields. These so-called Bloch oscillations form due to the Bragg scattering of the accelerated electrons at the Brillouin zone boundary [219, 220]. The oscillations eventually lead to a Wannier-Stark localization (WSL) of the accelerated electrons as well as the formation of a Wannier-Stark

ladder [89, 92]. These effects set a fundamental limit to coherent transport in crystals and their existence in a real system will provide further insight into its transport mechanisms.

The Bloch oscillation time for one cycle is given by $\tau_B = h/(e\mathcal{E}a)$, where h is the Planck constant, e the electron charge, \mathcal{E} the electric field present and a the lattice parameter in the direction of the electric field. In real crystals, the critical condition for Bloch oscillations to be possible is a τ_B smaller than the relaxation time τ of the system which is determined by the mean free path λ and the Fermi velocity v_F . In other words the electron has to complete one (or several) periods of the Bloch oscillation before being scattered at random lattice defects. This condition can not be met by applying an external electric field on single crystal semiconductors, because the required fields are orders of magnitudes higher than the breakdown voltages of these systems. This problem was successfully addressed by the engineering of artificial semiconductor lattices of high quality. In artificial superstructures, the lattice parameter a is replaced with the size of the superstructure and can therefore be increased. Thus the required electric field is lowered to an achievable value to observe Bloch oscillations and related effects [97, 221–225].

In this Letter we take a new approach, utilizing the electric field present in ferroelectric BaTiO₃ (BTO) to directly observe WSL of the two-dimensional states present at its surface by angle-resolved photoelectron spectroscopy (ARPES). Furthermore, it will be shown that this effect can be extended to thin overlayers of SrTiO₃ (STO) where the ferroelectric field of the BTO substrate localizes the STO surface states.

BTO is a well known ferroelectric material and closely related to the perovskites SrTiO₃, CaTiO₃ (CTO) and KTaO₃ (KTO). These materials are all known to host a two-dimensional electron gas at their surface [9, 10, 22, 61, 63, 87, 226]. It is expected that ferroelectric properties due to local lattice relaxations play a key role in the formation of the two-dimensional electron gas, especially regarding the Rashba-type spin splitting observed in STO [66]. These three perovskites are all classified as incipient ferroelectrics in which quantum fluctuations prevent a ferroelectric order [11, 12, 120, 121]. The closely related BTO presents an excellent opportunity to study the impact of a bulk ferroelectric material on these two-dimensional states and their transport properties [227] and offers a means of inducing ferroelectricity in other perovskites through doping or multilayer structure assembly. With the insights into fundamental transport mechanisms by the observation of WSL, new ways to directly manipulate and tailor transport properties of ferroelectric semiconductors become accessible.

Bulk crystalline BTO is ferroelectric below the transition temperature of 120°, exhibiting three different ferroelectric phases; the tetragonal phase [Fig. 5.1(a)] from 120° to 5°, the orthorhombic phase from 5° to -90°, and, for temperatures below -90°, the rhombohedral phase. Each of these phases has distinct electric-polarization anisotropies given by the symmetries of the unit cell (uc) [129, 130]. The phase diagram of BTO thin films is significantly different compared to bulk BTO. In films, the formation of ferroelectric phases and the preferred polarization direction can be directly manipulated by interface strain. The transition temperature is raised

5.1. Direct observation of Wannier-Stark localization at the surface of BaTiO₃ films

for compressive as well as tensile strain [135]. For tensile strain, it has been demonstrated that solely an orthorhombic phase, polarized in the in-plane direction, exists below the ferroelectric transition temperature [135, 143, 144]. For compressive strain the tetragonal phase is the only ferroelectric phase present below the transition temperature, with a preferred polarization along the out-of-plane axis in films with a thickness of around of 5 uc [144, 228]. With increasing film thickness, strain and growth-defect relaxation will be responsible for a mixture of in-plane and out-of-plane domains of the tetragonal phase. In thicker films of BTO grown on STO, a mixture of domains with the size of around 20 nm can be observed as a result of relaxation [135, 146]. Furthermore, the formation of domain walls with a 90° change in polarization direction are preferred energetically to 180° domain walls [145]. This also favors a mixture of domains with out-of- and in-plane polarization directions.

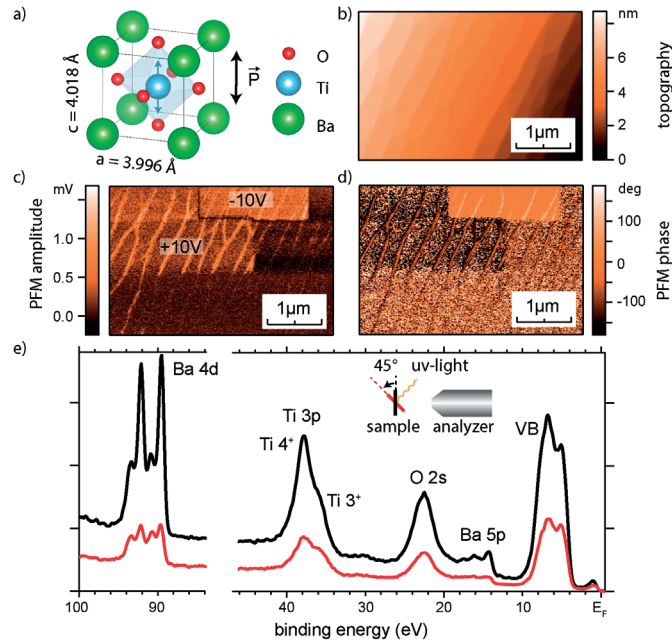


Figure 5.1 – (a) Tetragonal BTO uc with indicated polarization axis. (b) AFM topography of a film of 50 uc BTO grown on Nb:STO. (c) and (d) PFM phase and amplitude. Square on the left side is poled by +10 V applied to the probe tip, the square on the top with -10 V as indicated. (e) XPS measurements with $h\nu = 170$ eV photons for normal emission (black) and an emission angle of 45° (red).

The films investigated in this work were grown by pulsed laser deposition (PLD), allowing a controlled layer-by-layer growth monitored by reflective high-energy electron diffraction (RHEED). Films with a thickness of 20 uc were grown on commercially available, single-terminated SrTiO₃, Nb:SrTiO₃ and KTaO₃ (001) substrates (SurfaceNet GmbH). The growth was performed at a substrate temperature of 950 K, in a partial oxygen pressure of $1 \cdot 10^{-5}$ mbar. STO films of 3 and 5 uc thickness were grown on top of this BTO film under similar conditions (see Sec. 5.5.1). The samples were *in-situ* transferred to the high-resolution ARPES endstation and measured with circularly polarized synchrotron light. During the measurements the sample

was held at 20 K and kept in ultra high vacuum (UHV) conditions better than $1 \cdot 10^{-10}$ mbar. The films were *ex-situ* transferred to the NanoXAS beamline for piezo-response force microscopy (PFM) measurements at room temperature under UHV condition. The sample measured with PFM had a thickness of 50 uc and was grown on a 0.5wt% Nb doped STO substrate under the same conditions as described above. A conductive substrate was chosen in order to have a well-defined back electrode and the higher film thickness in favor of a stronger PFM response signal.

The PFM topography in Fig. 5.1(b) shows a uniform sample surface (Sec. 5.2) according to the vicinity of the substrate, where a 0.2° miscut to the (001) surface was chosen to promote a layer-by-layer growth. The PFM phase and amplitude in Fig. 5.1(c,d) of the as-grown sample (bottom part of the field of view) shows no noticeable contrast, indicating that no intrinsic domains of resolvable size ($\gtrsim 20$ nm) are present. After subsequent writing of the surface with +10 V and -10 V applied to the probe tip, a phase and amplitude contrast is noticeable, proving the presence of ferroelectric properties in our films. However, both of the written regions exhibit significant noise, reducing the difference of the mean phase value between the positive and negative poled region to approximately 72° (Sec. 5.2). This difference is significantly less than the 180° phase difference expected for completely opposite polarized regions. The reasons for this observation is a not completely homogeneously polarized surface in the written areas. This indicates a strong locking of the domains in the in-plane direction due to interface strain and relaxation mechanisms.

The X-ray photoelectron spectroscopy (XPS) measured at normal emission and at a more surface sensitive emission angle of 45° show the Ba 4d, Ti 3p and O 2s core levels [Fig. 5.1(e)]. The Ba 4d core level consists of the spin-orbit split Ba $4d_{3/2}$ and $4d_{5/2}$ doublet and a lower intensity doublet, shifted by 1.25 eV to higher binding energies. By comparing the peak areas of the two species for the two emission angles we can assign the higher binding energy, chemically-shifted doublet to undercoordinated Ba ions in the BTO surface region [229–231]. The Ti 3p core level includes two peaks assigned to the Ti 4^+ and Ti 3^+ ions whereas the latter is more surface localized. Close to the Fermi energy an in-gap state is located at a binding energy of 0.9 eV in the bulk band gap (Sec. 5.4.4, [232]). The intensity of the in-gap state and the Ti 3^+ peak increases under UV irradiation (Sec. 5.4.4). Similar effects are observed in the case of STO where the presence of Ti 3^+ ions and the in-gap state are explained by surface relaxation and oxygen vacancies [61]. Comparing the relative Ba 4d and Ti 3p peak areas for the two emission angles, we can conclude that the surface is TiO₂ terminated [209].

The ARPES measurements in Fig. 5.2 and Fig. 5.3(a-c) show metallic states emerging from the in-gap state, which do not disperse as a function of photon energy, indicating their two-dimensional nature (Sec. 5.4.2). As observed for STO, matrix element effects are responsible for the suppression of intensity at $k_x = 0 \text{ \AA}^{-1}$ due to the mainly xy-symmetry of the two-dimensional state (Sec. 5.4.2 and 5.4.3). These states can be attributed to the partially filled Ti $3d_{xy}$ orbital, that is split from the Ti $3d_{xz}$ and Ti $3d_{yz}$ orbitals due to a distortion of the TiO₆ octahedron by lattice relaxation [9, 22, 61]. However, the Fermi surface around the $\bar{\Gamma}$ -points

5.1. Direct observation of Wannier-Stark localization at the surface of BaTiO₃ films

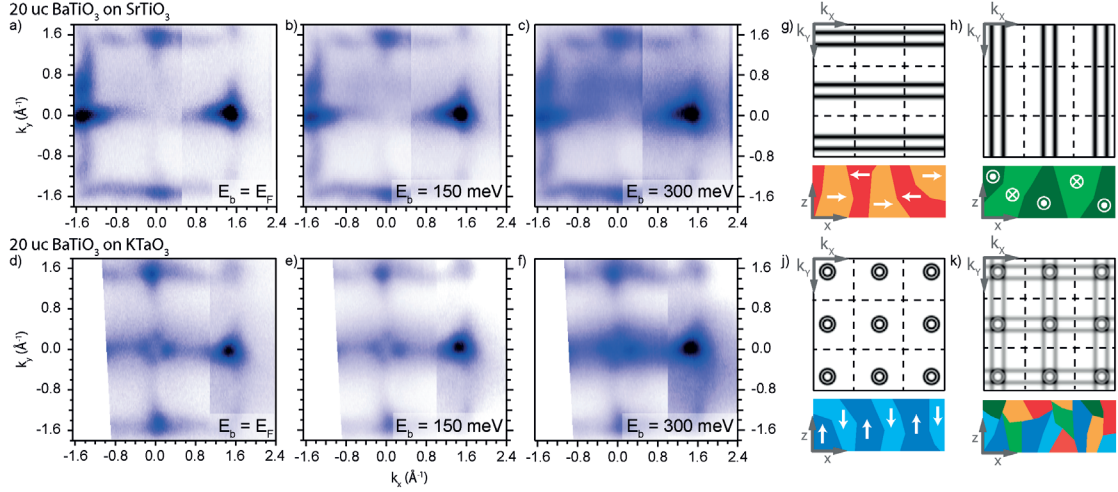


Figure 5.2 – (a-c) Constant energy surfaces of 20 uc of BTO grown on STO measured with $h\nu = 80$ eV for $E_b = E_F$ (a), $E_b = 150$ meV (b) and $E_b = 300$ meV (c). (d-f) Same as (a-c) for 20 uc BTO on KTO. (g-k) Different ferroelectric domain configurations of the films and the corresponding WSL states for in-plane polarizations along $\langle 100 \rangle$ (g) and $\langle 010 \rangle$ (h) and out-of-plane polarization along $\langle 001 \rangle$ (j). (k) Combined WSL states from the three configurations with equal weight.

shows no clear bands of the two-dimensional states but features spectral weight, elongated along both $\overline{\Gamma X}$ -directions. These elongated states extend over multiple surface Brillouin zones connecting the neighboring Γ -points as shown in Fig. 5.2(a,d). Comparing the Fermi surface with constant energy surfaces at higher binding energies [Fig. 5.2(b,c) and (e,f)], no dispersion of these states with respect to the binding energy is noticeable. As we will explain below, these non-dispersive states are WSL states and a direct consequence of the electric field present in the material.

The electrons in the two-dimensional state experience an accelerating force in the direction opposite to the electric field present in the ferroelectric domains. Due to the potential barrier at unit cell boundaries, the acceleration is not uniform but is described by Bloch oscillations [219, 220]. This localizes the electron in real space and hence shows smearing in reciprocal space. Considering the lattice parameter of BTO, the condition $\tau > \tau_B$ for Bloch oscillations to exist is fulfilled for an electric field $\mathcal{E} \gtrsim 10^9$ V/m assuming a typical relaxation time of $\tau = \lambda / v_F \approx 10^{-14}$ s [92], which exceeds the breakdown field strength of known insulators. Due to its ferroelectric properties, the local electric field in the BTO film is several order of magnitudes higher than any possible external electric field. An estimate of the electric field inside BTO films can be obtained from the spontaneous polarization which is $P \approx 0.25$ C/m² for tetragonal bulk BTO [125] and is predicted to increase for strained films [233]. For different approaches (see Sec. 5.3 for more details) an electric field between $5 \cdot 10^8$ V/m and $1.5 \cdot 10^{10}$ V/m is obtained, which is of the order of the electric field required to meet the condition for Bloch oscillations.

The BTO films grown on a STO substrate have a compressive strain of 2 % at the interface. As a result, the film is expected to stay in a single tetragonal phase below the ferroelectric phase transition [144, 228]. Tetragonal BTO can host a ferroelectric polarization along the $\langle 001 \rangle$ out-of-plane as well as the $\langle 100 \rangle$ and $\langle 010 \rangle$ in-plane directions. While at the interface the polarization direction is preferably along the out-of-plane axis, strain relaxation mediated by growth defects will be responsible for a mixture of domains close to the film surface. The domains with different electric field directions will all contribute differently to the Fermi surface. The in-plane domains, exhibiting an electric field along $\langle 100 \rangle$ [Fig. 5.2(g)] or $\langle 010 \rangle$ [Fig. 5.2(h)] directions will both give rise to WSL states. In ARPES, these WSL states are visible as one-dimensional states along the $\overline{\Gamma X}$ -directions. In domains where the electric field is along the out-of-plane or $\langle 001 \rangle$ directions [Fig. 5.2(j)], the electric field will lift the spin-degeneracy of the two-dimensional states. The resulting Rashba-type spin splitting consists of oppositely spin-polarized, concentric rings at the Fermi surface [66, 70, 77]. The direction of the spin polarization of the bands will be inverted depending on the sign of the ferroelectric polarization vector.

With a domain size on the order of 20 nm [146], the synchrotron beam with a size of around 100 μm will average over several domains with different ferroelectric polarization directions. The resulting model Fermi surface in Fig. 5.2(k), formed by an overlay of the contributions from the different domains is in good agreement with the ARPES measurements, especially if further modulation of the ARPES signal by matrix element effects are considered.

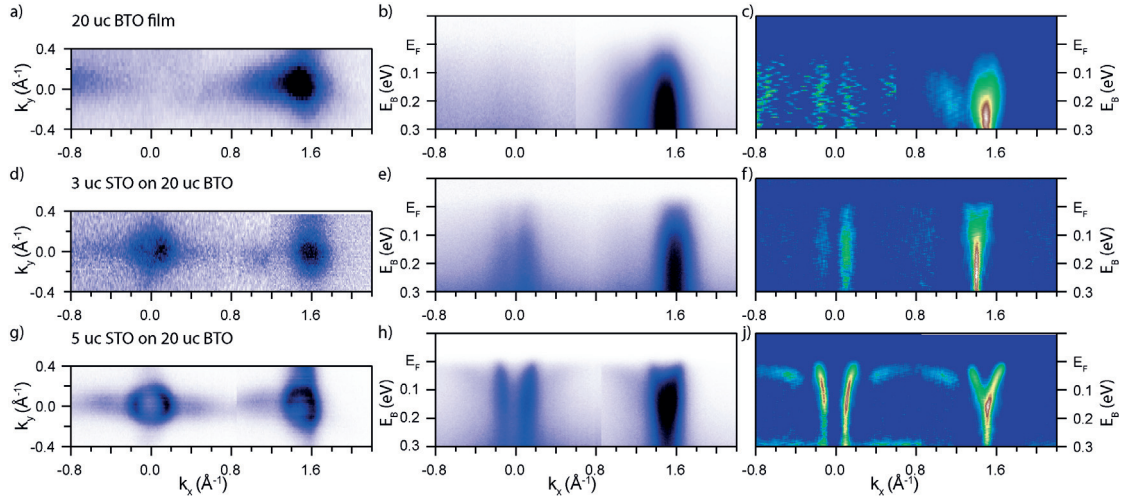


Figure 5.3 – (a,d,g) ARPES Fermi surface, (b,e,h) band map at $k_y = 0 \text{ \AA}^{-1}$, and (c,f,j) two-dimensional curvature [234] measured at $h\nu = 82 \text{ eV}$. (a-c) For the 20 uc BTO film, (d-f) for a 3 uc STO film on top of 20 uc of BTO, and (g-j) for a 5 uc STO film on top of 20 uc of BTO.

For BTO films grown on KTO the compressive strain is reduced to 0.2 % due to the larger lattice constant of KTO compared to STO. With the change in strain also the domain formation is expected to be different for the BTO films on KTO. When comparing the data of the film on KTO [Fig. 5.2(d-f)] with the results of the film grown on STO [Fig. 5.2(a-c)] two differences

5.1. Direct observation of Wannier-Stark localization at the surface of BaTiO₃ films

are noticeable: i) the signature of a circular Fermi surface contribution around $\overline{\Gamma_{00}}$ and ii) the WSL states are more intense along the k_x - than the k_y -direction. Both of these observations are in agreement with an altered domain configuration. The reduced interface strain is responsible for the formation of larger domains with a higher fraction polarized along the z - and x -directions in the measured BTO films grown on KTO.

The general nature of the WSL is illustrated by its presence in ultrathin STO films grown on top of the BTO layers. The ARPES data for a 3 uc thick STO film in Fig. 5.3(d-f) exhibits states very similar to pure BTO Fig. 5.3(a-c). The Fermi surface shows stripes extending over several surface Brillouin zones (see Sec. 5.5.3) characteristic for the WSL. However, the reduced electric field with increasing STO film thickness results in a lower intensity of the smearing and in Fig. 5.3(c) a shallow electron pocket with polaron replicas [54, 201] becomes visible. For the surface of the 5 uc film in Fig. 5.3(g-j) the fields of the BTO substrate are so far reduced that no indication WSL is visible. The ARPES data starts to resemble bulk STO with a measured Fermi surface consisting of the more filled circular d_{xy} states and elongated d_{xz} and d_{yz} states [61].

From these results we can estimate that about 4 uc of STO are needed so the electric field of BTO is lowered to a value that no longer influences the electronic properties at the sample surface. Furthermore, the sharp electron-like states at the surface of the STO films verify the high crystalline quality also of our BTO layer. RHEED and XPS data (see Sec. 5.5.1 and 5.5.2) indicate a layer-by-layer growth of the STO, opening the possibility to study whether a ferroelectric order is induced in the STO by high resolution transition electron microscopy in future work.

To conclude, we have presented combined effects of two different physical properties on BTO film surfaces: the formation of a two-dimensional state and the Wannier-Stark localization of these state. We have further demonstrated that ARPES provides a novel means of probing WSL in reciprocal space. To our knowledge, this is the first time WSL is directly observed in a single crystalline semiconductor. The combined presence of electric fields and two-dimensional states at the surface of a transition metal oxide opens up a rich field to study the interplay of ferroelectricity and interface states. For the study of the macroscopic influence of WSL on the transport properties, BTO films with preferred polarization directions should be prepared by the help of different substrates regarding orientation, lattice parameters and conductivity [148, 150, 235] and under different growth conditions [232]. Furthermore, our experiments suggest that WSL should be a general effect for ferroelectric materials with surface or interface states, and domains with an in-plane electric field.

5.2 Piezo-response force microscopy

The piezo-response force microscopy (PFM) data of Fig. 5.4 is the full data set of the measurements presented in Fig. 5.1 (b-d). The topography [Fig. 5.4(a)] features a uniform step formation over the whole measured range with step heights [Fig. 5.4(b)] corresponding to one or multiple unit cells. The position of the step edges are visible in the normal deflection [Fig. 5.4(c)]. The terrace width of $0.1 - 0.2 \mu\text{m}$ is given by the substrate misscut to the (001) surface of $0.1^\circ - 0.2^\circ$. The PFM amplitude and phase [Fig. 5.4(d,f)] show a visible contrast between the oppositely written areas as well as the unwritten area. The as-grown sample shows no formation of domains larger than the measurement lateral resolution of $\approx 20 \text{ nm}$. Due to the small PFM signal of the BaTiO₃ (BTO) film, the measurements were performed at the PFM resonance. This is causing a small cross talk of the PFM phase and amplitude with the topography signal, responsible for the visibility of the step edges in the PFM channels.

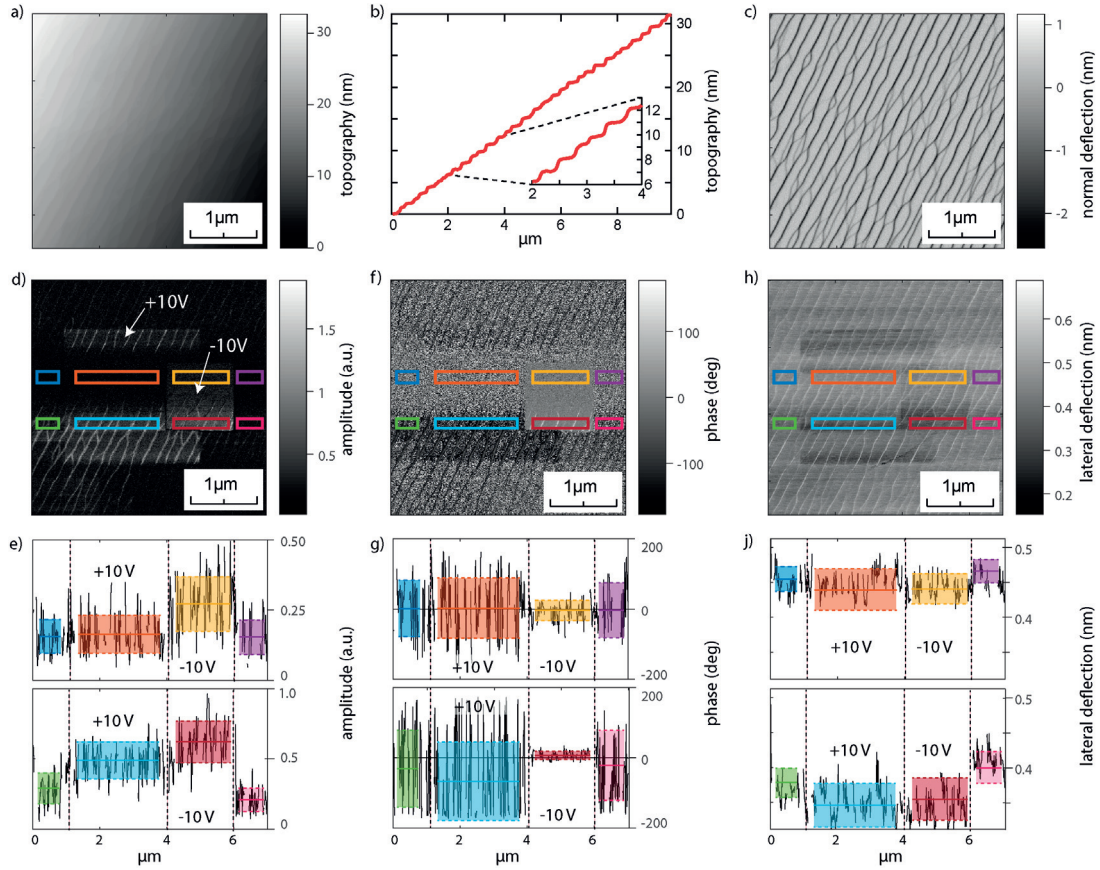


Figure 5.4 – (a) PFM topography of 50 uc BTO grown on Nb:STO. (b) Topographic line profile along the diagonal perpendicular to the step edges. (c) Normal deflection. (d) PFM amplitude including written areas for +10 V and -10 V applied to the tip, as indicated. (e) Line profiles along the center of the marked squares in (d) with indicated average values and standard deviation of the marked areas. (f) PFM phase with (g) line profiles and (h) lateral deflection with (j) line profiles.

Two line profiles are taken along the scanning direction in the center of the marked, colored squares for the PFM amplitude [Fig. 5.4(e)] and phase [Fig. 5.4(g)] each. The signal in the vicinity of the step edges are excluded from the line profiles. In the amplitude line profiles a clear difference between the positively, the negatively, and the unwritten areas is noticeable. Especially the amplitude of the negative poled region is clearly higher than the positive and the unwritten areas. On the phase signal a clear reduction of noise is noticeable for the negatively poled area, while for the positively poled part the noise is on the level of the unpoled region (see Table 5.1). The phase difference between the oppositely poled area is 6° for the top row and 72° for the bottom row with an error margin larger than the difference.

The measurements show that writing with a negative potential applied to the probe tip has a more noticeable effect than writing with a positive potential. Especially the strong noise reduction for the phase and the offset in the amplitude is obvious. In the phase, the mean value of the negative written area is, as for the unwritten part, very close to 0° . This indicates that a larger portion of the intrinsic domains are polarized pointing out of the plane than into the plane. Thus the writing with positive potential applied is less effective. In order to uniformly polarize the two areas by switching all the in-plane domains to the out-of-plane axis, a higher potential than 10 V would be needed. In the lateral deflection [Fig. 5.4(g,h)] of the probe tips a clear contrast is noticeable between the written regions and the unpoled area. This lowering of the friction at the previously written areas could be due to the reduction of in-plane domains in these regions changing the local polarization fields.

























		unpoled		-10 V		+10 V		unpoled
Amplitude (arb.units)		0.16 ± 0.06		0.16 ± 0.07		0.27 ± 0.10		0.15 ± 0.06
		0.29 ± 0.11		0.48 ± 0.13		0.62 ± 0.15		0.21 ± 0.08
Phase (deg.)		2 ± 80		2 ± 86		-4 ± 29		-2 ± 78
		-34 ± 109		-65 ± 111		7 ± 12		-25 ± 99
Lateral Deflection (nm)		0.45 ± 0.02		0.44 ± 0.03		0.44 ± 0.02		0.47 ± 0.02
		0.38 ± 0.02		0.34 ± 0.03		0.35 ± 0.02		0.40 ± 0.02

Table 5.1 – Table with the average values and corresponding standard deviation for the line profile areas in Fig. 5.4(e,g,j).

5.3 Estimation of the electric field

An estimation of the electric field inside tetragonal BTO is possible based on the expected dipole moment of a unit cell (uc), that is given by the polarization P and the uc volume dV as $|p| = P \cdot dV = 0.25 \text{ C/m}^2 \cdot (3.996^2 \cdot 4.018) \text{ \AA}^3 \approx 1.6 \cdot 10^{-29} \text{ Cm}$. The value $P \approx 0.25 \text{ C/m}^2$ for

tetragonal bulk BTO is taken from [125]. For a single dipole the resulting electric field at a distance r from the dipole and angle θ from the dipole axis is given by:

$$\mathcal{E}_r(r, \theta) = \frac{2 k |p| \cos(\theta)}{\epsilon_r \cdot r^3} \hat{r} \quad (5.1)$$

$$\mathcal{E}_\theta(r, \theta) = \frac{k |p| \sin(\theta)}{\epsilon_r \cdot r^3} \hat{\theta} \quad (5.2)$$

where k is the Coulomb's constant and ϵ_r the relative permittivity of BTO films. The relative permittivity ϵ_r for thin films is reduced by several orders of magnitude compared to bulk BTO and is distinguished to be $\epsilon_r \approx 60$ at 80 K for a 100 nm thick film [147, 236].

The resulting simple model to estimate the electric field in tetragonal BTO is shown in Fig. 5.5 and is based on the location of a dipole in each uc at the Ti site. This dipole represents the charge displacement between the Ti and O ions that is considered to be the main contribution to the electric field. The graph (Fig. 5.5) represents the electric field in the TiO₂ layer of BTO, parallel to the dipole vector. The electric field along the direct Ti-Ti line, that corresponds to the $\overline{\Gamma X}$ -direction in reciprocal space is always larger than $1 \cdot 10^9$ V/m and is therefore large enough to observe WSL in the uc of BTO. The representation of the ferroelectric properties of the BTO uc with a dipole is an oversimplification and can not be used to distinguish the local electric field in the unit cell and is only used to roughly estimate the magnitude of the electric field in BTO. The model further does not consider any effect expected at the vacuum interface or at domain boundaries. Due to depolarization fields and shielding charges the electric field is expected to look different in these regions.

Another approach to estimate the electric field is possible by considering the external electric field of a ferroelectric material given by its polarization P [92, 237].

$$|\mathcal{E}| = \frac{P}{(\epsilon_r - 1) \epsilon_0} \approx 5 \cdot 10^8 \text{ V/m} \quad (5.3)$$

Based on this external electric field \mathcal{E} it is possible to distinguish the local electric field \mathcal{E}_{loc} inside the material given as $\mathcal{E}_{loc} = 1/3 (\epsilon_r + 2) \mathcal{E}$ [92]. With the relation 5.3 for the external electric field, the local electric field can be written as a function of the polarization P , the relative permittivity ϵ_r and the vacuum permittivity ϵ_0 .

$$|\mathcal{E}_{loc}| = \frac{1}{3} \frac{P \cdot (\epsilon_r + 2)}{(\epsilon_r - 1) \cdot \epsilon_0} \approx 1 \cdot 10^{10} \text{ V/m} \quad (5.4)$$

The resulting electric fields obtained by the different approaches are all in the order of magnitude of the electric fields required to observe WSL in the uc of BTO. Due to the differences

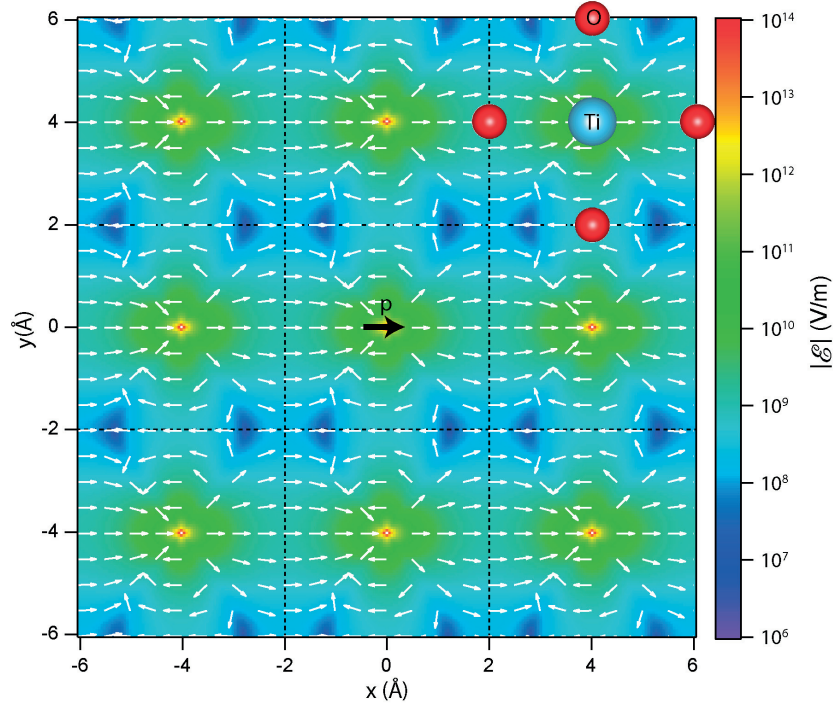


Figure 5.5 – Simple model of the electric field in the TiO_2 -layer of BTO based upon dipoles at the Ti sites. A sketch of the location of the atoms in this layer is given in the top right corner. The calculations are based on a superposition of the electric field of a dipole array given in equations 5.1 and 5.2. The color scale indicates the magnitude and the white arrows the direction of the resulting electric field based on this simple model.

in domain sizes and their respective polarization directions, the electric field amplitude is expected to vary within the BTO films.

In general, the WSL is expected to be accompanied by the formation of a Wannier-Stark ladder, a set of electron bands separated in energy and space. The energy separation between the steps is given as $\Delta E = e\mathcal{E}a$ [89, 92] and expected to be between 0.1-6 eV for our samples, based on an electric field between $5 \cdot 10^8$ V/m to $1.5 \cdot 10^{10}$ V/m. However, ARPES is not the method of choice to observe these ladders. Local probe techniques using tunneling or optical spectroscopy should be able to address this aspect in future work.

5.4 Additional ARPES measurements of BaTiO₃

5.4.1 Measurements along $\overline{\Gamma\text{M}}$

The angle-resolved photoelectron spectroscopy (ARPES) data presented in the main text are all measured with the same geometry where the entrance slit of the hemispherical analyzer is aligned along the $\overline{\Gamma\text{X}}$ -direction of the crystal. In the measurements in Fig. 5.6 the crystal is aligned with $\overline{\Gamma\text{M}}$ parallel to the analyzer entrance slit [along θ see Fig. 5.6(a)]. The angular scanning direction [ψ in Fig. 5.6(a)] is perpendicular to the alignment direction and consequently different for the two cases. Apart from changes in the relative intensities, the altering of the measurement geometry does not affect the data. In particular the WSL states are still visible, smeared along the $\overline{\Gamma\text{X}}$ -direction. This confirms that our observations are not measurements artifact caused by the probing geometry.

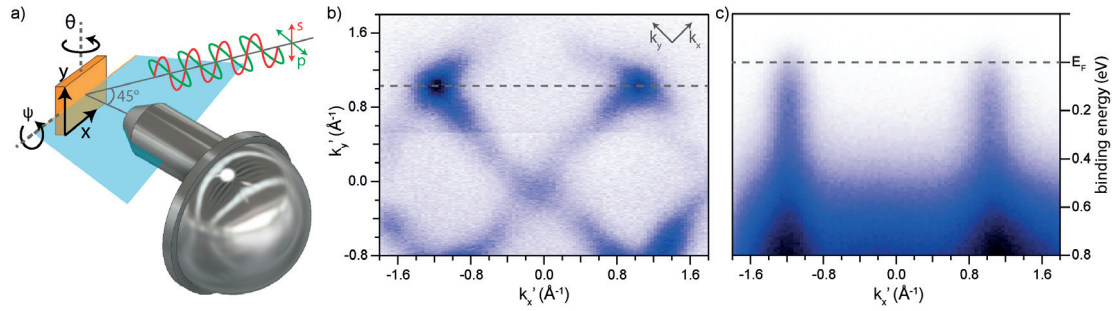


Figure 5.6 – (a) Measurement geometry of the ARPES setup. (b) ARPES Fermi surface of 10 uc BTO on STO for $h\nu = 77$ eV oriented with $\overline{\Gamma\text{M}}$ along the analyzer entrance slit. (c) Measured band dispersion across $\overline{\Gamma_{10}}$ and $\overline{\Gamma_{01}}$ as indicated in (a).

The data of Fig. 5.6 are taken from a sample of 10 uc BTO deposited on a SrTiO₃ (STO) substrate. In comparison with the data on 20 uc BTO on STO presented in the Fig.3 of the main text, the smearing tend to be more uniform. Possible reasons for this are the combined effect of altered matrix element contributions due to the different measurement geometry and a different domain pattern as a consequence of the reduced film thickness.

5.4.2 Photon energy dependency

Fig. 5.7 depicts measured Fermi surfaces, band maps, and photon energy dependence of the two-dimensional states around $k_x = 0$ Å⁻¹, the $\overline{\Gamma_{00}}$ point. The measured intensity at the Fermi energy as a function of k_x and photon energy [Fig. 5.7(c,e)] shows bands, forming two parallel lines with photon energy close to $k_x = 0$ Å⁻¹ that corresponds to $\overline{\Gamma_{00}}$. The different photon energies give access to different k_z . Therefore the lack of dispersion of these two parallel bands with photon energy indicates their two-dimensional (or one-dimensional) nature. Furthermore, the spectral enhancement at the photon energies of $h\nu = 45$ eV and $h\nu = 55$ eV [Fig. 5.7(d)] correspond to the energies of the Ti 3p - Ti 3d and Ti 3p - Ti 4sp resonance, respectively [238, 239]. The Ti 3p - 3d resonance has a sharp Fano-like lineshape

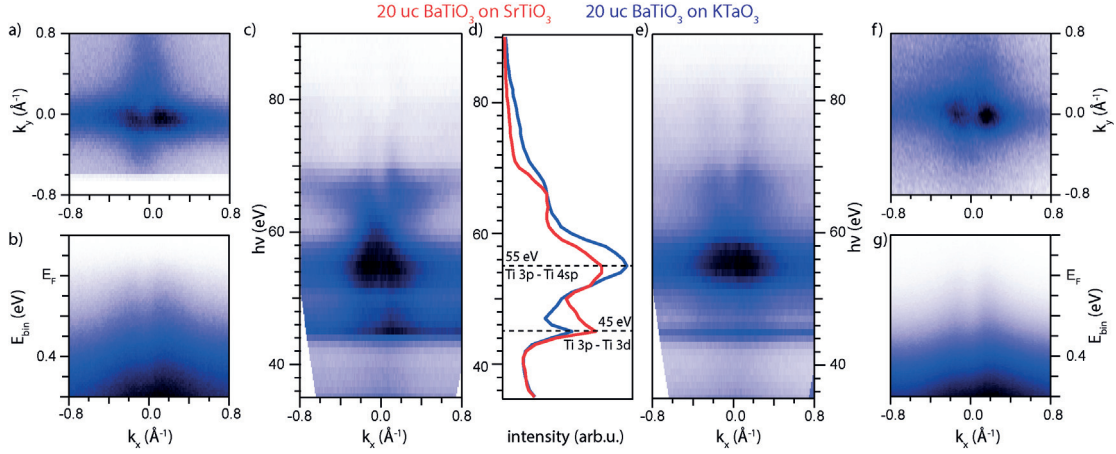


Figure 5.7 – ARPES data of 20 uc BTO grown on STO (a-c) and on KTO (e-g). (a,f) Fermi surface at $h\nu = 67$ eV and (b,g) Band dispersion in $\overline{\Gamma X}$ -direction. (c,e) Photon energy scan from $h\nu = 35$ eV to 90 eV at the Fermi energy. (d) Integrated photoemission intensity over $k_x = \pm 0.6 \text{ \AA}^{-1}$ at the Fermi energy for the sample grown on STO (red) and KTO (blue) substrate.

[240] indicating a low dimensionality of the excited state [239]; i.e. the Ti 3d states close to the Fermi level. On the other hand, the Ti 3p - Ti 4sp resonance is much broader implying that these states, hybridized with oxygen, are more delocalized along the z-direction [239].

5.4.3 Light polarizations

The Fermi surfaces and corresponding band structures for right- and left hand circularly polarized light as well as for s- and p-polarized linear light are depicted in Fig. 5.8 and Fig. 5.9. For these data, the analyzer entrance slit is aligned along the $\overline{\Gamma X}$ -direction of the sample as in the main text. For s-polarized light the electric field of the synchrotron light is along the k_y -direction, for p-polarized light along the k_x -direction [see Fig. 5.6(a)]. In the data in the vicinity $\overline{\Gamma_{00}}$ [Fig. 5.8] measured with a photon energy of $h\nu = 67$ eV no differences are noticeable for the two circular polarizations [Fig. 5.8(a,b)]. The band dispersion along the k_x -direction for circularly polarized light shows two features, connected to the in-gap state as discussed in the main text. Along k_y the band structure only hosts a single intensity feature at $k_y = 0 \text{ \AA}^{-1}$. For s-polarized light [Fig. 5.8(c)], the Fermi surface consist of two features elongated along the k_x -direction, separated by suppressed intensity at $k_x = 0 \text{ \AA}^{-1}$. Accordingly two features appear in the k_x dispersion, and the k_y dispersion only shows enhanced intensity around $k_y = 0 \text{ \AA}^{-1}$. The Fermi surface with p-polarized light [Fig. 5.8(d)] is similar to the one measured with s-polarized light but 90° rotated, with suppressed intensity along $k_y = 0 \text{ \AA}^{-1}$.

The suppressed intensity for $k_x = 0 \text{ \AA}^{-1}$ with s-polarized light and for $k_y = 0 \text{ \AA}^{-1}$ with p-polarized light is an indication for an xy-symmetry of the probed orbitals. In the case of the other known perovskites hosting a two-dimensional electron gas [9, 10, 22, 61, 63, 87], the two-dimensional states are attributed to the Ti $3d_{xy}$ orbitals and the three-dimensional bands,

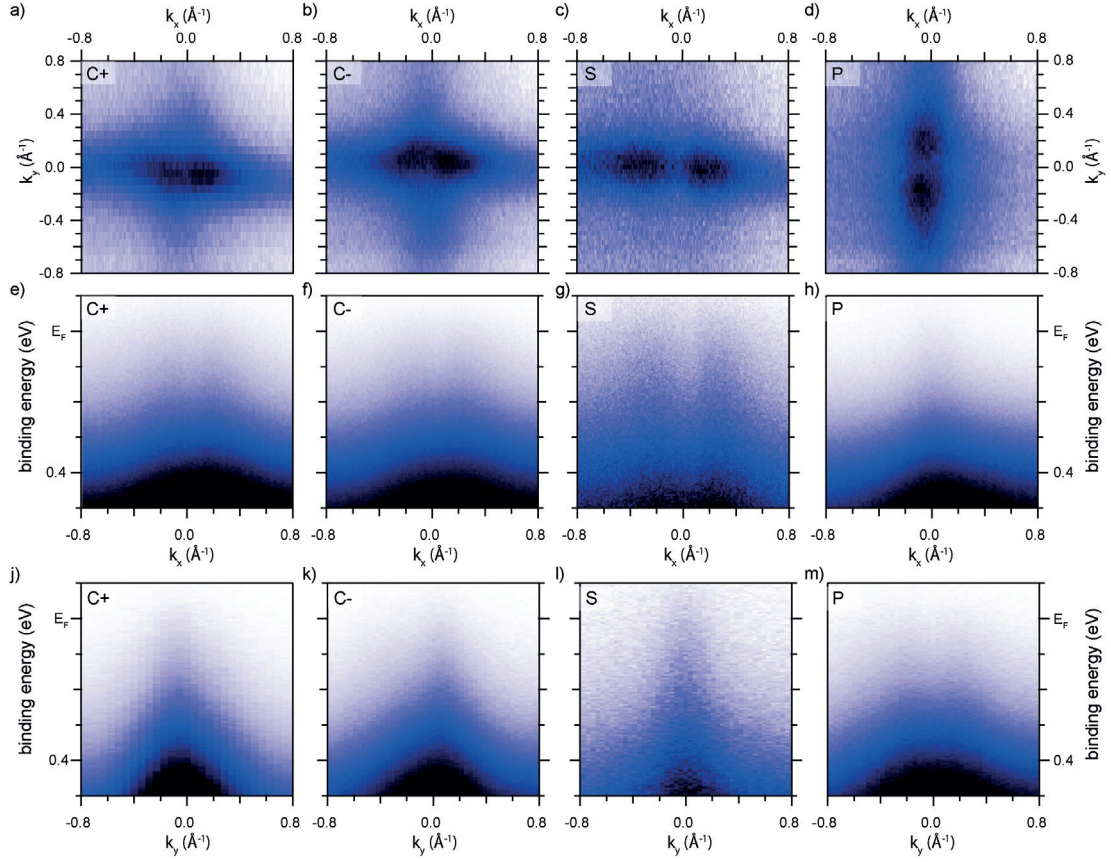


Figure 5.8 – ARPES data of 20 uc BTO on STO for different light polarizations measured with $h\nu = 67$ eV. (a-d) Fermi surfaces of the first Brillouin zone around $\overline{\Gamma}_{00}$ for (a) left- and (b) right-hand circularly polarized light and linear (c) s- and (d) p-polarized light. (e-h) Band dispersions along the k_x -direction for $k_y = 0 \text{ \AA}^{-1}$ and (j-m) band dispersions along the k_y -direction ($k_x = 0 \text{ \AA}^{-1}$) for the four light polarizations.

dispersing with photon energy, with the Ti $3d_{xz}$ and Ti $3d_{yz}$ orbitals. It seems likely for BTO to have a similar orbital ordering. However, due to the WSL of the states at the BTO surface, the orbital symmetries of the states present cannot be conclusively assigned.

The data in Fig. 5.9 of the Fermi surface at $\overline{\Gamma}_{10}$ for the different light polarizations are very similar to the data of $\overline{\Gamma}_{00}$ with respect to the light polarization effects. For right- as well as left-hand circularly polarized light [Fig. 5.9(a,b)] the intensity of the WSL along $\overline{\Gamma X}$ is visible. However, the intensity distribution along k_y around the Γ -point is inverted. For the linear polarized light only the WSL states in k_x -direction are visible for s-polarized light, while for p-polarized light only intensity elongated in k_y -direction are present. In contrast to the data taken at $\overline{\Gamma}_{00}$, the suppression of intensity at $k_x = 0 \text{ \AA}^{-1}$ or $k_y = 0 \text{ \AA}^{-1}$ for linear polarized light is absent due to the emission angle of $\overline{\Gamma}_{10}$ being far off normal emission. The band dispersion along the k_y -direction for the four different light polarizations consist of a main feature around $\overline{\Gamma}_{10}$, dispersing from the in-gap state. The band dispersions for the circular polarized lights,

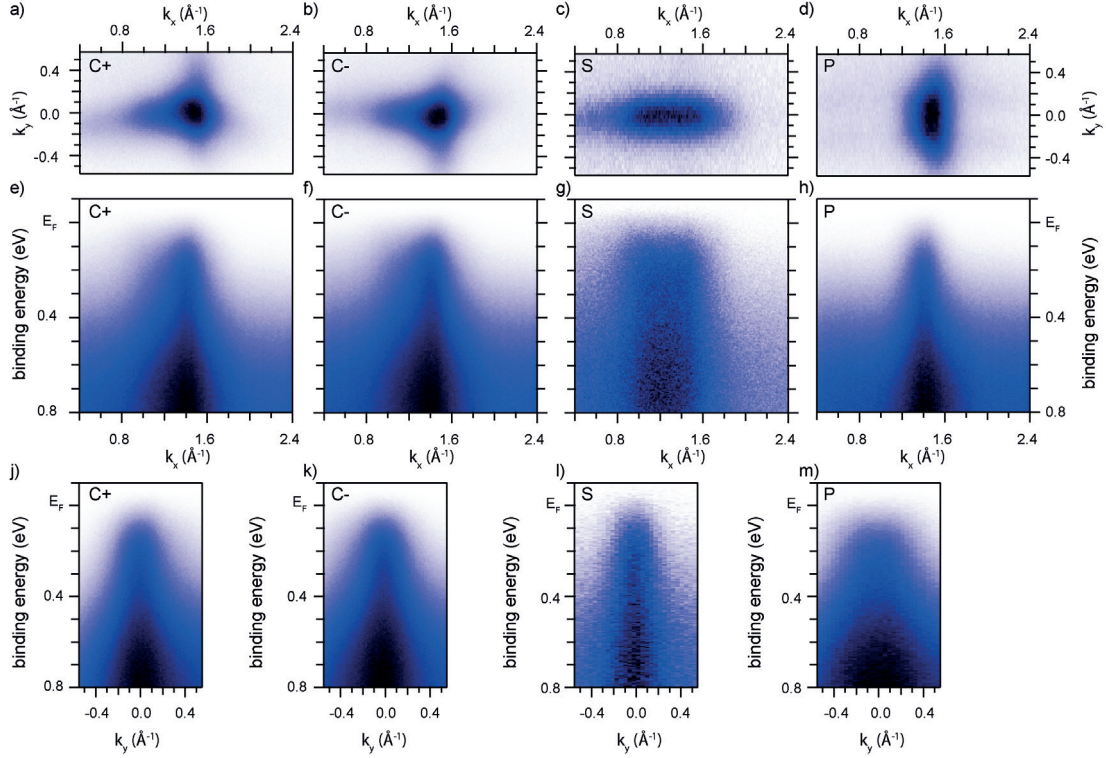


Figure 5.9 – Light polarization dependent ARPES of 20 uc BTO on STO measured with $h\nu = 80$ eV. (a-d) Fermi surfaces of the second Brillouin zone showing $\bar{\Gamma}_{10}$ for (a) C+, (b) C-, (c) s- and (d) p-polarized light. (e-h) Corresponding band dispersions along the k_x -direction for $k_y = 0 \text{ \AA}^{-1}$ and (j-m) band dispersion along the k_y -direction at $k_x = 1.57 \text{ \AA}^{-1}$ for the four light polarizations.

show an asymmetry around $k_y = 0 \text{ \AA}^{-1}$ corresponding with the Fermi surface. For s-polarized light the feature is narrow in the k_y -direction while for p-polarized light it is broad, opposite to the band dispersions along the k_x -direction.

5.4.4 Time dependent behavior

The BTO films show a time dependent behaviour under UV-irradiation. The spectral intensity of the in-gap state at 0.9 eV binding energy and of the Ti 3⁺ shoulder of the Ti 3p core level is increasing with time [see Fig. 5.10]. In case of the Ti 3⁺, its percentage on the total Ti 3p peak area rises from 7% to 18% within one hour [Fig. 5.10(a)]. This scales to a free charge carrier density of 0.18 electrons per uc after one hour, when saturation is reached. Within the same time frame, the intensity of the in-gap state rises by 300% [Fig. 5.10(b,c)]. However, the metallic state, visible as a second peak at the Fermi energy [Fig. 5.10(c)], only changes by 0.3% in peak area within the same time frame. Thus although the intensity of Ti 3⁺ and the in-gap state seem to be related, the intensity of the metallic states does not directly scale. The surface localized Ti 3⁺ ions are linked to the creation of oxygen vacancies and structural reordering of

the surface layers in the titanium based perovskites [61]. The changes implied in the distortion of the TiO₆ octahedrons and their respective binding angles due to the reordering will alter the hybridization of titanium and oxygen. Indications of this change in hybridization are observable in the altering peak intensity of the valence band with time. The observed changes under UV-light saturate within 30 min and are persistent with time regardless if the area is further irradiated or not.

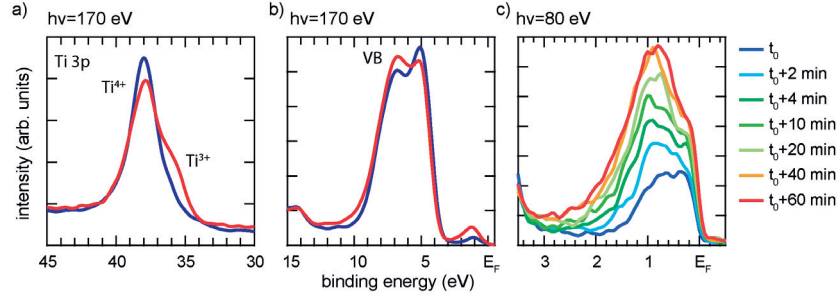


Figure 5.10 – Time-dependent, angle-integrated photoemission intensity of the (a) Ti 3p core level (b) valence band, measured with $h\nu = 170$ eV and (c) in-gap and surface states, measured with $h\nu = 80$ eV.

5.4.5 Temperature dependent measurements

The observed two-dimensional state present at the surface of BTO films, also persists at higher temperatures up to 150 K [see Fig. 5.11(a-d)]. Bulk BTO has no phase transition in this temperature range [129, 130, 135]. However, the STO substrate is expected to undergo a transition from cubic to tetragonal when cooling below 110 K [153]. This phase transition is expected to have a direct influence on the epitaxial strain at the interface. Upon annealing from 22 K to 90 K the band dispersion does not alter, except for the temperature related broadening of the Fermi level. At 150 K the spectral intensity is significantly reduced additionally to the temperature broadening. After cooling the sample back to 22 K the band structure is comparable to the initial one but is notably weaker in intensity.

In the core levels we see no change of the Ba 4d states, especially no shift of weight between the two observed species, with temperature. The Ti 3p states show a reduction of the lower binding energy shoulder associated with Ti³⁺ from initially 16% for $T_1=22$ K and $T_2=90$ K, to 6% for $T_3=150$ K. After cooling down again to $T_4=22$ K, 12% of the Ti atoms in the probed region are Ti³⁺. The presence of Ti³⁺ ions at the surface of BTO is likely, as for STO [61], related to the structural arrangement of the surface and the creation of oxygen vacancies in the probed surface region. Under UV irradiation, the intensity of the Ti³⁺ peak is increasing (see Chap. 5.4.4). This process seems to be inverted with rising temperature. However, when cooling the sample down to 22 K after the higher temperature measurements, this process is not completely reversed to the initial state. Oxygen vacancies should be created regardless of the systems history. According to this, a recovery of the sample to the initial state should be possible after the elevated temperature. More likely is a structural change of the surface

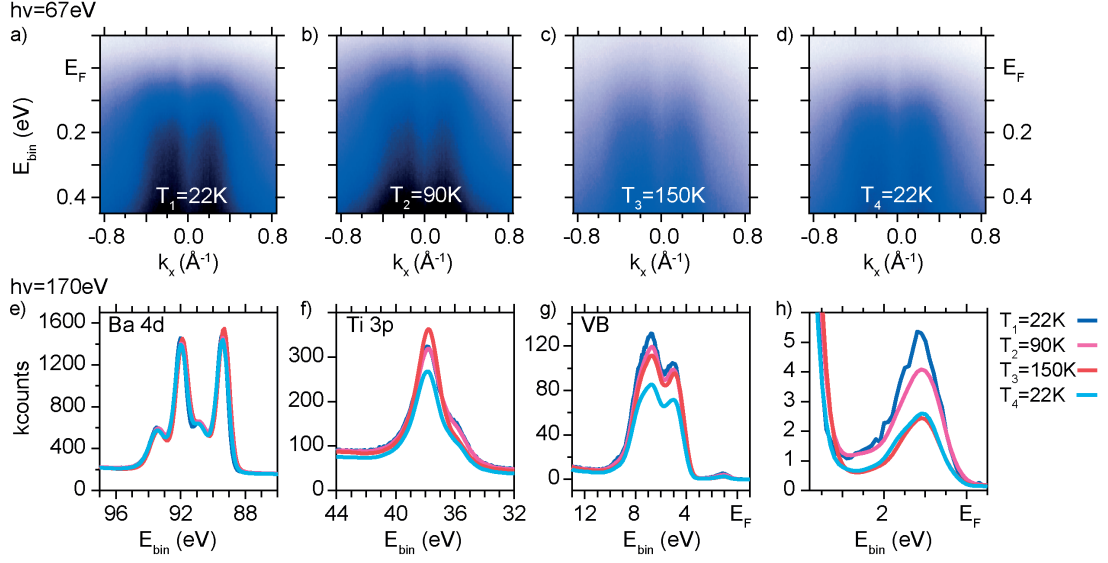


Figure 5.11 – Temperature dependent measurements of 20 uc BTO grown on Nb:SrTiO₃. a) to c) Band dispersion at Γ_0 , $h\nu=67\text{eV}$ for different temperatures (20 K, 90 K and 150 K) in the order of the measurements in time. d) Band dispersion after the temperature cycle at 20 K. e) to h) XPS measured with $h\nu=170\text{eV}$ at the same temperatures as in a) to d) of the Ba 4d e), Ti 3p f) core levels as well as the valence bands g) and in-gap states h).

ordering under the influence of UV-light at low temperatures. Upon rising temperature and UV-irradiation this phase is altered in a non reversible fashion affecting the formation of the two-dimensional state. In the valence band we can observe a clear reduction of the spectral intensity for the final temperature, similar to the reduction of intensity of the in-gap state located at 0.9 eV binding energy.

In ferroelectric BTO, the partial relief of interface stress at the tetragonal to cubic phase transition of the STO substrate at 110 K likely also alters the ferroelectric domain configuration in the BTO film. Possible is an increase of domains polarized along the out-of-the plane axis, enhancing a Rashba-like splitting of the two-dimensional state and lowering the fraction of domains contributing to the WSL. However, the effects of the WSL do not seem to be altered noticeably in the available data.

5.5 Further characterization of SrTiO₃ thin films on BaTiO₃

5.5.1 RHEED pattern and oscillations

The growth process with pulsed laser deposition (PLD), was monitored by reflective high-energy electron diffraction (RHEED) patterns and oscillations. The RHEED pattern and oscillations of a film of 20 uc BTO grown on a STO substrate are depicted in Fig. 5.12(a,d). The RHEED pattern was obtained after the growth and indicates a crystalline two-dimensional

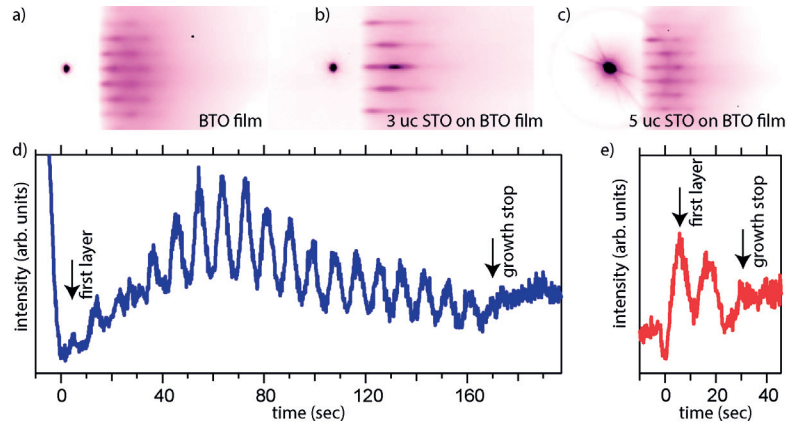


Figure 5.12 – (a) RHEED pattern of 19 uc BTO film grown on STO , (b) pattern of 3 uc STO grown on a BTO film and (c) pattern of 5 uc STO grown on a BTO film. (d) RHEED oscillations during the growth of the BTO film. (e) RHEED oscillations of 3 uc STO grown on a 20 uc STO film.

surface. Each maxima of the RHEED oscillation corresponds to the formation of a complete BTO layer and therefore allows a precise thickness control of the growing film. The RHEED pattern of the 3 uc [Fig. 5.12(b)] and 5 uc [Fig. 5.12(c)] film of STO deposited on a previously grown BTO film of 20 uc shows a good crystalline surface. By the help of the RHEED oscillations of the STO thin film growth [Fig. 5.12(e)], a precise termination of the growth process is possible at the oscillation maxima.

5.5.2 XPS measurements

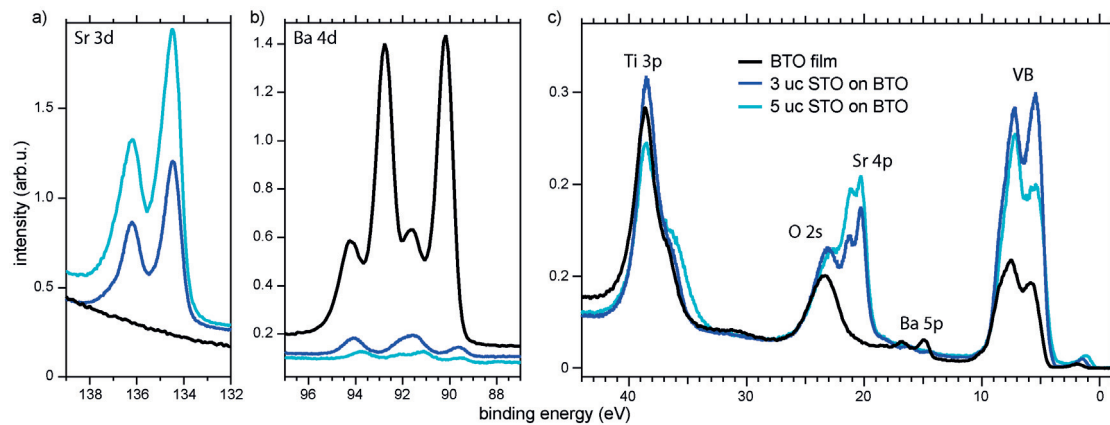


Figure 5.13 – XPS spectra obtained with $h\nu = 170$ eV for the clean BTO film and with 3 and 5 uc of STO on top. (a) Sr 3d, (b) Ba 4d, (c) Ti 3p, O 2s, Sr 4p, Ba 5p, and the valence band.

In Fig. 5.13 a comparison of XPS spectra is shown for the clean BTO films and 3 and 5 uc of STO grown on top. The data were normalized to the background after the O 2s core level and the BTO data was offset in Fig. 5.13(a) for clarity. As expected the Sr core levels increase with STO

coverage whereas the Ba core levels show a decay with coverage and are almost completely suppressed for the 5 uc thick STO film. This indicates a layer-by-layer growth of a closed STO film on top of the BTO substrate.

The small changes of binding energies in the Ba 4d core levels could give insight in the detailed atomic structure of the BTO/STO interface and possible intermixing in the first unit cell. However, this goes far beyond the scope of this work and is best combined with detailed structural investigations.

5.5.3 ARPES measurements

In Fig. 3(a) of the main text a subsection of the Fermi surface for a 3 uc thick film of STO grown on a 20 uc film of BTO was shown. Although the WSL states are readily discernible their extension becomes more clearly visible in the large range Fermi surface map in Fig. 5.14(a).

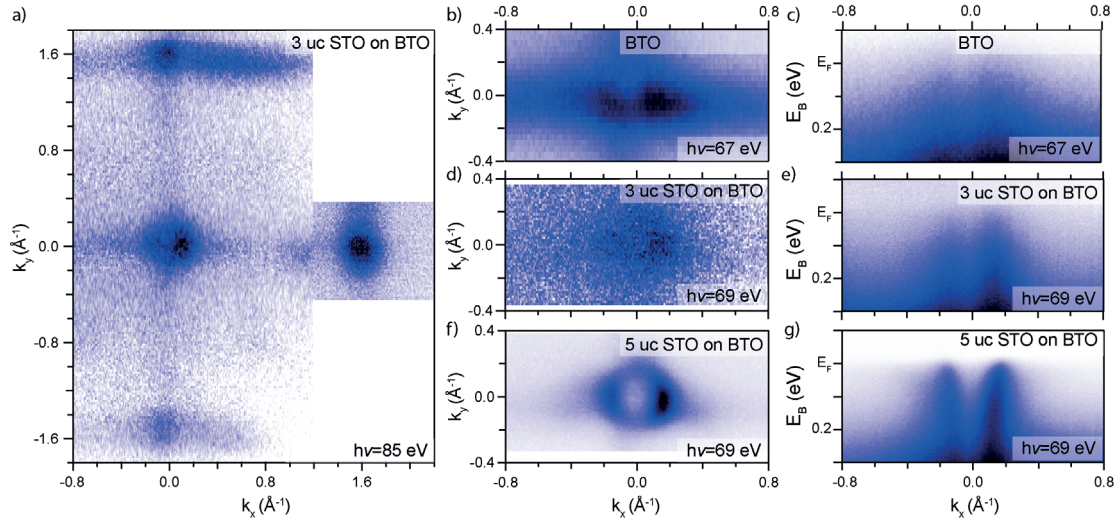


Figure 5.14 – (a) ARPES Fermi surface of 3 uc of STO on BTO obtained at $h\nu = 85$ eV. (b,d,f) Fermi surfaces around the surface Brillouin zone center for pure BTO, 3 uc, and 5 uc of STO on BTO at the indicated photon energies. (c,e,g) ARPES band maps at $k_y = 0$ for BTO film, 3 uc, and 5 uc of STO on a BTO film at the indicated photon energies.

In Fig 5.14(b-g) a comparison between pure BTO, 3 uc of STO on BTO, and 5 uc of STO on BTO is shown for a different photon energy as in Fig. 3 of the main text. Although the intensity ratio between the $3d_{xy}$ and $3d_{xz}$ (or $3d_{yz}$) bands has changed for the 5 uc data, the general features are independent of photon energy.

5.6 SX-ARPES measurements of BaTiO₃

The photonenergies available in the Soft-X-ray range allow to perform ARPES in the vicinity of adsorption edges. The total electron yield over the range of the Ti L₂ and L₃ adsorption edges shows, apart from the resonance energies of Ti 4⁺ a low intense contribution of a Ti 3⁺ resonance [see Fig. 5.15(a)]. The intensity of the Ti 3⁺ resonance is considerably lower than for STO [33]. The angle integrated photoemission intensity over the Ti 2p-3d adsorption range is shown in Fig. 5.15(b) with line profiles extracted at the binding energy of the O 2s valence band, the in-gap state and at the Fermi energy [Fig. 5.15(c)]. The sharp t_{2g} resonance is visible in all three extracted line profiles. The valence band line profile features intensity between the Ti 4⁺ and Ti 3⁺ resonant energies indicating a strong hybridization of O 2p with Ti 3d orbitals for both oxidation states of Ti. The in-gap state at a binding energy of 0.9 eV shows its intensity maximum clearly aligned with Ti 3⁺ resonance. In contrast to this, the line profile at the Fermi energy, showing the existence of metallicity at the surface, has its intensity maximum in between the Ti 4⁺ and Ti 3⁺ resonance similar to the valence band. For STO a similar behavior is observed and the existence of different Ti 3⁺ species in the surface region is suggested being of localized or delocalized metallic nature [33, 241]. This opens up different resonant photoemission channels i.e. with and without coupling to the in-gap state.

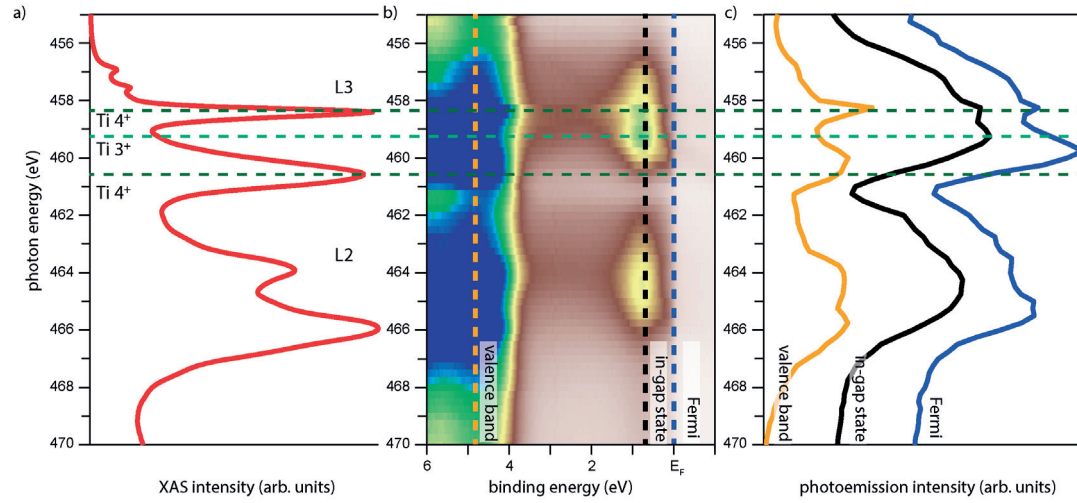


Figure 5.15 – (a) XAS spectrum over the energy range of the Ti L₂ and L₃ edge. (b) Angle integrated photoemission intensity over the same photon energy range as (a). (c) Line profiles taken from (b) at different binding energies as indicated in (b). The integrated energy window is 100 meV.

ARPES measurements at the intensity maximum of the metallic states at the Fermi energy corresponding to a photon energy of $h\nu = 460.25$ eV (see Fig. 5.16) show a similar dispersion as in UV-ARPES (see Fig. 5.8). The WSL states are present, smeared along the $\overline{\Gamma X}$ -direction. With the increased photon energy, however, the two-dimensional states are only measurable at the resonant photo energy. This is due to the increased escape depth of the photoelectrons excited with energies in the SX-range and the strong localization of these state along the out-

of-plane axis due to their origin in the surface crystal structure. As a result, the fraction of the electrons emitted from the 2D, surface localized states on the the total photoemission intensity is reduced compared to measurements in UV-ARPES. The different light polarizations reflect to the SX-ARPES measurements in the same fashion as in UV-ARPES. For s- and p-polarized light, band intensity is enhanced in k_x and k_y direction respectively according to the orbital symmetries.

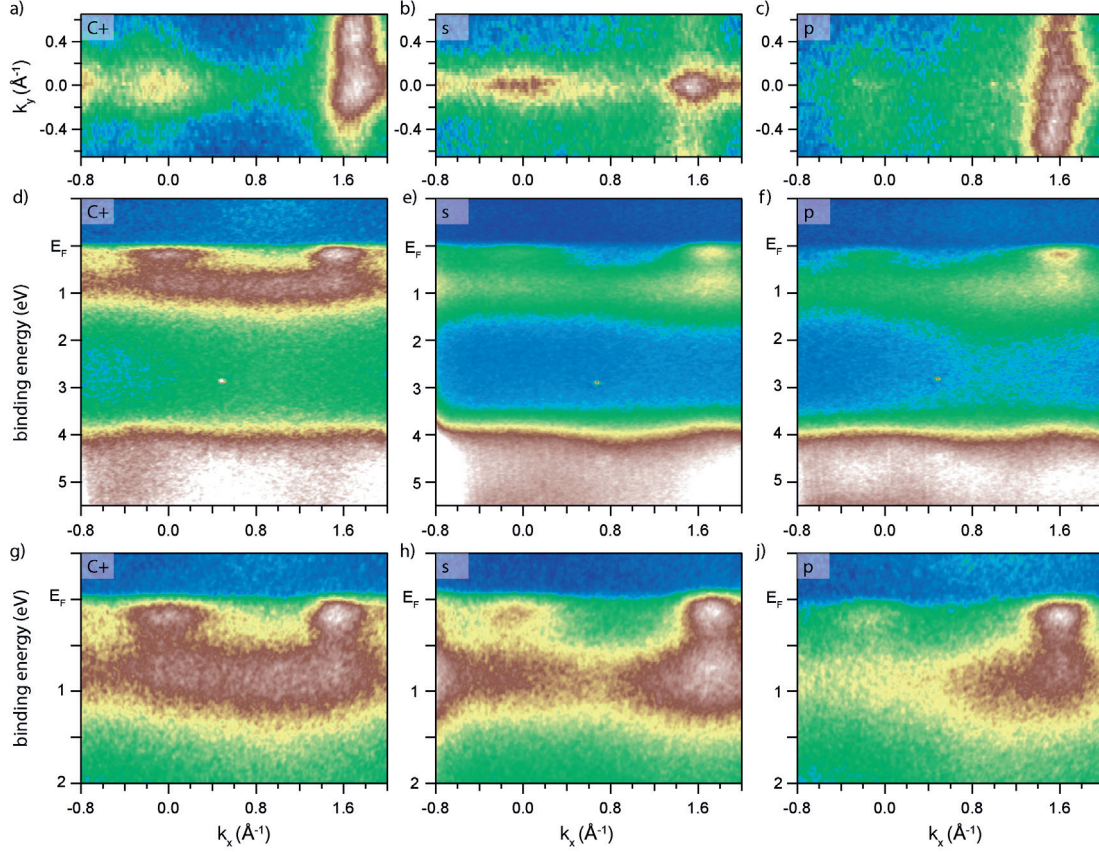


Figure 5.16 – (a-c) ARPES Fermi surface taken with soft X-ray photons of $h\nu = 460.25$ eV covering $\bar{\Gamma}_{00}$ and $\bar{\Gamma}_{10}$ for C+ (a) s- (b) and p-polarized light (c). (d-f) Band dispersion along $\bar{\Gamma}\bar{X}$ at $k_y = 0$ Å⁻¹ for the three polarizations and (g-i) enlarged region of the band dispersion in (d-f) covering the metallic and the in-gap states.

The observed light induced effects in titanates are commonly connected with the creation of oxygen vacancies. It is known in the case of STO crystals that oxygen vacancies induced in the growth process or by high-temperature annealing will change the color from yellowish-transparent to black [9]. As this directly visible change already indicates oxygen deficient sample are conducting. A way to counter act the creation of oxygen vacancies by UV-irradiation is the *in-situ* dosing of oxygen to the sample surface by a capillary during the illumination. In the case of anatase TiO₂ a direct control of the surface charge carrier density in the 2DEG is possible by this approach [54]. Measurements in the SX energy range are less affected by

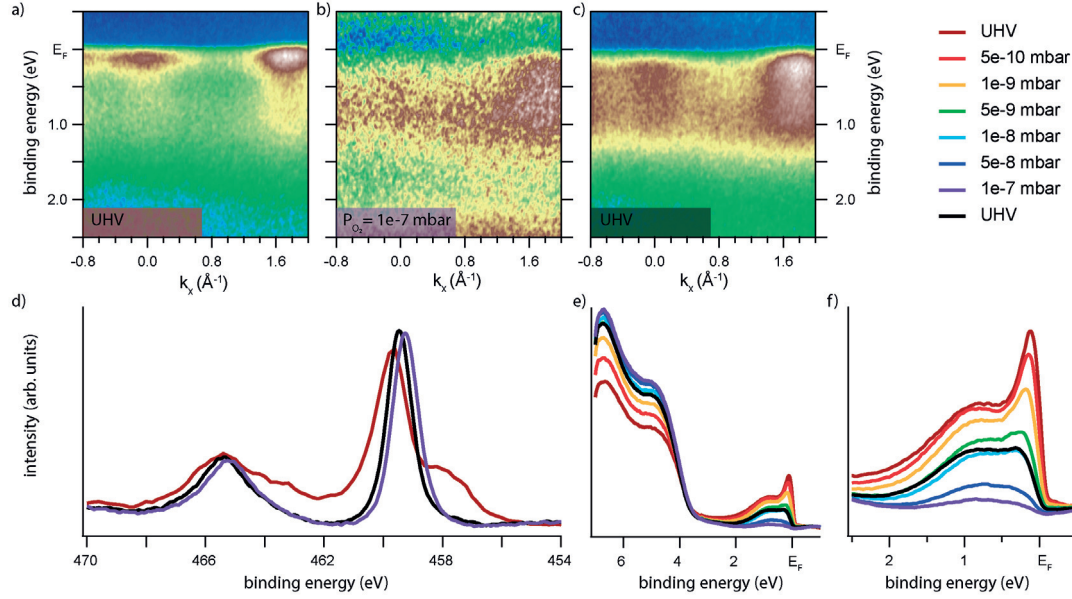


Figure 5.17 – (a) Initial band dispersion measured with $h\nu = 460.25$ eV. (b) Band dispersion at a partial oxygen pressure of 1×10^{-7} mbar. (c) Band dispersion after the oxygen dosing experiments with at a base pressure better than 1×10^{-10} mbar. (d) Angular integrated intensity of the Ti 2p corelevels for the three cases of (a-c) measured with $h\nu = 1000$ eV. (e) Angle-integrated spectrum of the valence band region for different oxygen doses. (f) Zoom in on the in-gap and metallic states.

higher pressures due to the increased kinetic energy of the photoelectrons and thus ideal for experiments of this kind.

Our ARPES measurements for oxygen dosing with different partial pressures in the chamber are presented in Fig. 5.17. In the initial spectrum [Fig. 5.17(a)] the metallic bands at the Fermi energy are of high intensity, higher than the in-gap state. With increasing oxygen pressure, from a starting base pressure of $1 \cdot 10^{-10}$ mbar up to a maximal partial oxygen pressure of $1 \cdot 10^{-7}$ mbar, the intensity of the in-gap state, as well as of the metallic state is drastically reduced [Fig. 5.17(a,b,e,f)]. Nevertheless, even at the final pressure, the metallic states are still present in the band dispersion [Fig. 5.17(b)]. When looking at the Ti 2p core levels in Fig. 5.17(d) for the start and final pressure, a clear suppression of the initially present Ti 3⁺ is noticeable. This is accompanied by a bandshift of approximately 400 meV of the Ti 2p to lower binding energies. In the valence band region in increase of intensity with oxygen dosing is observable. When restoring the base pressure of the system after the oxygen dosing, the intensity of the in-gap state as well as the metallic state is increasing again. However, the initial conditions are not entirely recovered. The Ti 2p core levels are still lacking peak contribution of Ti 3⁺ ions but are shifted back to higher binding energies. This behavior is similar to the observed behavior with temperature (see Chap. 5.4.5) were the system recovers to a different state compared to the initial one.

5.7 Conclusion

In this chapter, photo-emission results of ferroelectric BaTiO₃ films are presented. The BTO films exhibit a 2D state at its vacuum interface. It is likely of similar origin as the STO and CTO 2DEG, indicated by the xy -symmetry of this state, evaluated by light-polarization dependent measurements. The states show a resonant enhancement in the Ti L3 edge energies and are robust to temperatures above the phase transition of the STO substrate and with *in-situ* oxygen dosing.

However, due to the presence of a high electric field, that is estimated to be in the order of $1 \cdot 10^9$ V/m inside the ferroelectric BTO, the electrons of the conduction band experience a Wannier-Stark localization. This localization in real space smears the bands in the direction of the electric field in reciprocal space. The measured Fermi surfaces can be explained by an combined contribution from ferroelectric domains, polarized along the two $\overline{\Gamma X}$ in-plane axes and along the out-of-plane direction. This matches with a tetragonal phase at low temperatures with polarization directions locked by strain relaxations. A locking of the domains polarized along the in-plane direction is also indicated by PFM measurements, proving ferroelectric properties of the grown film.

The effects of Wannier-Stark localization are visible for ARPES measurements of BTO films grown on STO as well as on KTO substrates, although changes attributed to the altered interface strain are visible. Furthermore, the effects are also present in thin films of STO with thickness of 3 uc grown on top of a BTO film with a Fermi surface showing similar smearing of the states as for the BTO films. With increasing film thickness the effects of the electric field are reduced and therefore the states at the surface of a 5 uc thick STO film on BTO shows no more effect of the electric field.

The studied BTO films show an interplay between the presence of a two-dimensional state and large electric fields in a semiconductor and opens new possibilities to further explore this interaction. The existence of Wannier-Stark localization in a single crystal semiconductor is shown in the presented data for the first time and suggests that WSL should be a effect observable also for different ferroelectric materials with in-plane polarization and surface or interface states. Ferroelectric films with preferred large range polarization domains with in-plane polarization should give access to the effects of WSL in transport properties.

6 Manipulation of the SrTiO₃ surface states

Since the discovery of two-dimensional metallic states at the vacuum surface of STO [9, 10] the mechanism responsible for their formation is under debate. Apart from the creation of surface charge carriers by existing and *in-situ* created oxygen vacancies, the crystal arrangement of the surface layers seems to play a key role in the formation and structure of the 2DEG. Experimental observations and theoretical calculations show a buckling distortion of the surface SrO and TiO₂ layers distinct from the bulk crystal structure [161–164]. Regardless of their origin, one of the main goals is to be able to manipulate their properties.

In this chapter three different approaches to alter the formation of the 2DEG are presented. In the first part the 2DEG at the surface of vicinal STO substrates are studied. In comparison with nominally flat STO (001) an altered band bending is observed shifting both, the 3D d_{xz}/d_{yz} bands as well as the 2D d_{xy} bands to lower binding energies. This change in surface band bending is likely due to the altered electron affinity of the vicinal surfaces compared to the flat one. Additionally, a lowered energy splitting between the 2D and 3D bands as a function of the step edges is observed. The origin of this splitting of the t_{2g} orbitals is the tetragonal distortion of the TiO₆ octahedron. The relaxation of this distortion due to the step edges is a possible reason for the observed changes. In further measurements, the altering of the band bending and band splitting with temperature is studied, showing vanishing bands at 150 K.

In the second part of this chapter, films of STO grown on Nb doped STO are discussed. In these systems the 3D bands are absent at the Fermi energy and a (2×2) reconstruction can be observed. The 2D states are unaltered with film thickness implying an effect related to the films properties responsible for the changed formation, compared to bulk STO. A similar effect on the 2DEG is achieved in the last part of this chapter, by the growth of films of Ba_xSr_{1-x}TiO₃ with $x=0.07$ and $x=0.1$. For these Ba dopings a ferroelectric phase is observed in bulk crystals at low temperatures. As possible reasons for the altered dispersion of the film systems, the altered dielectric constant and the formation of crystal defects are discussed.

6.1 Altered octahedral distortion by vicinal surfaces

6.1.1 Sample preparation

For this study, commercially available STO substrates (SurfaceNet GmbH) with a misscuts of 5° and 10° to the nominal (001) surface were used. Considering a step height of one uc, the terraces are expected to have a width of 44 Å or 11-12 uc for the 5° sample and a terrace width of 22 Å or 5-6 uc for the 10° substrate (see Fig. 6.1(a,b) for a sketch of the surface). Both of the substrates therefore have a step density low enough to prevent the formation of a electron wave function on the macroscopic surface [242].

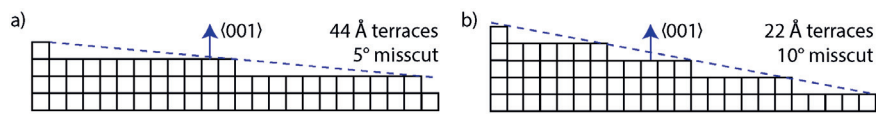


Figure 6.1 – (a) Illustration of the 5° miscut to the (001) surface with resulting terrace sizes. (b) Illustration for the surface with 10° miscut.

The samples have a size of $5 \times 10 \times 0.5 \text{ mm}^3$ and are cut and polished by the manufacturer. In order to obtain an single TiO₂ terminated sample surface, the sample were treated by a well established procedure [61, 243, 244] prior to the experiments. For this, the samples are submerged in deionized water for approximately 30 min and then etched in buffered HF solution for 30 sec. After this step, the samples are washed in a sequence of baths in deionized water to terminate the etching. By this procedure, possible SrO patches at the surface should be etched off. Subsequently the samples are dried by annealing them in a constant high-purity oxygen flow to 1000° C. After the *ex-situ* treatment, the samples are annealed to 550° C in 100 mbar O₂ *in-situ*. This step is necessary to get rid of possible surface contamination and to ensure a full oxidation of the sample. Finally the sample is low temperature annealed at 300° C for approximately 12 hours. After this treatment, the samples can be *in-situ* transferred to the ARPES manipulator and measured without further treatment.

The LEED patterns for the two substrates prepared as explained above, are illustrated in Fig. 6.2 and prove a high crystallinity of the sample surface. For both of the substrates, clear diffraction spot corresponding to the surface Brillouin zone of STO (001) are visible. Due to the presence of step edges, a slight deflection of the diffracted beam, orthogonal to the edge is visible in the form of a splitting of the beam spot in vertical direction in the image. This effect is in particular visible at the higher electron energies (Fig. 6.2(b,d)) and is slightly more pronounced for the 10° sample as an effect of the increased step density. Both samples have indication of a (2 × 1) reconstruction that is more present in the 10° sample and is also better visible at the higher electron energy. However, the diffraction spots attributed to the reconstruction are very weak in intensity verifying a low density of scattering centers that leads to the conclusion that only a small portion of the surface is reconstructed.

6.1. Altered octahedral distortion by vicinal surfaces

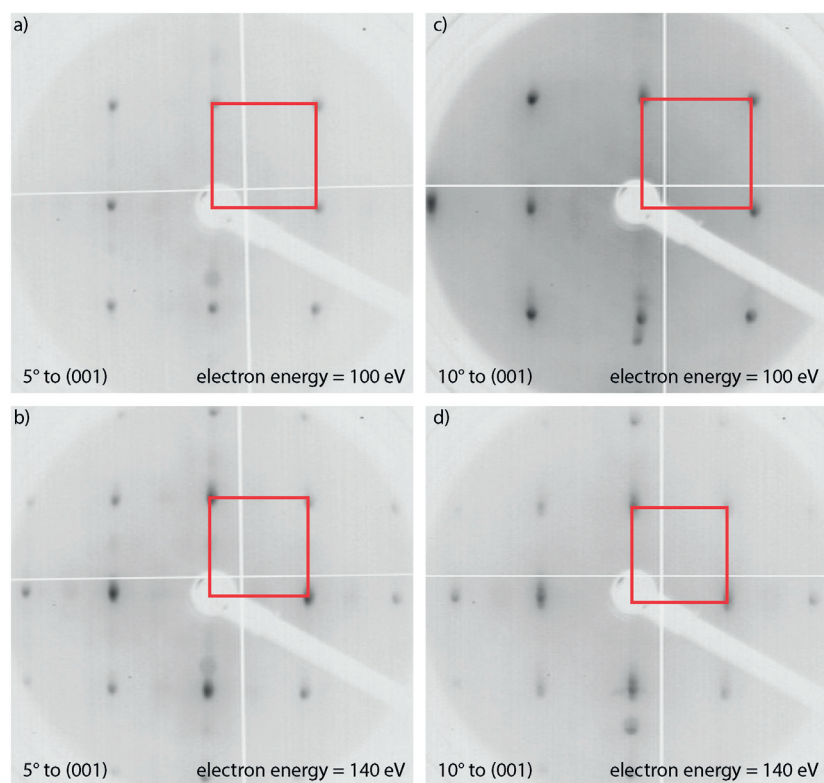


Figure 6.2 – LEED patterns of the the vicinal samples. (a,b) Diffraction pattern of the 5° miscut sample for an electron energy of 100 eV (a) and 140 eV (b). (c,d) Pattern of the 10° misscut sample for the same energies as (a,b). The red squares indicate the surface Brillouin zone of STO (001).

6.1.2 Changes in the band structure

The ARPES measurements of the substrate with 5° and 10° (Fig. 6.3) miscut to the STO (001) surface show a dispersion similar to "flat" STO (001) [61]. In Fig. 6.3(a,c) the dispersion with k_z , obtained by scanning the photon energy, is displayed for $\bar{\Gamma}_{00}$ (at $k_x = 0 \text{ \AA}^{-1}$) and $\bar{\Gamma}_{10}$ (at $k_x \approx 1.6 \text{ \AA}^{-1}$). For the conversion of $h\nu$ to k_z with a free-electron final state approximation (see Sec. 3.1) an inner potential of 14.5 eV was assumed. This is the same value used for the conversion in Ref. [61] for STO (001) and is in good agreement with the periodicity observed in the measurements. The scan over k_z shows the presence of the 2DEG that does not disperse as a function of photon energy and 3D dispersing or heavy-bands, located in the vicinity of the Γ -point ($k_z \approx 6 \pi/a \approx 4.85 \text{ \AA}^{-1}$). The Fermi surface over multiple surface Brillouin zones [Fig. 6.3(b,d)] at a photon energy of $h\nu = 85 \text{ eV}$ that corresponds to a Γ -point shows the 2DEG as circles, centered at the $\bar{\Gamma}$ -points and the 3D bands as elongated bands, pointing in $\bar{\Gamma}\bar{X}$ -direction.

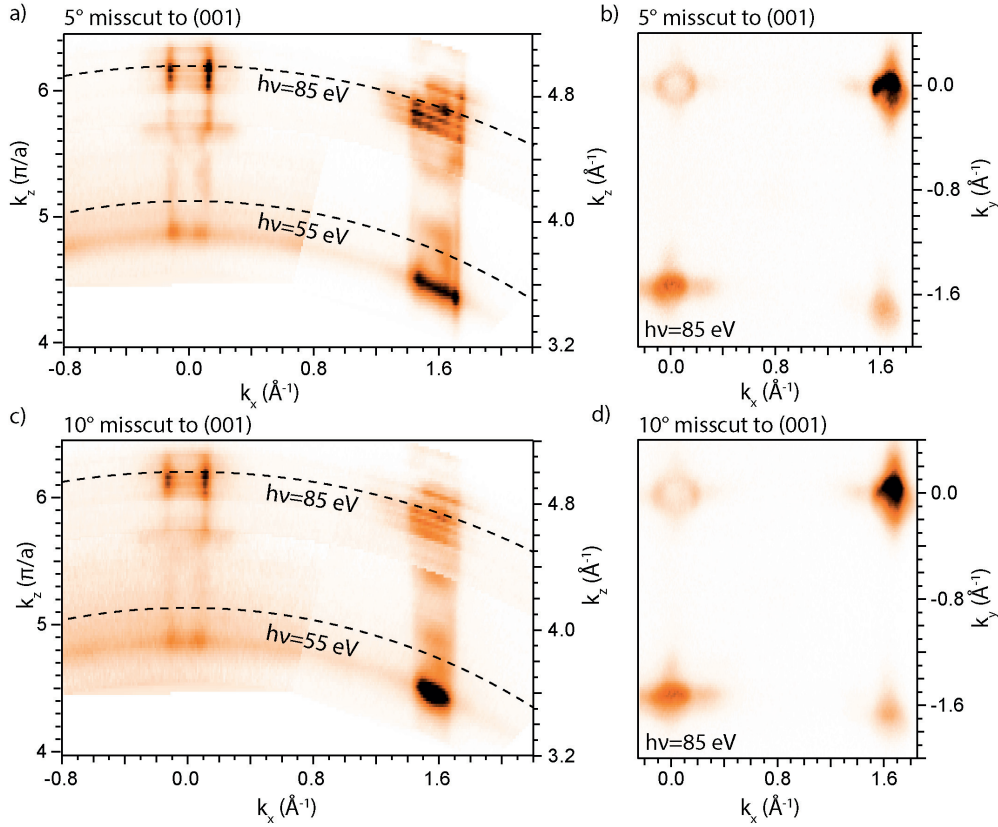


Figure 6.3 – (a) Dispersion with k_z at the Fermi energy for Γ_{00} and Γ_{01} of the sample with 5° miscut from $h\nu = 40 \text{ eV}$ to $h\nu = 100 \text{ eV}$. (b) ARPES Fermi surface at $h\nu = 85 \text{ eV}$ over multiple Brillouin zones. (c,d) Same as (a,d) but for the sample with 10° miscut.

The photon energy dispersion, as well as the the Fermi surface show no indication of reconstructions as observed in the LEED measurements (Fig. 6.2). A reason for this absence could be a non uniform nature of the reconstruction over the sample surface that are observed

with the considerably larger LEED spot (approximately 1 mm) while the synchrotron beam only covers (approximately 100 μm) a non reconstructed area. However due to the random choice of the exact beam location in the proximity of the sample center for the LEED as well as for the ARPES measurements this does not seem to be very likely. Another explanation is change of the partial reconstruction of the sample surface by the UV-beam. A similar behavior was observed for the CTO films, where a $c(4 \times 2)$ reconstruction was observed in the LEED measurements but not in the ARPES data (see Sec. 4.1). Since the UV-irradiation plays a role in the formation of the 2DEG at the surface of the oxides STO, BTO and CTO and therefore is also expected to alter the surface structure, a change of surface reconstruction is thinkable.

By comparing the k_z dispersion for the two samples [Fig. 6.3(a,c)] we notice a reduction of k_F with increasing miscut angle. For the 5° sample it is still possible to distinguish clearly between the two split, two-dimensional d_{xy} bands for the measurements around $\bar{\Gamma}_{10}$. For the 10° sample this distinction is not possible anymore due to a smaller of k_F . This reduction becomes more evident in the measurements for different light polarizations in Fig. 6.4 and Fig. 6.5. Due to the distinct symmetry of the d_{xy} , d_{xz} and d_{yz} orbitals they can be selectively probed by the use of matrix element effects. Whereas for the circularly polarized light [Fig. 6.3(b,d)] all orbitals are probed, s-polarized light suppresses the d_{xz} bands [Fig. 6.4] and p-polarized light the d_{xy} and d_{yz} bands [Fig. 6.5]. Therefore the bands visible in the vicinity of the $\bar{\Gamma}_{10}$ -point for s-polarized light are mainly the 2D d_{xy} states and only the d_{xz} for p-polarized light (compare Sec. 1.3, Fig. 1.6).

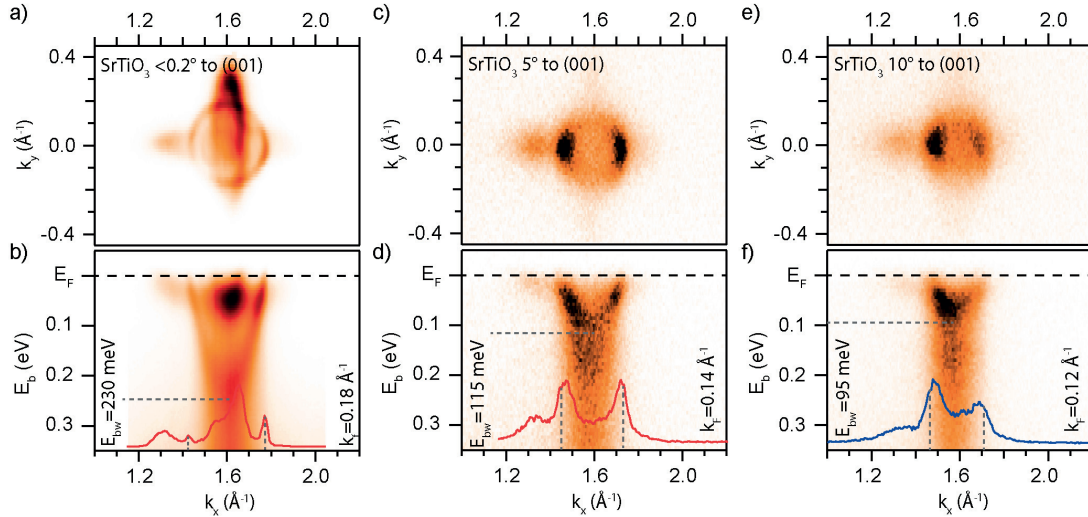


Figure 6.4 – Measurements at $\bar{\Gamma}_{10}$ with $h\nu = 85$ eV photons for nominally flat STO (001) (a,b) with circularly-polarized light and with s-polarized light for the sample with 5° (c,d) and 10° (e,f) miscut. (a,c,e) ARPES Fermi surface with band structure along k_x at $k_y = 0 \text{ \AA}^{-1}$ in (b,d,f). Data of the flat STO are taken from [61].

Due to the disentangling of the different orbital contributions in the ARPES intensity, we can distinguish the band bottom of the 2D d_{xy} bands to be approximately 115 meV for the 5° sample and 95 meV for the 10° sample. This shift to lower binding energies with higher

step density is accompanied with a reduction in k_F of the outer of the two d_{xy} bands from $k_F = 0.14 \text{ \AA}^{-1}$ to $k_F = 0.12 \text{ \AA}^{-1}$ (see Fig. 6.4). If we compare this findings to the band structure of nominally flat STO [see Fig. 6.4(a,b)] measured with circularly polarized light where a band bottom of 230 meV and a $k_F = 0.18 \text{ \AA}^{-1}$ is reported [61], the change as a function of step density is even more obvious.

The 3D dispersing, heavy band with xz -symmetry is the only band contributing to the ARPES intensity, measured with p-polarized photons of an energy of $h\nu = 85 \text{ eV}$ (Fig. 6.5). Therefore we can distinguish the bottom of the band of the d_{xz} state to be approximately 35 meV, unaltered within the resolution limit for the two samples, whereas for flat STO a bottom of the band of 50 meV is reported for the d_{xz}/d_{yz} bands [61]. Since the d_{xz} orbitals are 3D and therefore disperse with photon energy, these values can not be considered as absolute value of the d_{xz} band bottom but serve well for a relative comparison, since the choose photon energy corresponds to a k_z close to the Γ_{103} point (see Fig. 6.3(a,c) and [61]).

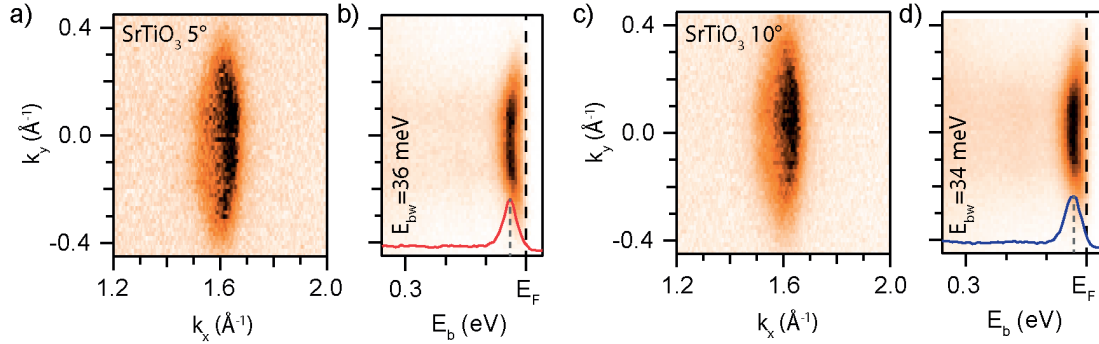


Figure 6.5 – Measurements with p-polarized photons at $\overline{\Gamma}_{10}$ for the 5° miscut (a,b) and the 10° miscut (c,d) sample. (a,c) Measured ARPES Fermi surfaces and (b,d) band dispersion for k_y at $k_x = 1.6 \text{ \AA}^{-1}$. Inset in (b,d) shows the extracted EDC at $k_y = 0 \text{ \AA}^{-1}$.

The observed shift of the bottom of the 3D d_{xz} band to lower binding energies, especially compared to nominally flat STO, fits into a picture of a rigid bands shift due to an altered surface band bending. Possible reasons for a changed surface band bending are a lower surface quality of the vicinal STO substrates or the altered electron affinity due to the presence of the step edges [245, 246]. However, with the change in binding energy of the d_{xz} bands much smaller than the observed shift of the d_{xy} bands the change in surface band bending can not be the only mechanism, affecting the band structure.

Additional to the altered surface band bending, we observe a reduction of the energy separation between the d_{xy} and the d_{xz}/d_{yz} orbital band. This separation changes from initially 180 meV for flat STO to approximately 80 meV for the sample with a terrace size of 44 Å and 60 meV for 22 Å terrace size. The energy separation of the suborbitals of Ti 3d t_{2g} is related to the distortion of the TiO₆ octahedron (see Sec. 2.1). In order to have the orbital ordering observed at the surface of STO (001), the octahedron has to be tetragonally distorted with two short and four long Ti-O bonds. With the additional degree of freedom of the surface

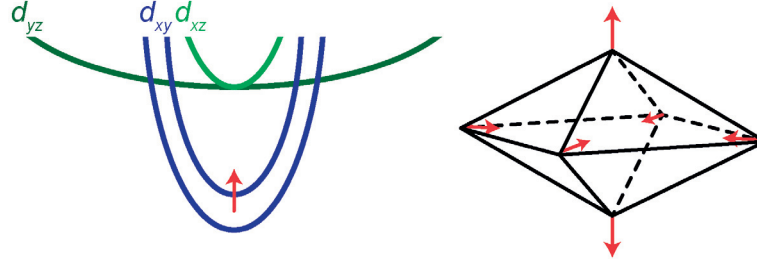


Figure 6.6 – Illustration of the change in the tetragonal distortion of the TiO_6 octahedron and the resulting reduction of the splitting between the d_{xy} and the d_{xz}/d_{yz} orbitals.

layers given by the step edges of the vicinal samples, the sample surface can relax more. This is expected to alter the buckling of the surface layers that is observed for nominally flat STO and therefore reduces the degree of the tetragonal distortion of the TiO_6 octahedron. As a result we can observe a reduction of the energy separation between d_{xy} and the d_{xz}/d_{yz} orbitals with increasing step density as an effect of the surface relaxation. A simple illustration of the described mechanism is depicted in Fig. 6.6. With a relaxation of the octahedron a change in the Ti-O-Ti binding angle between neighboring octahedrons is also likely. The resulting changes in the hopping probabilities will affect the effective mass of the bands and therefore their band width [247]. This could additionally contribute to the observed changes in the band structure.

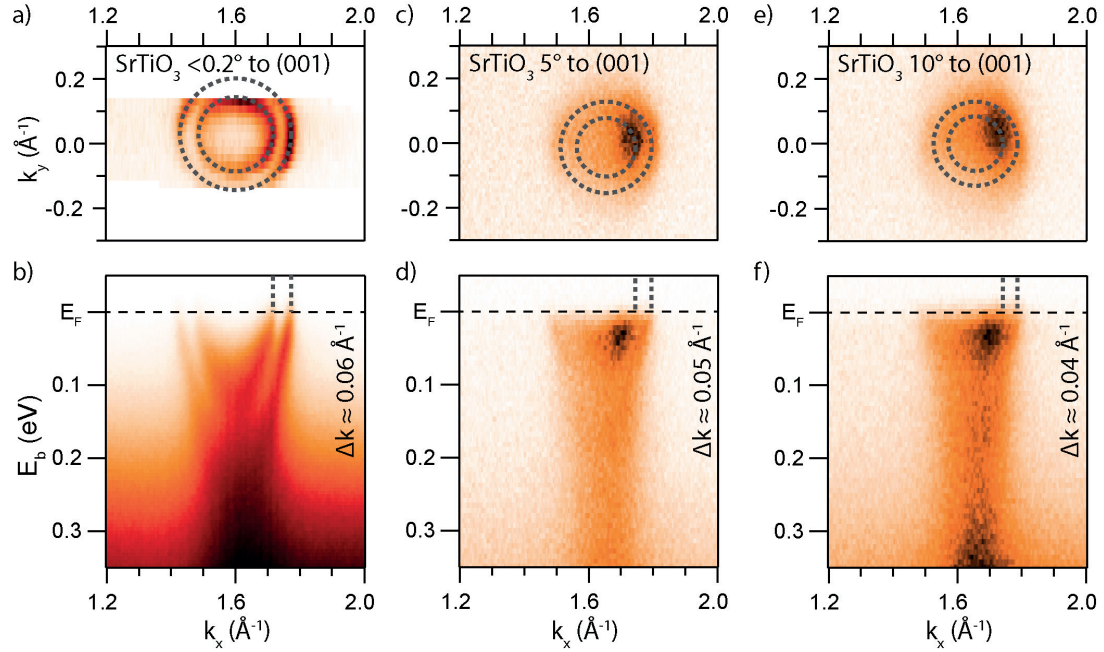


Figure 6.7 – ARPES measurements at lower energy for flat STO (a,b) with circularly polarized light with $h\nu = 51$ eV. (c,d) Measurements of the 5° miscut sample and (e,f) of the 10° miscut sample with $h\nu = 55$ eV, s-polarized light. Fermi surfaces (a,c,e) with concentric rings, marking the split d_{xy} band and corresponding band dispersions (b,d,f).

The splitting of the d_{xy} into two sub-bands commonly observed for STO (001) is clearly visible for both vicinal substrates in the k_z -dispersion [Fig. 6.3(a,c)] as well as in the band dispersion at a photon energy of $h\nu = 55$ eV (Fig. 6.7). The splitting of the two concentric rings, forming the Fermi surface [Fig. 6.7(a,c,e)], is slightly reduced from $\Delta k = 0.06 \text{ \AA}^{-1}$ for STO (001) to $\Delta k = 0.05 \text{ \AA}^{-1}$ and $\Delta k = 0.04 \text{ \AA}^{-1}$ for 5° and 10° miscut respectively. However, this observed reduction is at the limit of the resolution of the obtained data. The possible influence of the step edge density on the energy splitting and on the parameters of a possible Rashba-like splitting can not be resolved with the currently available data. Since the splitting is partially explained by (anti)ferroelectric properties at the surface of STO due to the buckling of the surface layers [66] an effect of the step density and the related surface relaxation would be expected.

6.1.3 Temperature dependent behavior

The evolution of the 2DEG at the surface of the STO sample with 10° miscut to the (001) as a function of temperature over the tetragonal to cubic phase transition of bulk SrTiO₃ at 110 K [153] is depicted in Fig. 6.8. With increasing temperature, the bottom of the band of the 2D d_{xy} states shifts to lower binding energy. At a sample temperature of $T_5 = 130$ K, above the bulk phase transition the d_{xy} is barely filled and finally the bands are completely absent at 150 K. In the not normalized EDCs in Fig. 6.8(j,k) a rise of intensity between 20 K and 50 K is observed, before the intensity gradually decreases. This initial rise could be an effect of one of the reported low temperature phase transitions [152, 157, 158]. The tracking of the band bottom and k_F of the d_{xy} band with temperature [Fig. 6.8 (l)], shows a gradual decrease of the two parameters with temperature. The EDC at $k_x = 1.24 \text{ \AA}^{-1}$, too far from the Γ -point to exhibit contribution from the d_{xy} band, gives an indication of the presence of the heavy bands. The intensity close to the Fermi energy in these EDCs, that is attributed to the heavy bands, is visible for temperatures up to 130 K where the intensity vanishes. Therefore the states visible at 130 K are likely only the two dimensional d_{xy} bands. If only a rigid band shift of the spectrum with temperature is considered, the necessary energy shift of 35 meV (see Fig. 6.5) to shift the heavy bands above the Fermi energy is reached around a temperature of 110 K. Since there is still indication of heavy bands at this temperature in the EDC at $k_x = 1.24 \text{ \AA}^{-1}$, where the indication of the band should vanish with even less shift due to its parabolic shape, a rigid band shift does not describe the observations entirely.

When lowering the temperature after the complete vanishing of the bands at $T_6 = 150$ K back towards 20 K the bands appear again and shifts to higher binding energies. However, the mechanisms induced by the elevated temperature does not seem to be fully reversible. At 20 K the band bottom of the d_{xy} band is located at 70 meV, 25 meV lower than before the temperature cycle. The heavy bands on the other side, are recovered to a similar binding energy, judging by Fig. 6.8(k).

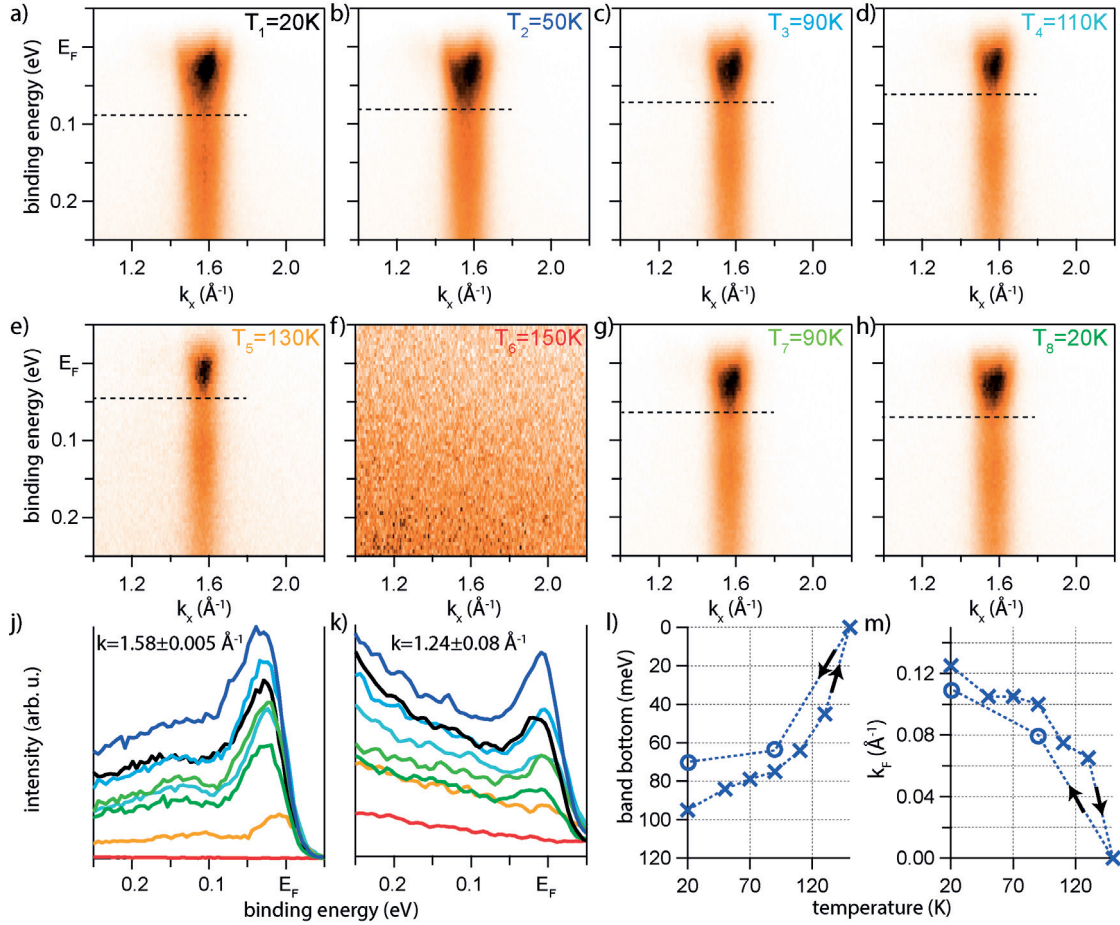


Figure 6.8 – (a-h) Temperature dependent ARPES band structure of vicinal STO with 10° miscut to (001) at Γ_{10} with circularly-polarized photons of $h\nu = 85 \text{ eV}$. (j) EDC at the Γ_{10} -point and (k) EDC at $k_x = 1.24 \text{ \AA}^{-1}$ over the d_{yz} bands for different temperatures (colors indicated in (a-h)). (l) Band bottom of the d_{xy} state and (m) k_F of the outer d_{xy} state for the different temperatures (crosses for increasing, circles for decreasing temperatures).

A possible explanation of the observation, is an interplay between band bending, distortion of the TiO_6 octahedron and their respective Ti-O-Ti bond angles, similar to the explanation for the altered band dispersion with step density as elaborated above in Sec. 6.1.2. The altered band bending at the surface with temperature can be of different origin. One possible reason is a change in defect density with temperature that is enhanced under the constant UV-irradiation or the lowering of the dielectric constant with increasing temperature. The altered distortion of the TiO_6 octahedron is responsible for a reduction of the splitting between the 2D d_{xy} and the 3D heavy bands d_{xz}/d_{yz} . Possible reasons for a reduction of the octahedral distortion are an altering of the surface relaxation due to the phase transitions of the bulk STO or due to the increased lattice mobility at higher temperatures. Another influence might be a light assisted reduction of the lattice stress and strain induced by vacancies and/or excess atoms in the crystal. Accompanied with a change in the octahedral distortion and lattice relaxation is

likely also a change in bond angle between neighboring octahedral, affecting the band width and therefore altering the band dispersion [247].

The XPS measurements (Fig. 6.9) shows a change of the Ti 3p, the valence band as well as the in-gap state with temperature. The Ti 3p core level features a low binding energy shoulder of Ti 3⁺ ions commonly observed for titanates (see Fig. 5.1 for results of BTO and Ref. [61] for STO). With temperature the fraction of Ti 3⁺ vanishes and recovers to a slightly lower fraction of Ti 3⁺ ions than in the initial state when cooling again to $T_8 = 20$ K. This is in agreement with a reduced amount of lattice defects as oxygen vacancies or an altered surface rearrangement with temperature that only partially recovers. In the valence band [Fig. 6.9(b)], the additional peak at approximately 10.5 eV binding energy indicates the formation of a different O-Ti hybridization at higher temperature. In both, the Ti 3p as well as the valence band, a shift of the peak maximum to lower binding energy with temperature is visible. This confirms the change of the band bending with elevated temperature.

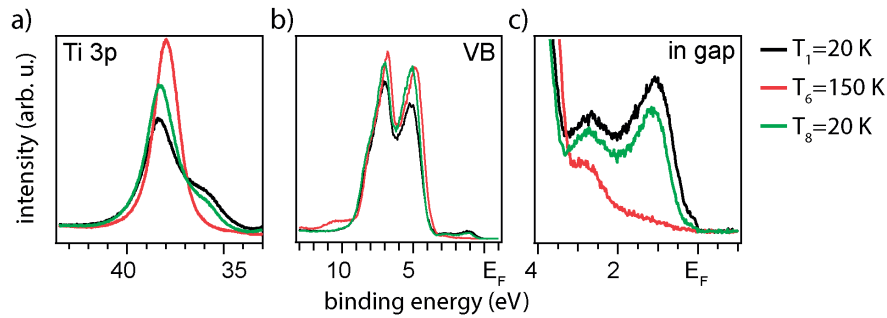


Figure 6.9 – Photoemission intensity of the (a) Ti 3p corelevels, (b) valence band and (c) in-gap states for the initial sample, the sample at 150 K and the sample after the temperature cycle.

In the bulk band gap of the measured samples, the existence two in-gap states is visible [Fig. 6.9(c)] also observed but not discussed for nominally flat STO (001) [61]. With temperature, the first peak is getting lower in intensity while the second peak is not affected. After cooling down, the two in-gap states show a similar ratio as before the measurements at elevated temperature. The origin of the first in-gap state at 1.2 eV is related to the formation of a small polaron that is commonly assigned to the existence of oxygen related defect or vacancies [10, 59, 248, 249]. Its lowering of intensity with temperatures corresponds to the behavior of the Ti 3⁺ peak. The second in-gap state at a binding energy of 2.8 eV is in the energy range of a polaron, originating from Sr or Ti vacancy [250]. These vacancies are likely induced in the growth of the substrates that matches with absence of any change of the second in-gap state with temperature.

6.2 $\text{Ba}_x\text{Sr}_{1-x}\text{TiO}_3$ Thin Films

6.2.1 Film preparation

The samples discussed in this sections are all PLD grown films. The growth took place at a substrate temperature of 680° to 700° in an partial oxygen pressure of $1 \cdot 10^{-5}$ mbar, same as for the discussed films of BTO and CTO. After growth, the samples are *in-situ* transferred to the ARPES experimental chamber. No further treatment of the samples is necessary before the measurements.

The STO thin films discussed in Sec. 6.2.2, are grown on commercially available, single TiO_2 terminated 0.5% wt Nb doped STO (001) substrates (Twente Solid State Technology). The STO target for the PLD growth consists of a crystalline STO disk. The RHEED oscillations, used to control the different thicknesses of the three films, are displayed in Fig. 6.10(a-c). The oscillations for the 3 uc thick film are with 15 s per complete layer slower compared to the oscillations for the 5 uc and 20 uc thick films (10 s per layer). This is due to lower power of the PLD laser during this growth. The RHEED patterns recorded after the growth show straight lines indicating a flat, 2D film surface. Between the main diffraction intensities, low intense lines are visible [see line profiles in Fig. 6.10(d-f)]. These line correspond to the (2×2) reconstruction with half the lattice periodicity discussed below for the ARPES results.

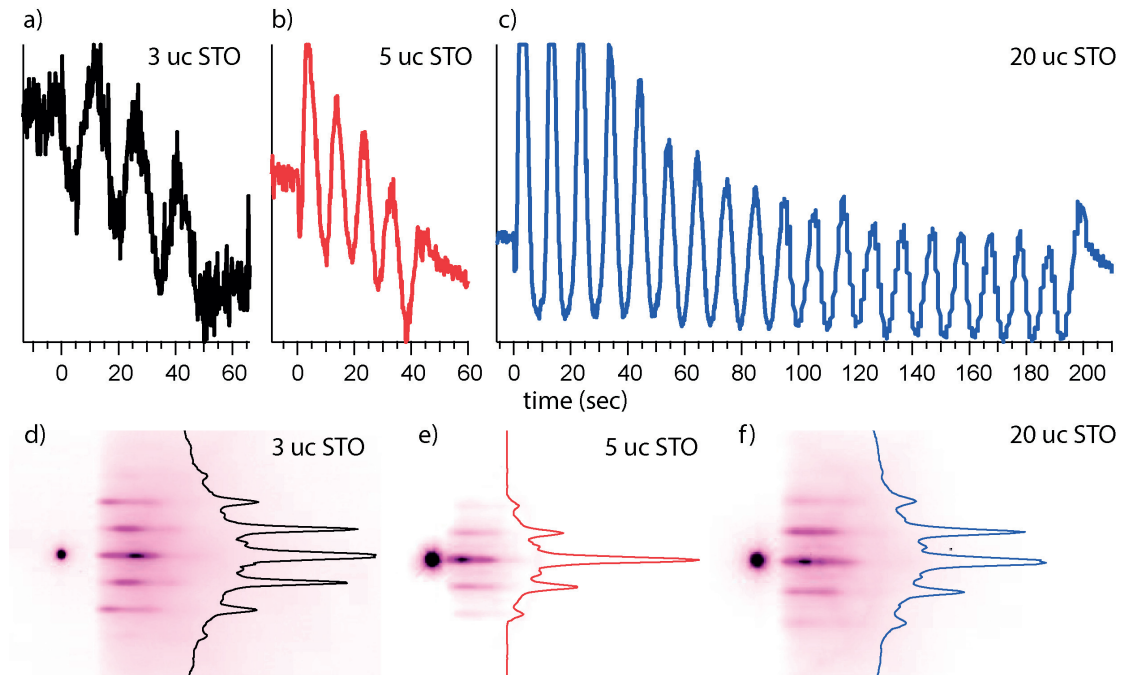


Figure 6.10 – (a-c) RHEED oscillations of the film growth of 3 uc (a), 5 uc (b) and 20 uc (c) STO on Nb:STO (001) substrates. (d-f) RHEED pattern of the three films of (a-c) after the film growth at the grow temperature with intensity line profiles.

Results of two films of Ba_xSr_{1-x}TiO₃, with different Ba content, one with $x=0.07$ and one with $x=0.1$, are discussed in Sec. 6.2.3. Both films have a thickness of 20 uc and are grown on commercially available, polished STO (001) substrates (SurfaceNet GmbH). The PLD target for the film growth are pressed powder targets with the desired chemical composition. The RHEED pattern after the growth at grow temperature shows lines with little indication of spots as well as Kikuchi lines [251] proving a 2D, well crystallized surface. The LEED images, taken at the measurement temperature of 20 K show clear, sharp (1 × 1) spots. There are no indications of reconstruction visible in the RHEED pattern or the LEED images.

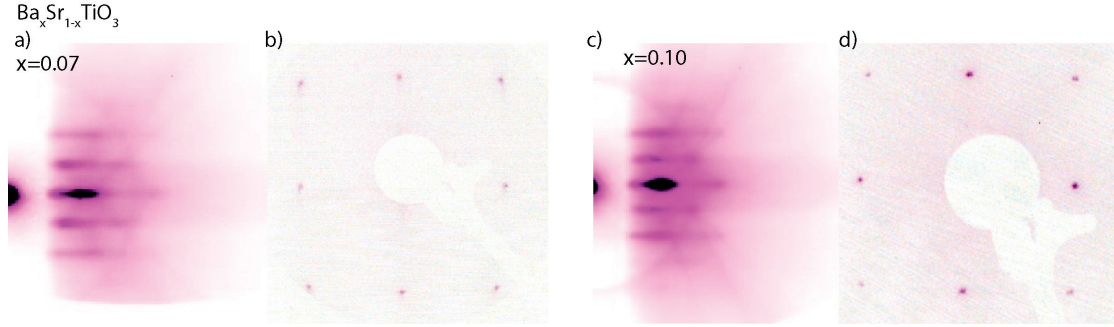


Figure 6.11 – (a,c) RHEED pattern at grow temperature and (b,d) LEED image at the base measurement temperature of 20 K with 70 eV electron energy for 20 uc Ba_xSr_{1-x}TiO₃, with (a,b) $x=0.07$ and (c,d) $x=0.1$ grown on a STO (001) substrate.

6.2.2 Band dispersion of thin SrTiO₃ films

The STO films grown on a TiO₂ terminated 0.5 wt% Nb doped STO substrate show different results in ARPES compared to measurements on the substrate surface. The Fermi surface of 3, 5 and 20 uc thick STO films [Fig. 6.12(a-c)] show the presence of free electron like parabolae at the primary $\bar{\Gamma}$ -points with $g \approx 1.6 \text{ \AA}^{-1}$ corresponding to the lattice constant of STO ($a \approx 4 \text{ \AA}$). Additionally there is intensity of folded $\bar{\Gamma}'$ points in agreement with a (2×2) reconstruction present in all three grown films [Marked in Fig. 6.12(c)]. For the thickest film of 20 uc additionally to the (2×2) reconstruction, intensity of folded $\bar{\Gamma}'$ -points according to a (2×1) reconstruction are visible. In the displayed Fermi surfaces, especially for the 5 uc thick film [Fig. 6.12(b)] the $\bar{\Gamma}_{01}$ is lower in intensity, compared to $\bar{\Gamma}_{00}$. This is due to the response of the 2DEG at the STO surface to the UV-irradiation, that increases its intensity and charge density [10]. With the scanning over an angular range of 50°, the synchrotron beam moves slightly on the sample surface, illuminating new areas. Therefore the, due to the alignment, longer irradiated $\bar{\Gamma}_{00}$ at normal emission is more intense than the other $\bar{\Gamma}$ -points.

The dispersion along k_z [Fig. 6.12(d)], obtained for photon energies scanning from $h\nu = 35 - 120 \text{ eV}$ shows a clear indication of the bands at $\bar{\Gamma}_{00}$ and $\bar{\Gamma}_{10}$. There is no dispersion visible with photon energy, confirming their 2D nature. The k_z dispersion along the high symmetry direction $\bar{\Gamma}\bar{M}$ [Fig. 6.12(e)] covers $\bar{\Gamma}_{00}$ and $\bar{\Gamma}_{11}$, located at $k'_x = 2.25 \text{ \AA}^{-1} \approx \sqrt{2} \cdot 2\pi/a$, and the folded $\bar{\Gamma}'_{1/2, 1/2}$ of the (2×2) reconstruction. Whereas a clear signal of the 2D bands at the

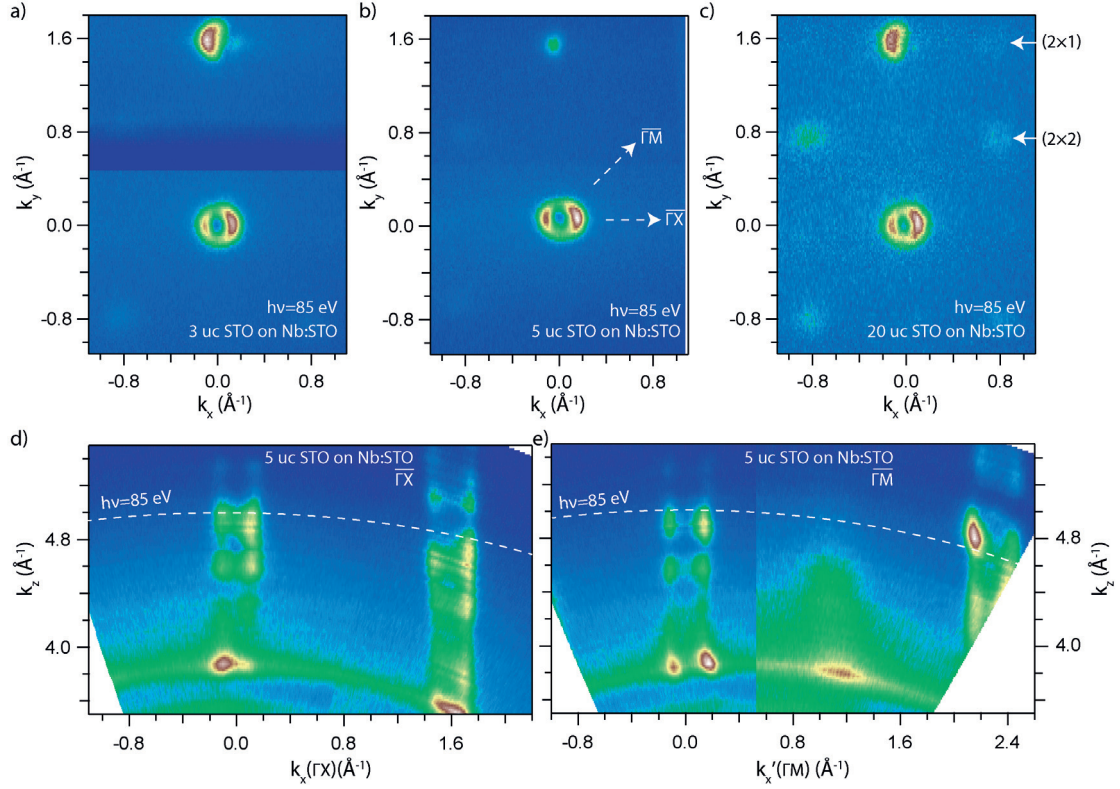


Figure 6.12 – (a-c) ARPES Fermi surface of the three discussed STO films at $h\nu = 85$ eV with circularly polarized light covering Γ_{00} and Γ_{01} as well as reconstructed $\bar{\Gamma}$ points. (a) Measured Fermi surface for 3 uc STO on Nb:STO, (b) 5 uc STO on Nb:STO and (c) 20 uc STO on Nb:STO. The lack of signal in (a) at $k_y = 0.5 \text{ \AA}^{-1}$ is due to a synchrotron beam-dump. (d,e) Dispersion with k_z for the sample with 5 uc STO on Nb:STO along $\Gamma\bar{X}$ (d) and along $\Gamma\bar{M}$ as indicated in (b).

primary Γ -points is visible, only a broad intensity feature is present at the reconstructed $\bar{\Gamma}$ -point. The intensity of the reconstruction further does not follow the intensity variations of the primary Γ -points except for the strong enhancement at the Ti 3p-3d resonance at $h\nu = 45$ eV. The significantly weaker intensity of the folded, compared to the primary Fermi surfaces, suggests that the reconstruction is not uniformly present and therefore has a low contribution to the ARPES signal.

In the Fermi surface at $h\nu = 85$ eV [Fig. 6.12(a-c)], in the vicinity of the Γ -point in 3D, there is, apart from the clear indication of the circular Fermi surface attributed to the d_{xy} bands, no indication of the 3D heavy bands. Also in the dispersion along k_z in Fig. 6.12(d,e) only the 2D, non-dispersing states are present at the primary $\bar{\Gamma}$ points. This absence of the heavy bands with xz - and yz -symmetry, is also confirmed in the measurements of the Fermi surface with different light polarizations [Fig. 6.13(a-c)]. None of the light-polarizations show a clear contribution of the heavy bands, elongated along $\Gamma\bar{X}$ direction. The only band present forms a circular Fermi surface with a xy -symmetry that can be associated with the Ti $3d_{xy}$ bands.

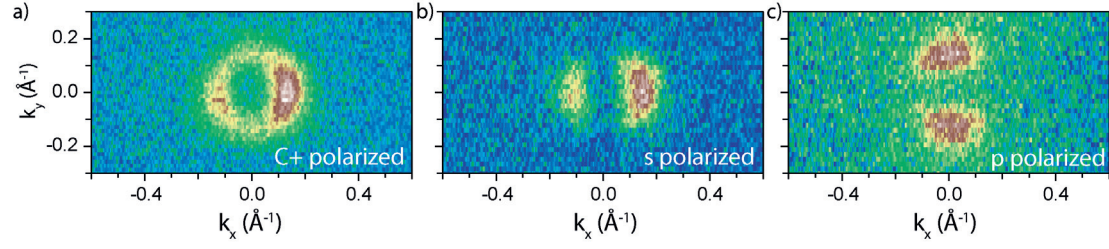


Figure 6.13 – (a-c) ARPES Fermi surface at $\bar{\Gamma}_{00}$ of 20 uc STO on Nb:STO, measured with $h\nu = 69$ eV with (a) circularly, (b) s- and (c) p-polarized light.

A close comparison of the band structures of the STO films with different thicknesses, shows a very similar dispersion for all the three cases [Fig. 6.14(a-f)]. There is no change noticeable regarding the k_F [Fig. 6.14(k)] and also the formation of the valence band [Fig. 6.14(l)] and the in-gate state [Fig. 6.14(m)] is similar for the three films. In the 2D curvature [252] [Fig. 6.14(g-j)] and the k_x integrated EDCs [Fig. 6.14(n)], polaron replicas of the d_{xy} with an energy separation of 100 meV are visible. These are large polarons formed in the photoemission process commonly observed in titanates [54, 201].

The 2D curvature data shows the shape of the d_{xy} band that forms a free-electron-like parabola. The parabola plotted in Fig. 6.14(f,j) with a band bottom of 60 meV and an effective mass of $m^* = 1 \cdot m_e$ represents the observed dispersion of the three samples well (fit by eye). Therefore the splitting between the d_{xy} and the unoccupied d_{xz}/d_{yz} orbitals has to be at least 60 meV, similar to the splitting observed for the vicinal substrates or larger (see Sec. 6.1.2). The increase of the observed effective mass compared to bulk STO [61], agrees with an altered bond angle between neighboring octahedrons responsible for an altered bandwidth [247]. This would indicate an altered crystal relaxation that affects the bond angle in the film and therefore likely also the distortion of the TiO₆ octahedron compared to bulk STO surfaces. Changes in the crystal relaxation like this are expected, considering the fundamental differences between the film growth and the crystallization process of STO bulk crystals. It is reasonable to assume that the type of defects and possible excess atoms in the lattice are different for the two methods and can affect the crystal relaxation and distortion of the octahedron differently. However, due to the absence of the heavy d_{xz}/d_{yz} bands, the change in size of the splitting and therefore the possibly altered distortion of the TiO₆ octahedron cannot be confirmed.

Apart from the octahedral distortion and the altered bond angle, the shift of the band bottom from 230 meV for bulk STO (001) to 60 meV for thin films can be mainly associated with a change in band bending. The band bending in semiconductors depends on the electron affinity and the dielectric constant [245, 246]. The crystal quality and the local structure of the surface layers will alter the electron affinity of the system. The distinct growth methods and the resulting differences in the formed defects therefore contribute to the observed lowering of the band bending. It is reported that the dielectric constant of STO films is different from bulk STO crystals. The change in dielectric constant varies with growth method and thickness

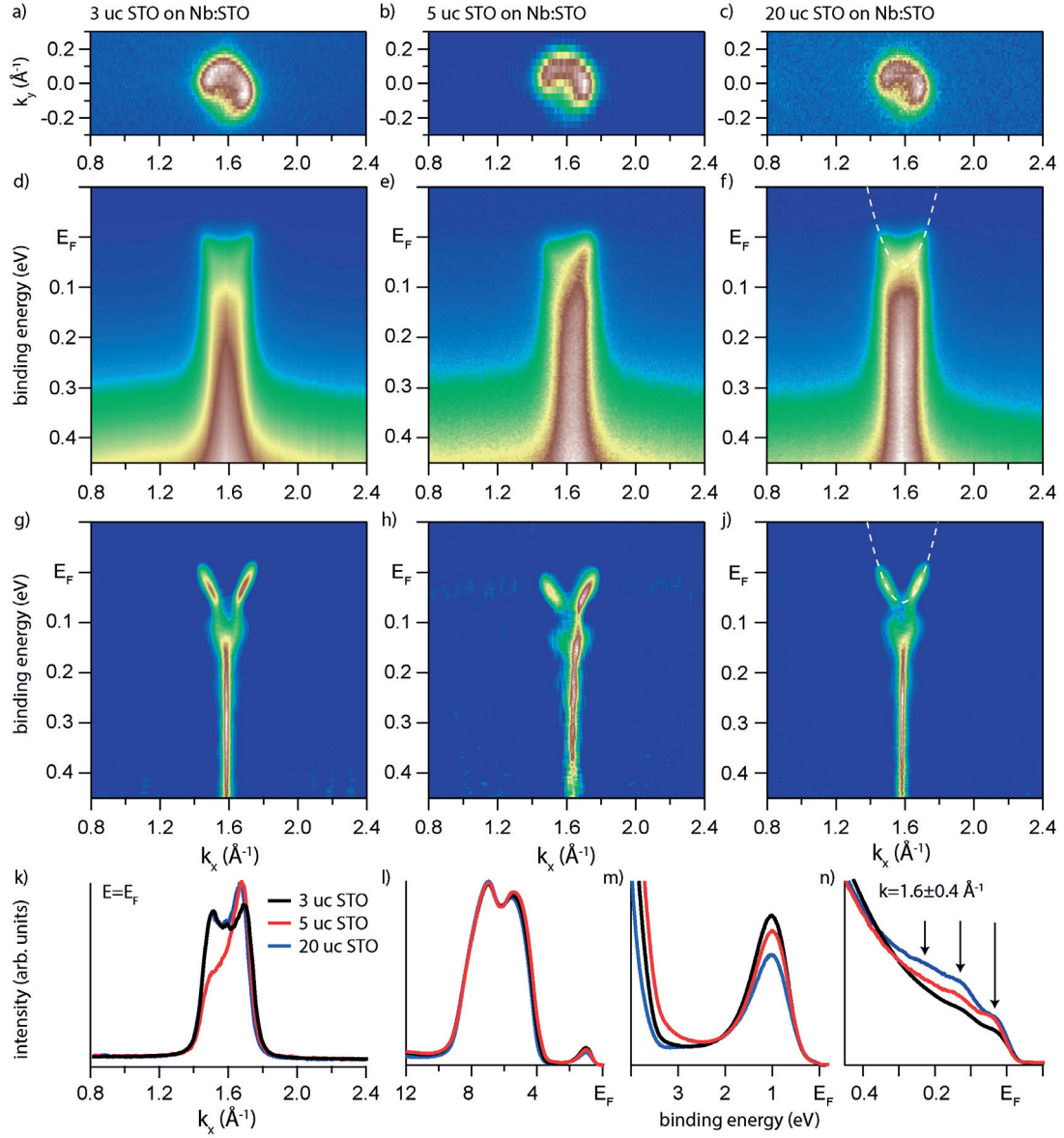


Figure 6.14 – Measurements with $h\nu = 85$ eV, circularly polarized photons at $\overline{\Gamma}_{10}$ of the three different films. ARPES Fermi surface (a), band structure (d) and 2D curvature (g) for 3 uc STO on Nb:STO. (b,e,h) and (c,f,i) same as (a,d,g) but for 5 uc STO on Nb:STO and 20 uc STO on Nb:STO respectively. Free electron like parabola is indicated in (f,i). (k) MDCs of the three films at the Fermi energy from (d,e,f). (l) EDC of the valence band, (m) the in-gap state and (n) close to the Fermi energy with indicated polaron replicas (black arrows).

[253–256]. It is therefore valid to assume that our PLD grown thin STO film will have a altered dielectric constant compared to bulk STO and will consequently also result in a change in band bending. The grown STO films are considered to be insulating while the choosen substrate of Nb:STO is conducting. The effects of this metal-insulator interface on the 2DEG at the insulator surface is not known and could also contribute to the observed differences between the bulk and film STO surface states.

In the presented data no indication of a splitting of the d_{xy} into sub-bands can be observed [Fig. 6.14(k)]. The splitting is either too low (or not existent) to be observed in the data or the splitting in energy exceeds the band width of the occupied band. If we consider the Zeeman splitting of $\Delta Z = 80$ meV reported for bulk STO [66], the later scenario is possible. This would imply that as an effect of the Rashba- and Zeeman-type splitting observed in the case of STO (001) a single spin-polarized band is present at the Fermi energy of the STO thin films. In connection with the superconducting properties of STO at low temperatures this could lead to the creation of Majorana fermions [257]. However, with the discussed changes in band bending and local crystal structure an altered splitting cannot be excluded.

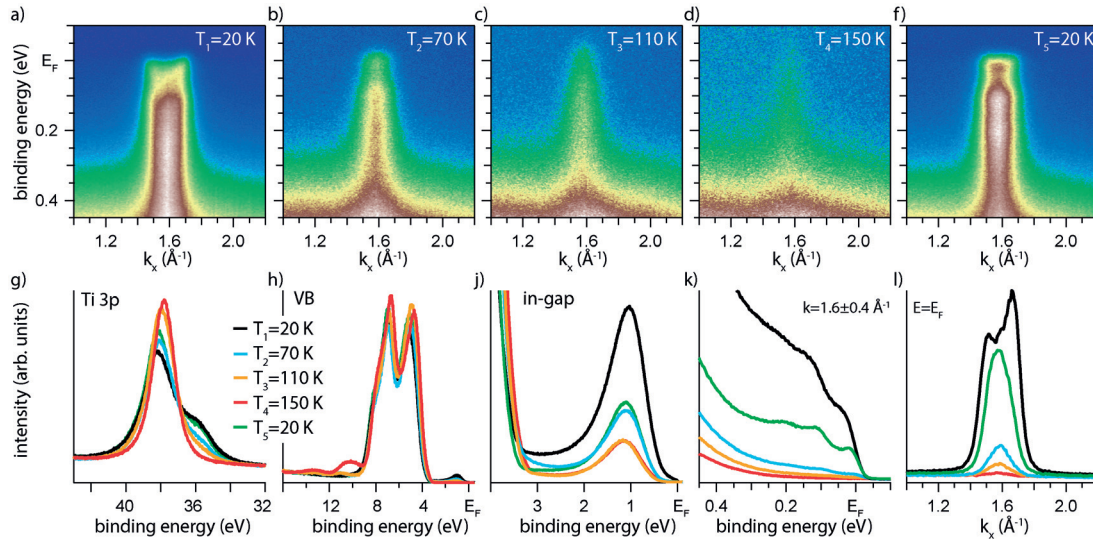


Figure 6.15 – (a-f) Measured band structure of the second $\overline{\Gamma}_{10}$ point of 20 uc STO on Nb:STO obtained with circularly polarized photons of $h\nu = 85$ eV for different temperatures. (g-j) Angle integrated photoemission intensity of the Ti 3p corelevels (g), the valence band (h) and the in-gap state (j) for the different temperature. (k) EDCs of the bandmaps in (a-f) and (l) MDCs at the Fermi energy.

The evolution of the band structure of 20 uc of STO on Nb:STO with temperature is illustrated in Fig. 6.15. We can observe a loss of the intensity attributed to the 2DEG at a temperature of $T_3 = 110$ K. However, there is still intensity present between the in-gap state and the Fermi energy at a temperature of $T_3 = 110$ K and $T_4 = 150$ K [Fig. 6.15(c,d)]. This intensity consists mostly of the polaronic tail, but for electron-polaron interactions taking place there must be still a only slightly filled band at the Fermi energy. Despite the difference in the initial band structure,

the behavior with temperature is in certain aspects similar to the temperature dependent measurements of the vicinal surfaces discussed in Sec. 6.1.3. Especially the behavior of the Ti 3p core level and the valence band are similar. The in-gap state consist only of one contribution at a binding energy of 1.2 eV that loses intensity with temperature. The absence of the higher binding energy in-gap state, observed for the vicinal surfaces and for bulk STO, is due to the absence of the responsible lattice defects in the films grown by PLD. More specifically the Sr and Ti defects that are held responsible for the second in-gap states [250] are not present in the grown films. Due to the similarities with the vicinal surfaces, the possible mechanisms responsible for the observed altering and shift of the band dispersion with temperature are expected to be the same as discussed in Sec. 6.1.3.

6.2.3 Altering of the band structure by Ba doping

In bulk STO crystals, ferroelectric properties can be induced by partially exchanging Sr with Ba. With the resulting lattice strain, the transition temperature of the bulk crystals of $\text{Ba}_x\text{Sr}_{1-x}\text{TiO}_3$ with a Ba doping content of $x=0.07$ is distinguished to be around 50 K, whereas for a doping content of $x=0.1$ the transition temperature is at approximately 75 K [172, 258]. However, the ferroelectric properties of films can be vastly different than of bulk systems. Although the grown film are expected to be unstressed if the lattice constant of $\text{Ba}_x\text{Sr}_{1-x}\text{TiO}_3$ is considered to be unchanged compared to STO for these low doping contents, effects related to the film growth are expected as discussed in the section before.

The ARPES measurements for the grown film with different Ba content are displayed in Fig. 6.16. The two samples show metallic states with a very similar, circular Fermi surface [Fig. 6.16(a-d)] and a band structure with intensity connecting the metallic states to the in-gap state. The dispersions have close similarities to the measurements obtained for STO thin films (see Fig. 6.14 for comparison). Indeed the free-electron-like parabola with a band bottom of 60 meV and an effective mass of $m^* = m_e$ also displayed in 6.14(f,j) for the thin films is in good agreement with the observed dispersion for the Ba doped STO films [see Fig. 6.16(j-m)]. There is also no indication of bands elongated in $\overline{\Gamma X}$ -direction that could be associated with the 3D dispersing d_{xz}/d_{yz} bands. The observed state can therefore be attributed to the 2D d_{xy} bands observed in these systems. The 2D curvature [234] further shows the presence of polaron replicas of the 2D state, separated by approximately 100 meV [54, 201]. The ample similarities between the measurements performed on thin films of STO with the measurements on Ba doped STO films let us conclude that the film related properties have considerable stronger effects on the formation of the 2DEG than the Ba doping.

The evolution of the band structure with temperature is of particular interest in the $\text{Ba}_x\text{Sr}_{1-x}\text{TiO}_3$ system, due to the allocation of the para- to ferroelectric phase transition in the covered temperature range. The measurements for the lower doped film with a Ba doping of 7% (Fig. 6.17) show a small reduction of k_F at the first elevated temperature of $T_2 = 80$ K [Fig. 6.17(j,l)]. At a temperature of $T_3 = 140$ K, the metallic states completely disappear and reappear again after

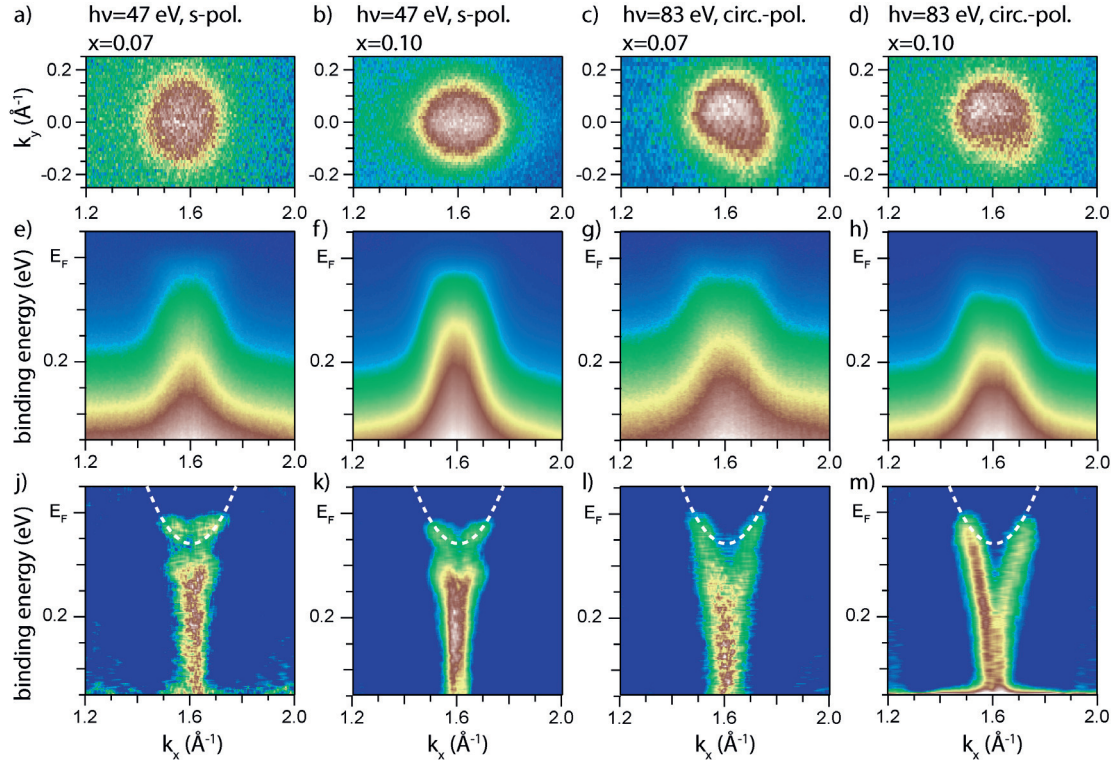


Figure 6.16 – Comparison of Ba_xSr_{1-x}TiO₃ for two different dopings. (a,b) ARPES Fermi surfaces with s-polarized photons of $h\nu = 47$ eV energy with a doping of $x=0.07$ (a) and $x=0.1$ (b). Corresponding band structure (e,f) and 2D curvature (j,k) with indicated free-electron-like dispersion (fit by eye). (c,d) Fermi surfaces with $h\nu = 83$ eV, circularly polarized photons for the two dopings with (g,h) band structure and (l,m) 2D curvature.

cooling back to the initial temperature. As for in the other temperature dependent measurements of oxides discussed in this thesis, the system does not recovery completely after the temperature cycle, indicating non reversible structural changes induced by the combination of UV irradiation and rised temperatures.

The temperature dependent measurements of the film with 10% Ba doping, depicted in Fig. 6.18, shows a similar behavior as the lower doped film. With elevating temperature the k_F of the 2DEG is gradually reduced. At a temperature of $T_5 = 150$ K the signature of the metallic state is barely recognizable in the band dispersion. This indicates that there is a difference in the temperature dependent mechanisms for the two different Ba dopings. Due to the second order nature of the para- to ferroelectric phase transition the observed gradual change with temperature could be related to ferroelectric properties. The ferroelectric phase transition implies changes in the dielectric constant [120, 258] that show a tip at the phase transition temperature and is then decreasing with rising temperatures. This decrease of dielectric constant with temperature is also observed for undoped STO with the peak of a phase transition missing [258]. Therefore the altering of the dielectric constant and consequently the band bending could be an explanation of the similar behavior with temperature of the

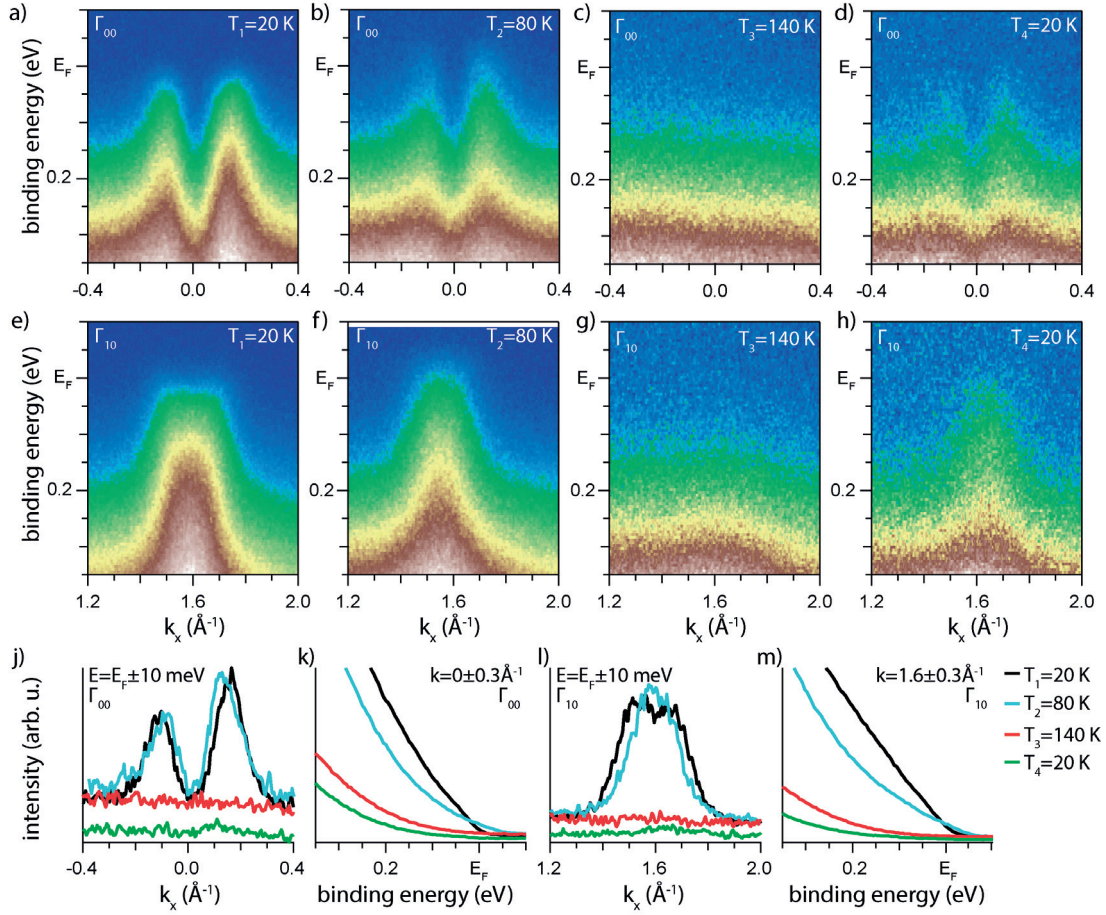


Figure 6.17 – Temperature dependent measurements of the $\text{Ba}_{0.07}\text{Sr}_{0.93}\text{TiO}_3$ film with $h\nu = 83$ eV, s-polarized light. (a-d) ARPES band structure at $\overline{\Gamma}_{00}$ and (e-h) ARPES band structure at $\overline{\Gamma}_{10}$ for the indicated temperature. (j,l) MDCs at the Fermi energy and (k,m) EDCs for the two $\overline{\Gamma}$ -points.

measured compounds. In the two Ba doped systems, the higher dielectric constant of the $x=0.1$ sample around 150 K due to the higher phase transition temperature is a possible explanation for the still present 2DEG at $T_5 = 150$ K. After the elevated temperature, however, the higher doped sample behaves in the same way as lower doped or undoped one and does not completely recover to the initial state.

An other view on the mechanisms taking place with increasing temperature can be gained by the core level intensities measured at the different temperatures at normal emission and an emission angle of $\theta = 45^\circ$ (see Fig. 3.3 for a sketch of the setup) for the two samples. The measurements at the higher emission angle are more surface sensitive due to the limited escape depth of the photoelectrons. The results of the $x=0.07$ and $x=0.1$ doped $\text{Ba}_x\text{Sr}_{1-x}\text{TiO}_3$ films are displayed in Fig. 6.19 and Fig. 6.20. The shown XPS intensities of the core levels have a Shirley background removed to account for the increase in secondary electrons at

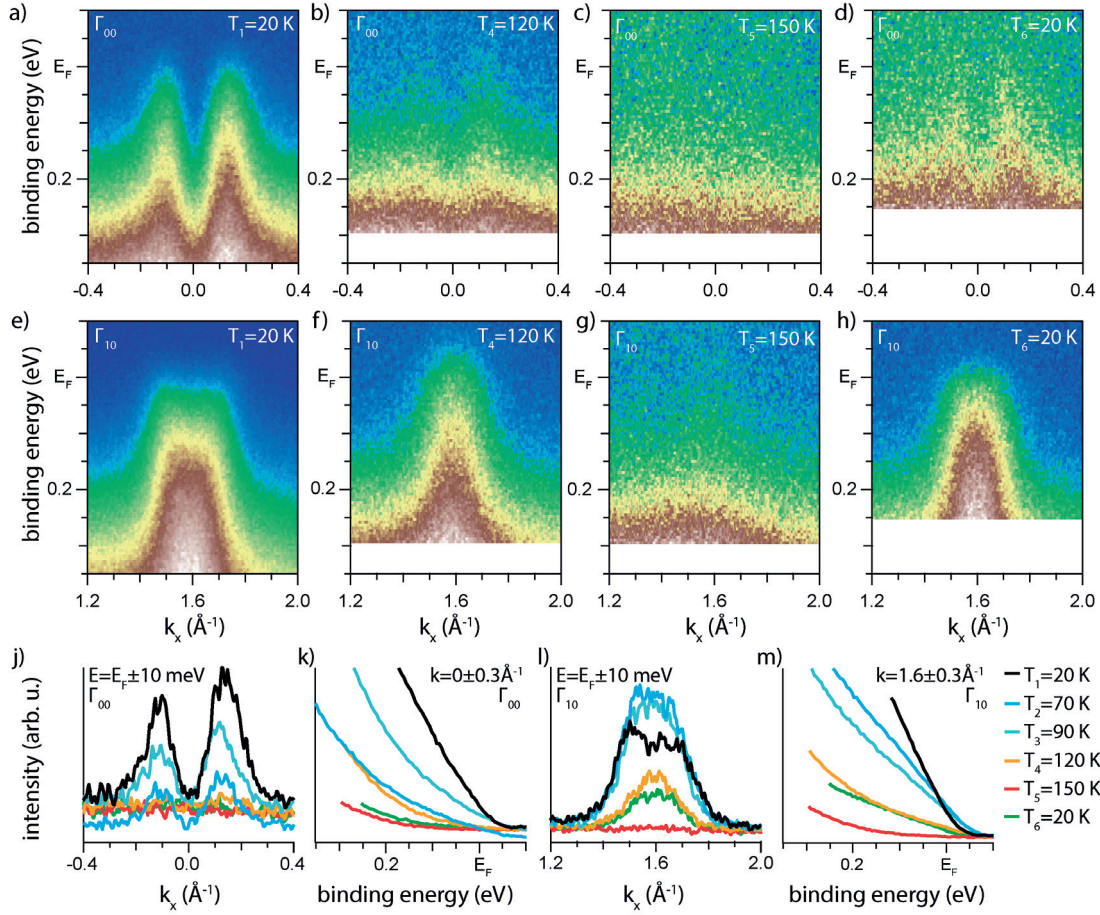


Figure 6.18 – Temperature dependent measurements of the Ba_{0.1}Sr_{0.9}TiO₃ film with $h\nu = 83$ eV, s-polarized light. (a-d) Measured band structure at $\bar{\Gamma}_{00}$ for the indicated temperatures with corresponding MDCs (j) at the Fermi energy and EDCs (k). (e-h) Band structure for the $\bar{\Gamma}_{10}$ point with MDCs (l) and EDCs (m) at the same temperatures as (a-d).

the peak position. However, the removal for the Sr 3d corelevel and the Ba 4d corelevel are not ideal, since the Sr 3d corelevel is on the rising intensity tail of the secondary electrons ($h\nu = 170$ eV) and the Ba 4d corelevel is very low in intensity. Fig. 6.19(j,k) and Fig. 6.20(j,k) summarize the results of a peak fitting with Gaussian peaks for the Sr 3d, Ba 4d and Ti 3p core levels. In Figs. 6.19, 6.20(j) the percentage of the elements peak on the total peak intensity ($I_{total} = I_{Sr\ 3d} + I_{Ba\ 4d} + I_{Ti\ 3p}$) is plotted as a function of temperature for the two emission angles. Figs. 6.19, 6.20(k) focus on the peak contribution of the lower intense Sr-shoulder, the Ti 3+ peak and the bulk Ba peak [see arrows in Figs. 6.19, 6.20(a,b,c)] to the Sr 3d, Ti 3p and Ba 4d core levels respectively.

The Sr 3d, Ba 4d and Ti 3p peak maximas all exhibit a shift to lower binding energies with temperature of approximately 300 meV. In the valence band, this shift is also present but with 250 meV slightly smaller. A similar shift can also be observed for the temperature dependent

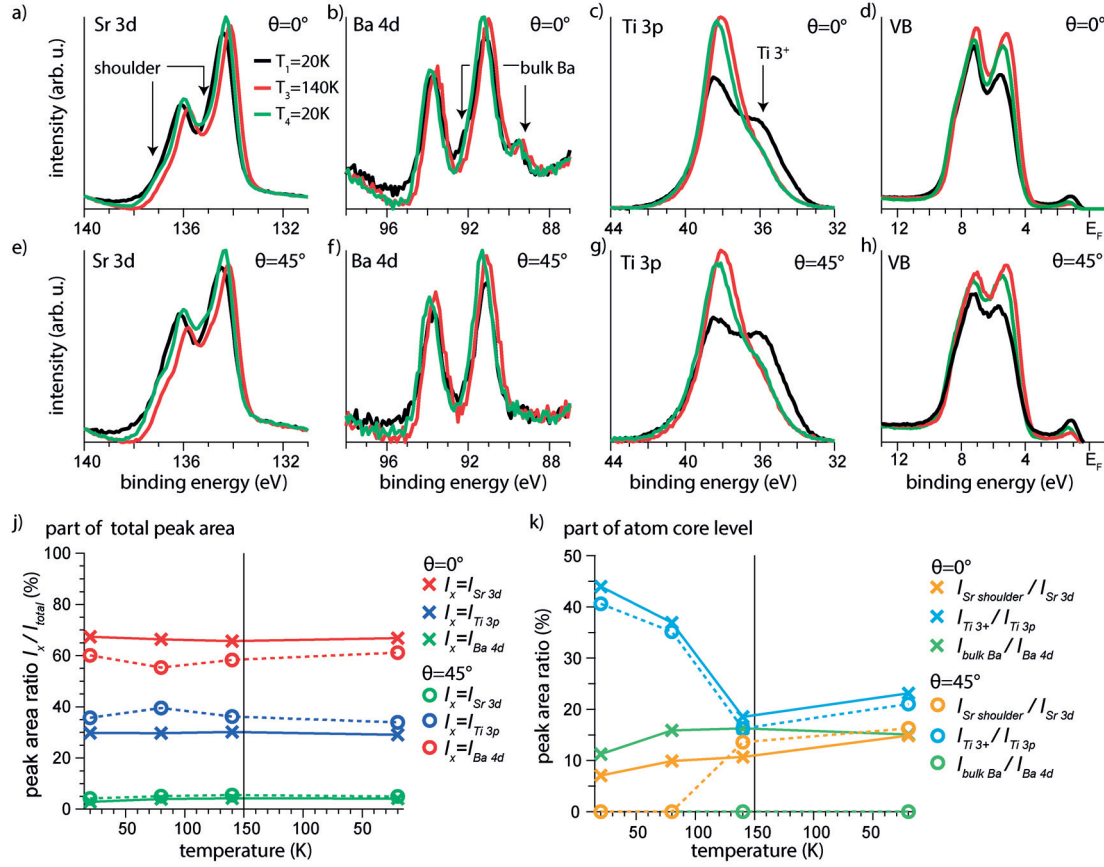


Figure 6.19 – Sr 3d, Ba 4d, Ti 3p and VB photoemission intensity for $\text{Ba}_{0.07}\text{Sr}_{0.93}\text{TiO}_3$ as a function of temperature, measured with $h\nu = 170$ eV for normal emission (a-d) and for an angle of $\theta = 45^\circ$ (e-h). (j) Percentage of the Sr 3d, Ti 3p and Ba 4d core level area on the combined peak area of these three core levels. (k) Percentage of the Sr shoulder on the Sr 3d core level, of the Ti 3^+ shoulder on the Ti 3p core level and of the bulk Ba peak on the Ba 4d core level.

measurements on the vicinal surface (Fig. 6.9). For both films only one in-gap state is observed in contrast to the vicinal substrate, indicating a different Sr and Ti vacancy formation. The contribution of the elements peak area to the total peak area [Figs. 6.19, 6.20(j)] shows no significant evolution with temperature. The Ti 3p corelevel shows lower contribution to the total intensity at normal emission than $\theta = 45^\circ$. This is contrary to the Sr 3d intensity indicating a TiO_2 termination of the grown films. The Ba 4d core level intensity is higher for $\theta = 45^\circ$ than normal emission over the whole temperature range for the two films. A possible explanation for this is a non uniform distribution of Ba atoms in the film or a possible clustering of Ba at the surface.

The Ba 4d core level consist out of two doublets split by 2.7 eV and separated by 1.8 eV from each other. Whereas for the BTO films the doublet at lower binding energy was more intense [see Sec. 5.1, Fig. 5.1(e)], the core levels of Ba doped STO films show an inverted

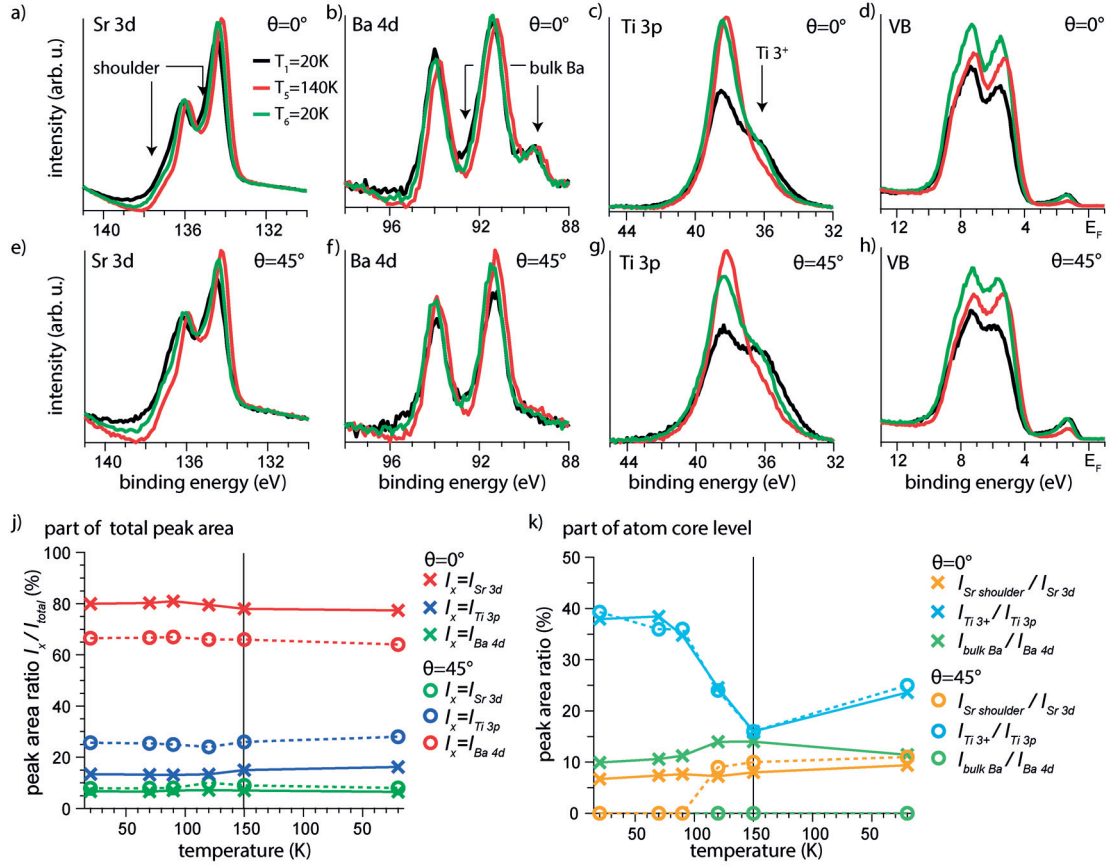


Figure 6.20 – Core levels photoemission intensity measured with $h\nu = 170$ eV as a function of temperature of the Ba_{0.1}Sr_{0.9}TiO₃ film measured at normal emission (a-d) and $\theta = 45^\circ$ (e-h). (j) and (k) peak area analysis obtained the same way as Fig. 6.19(j,k).

behavior. In literature the peak at lower binding energy is associated with bulk Ba [labeled in Figs. 6.19, 6.20(b)] whereas the peak at higher binding energy is attributed to undercoordinated Ba [229–231]. The fraction of the bulk Ba on the Ba 4d core level is around 10% for all the temperatures and only visible at normal emission, confirming its location in the bulk of the films. These observations match with the presence of excess Ba at the film surfaces. The resulting altered stoichiometry of the sample would consequently also affect possible ferroelectric properties. However, photo electron spectroscopy only offers limited possibilities to study the spatial location of elements in a crystal lattice.

The peak of the Ti 3p core level has a shoulder on the low binding energy side that is associated with Ti 3⁺ ions. Their existence is commonly explained by the presence of oxygen vacancies Ti 3⁺ ions or could also be related to a structural rearrangement of the surface Ti for example from a octahedral to a tetrahedral configuration. The ratio of approximately 40% of the Ti 3⁺ on the total Ti 3p peak area is similar for the two emission angles. Therefore their presence is not restricted to the surface but rather uniform in the probed area. With temperature the fraction of Ti 3⁺ ions is reduced to about 15% around 150 K and only partially recovered after

cooling the samples back to the initial temperature. This behavior can be explained by two mechanisms; a reduction in oxygen vacancies or a change in the crystal arrangements and bonds.

An indication for atomic rearrangement can also be found in the evolution of the Sr 3d core level. Additionally to the intense, split doublet with a separation of approximately 2 eV a low intense shoulder is visible indicating the existence of a second doublet, shift by 1.2 eV to higher binding energy. This second doublet is also observed for bulk STO [61] and is suggested to be an indication of the formation of SrO at the surface. The fraction of this Sr shoulder is constant over the temperature range for the measurements at normal emission. At an emission angle of $\theta = 45^\circ$, however, a sudden increase is observable around a temperature of 100 K. With the unchanged fraction of the Sr shoulder in the measurements at normal emission, this indicates the formation of SrO at the surface at this temperature. After cooling the sample back to the initial 20 K the area of the Sr shoulder stays constant. This associated changes are therefore not reversible and could offer an explanation for the also non reversible behavior of the 2DEG. The formation of SrO at the surface would likely alter the possible ways of surface relaxation and therefore could alter the 2DEG formation. Due to the low intensity of these SrO related shoulder, more detailed experiments are necessary to make final conclusion. Further it is unclear if the effects are related to the Ba doping or if similar effects also take place in bulk STO.

6.3 Conclusion

In this chapter, three different approaches to manipulate the 2DEG formation at the STO surface were presented. Step edge density on vicinal surfaces, STO thin films grown on STO substrates and Ba doping to induce a ferroelectric phase. In this approaches two mechanism play a key role, the deformation of the TiO_6 octahedron, responsible for the splitting between the 2D d_{xy} bands and the 3D d_{xz}/d_{yz} bands and the band bending affecting the filling of the Ti 3d states.

The vicinal substrates show a reduction of the splitting between the d_{xy} and the d_{xz}/d_{yz} bands from the literature value of 180 meV for STO to 80 meV at the surface of the sample with 44 Å terrace size and to 60 meV for the 22 Å terrace size sample. This change is attributed to a changed surface relaxation due to the step edges, reducing the trigonal distortion of the TiO_6 octahedron. Apart from this, the altered electron affinity of the surface due to the presence of step edges is expected to reduce the surface band bending, causing the observed shift of the d_{xz}/d_{yz} bands to lower binding energies. With temperature the bottom of the band of the d_{xy} bands gradually shifts to lower binding energies indicating an altering of the band bending as well as the distortion of the octahedron.

The STO thin films, grown on Nb:STO substrate show a band dispersion different from bulk STO but similar for the measured films of 3 uc, 5 uc and 20 uc thickness. The 3D d_{xz}/d_{yz} bands are not present in the dispersion. The 2DEG is therefore the only band contributing

to the metallic properties of the system with a band bottom at approximately 60 meV. The increased effective mass is indicating an altered Ti-O-Ti bond angle. The most striking effect responsible for the different formation of the band structure of STO films compared to bulk STO is likely a change in dielectric constant. This, together with an altered defect density in grown films will alter the band bending at the vacuum interface.

As a last example, results of films of Ba doped STO were presented. In bulk STO already a small amount of Ba doping induces a ferroelectric phase at low temperatures. The band structure of the two studied Ba_xSr_{1-x}TiO₃ films with x=0.07 and x=0.1 are similar to the bands observed for STO thin films and lack the presence of the 3D d_{xz}/d_{yz} bands. With temperature a different behavior is observed. Whereas the lower doped sample has no bands presence at a temperature of 140 K the higher doped sample still has indications of bands at a temperature of 150 K. A possible reason for this altered behavior could be the different evolution of the dielectric properties with temperature due to the different ferroelectric transition temperatures of the two films. In order to make more profound statements on the effect of ferroelectric properties and their impact on the 2DEG formation, measurements proving the existence of a ferroelectric phase in the grown films at low temperature would be necessary. The XPS measurements show the presence of under coordinated Ba at the film surfaces. In the temperature cycle a not reversed increase in peak intensity of a higher binding energy Sr species is observed. Likely this peak intensity can be attributed to SrO and is a possible reason for the altered band structure after the temperature cycle. However, spatially resolved techniques would be necessary to make conclusive statements about surface ad-atoms and their evolution with temperature.

7 Conclusion and Outlook

Oxide materials are considered as valuable candidates to find new possibilities for applications in electronic devices due to the broad range of observed properties. The two-dimensional states found at the interface and surfaces of titanates are of particular interest. With the various bulk properties of titanates, they offer a playground to observe the interaction of these properties with the formation of the two-dimensional states. Furthermore, the mechanism responsible for the formation of the two-dimensional states can be explored and manipulated through the surface and bulk properties. The goal of this thesis was to find different approaches to manipulate the formation of the two-dimensional electron gas (2DEG) at the surface of titanates with perovskite structure. On one hand this was done by observing the states at materials with different ferro- and dielectric properties and on the other hand by altering the surface lattice arrangements and relaxations.

In the first part of the thesis it was shown that the existence of a 2DEG can be extended from the well known STO surface to the related compound CaTiO_3 . At low temperatures CTO shows, like STO and KTaO_3 a quantum paraelectric behavior. The CTO films, grown by pulsed laser deposition exhibit a symmetry given by the pseudo cubic unit cell of the bulk orthorhombic perovskite. The film alters its surface reconstruction under irradiation with UV-light from a $c(4 \times 2)$ to a $p(2 \times 2)$ symmetry. At the surface of the CTO films, a 2DEG is present that is only of d_{xy} character and shows folded Fermi surfaces according to the reconstruction. The band bottom of the state is around 400 meV and has an effective mass of $0.4 \cdot m_e$. Whereas the band bottom of the CTO d_{xy} band is higher, its effective mass is lower compared to the d_{xy} bands of STO. The 2DEG further shows a splitting into two subbands that could possibly be Rashba-like. Spin-resolved ARPES measurements are necessary to clarify the spin polarization of the two subbands. The absence of d_{xz}/d_{yz} bands indicates a strong tetragonal distortion of the TiO_6 octahedron, altering the crystal field splitting, whereas the binding angle between the octahedrons is more straight than for STO according to the bands effective mass. Therefore, the surface of the CTO film is clearly different from the bulk CTO with its orthorhombic structure and the strongly altered binding angles. The affinity of the metallic states to the reconstruction opens ways to further manipulate the system by different

substrates and surface terminations with the goal to achieve an overlap of neighboring Fermi surfaces. This could lead to a hybridization of the possibly spin-polarized bands. Furthermore with the existence of a 2DEG at the surface of CTO, experiments to explore the phase space of CTO - STO intermixture with its (anti-)ferroelectric properties are feasible.

In BTO the ferroelectric properties of the material affect the observed band dispersion in a drastic way. The ferroelectric properties of PLD grown BTO films are explored with piezore-sponse force microscopy. The films have no intrinsic ferroelectric domains of resolvable size, but regions with increased out-of- and into-the-plane polarization can be written. However, the surface cannot be polarized completely along this axis, indicating the presence of strain-locked in-plane domains. The presented ARPES measurements reveal that the BTO vacuum surface also hosts a two-dimensional state. The intrinsic electric fields in in-plane direction, originating from the ferroelectric, in-plane locked tetragonal domains, are responsible for a Wannier-Stark localization of the conduction band electrons. This localization of the electrons in the unit-cell of the crystal smears the bands along the electric field direction in reciprocal space. The mixture of domains present, lead to smearing of the band dispersion along both high-symmetry $\overline{\Gamma X}$ directions and out-of-plane polarized domains possibly also lift the spin-degeneracy of the bands. The Wannier-Stark localization is also observable in overlayers of 3 unit cells of STO deposited on top of the BTO film and is reduced as a function of film thickness. The electric field responsible for the localization in the STO overlayer could be the electric field of the BTO underneath or it could originate from ferroelectric properties induced in the thin STO layer by strain. By the help of BTO films with preferred polarization directions or the possibility of an *in-situ* polarization of the films the interaction of the ferroelectric field with the two-dimensional state could be further explored. Under uniform in-plane polarization, the effects of the Wannier-Stark localization of the surface states on their transport properties could be studied. A completely out-of-plane ferroelectric polarization is expected to alter the Rashba-like splitting of the d_{xy} . For high enough splittings, a single spin polarized band would form the Fermi surface.

The effect of an altered surface arrangement on the 2DEG at the STO surface was investigated by the help of vicinal STO substrates. With increasing step density, the band bottom of the d_{xy} band is shifting to higher binding energies. This shift is not represented in the heavy d_{xz}/d_{yz} bands and is therefore due to an altered distortion of the TiO_6 octahedron affecting the splitting between the d_{xy} and d_{xz}/d_{yz} bands. This is a direct indication of an altered surface relaxation that can be controlled by the step-density. With rising temperature the separation between the d_{xy} and d_{xz}/d_{yz} bands is further reduced, accompanied by a rigid shift likely due to altered dielectric properties with temperature affecting the surface band bending. At 150 K, the bands are not visible anymore and the vicinal substrate turns insulating. After cooling back to 20 K, the bands are not fully recovered to the initial state similar as observed for BTO. The presence of a second in-gap state at a binding energy of 2.8 eV, indicates a different type of defects, likely related to Sr or Ti, in the commercial substrates that is not present in PLD grown films.

STO thin films grown on Nb doped STO substrates show metallic states only consisting of a two-dimensional d_{xy} band with a band bottom of approximately 60 meV. There is no indication of the d_{xz}/d_{yz} that are present at the surface of STO substrates. The two-dimensional bands of the STO films show a higher effective mass, compared to the STO substrates which indicates an altered bonding angle between the TiO_6 octahedron. The lower binding energy of the d_{xy} band can be due to an changed octahedron distortion or a different surface band bending. The band bending is likely affected by the different dielectric properties of STO films and the altered defect density of PLD grown films compared to STO substrates. The d_{xy} bands show no indication of a Rashba-like splitting. This implies that the splitting is either reduced below the resolving power or only the d_{xy} band with higher binding energy is filled, resulting in a single, spin-polarized band forming the Fermi surface. Spin-resolved measurements are necessary to clarify this. Also here the existence of a single spin-polarized band in combination with the superconducting properties of STO at low temperatures could be a platform to observe Majorana fermions.

A similar band dispersion as for the STO thin films is also measured for 20 nm thick PLD grown films of Ba doped STO. Bulk crystals with Ba doping are reported to exhibit ferroelectric properties at low temperatures. The two investigated films with a doping of 7 % and 10 % Ba respectively show a similar band structure at low temperature but behave differently with rising temperature. For the lower doping, with a ferroelectric phase transition for the bulk material reported to be at 50 K, the sample shows no more conducting states at a temperature of 140 K, whereas for the higher doping with a bulk transition temperature of 75 K, faint states are still present at 150 K. The different transition temperatures are likely due to a different behavior of the dielectric constant with temperature that is expected in relation with the altered ferroelectric properties. Emission angle and temperature dependent XPS measurements show the presence of under coordinated, likely excess Ba at the surface of the thin films. Therefore the stoichiometry of the films is not uniform and does not represent the composition of the PLD target exactly. Further experiments to distinguish the ferroelectric properties of the grown films at low temperatures would be necessary. This could be for example low temperature PFM measurements or measurements of the dielectric behavior. In future experiments Ba doped bulk STO substrates could be measured, that likely achieve a better stoichiometry and are also expected to exhibit a different dielectric behavior than films as observed for the STO films.

For both samples the state is not completely recovered after cooling back to the initial temperature, similar to the observations for BTO and vicinal STO. A non reversible change is also observed on the Sr core levels. They exhibit a change in lineshape that is likely due to excess Sr or SrO at the surface formed at elevated temperature under UV irradiation. The onset of this change is in the region of the tetragonal phase transition of the STO substrate. Therefore the observed changes in the 2DEG band structure after the temperature treatment could be related to an altered surface ordering and quality. Further measurements on other systems would have to clarify if this effect is only observed for the Ba doped STO films or is of a general nature. This finding could also be supported by spatial resolved techniques as photoemission

electron microscopy (PEEM) or non contact AFM, identifying the nature of the Sr species that are formed at the surface at elevated temperatures under UV irradiation.

The findings of the vicinal substrates, the STO films and the Ba doped STO films directly show possible ways to alter the formation of the STO 2DEG. The formation of the 2DEG is sensitive to the surface structure and relaxation and the splitting can be lowered by allowing the surface to relax. This relaxation could also be affected by inducing compressive or tensile strain in thin STO films or by external stress on STO substrates. Of crucial role for the formation of the 2DEG is the surface band bending that controls the band filling. The extend of the band bending is linked to the dielectric properties of the material. Due to the crucial role of the surface arrangement, *in-situ* techniques to measure the dielectric properties of thin films could clarify this. Combining the ability of the existing ARPES system with the *in-situ* PLD growth chamber with additionally a PFM system would give the possibility to investigate the ferroelectric properties of the grown systems at the conditions of the ARPES measurements. This would be particularly interesting for bulk ferroelectric systems as BTO but also for the quantum paraelectric CTO and STO where surface ferroelectric properties could exist. Unclear is also the effect of the UV irradiation on the ferroelectric properties. Possible is for example that the light locally induces ferroelectric properties and/or writes the already ferroelectric surface. The possibility of *in-situ* PFM could also address this question by having the possibility to change between ARPES and PFM and track the light induced changes.

The transition metal oxides are interesting due to their interplay of spin, lattice, charge and orbital degree of freedoms. In this thesis mainly the lattice degree of freedom was touched, resulting in effects on the charge and orbital degree of freedom and likely also the spin. Due to the properties of the investigated titanates there were already numerous effects on the formation of the two-dimensional states observed as a result of the small changes of the lattice degree of freedom. The mutual interaction of these properties gave rise to new observations as Wannier-Stark localization and gives access to the responsible mechanisms of the formation of the two-dimensional surface state. The phase space to explore in titanates is vast and only a small portion of it was accessed by this thesis, giving a perspective on the possibilities that are still undiscovered.

Apart from the projects on oxides, covered in this thesis, the thesis author collaborated closely in two projects. The first project focused on the spin-texture of the Fermi arc of the Weyl semimetal TaAs [259]. The Fermi arc shows a chiral spin-texture that indicates the existence of topological nontrivial states in TaAs. The second project is the ferroelectric α -GeTe that shows multiferroic properties by Mn doping [77, 260]. In the undoped case, α -GeTe exhibits a Rashba splitting of its bulk bands due to the noncentrosymmetric lattice structure. Under Mn-doping the degeneracy at the Γ -point is lifted due to the magnetic moments. The spin polarization of the bands at the Γ -point can be controlled by external magnetic fields. Further experiments are performed to explore the multiferroic properties by observing the spin polarization with applied electric fields.

Acknowledgements

During the years of my PhD studies at the Paul Scherrer Institut and the École Polytechnique Fédérale de Lausanne I could always rely on the support of a lot of people I worked with. It is my pleasure to thank everybody for his contribution. Foremost I would like to thank Hugo Dil for giving me the opportunity to conduct my PhD studies under his supervision. He always was a source for inspiration and ideas and was always approachable to answer my numerous questions. Further I would like to thank Milan Radovic for his indispensable support and for sharing his knowledge on oxides, PLD growth and the world with me.

If help was needed I could always rely on my present and past colleagues from the COPHEE endstation; Mauro Fanciulli, Andrew Weber and Gabriel Landolt. It was a pleasure to work and discuss with them; shared troubles are always easier to deal with. As part of the extended COPHEE team I also thank Juraj Krempasky for involving me in his GeTe project and for always being an emergency contact for software issues. I also thank Nicholas Pilet who performed the PFM measurements and helped me to interpret and understand them.

A special thanks goes to Nick Plumb for sharing his knowledge and data of SrTiO_3 with me. I also thank him and Ming Shi for keeping the beamline and ARPES endstation in excellent condition. For my beamtimes I could profit from the experience and advice of the PLD post-docs Zoran Ristic and Zhiming Wang who spend numerous hours at the beamline with me to grow the perfect film. I also like to acknowledge the help of Valdimir Strocov, Federico Bisti, Victor Rogalev and Adrian Husanu during the SXARPES beamtime. I would further like to thank all the present and past members of the Spectroscopy of Novel Materials Group at PSI, I interacted with the past years; Thorsten Schmitt, Christian Matt, Marcus Dantz, Jonathan Pelliciari, Muntaser Naameh, Nan Xu, Daniel McNally, Eugenio Paris, Alla Chikina, Marco Caputo, Baiqing Lu and Binbin Fu. They were always a source of advice, or when needed a source of distraction. A special thanks goes to the beamline technicians Fritz Dubi, Leonard Nue, Andreas Pfister and Markus Kropf for the technical advice and support and Luka Debenjak for the software support.

Last but not least I would like to thank my family and friends for the moral support during the past years and their understanding if plans were canceled on short notice due to beam-times. Finally I would like to especially thank my parents for their tremendous support and encouragement during my studies.

Bibliography

- [1] K. v. Klitzing, G. Dorda, and M. Pepper. New method for high-accuracy determination of the fine-structure constant based on quantized Hall resistance. *Phys. Rev. Lett.*, 45:494–497, Aug 1980.
- [2] Gordon E Moore et al. Cramming more components onto integrated circuits. *Proceedings of the IEEE*, 86(1):82–85, 1998.
- [3] L Bjaalie, B Himmetoglu, L Weston, A Janotti, and CG Van de Walle. Oxide interfaces for novel electronic applications. *New Journal of Physics*, 16(2):025005, 2014.
- [4] JG Bednorz. Perovskites and their new role in oxide electronics. In *High T_c Superconductors and Related Transition Metal Oxides*, pages 29–34. Springer, 2007.
- [5] Pavlo Zubko, Stefano Gariglio, Marc Gabay, Philippe Ghosez, and Jean-Marc Triscone. Interface physics in complex oxide heterostructures. *Annu. Rev. Condens. Matter Phys.*, 2(1):141–165, 2011.
- [6] M Lorenz, MS Ramachandra Rao, T Venkatesan, E Fortunato, P Barquinha, R Branquinho, D Salgueiro, R Martins, E Carlos, A Liu, et al. The 2016 oxide electronic materials and oxide interfaces roadmap. *Journal of Physics D: Applied Physics*, 49(43):433001, 2016.
- [7] A Ohtomo and HY Hwang. A high-mobility electron gas at the $\text{LaAlO}_3/\text{SrTiO}_3$ heterointerface. *Nature*, 427(6973):423–426, 2004.
- [8] Pouya Moetakef, Tyler A. Cain, Daniel G. Ouellette, Jack Y. Zhang, Dmitri O. Klenov, Anderson Janotti, Chris G. Van de Walle, Siddharth Rajan, S. James Allen, and Susanne Stemmer. Electrostatic carrier doping of $\text{GdTiO}_3/\text{SrTiO}_3$ interfaces. *Applied Physics Letters*, 99(23):232116, 2011.
- [9] A. F. Santander-Syro, O. Copie, T. Kondo, F. Fortuna, S. Pailhès, R. Weht, X. G. Qiu, F. Bertran, A. Nicolaou, A. Taleb-Ibrahimi, P. Le Fèvre, G. Herranz, M. Bibes, N. Reyren, Y. Apertet, P. Lecoeur, A. Barthélémy, and M. J. Rozenberg. Two-dimensional electron gas with universal subbands at the surface of SrTiO_3 . *Nature*, 469:189, 2011.

Bibliography

- [10] W. Meevasana, P. D. C. King, R. H. He, S-K. Mo, M. Hashimoto, A. Tamai, P. Songsiriritthigul, F. Baumberger, and Z-X. Shen. Creation and control of a two-dimensional electron liquid at the bare SrTiO₃ surface. *Nat Mater*, 10:114, 2011.
- [11] H.E. Weaver. Dielectric properties of single crystals of SrTiO₃ at low temperatures. *Journal of Physics and Chemistry of Solids*, 11(3):274 – 277, 1959.
- [12] K. A. Müller and H. Burkard. SrTiO₃: An intrinsic quantum paraelectric below 4 k. *Phys. Rev. B*, 19:3593–3602, Apr 1979.
- [13] A. Levstik, C. Filipič, R. Pirc, V. Bobnar, R. Blinc, and M. Itoh. Low-temperature phase of SrTiO₃. *Applied Physics Letters*, 87(3):032901, 2005.
- [14] M. Itoh, R. Wang, Y. Inaguma, T. Yamaguchi, Y-J. Shan, and T. Nakamura. Ferroelectricity induced by oxygen isotope exchange in strontium titanate perovskite. *Phys. Rev. Lett.*, 82:3540–3543, Apr 1999.
- [15] JH Haeni, P Irvin, W Chang, R Uecker, P Reiche, YL Li, S Choudhury, W Tian, ME Hawley, B Craigo, et al. Room-temperature ferroelectricity in strained SrTiO₃. *Nature*, 430(7001):758–761, 2004.
- [16] HW Jang, Amit Kumar, Sava Denev, Michael D Biegalski, Petro Maksymovych, CW Bark, Craig T Nelson, CM Folkman, Seung Hyub Baek, Nina Balke, et al. Ferroelectricity in strain-free SrTiO₃ thin films. *Physical Review Letters*, 104(19):197601, 2010.
- [17] J. F. Schooley, W. R. Hosler, E. Ambler, J. H. Becker, Marvin L. Cohen, and C. S. Koonce. Dependence of the superconducting transition temperature on carrier concentration in semiconducting SrTiO₃. *Phys. Rev. Lett.*, 14:305–307, Mar 1965.
- [18] C. S. Koonce, Marvin L. Cohen, J. F. Schooley, W. R. Hosler, and E. R. Pfeiffer. Superconducting transition temperatures of semiconducting SrTiO₃. *Phys. Rev.*, 163:380–390, Nov 1967.
- [19] Xiao Lin, German Bridoux, Adrien Gourgout, Gabriel Seyfarth, Steffen Krämer, Marc Nardone, Benoît Fauqué, and Kamran Behnia. Critical doping for the onset of a two-band superconducting ground state in SrTiO_{3-δ}. *Phys. Rev. Lett.*, 112:207002, May 2014.
- [20] JJ Lee, FT Schmitt, RG Moore, S Johnston, Y-T Cui, W Li, M Yi, ZK Liu, M Hashimoto, Y Zhang, et al. Interfacial mode coupling as the origin of the enhancement of T_c in FeSe films on SrTiO₃. *Nature*, 515(7526):245–248, 2014.
- [21] S. N. Rebec, T. Jia, C. Zhang, M. Hashimoto, D.-H. Lu, R. G. Moore, and Z.-X. Shen. Coexistence of replica bands and superconductivity in FeSe monolayer films. *Phys. Rev. Lett.*, 118:067002, Feb 2017.

-
- [22] Stefan Muff, Maura Fanciulli, Andrew P. Weber, Nicolas Pilet, Zoran Ristic, Zhiming Wang, Nicolas C. Plumb, Milan Radovic, and J. Hugo Dil. Observation of a two-dimensional electron gas at CaTiO_3 film surfaces. *in print at Applied Surface Science*, 2017.
- [23] Susanne Stemmer and S James Allen. Two-dimensional electron gases at complex oxide interfaces. *Annual Review of Materials Research*, 44:151–171, 2014.
- [24] Nini Pryds and Vincenzo Esposito. When two become one: An insight into 2D conductive oxide interfaces. *Journal of Electroceramics*, 38(1):1–23, 2017.
- [25] Stefan Thiel, German Hammerl, A Schmehl, CW Schneider, and Jochen Mannhart. Tunable quasi-two-dimensional electron gases in oxide heterostructures. *Science*, 313(5795):1942–1945, 2006.
- [26] Darrell G Schlom and Jochen Mannhart. Oxide electronics: interface takes charge over Si. *Nature materials*, 10:168–169, 2011.
- [27] G. Herranz, F. Sanchez, N. Dix, M. Scigaj, and J. Fotcuberta. High mobility conduction at (110) and (111) $\text{LaAlO}_3/\text{SrTiO}_3$ interfaces. *Scientific Reports*, 2(758), 2012.
- [28] C. Cancellieri, M. L. Reinle-Schmitt, M. Kobayashi, V. N. Strocov, P. R. Willmott, D. Fontaine, Ph. Ghosez, A. Filippetti, P. Delugas, and V. Fiorentini. Doping-dependent band structure of $\text{LaAlO}_3/\text{SrTiO}_3$ interfaces by soft x-ray polarization-controlled resonant angle-resolved photoemission. *Phys. Rev. B*, 89:121412, Mar 2014.
- [29] Alexey Kalabukhov, Robert Gunnarsson, Johan Börjesson, Eva Olsson, Tord Claeson, and Dag Winkler. Effect of oxygen vacancies in the SrTiO_3 substrate on the electrical properties of the $\text{LaAlO}_3/\text{SrTiO}_3$ interface. *Phys. Rev. B*, 75:121404, Mar 2007.
- [30] Z. Q. Liu, C. J. Li, W. M. Lü, X. H. Huang, Z. Huang, S. W. Zeng, X. P. Qiu, L. S. Huang, A. Annadi, J. S. Chen, J. M. D. Coey, T. Venkatesan, and Ariando. Origin of the two-dimensional electron gas at $\text{LaAlO}_3/\text{SrTiO}_3$ interfaces: The role of oxygen vacancies and electronic reconstruction. *Phys. Rev. X*, 3:021010, May 2013.
- [31] L Qiao, T C Droubay, V Shutthanandan, Z Zhu, P V Sushko, and S A Chambers. Thermodynamic instability at the stoichiometric $\text{LaAlO}_3/\text{SrTiO}_3$ (001) interface. *Journal of Physics: Condensed Matter*, 22(31):312201, 2010.
- [32] Frank Schoofs, Michael A Carpenter, Mary E Vickers, Mehmet Egilmez, Thomas Fix, Josée E Kleibeuker, Judith L MacManus-Driscoll, and Mark G Blamire. Carrier density modulation by structural distortions at modified $\text{LaAlO}_3/\text{SrTiO}_3$ interfaces. *Journal of Physics: Condensed Matter*, 25(17):175005, 2013.
- [33] N.C. Plumb, M. Kobayashi, M. Salluzzo, E. Razzoli, C.E. Matt, V.N. Strocov, K.J. Zhou, M. Shi, J. Mesot, T. Schmitt, L. Patthey, and M. Radović. Evolution of the SrTiO_3 surface electronic state as a function of LaAlO_3 overlayer thickness. *Applied Surface Science*, 412:271 – 278, 2017.

Bibliography

- [34] N. Reyren, S. Thiel, A. D. Caviglia, L. Fitting Kourkoutis, G. Hammerl, C. Richter, C. W. Schneider, T. Kopp, A.-S. Rüetschi, D. Jaccard, M. Gabay, D. A. Muller, J.-M. Triscone, and J. Mannhart. Superconducting interfaces between insulating oxides. *Science*, 317(5842):1196–1199, 2007.
- [35] AD Caviglia, Stefano Gariglio, Nicolas Reyren, Didier Jaccard, T Schneider, M Gabay, S Thiel, G Hammerl, Jochen Mannhart, and J-M Triscone. Electric field control of the $\text{LaAlO}_3/\text{SrTiO}_3$ interface ground state. *Nature*, 456(7222):624–627, 2008.
- [36] S Gariglio, N Reyren, AD Caviglia, and JM Triscone. Superconductivity at the $\text{LaAlO}_3/\text{SrTiO}_3$ interface. *Journal of Physics: Condensed Matter*, 21(16):164213, 2009.
- [37] Alexander Brinkman, M Huijben, M Van Zalk, J Huijben, U Zeitler, JC Maan, WG Van der Wiel, G Rijnders, DHA Blank, and H Hilgenkamp. Magnetic effects at the interface between non-magnetic oxides. *Nature materials*, 6(7):493–496, 2007.
- [38] A Ariando, X Wang, ZQ Liu, JB Yi, A Annadi, A Roy Barman, A Rusydi, S Dhar, YP Feng, J Ding, et al. Electronic phase separation at the $\text{LaAlO}_3/\text{SrTiO}_3$ interface. In *APS Meeting Abstracts*, volume 1, page 34014, 2011.
- [39] Julie A Bert, Beena Kalisky, Christopher Bell, Minu Kim, Yasuyuki Hikita, Harold Y Hwang, and Kathryn A Moler. Direct imaging of the coexistence of ferromagnetism and superconductivity at the $\text{LaAlO}_3/\text{SrTiO}_3$ interface. *Nature physics*, 7(10):767–771, 2011.
- [40] X Wang, WM Lü, A Annadi, ZQ Liu, K Gopinadhan, S Dhar, T Venkatesan, et al. Magnetoresistance of two-dimensional and three-dimensional electron gas in $\text{LaAlO}_3/\text{SrTiO}_3$ heterostructures: Influence of magnetic ordering, interface scattering, and dimensionality. *Physical Review B*, 84(7):075312, 2011.
- [41] A. D. Caviglia, M. Gabay, S. Gariglio, N. Reyren, C. Cancellieri, and J. M. Triscone. Tunable rashba spin-orbit interaction at oxide interfaces. *Physical Review Letters*, 104(12):126803, 03 2010.
- [42] M. Salluzzo, J. C. Cezar, N. B. Brookes, V. Bisogni, G. M. De Luca, C. Richter, S. Thiel, J. Mannhart, M. Huijben, A. Brinkman, G. Rijnders, and G. Ghiringhelli. Orbital reconstruction and the two-dimensional electron gas at the $\text{LaAlO}_3/\text{SrTiO}_3$ interface. *Phys. Rev. Lett.*, 102:166804, Apr 2009.
- [43] Arjun Joshua, S Pecker, J Ruhman, E Altman, and S Ilani. A universal critical density underlying the physics of electrons at the $\text{LaAlO}_3/\text{SrTiO}_3$ interface. *Nature communications*, 3:1129, 2012.
- [44] G. Berner, M. Sing, H. Fujiwara, A. Yasui, Y. Saitoh, A. Yamasaki, Y. Nishitani, A. Sekiyama, N. Pavlenko, T. Kopp, C. Richter, J. Mannhart, S. Suga, and R. Claessen. Direct k -space mapping of the electronic structure in an oxide-oxide interface. *Phys. Rev. Lett.*, 110:247601, Jun 2013.

-
- [45] A. Dubroka, M. Rössle, K. W. Kim, V. K. Malik, L. Schultz, S. Thiel, C. W. Schneider, J. Mannhart, G. Herranz, O. Copie, M. Bibes, A. Barthélémy, and C. Bernhard. Dynamical response and confinement of the electrons at the $\text{LaAlO}_3/\text{SrTiO}_3$ interface. *Phys. Rev. Lett.*, 104:156807, Apr 2010.
- [46] Yasuhiro Yamada, Hiroki K. Sato, Yasuyuki Hikita, Harold Y. Hwang, and Yoshihiko Kanemitsu. Spatial density profile of electrons near the $\text{LaAlO}_3/\text{SrTiO}_3$ heterointerface revealed by time-resolved photoluminescence spectroscopy. *Applied Physics Letters*, 104(15):151907, 2014.
- [47] Akira Fujishima and Kenichi Honda. Electrochemical photolysis of water at a semiconductor electrode. *nature*, 238(5358):37–38, 1972.
- [48] Ryoji Asahi, Takeshi Morikawa, T Ohwaki, K Aoki, and Y Taga. Visible-light photocatalysis in nitrogen-doped titanium oxides. *Science*, 293(5528):269–271, 2001.
- [49] Kazuya Nakata and Akira Fujishima. TiO_2 photocatalysis: design and applications. *Journal of Photochemistry and Photobiology C: Photochemistry Reviews*, 13(3):169–189, 2012.
- [50] Z. Wang, Z. Zhong, S. McKeown Walker, Z. Ristic, J.-Z. Ma, F. Y. Bruno, S. Riccò, G. Sangiovanni, G. Eres, N. C. Plumb, L. Patthey, M. Shi, J. Mesot, F. Baumberger, and M. Radovic. Atomically precise lateral modulation of a two-dimensional electron liquid in anatase TiO_2 thin films. *Nano Letters*, 17(4):2561–2567, 2017.
- [51] A. Vittadini, A. Selloni, F. P. Rotzinger, and M. Grätzel. Structure and energetics of water adsorbed at TiO_2 anatase (101) and (001) surfaces. *Phys. Rev. Lett.*, 81:2954–2957, Oct 1998.
- [52] Michele Lazzeri, Andrea Vittadini, and Annabella Selloni. Structure and energetics of stoichiometric TiO_2 anatase surfaces. *Phys. Rev. B*, 63:15409, Mar 2001.
- [53] ML Knotek and Peter J Feibelman. Ion desorption by core-hole Auger decay. *Physical Review Letters*, 40(14):964, 1978.
- [54] S. Moser, L. Moreschini, J. Jaćimović, O. S. Barišić, H. Berger, A. Magrez, Y. J. Chang, K. S. Kim, A. Bostwick, E. Rotenberg, L. Forró, and M. Grioni. Tunable polaronic conduction in anatase TiO_2 . *Phys. Rev. Lett.*, 110:196403, May 2013.
- [55] Martin Setvin, Cesare Franchini, Xianfeng Hao, Michael Schmid, Anderson Janotti, Merzuk Kaltak, Chris G. Van de Walle, Georg Kresse, and Ulrike Diebold. Direct view at excess electrons in TiO_2 rutile and anatase. *Phys. Rev. Lett.*, 113:086402, Aug 2014.
- [56] TC Rödel, F Fortuna, F Bertran, M Gabay, MJ Rozenberg, AF Santander-Syro, and P Le Fevre. Engineering two-dimensional electron gases at the (001) and (101) surfaces of TiO_2 anatase using light. *Physical Review B*, 92(4):041106, 2015.

Bibliography

- [57] Victor E Henrich, G Dresselhaus, and HJ Zeiger. Surface defects and the electronic structure of SrTiO_3 surfaces. *Physical Review B*, 17(12):4908, 1978.
- [58] R Courths, B Cord, and H Saalfeld. Bulk and surface Ti3d valence and defect states in SrTiO_3 (001) from resonant photoemission. *Solid state communications*, 70(11):1047–1051, 1989.
- [59] Y Aiura, I Hase, H Bando, T Yasue, T Saitoh, and DS Dessau. Photoemission study of the metallic state of lightly electron-doped SrTiO_3 . *Surface science*, 515(1):61–74, 2002.
- [60] Warawat Meevasana, XJ Zhou, B Moritz, CC Chen, RH He, SI Fujimori, DH Lu, SK Mo, RG Moore, Félix Baumberger, et al. Strong energy–momentum dispersion of phonon-dressed carriers in the lightly doped band insulator SrTiO_3 . *New Journal of Physics*, 12(2):023004, 2010.
- [61] N. C. Plumb, M. Salluzzo, E. Razzoli, M. Månsson, M. Falub, J. Krempasky, C. E. Matt, J. Chang, M. Schulte, J. Braun, H. Ebert, J. Minár, B. Delley, K.-J. Zhou, T. Schmitt, M. Shi, J. Mesot, L. Patthey, and M. Radović. Mixed dimensionality of confined conducting electrons in the surface region of SrTiO_3 . *Phys. Rev. Lett.*, 113:086801, Aug 2014.
- [62] PDC King, S McKeown Walker, Anna Tamai, Alberto De La Torre, T Eknapakul, P Buaphet, S-K Mo, W Meevasana, MS Bahramy, and Félix Baumberger. Quasiparticle dynamics and spin–orbital texture of the SrTiO_3 two-dimensional electron gas. *Nature communications*, 5, 2014.
- [63] P. D. C. King, R. H. He, T. Eknapakul, P. Buaphet, S. K. Mo, Y. Kaneko, S. Harashima, Y. Hikita, M. S. Bahramy, C. Bell, Z. Hussain, Y. Tokura, Z. X. Shen, H. Y. Hwang, F. Baumberger, and W. Meevasana. Subband structure of a two-dimensional electron gas formed at the polar surface of the strong spin-orbit perovskite KTaO_3 . *Physical Review Letters*, 108(11):117602–, 03 2012.
- [64] R Di Capua, M Radovic, GM De Luca, I Maggio-Aprile, F Miletto Granozio, NC Plumb, Z Ristic, U Scotti di Uccio, R Vaglio, and M Salluzzo. Observation of a two-dimensional electron gas at the surface of annealed SrTiO_3 single crystals by scanning tunneling spectroscopy. *Physical Review B*, 86(15):155425, 2012.
- [65] Nicholas C. Plumb and Milan Radovic. Angle-resolved photoemission spectroscopy studies of metallic surface and interface states of oxide insulators. *J. Phys.: Condens. Matter*, 2017. in press.
- [66] AF Santander-Syro, F Fortuna, C Bareille, TC Rödel, G Landolt, NC Plumb, JH Dil, and M Radović. Giant spin splitting of the two-dimensional electron gas at the surface of SrTiO_3 . *Nature materials*, 13(12):1085–1090, 2014.
- [67] É. I. Rashba. Properties of semiconductors with an extremum loop i. cyclotron and combinational resonance in a magnetic field perpendicular to the plane of the loop. *Soviet Physics - Solid State*, 2:1109, 1960.

-
- [68] Yu A Bychkov and E I Rashba. Oscillatory effects and the magnetic susceptibility of carriers in inversion layers. *Journal of Physics C: Solid State Physics*, 17(33):6039–6045, 1984.
- [69] M. Hoesch, M. Muntwiler, V. N. Petrov, M. Hengsberger, L. Patthey, M. Shi, M. Falub, T. Greber, and J. Osterwalder. Spin structure of the Shockley surface state on Au(111). *Phys. Rev. B*, 69(24):241401, Jun 2004.
- [70] J Hugo Dil. Spin and angle resolved photoemission on non-magnetic low-dimensional systems. *Journal of Physics: Condensed Matter*, 21(40):403001 (22pp), 2009.
- [71] Gabriel Landolt, Sergey V. Eremeev, Yury M. Koroteev, Bartosz Slomski, Stefan Muff, Titus Neupert, Masaki Kobayashi, Vladimir N. Strocov, Thorsten Schmitt, Ziya S. Aliev, Mahammad B. Babanly, Imamaddin R. Amiraslanov, Evgueni V. Chulkov, Jürg Osterwalder, and J. Hugo Dil. Disentanglement of surface and bulk Rashba spin splittings in noncentrosymmetric BiTeI. *Phys. Rev. Lett.*, 109:116403, Sep 2012.
- [72] Taichi Okuda and Akio Kimura. Spin- and angle-resolved photoemission of strongly spin–orbit coupled systems. *Journal of the Physical Society of Japan*, 82(2):021002, 2014/06/23 2013.
- [73] Bartosz Slomski, Gabriel Landolt, Gustav Bihlmayer, Jürg Osterwalder, and J. Hugo Dil. Tuning of the Rashba effect in Pb quantum well states via a variable Schottky barrier. *Sci. Rep.*, 3:1963, 06 2013.
- [74] J Hugo Dil, Fabian Meier, and Jürg Osterwalder. Rashba-type spin splitting and spin interference of the Cu (111) surface state at room temperature. *Journal of Electron Spectroscopy and Related Phenomena*, 201:42–46, 2015.
- [75] G. Bihlmayer, S. Blügel, and E. V. Chulkov. Enhanced Rashba spin-orbit splitting in Bi/Ag(111) and Pb/Ag(111) surface alloys from first principles. *Physical Review B (Condensed Matter and Materials Physics)*, 75(19):195414, 2007.
- [76] Isabella Gierz, Benjamin Stadtmüller, Johannes Vuorinen, Matti Lindroos, Fabian Meier, J. Hugo Dil, Klaus Kern, and Christian R. Ast. Structural influence on the Rashba-type spin splitting in surface alloys. *Phys. Rev. B*, 81(24):245430, Jun 2010.
- [77] J. Krempaský, H. Volfová, S. Muff, N. Pilet, G. Landolt, M. Radović, M. Shi, D. Kriegner, V. Holý, J. Braun, H. Ebert, F. Bisti, V. A. Rogalev, V. N. Strocov, G. Springholz, J. Minár, and J. H. Dil. Disentangling bulk and surface Rashba effects in ferroelectric α -GeTe. *Phys. Rev. B*, 94:205111, Nov 2016.
- [78] WD Rice, P Ambwani, M Bombeck, JD Thompson, G Haugstad, C Leighton, and SA Crooker. Persistent optically induced magnetism in oxygen-deficient strontium titanate. *Nature materials*, 13(5):481–487, 2014.

- [79] S. S. Rao, Y. F. Lee, J. T. Prater, A. I. Smirnov, and J. Narayan. Laser annealing induced ferromagnetism in SrTiO_3 single crystal. *Applied Physics Letters*, 105(4):042403, 2014.
- [80] Michaela Altmeyer, Harald O. Jeschke, Oliver Hijano-Cubelos, Cyril Martins, Frank Lechermann, Klaus Koepnik, Andrés F. Santander-Syro, Marcelo J. Rozenberg, Roser Valentí, and Marc Gabay. Magnetism, spin texture, and in-gap states: Atomic specialization at the surface of oxygen-deficient SrTiO_3 . *Phys. Rev. Lett.*, 116:157203, Apr 2016.
- [81] A. C. Garcia-Castro, M. G. Vergniory, E. Bousquet, and A. H. Romero. Spin texture induced by oxygen vacancies in strontium perovskite (001) surfaces: A theoretical comparison between SrTiO_3 and SrHfO_3 . *Phys. Rev. B*, 93:045405, Jan 2016.
- [82] Soham S. Ghosh and Efstratios Manousakis. Structure and ferromagnetic instability of the oxygen-deficient SrTiO_3 surface. *Phys. Rev. B*, 94:085141, Aug 2016.
- [83] S. McKeown Walker, S. Riccò, F. Y. Bruno, A. de la Torre, A. Tamai, E. Golias, A. Varykhalov, D. Marchenko, M. Hoesch, M. S. Bahrany, P. D. C. King, J. Sánchez-Barriga, and F. Baumberger. Absence of giant spin splitting in the two-dimensional electron liquid at the surface of SrTiO_3 (001). *Phys. Rev. B*, 93:245143, Jun 2016.
- [84] TC Rödel, C Bareille, F Fortuna, C Baumier, F Bertran, P Le Fèvre, M Gabay, O Hijano Cubelos, MJ Rozenberg, T Maroutian, et al. Orientational tuning of the fermi sea of confined electrons at the SrTiO_3 (110) and (111) surfaces. *Physical Review Applied*, 1(5):051002, 2014.
- [85] S McKeown Walker, Alberto De La Torre, Flavio Yair Bruno, Anna Tamai, TK Kim, M Hoesch, M Shi, MS Bahrany, PDC King, and Félix Baumberger. Control of a two-dimensional electron gas on SrTiO_3 (111) by atomic oxygen. *Physical Review Letters*, 113(17):177601, 2014.
- [86] Zhiming Wang, Zhicheng Zhong, Xianfeng Hao, Stefan Gerhold, Bernhard Stöger, Michael Schmid, Jaime Sánchez-Barriga, Andrei Varykhalov, Cesare Franchini, Karsten Held, et al. Anisotropic two-dimensional electron gas at SrTiO_3 (110). *Proceedings of the National Academy of Sciences*, 111(11):3933–3937, 2014.
- [87] A. F. Santander-Syro, C. Bareille, F. Fortuna, O. Copie, M. Gabay, F. Bertran, A. Taleb-Ibrahimi, P. Le Fèvre, G. Herranz, N. Reyren, M. Bibes, A. Barthélémy, P. Lecoeur, J. Guevara, and M. J. Rozenberg. Orbital symmetry reconstruction and strong mass renormalization in the two-dimensional electron gas at the surface of KTaO_3 . *Phys. Rev. B*, 86:121107, Sep 2012.
- [88] C Bareille, F Fortuna, TC Rödel, F Bertran, M Gabay, O Hijano Cubelos, A Taleb-Ibrahimi, P Le Fèvre, M Bibes, A Barthélémy, et al. Two-dimensional electron gas with six-fold symmetry at the (111) surface of KTaO_3 . *Scientific reports*, 4:3586, 2014.
- [89] Michael P. Marder. *Condensed Matter Physics, 2nd Edition*. Wiley, 2010.

-
- [90] Philip Hofmann. *Solid State Physics - An Introduction*. Wiley VCH, 2014.
- [91] Neil W Ashcroft and N David Mermin. *Solid State Physics*. Holt, Rinehart and Winston, New York 1976, 2005.
- [92] Philip Hofmann. *Solid State Physics - An Introduction*. Wiley VCH, 2014. online notes.
- [93] Duan Feng and Guojun Jin. *Introduction to condensed matter physics*, volume 1. World Scientific, 2005.
- [94] Emilio E Mendez and Gérald Bastard. Wannier-Stark ladders and Bloch oscillations in superlattices. *Physics Today*, 46(6):34–42, 1993.
- [95] Cem Celebi. *Band Formation and Stark Effect in Finite Size Superlattices with Application to Stacked Layers of Graphene*. PhD thesis, University of Antwerp, 2004.
- [96] Fanqi Meng. *Bloch oscillations and Wannier Stark Ladder study in Semiconductor Superlattice*. PhD thesis, Universite Paris Sud - Paris XI, 2012.
- [97] EE Mendez, F Agullo-Rueda, and JM Hong. Stark localization in GaAs-GaAlAs superlattices under an electric field. *Physical Review Letters*, 60(23):2426, 1988.
- [98] N. Sekine and K. Hirakawa. Dispersive terahertz gain of a nonclassical oscillator: Bloch oscillation in semiconductor superlattices. *Phys. Rev. Lett.*, 94:057408, Feb 2005.
- [99] Masayoshi Tonouchi. Cutting-edge terahertz technology. *Nature photonics*, 1(2):97–105, 2007.
- [100] Qiang Fan, Jianhui Yang, Chi Deng, Jianping Zhang, and Jin Cao. Electronic structure and optical properties of CaTiO_3 : An ab initio study. In *Sixth International Conference on Electronics and Information Engineering*, pages 97942I–97942I. International Society for Optics and Photonics, 2015.
- [101] Wei Liu, Yaohui Zhang, Desheng Jiang, Ruozhen Wang, Junming Zhou, and Xiaobing Mei. Wannier–stark localization in InGaAs/GaAs superlattices and its application to electro-optical devices. *Journal of applied physics*, 74(6):4274–4276, 1993.
- [102] R Asahi, Y Taga, W Mannstadt, and Arthur J Freeman. Electronic and optical properties of anatase TiO_2 . *Physical Review B*, 61(11):7459, 2000.
- [103] Koun Shirai and Kazunori Yamanaka. Mechanism behind the high thermoelectric power factor of SrTiO_3 by calculating the transport coefficients. *Journal of Applied Physics*, 113(5):053705, 2013.
- [104] Paul Flowers, Klaus Theopold, and Richard Langley. Chemistry. <https://courses.lumenlearning.com/chemistryformajors/chapter/spectroscopic-and-magnetic-properties-of-coordination-compounds/>, 2017. [Online; accessed 07-June-2017].

Bibliography

- [105] F Ann Walker. Magnetic spectroscopic (EPR, ESEEM, Mössbauer, MCD and NMR) studies of low-spin ferriheme centers and their corresponding heme proteins. *Coordination Chemistry Reviews*, 185:471–534, 1999.
- [106] Kurt H Jürgen Buschow. *Handbook of magnetic materials*, volume 15. Elsevier, 2003.
- [107] Rickard Armiento, Boris Kozinsky, Geoffroy Hautier, Marco Fornari, and Gerbrand Ceder. High-throughput screening of perovskite alloys for piezoelectric performance and thermodynamic stability. *Physical Review B*, 89(13):134103, 2014.
- [108] Gustav Rose. Beschreibung einiger neuen Mineralien des Urals. *Annalen der Physik*, 124(12):551–573, 1839.
- [109] Satoshi Sasaki, Charles T Prewitt, Jay D Bass, and WA Schulze. Orthorhombic perovskite CaTiO_3 and CdTiO_3 : structure and space group. *Acta Crystallographica Section C: Crystal Structure Communications*, 43(9):1668–1674, 1987.
- [110] Philippe Gillet, François Guyot, Geoffrey D Price, Benoit Tournier, and Andrée Cleach. Phase changes and thermodynamic properties of CaTiO_3 . spectroscopic data, vibrational modelling and some insights on the properties of MgSiO_3 perovskite. *Physics and Chemistry of Minerals*, 20(3):159–170, 1993.
- [111] F Guyot, P Richet, Ph Courtial, and Ph Gillet. High-temperature heat capacity and phase transitions of CaTiO_3 perovskite. *Physics and Chemistry of Minerals*, 20(3):141–146, 1993.
- [112] Xing Liu and Robert C Liebermann. X-ray powder diffraction study of CaTiO_3 perovskite at high temperatures. *Physics and Chemistry of Minerals*, 20(3):171–175, 1993.
- [113] T Vogt and Wolfgang W Schmahl. The high-temperature phase transition in perovskite. *EPL (Europhysics Letters)*, 24(4):281, 1993.
- [114] Simon AT Redfern. High-temperature structural phase transitions in perovskite (CaTiO_3). *Journal of Physics: Condensed Matter*, 8(43):8267, 1996.
- [115] Tsuneo Matsui, Hirotake Shigematsu, Yuji Arita, Yutaka Hanajiri, Norihiko Nakamitsu, Nakanori Nagasaki, and Takanori Nagasaki. High temperature phase transitions of CaTiO_3 and $(\text{Ca}_{0.85}\text{Nd}_{0.15})\text{TiO}_3$ by x-ray diffractometry and differential thermal analysis. *Journal of nuclear materials*, 247:72–75, 1997.
- [116] CJ Ball, BD Begg, DJ Cookson, GJ Thorogood, and ER Vance. Structures in the system $\text{CaTiO}_3/\text{SrTiO}_3$. *Journal of Solid State Chemistry*, 139(2):238–247, 1998.
- [117] Brendan J Kennedy, Christopher J Howard, and Bryan C Chakoumakos. Phase transitions in perovskite at elevated temperatures-a powder neutron diffraction study. *Journal of Physics: Condensed Matter*, 11(6):1479, 1999.

-
- [118] Masatomo Yashima. In situ observations of phase transition using high-temperature neutron and synchrotron x-ray powder diffractometry. *Journal of the American Ceramic Society*, 85(12):2925–2930, 2002.
- [119] Masatomo Yashima and Roushown Ali. Structural phase transition and octahedral tilting in the calcium titanate perovskite CaTiO_3 . *Solid State Ionics*, 180(2):120–126, 2009.
- [120] V.V. Lemanov, A.V. Sotnikov, E.P. Smirnova, M. Weihnacht, and R. Kunze. Perovskite CaTiO_3 as an incipient ferroelectric. *Solid State Communications*, 110(11):611 – 614, 1999.
- [121] W. Zhong and David Vanderbilt. Effect of quantum fluctuations on structural phase transitions in SrTiO_3 and BaTiO_3 . *Phys. Rev. B*, 53:5047–5050, Mar 1996.
- [122] Tetsur Nakamura, Pai-Hsuan Sun, Yue Jin Shan, Yoshiyuki Inaguma, Mitsuru Itoh, In-Seon Kim, Jeong-Ho Sohn, Michihiro Ikeda, Toshiki Kitamura, and Hideaki Konagaya. On the perovskite-related materials of high dielectric permittivity with small temperature dependence and low dielectric loss. *Ferroelectrics*, 196(1):205–209, 1997.
- [123] C-J Eklund, CJ Fennie, and KM Rabe. Strain-induced ferroelectricity in orthorhombic CaTiO_3 from first principles. *Physical Review B*, 79(22):220101, 2009.
- [124] Michael D Biegalski, Liang Qiao, Yijia Gu, Apurva Mehta, Qian He, Yayoi Takamura, Albina Borisevich, and Long-Qing Chen. Impact of symmetry on the ferroelectric properties of CaTiO_3 thin films. *Applied Physics Letters*, 106(16):162904, 2015.
- [125] Walter J. Merz. Double hysteresis loop of BaTiO_3 at the curie point. *Phys. Rev.*, 91:513–517, Aug 1953.
- [126] Mark D Waugh. Design solutions for DC bias in multilayer ceramic capacitors. *Electronic Engineering Times*, 2010.
- [127] Malcolm E Lines and Alastair M Glass. *Principles and applications of ferroelectrics and related materials*. Oxford university press, 1977.
- [128] S. Sanna, C. Thierfelder, S. Wippermann, T. P. Sinha, and W. G. Schmidt. Barium titanate ground- and excited-state properties from first-principles calculations. *Phys. Rev. B*, 83:054112, Feb 2011.
- [129] Prashant R Potnis, Nien-Ti Tsou, and John E Huber. A review of domain modelling and domain imaging techniques in ferroelectric crystals. *Materials*, 4(2):417–447, 2011.
- [130] Walter J. Merz. The electric and optical behavior of BaTiO_3 single-domain crystals. *Phys. Rev.*, 76:1221–1225, Oct 1949.
- [131] Ashim Kumar Bain and Prem Chand. *Ferroelectrics: Principles and Applications*. John Wiley & Sons, 2017.

Bibliography

- [132] R.A. Cowley. Structural phase transitions I. Landau theory. *Advances in Physics*, 29(1):1–110, 1980.
- [133] Martin T Dove. Review: Theory of displacive phase transitions in minerals. *American Mineralogist*, 82(3-4):213–244, 1997.
- [134] K. J. Choi, M. Biegalski, Y. L. Li, A. Sharan, J. Schubert, R. Uecker, P. Reiche, Y. B. Chen, X. Q. Pan, V. Gopalan, L.-Q. Chen, D. G. Schlom, and C. B. Eom. Enhancement of ferroelectricity in strained BaTiO₃ thin films. *Science*, 306(5698):1005–1009, 2004.
- [135] YL Li and LQ Chen. Temperature-strain phase diagram for BaTiO₃ thin films. *Applied physics letters*, 88(7):072905, 2006.
- [136] JL Parsons and L Rimai. Raman spectrum of BaTiO₃. *Solid State Communications*, 5(5):423–427, 1967.
- [137] R Comes, M Lambert, and A Guinier. Désordre linéaire dans les cristaux (cas du silicium, du quartz, et des pérovskites ferroélectriques). *Acta Crystallographica Section A: Crystal Physics, Diffraction, Theoretical and General Crystallography*, 26(2):244–254, 1970.
- [138] B Ravel, EA Stern, RI Vedrinskii, and V Kraizman. Local structure and the phase transitions of BaTiO₃. *Ferroelectrics*, 206(1):407–430, 1998.
- [139] Igor Levin, Victor Krayzman, and Joseph C Woicik. Local structure in perovskite (Ba,Sr)TiO₃: Reverse Monte Carlo refinements from multiple measurement techniques. *Physical Review B*, 89(2):024106, 2014.
- [140] A. S. Chaves, F. C. S. Barreto, R. A. Nogueira, and B. Zeks. Thermodynamics of an eight-site order-disorder model for ferroelectrics. *Phys. Rev. B*, 13:207–212, Jan 1976.
- [141] MS Senn, DA Keen, TCA Lucas, JA Hriljac, and AL Goodwin. Emergence of long-range order in BaTiO₃ from local symmetry-breaking distortions. *Physical Review Letters*, 116(20):207602, 2016.
- [142] Raša Pirc and Robert Blinc. Off-center Ti model of barium titanate. *Physical Review B*, 70(13):134107, 2004.
- [143] D. A. Tenne, X. X. Xi, Y. L. Li, L. Q. Chen, A. Soukiasian, M. H. Zhu, A. R. James, J. Lettieri, D. G. Schlom, W. Tian, and X. Q. Pan. Absence of low-temperature phase transitions in epitaxial BaTiO₃ thin films. *Phys. Rev. B*, 69:174101, May 2004.
- [144] Jelle Dionot, Grégory Geneste, Claire Mathieu, and Nick Barrett. Surface polarization, rumpling, and domain ordering of strained ultrathin BaTiO₃(001) films with in-plane and out-of-plane polarization. *Phys. Rev. B*, 90:014107, Jul 2014.
- [145] Jelle Dionot. *Topology of ferroelectric polarization at the BaTiO₃(001) surface from ab initio calculations and electron microscopy-spectroscopy*. PhD thesis, Université Paris Sud - Paris XI, 2015.

-
- [146] Catherine Dubourdieu, John Bruley, Thomas M Arruda, Agham Posadas, Jean Jordan-Sweet, Martin M Frank, Eduard Cartier, David J Frank, Sergei V Kalinin, Alexander A Demkov, et al. Switching of ferroelectric polarization in epitaxial BaTiO₃ films on silicon without a conducting bottom electrode. *Nature nanotechnology*, 8(10):748–754, 2013.
- [147] O Trithaveesak, J Schubert, and Ch Buchal. Ferroelectric properties of epitaxial BaTiO₃ thin films and heterostructures on different substrates. *Journal of applied Physics*, 98(11):114101, 2005.
- [148] J Sinsheimer, SJ Callori, B Ziegler, B Bein, PV Chinta, A Ashrafi, RL Headrick, and M Dawber. In-situ x-ray diffraction study of the growth of highly strained epitaxial BaTiO₃ thin films. *Applied Physics Letters*, 103(24):242904, 2013.
- [149] Gang Chen and Leon Balents. Ferromagnetism in itinerant two-dimensional t_{2g} systems. *Phys. Rev. Lett.*, 110:206401, May 2013.
- [150] Rui Guo, Lei Shen, Han Wang, Zhishiuh Lim, Wenlai Lu, Ping Yang, Alexei Gruverman, Thirumalai Venkatesan, Yuan Ping Feng, and Jingsheng Chen. Tailoring self-polarization of BaTiO₃ thin films by interface engineering and flexoelectric effect. *Advanced Materials Interfaces*, 3(23), 2016.
- [151] K Van Benthem, C Elsässer, and RH French. Bulk electronic structure of SrTiO₃: experiment and theory. *Journal of Applied Physics*, 90(12):6156–6164, 2001.
- [152] Farrel W. Lytle. X-ray diffractometry of low-temperature phase transformations in strontium titanate. *Journal of Applied Physics*, 35(7):2212–2215, 1964.
- [153] G. Shirane and Y. Yamada. Lattice-dynamical study of the 110 K phase transition in SrTiO₃. *Phys. Rev.*, 177:858–863, Jan 1969.
- [154] Z. Salman, R. F. Kiefl, K. H. Chow, M. D. Hossain, T. A. Keeler, S. R. Kreitzman, C. D. P. Levy, R. I. Miller, T. J. Parolin, M. R. Pearson, H. Saadaoui, J. D. Schultz, M. Smadella, D. Wang, and W. A. MacFarlane. Near-surface structural phase transition of SrTiO₃ studied with zero-field β -detected nuclear spin relaxation and resonance. *Phys. Rev. Lett.*, 96:147601, Apr 2006.
- [155] M Smadella, Z Salman, KH Chow, M Egilmez, I Fan, MD Hossain, RF Kiefl, SR Kreitzman, CDP Levy, WA MacFarlane, et al. Surface dependent structural phase transition in SrTiO₃ observed with spin relaxation of ^{87}Li . *Physica B: Condensed Matter*, 404(5):924–926, 2009.
- [156] Z. Salman, M. Smadella, W. A. MacFarlane, B. D. Patterson, P. R. Willmott, K. H. Chow, M. D. Hossain, H. Saadaoui, D. Wang, and R. F. Kiefl. Depth dependence of the structural phase transition of SrTiO₃ studied with β -nmr and grazing incidence x-ray diffraction. *Phys. Rev. B*, 83:224112, Jun 2011.

Bibliography

- [157] Hideshi Fujishita, Yoichi Shiozaki, and Etsuro Sawaguchi. X-ray crystal structure analysis of low temperature phase of SrTiO_3 . *Journal of the Physical Society of Japan*, 46(2):581–586, 1979.
- [158] NV Krainyukova and VV Butskii. Evidence for a low-temperature phase transition on the SrTiO_3 (001) surface. *Surface science*, 454:628–633, 2000.
- [159] J. Bardeen, L. N. Cooper, and J. R. Schrieffer. Theory of superconductivity. *Phys. Rev.*, 108:1175–1204, Dec 1957.
- [160] Zhi-Qiang Li, Jia-Lin Zhu, CQ Wu, Z Tang, and Yoshiyuki Kawazoe. Relaxations of TiO_2 -and SrO -terminated SrTiO_3 (001) surfaces. *Physical Review B*, 58(12):8075, 1998.
- [161] P.A.W van der Heide, Q.D Jiang, Y.S Kim, and J.W Rabalais. X-ray photoelectron spectroscopic and ion scattering study of the SrTiO_3 (001) surface. *Surface Science*, 473(1):59 – 70, 2001.
- [162] Tokihisa Hikita, Takashi Hanada, Masahiro Kudo, and Maki Kawai. Structure and electronic state of the TiO_2 and SrO terminated SrTiO_3 (100) surfaces. *Surface Science*, 287:377 – 381, 1993.
- [163] A. Ikeda, T. Nishimura, T. Morishita, and Y. Kido. Surface relaxation and rumpling of TiO_2 -terminated SrTiO_3 (001) determined by medium energy ion scattering. *Surface Science*, 433:520 – 524, 1999.
- [164] E. Heifets, R. I. Eglitis, E. A. Kotomin, J. Maier, and G. Borstel. Ab initio modeling of surface structure for SrTiO_3 perovskite crystals. *Phys. Rev. B*, 64:235417, Nov 2001.
- [165] Z. Q. Liu, W. M. Lü, S. L. Lim, X. P. Qiu, N. N. Bao, M. Motapothula, J. B. Yi, M. Yang, S. Dhar, T. Venkatesan, and Ariando. Reversible room-temperature ferromagnetism in Nb-doped SrTiO_3 single crystals. *Phys. Rev. B*, 87:220405, Jun 2013.
- [166] JG Bednorz and KA Müller. $\text{Sr}_{1-x}\text{Ca}_x\text{TiO}_3$: An xy quantum ferroelectric with transition to randomness. *Physical Review Letters*, 52(25):2289, 1984.
- [167] Rajeev Ranjan and Dhananjai Pandey. Antiferroelectric phase transition in $(\text{Sr}_{1-x}\text{Ca}_x)\text{TiO}_3$: II. x-ray diffraction studies. *Journal of Physics: Condensed Matter*, 13(19):4251, 2001.
- [168] Hiromoto Uwe and Tunetaro Sakudo. Stress-induced ferroelectricity and soft phonon modes in SrTiO_3 . *Phys. Rev. B*, 13:271–286, Jan 1976.
- [169] U. T. Höchli and L. A. Boatner. Quantum ferroelectricity in $\text{K}_{1-x}\text{Na}_x\text{TaO}_3$ and $\text{KTa}_{1-y}\text{Nb}_y\text{O}_3$. *Phys. Rev. B*, 20:266–275, Jul 1979.
- [170] Rajeev Ranjan and Dhananjai Pandey. Antiferroelectric phase transition in $(\text{Sr}_{1-x}\text{Ca}_x)\text{TiO}_3$ ($0.12 < x \leq 0.40$): I. Dielectric studies. *Journal of Physics: Condensed Matter*, 13(19):4239, 2001.

-
- [171] Shinsuke Miura, Masakazu Marutake, Hiromi Unoki, Hiromoto Uwe, and Tunetaro Sakudo. Composition dependence of the phase transition temperatures in the mixed crystal systems near SrTiO_3 . *Journal of the Physical Society of Japan*, 38(4):1056–1060, 1975.
- [172] VV Lemanov, EP Smirnova, PP Syrnikov, and EA Tarakanov. Phase transitions and glasslike behavior in $\text{Sr}_{1-x}\text{Ba}_x\text{TiO}_3$. *Physical Review B*, 54(5):3151, 1996.
- [173] Desheng Fu and Mitsuru Itoh. Role of Ca off-centering in tuning ferroelectric phase transitions in $\text{Ba}(\text{Zr,Ti})\text{O}_3$ system. In Aime Pelaiz Barranco, editor, *Ferroelectric Materials - Synthesis and Characterization*, chapter 05. InTech, Rijeka, 2015.
- [174] T. Mitsui and W. B. Westphal. Dielectric and x-ray studies of $\text{Ca}_x\text{Ba}_{1-x}\text{TiO}_3$ and $\text{Ca}_x\text{Sr}_{1-x}\text{TiO}_3$. *Phys. Rev.*, 124:1354–1359, Dec 1961.
- [175] T. Wei, Q.J. Zhou, Q.G. Song, Z.P. Li, S.Q. Guo, Y.R. Guo, Y.F. Chen, X.L. Qi, and J.-M. Liu. The interaction of multifold polar orderings in Ba-doped $\text{Sr}_{0.7}\text{Ca}_{0.3}\text{TiO}_3$. *Materials Research Bulletin*, 47(6):1316 – 1322, 2012.
- [176] Carl Willem Rischau, Xiao Lin, Christoph P Grams, Dennis Finck, Steffen Harms, Johannes Engelmayer, Thomas Lorenz, Yann Gallais, Benoît Fauqué, Joachim Hemberger, et al. A ferroelectric quantum phase transition inside the superconducting dome of $\text{Sr}_{1-x}\text{Ca}_x\text{TiO}_{3-\delta}$. *Nature Physics*, 2017.
- [177] Heinrich Hertz. Ueber den Einfluss des ultravioletten Lichtes auf die elektrische Entladung. *Ann. Phys*, 31, 1987.
- [178] A. Einstein. Ueber einen die Erzeugung und Verwandlung des Lichtes betreffenden heuristischen Gesichtspunkt. *Annalen der Physik*, 14(S1):164–181, 2005.
- [179] S. Hüfner. *Photoelectron Spectroscopy: Principles and Applications*, 3rd edn. Springer, Berlin Heidelberg New York, 2003.
- [180] Andrea Damascelli. Probing the electronic structure of complex systems by ARPES. *Physica Scripta*, 2004(T109):61, 2004.
- [181] Jürg Osterwalder. Spin-polarized photoemission. In *Magnetism: A Synchrotron Radiation Approach*, pages 95–120. Springer, 2006.
- [182] Charles C Chusuei and D Wayne Goodman. X-ray photoelectron spectroscopy. *Encyclopedia of physical science and technology*, 17:921–938, 2002.
- [183] Christian Egon Matt. *Electron Correlation in Copper and Iron-Based High Temperature Superconductors-An Angle-Resolved Photoemission Spectroscopy Perspective*. PhD thesis, ETH Zurich, 2016.

Bibliography

- [184] VN Strocov, X Wang, M Shi, M Kobayashi, J Krempasky, C Hess, T Schmitt, and L Patthey. Soft-X-ray ARPES facility at the ADRESS beamline of the SLS: Concepts, technical realisation and scientific applications. *Journal of synchrotron radiation*, 21(1):32–44, 2014.
- [185] Gabriel Landolt. *Spin-and angle-resolved photoelectron spectroscopy on topological insulators and bulk Rashba systems*. PhD thesis, University of Zurich, 2014.
- [186] Vladimir Strocov. Electron momentum calculations. <https://www.psi.ch/sls/adress/manuals>, 2017. [Online; accessed 11-June-2017].
- [187] Hans M Christen and Gyula Eres. Recent advances in pulsed-laser deposition of complex oxides. *Journal of Physics: Condensed Matter*, 20(26):264005, 2008.
- [188] T Ohnishi, T Yamamoto, S Meguro, H Koinuma, and M Lippmaa. Pulsed laser ablation and deposition of complex oxides. In *Journal of Physics: Conference Series*, volume 59, page 514. IOP Publishing, 2007.
- [189] Chunrui Ma and Chonglin Chen. Pulsed laser deposition for complex oxide thin film and nanostructure. *Advanced Nano Deposition Methods*, 2016.
- [190] Bartosz Slomski. *A Spin-and Angle-resolved Photoemission Study of the Rashba-Bychkov Effect in Lead Quantum Well States*. PhD thesis, University of Zurich, 2013.
- [191] Wolfgang Braun. *Reflection high-energy electron diffraction studies of semiconductor interfaces during molecular beam epitaxy growth*. PhD thesis, Humboldt-University Berlin, 1996.
- [192] AL Kholkin, SV Kalinin, Andreas Roelofs, and Alexei Gruverman. Review of ferroelectric domain imaging by piezoresponse force microscopy. In *Scanning probe microscopy*, pages 173–214. Springer, 2007.
- [193] Elisabeth Soergel. Piezoresponse force microscopy (PFM). *Journal of Physics D: Applied Physics*, 44(46):464003, 2011.
- [194] Patrycja Paruch. Scanned probe microscopy: measuring forces to map material properties. 7th MaNEP Winter School Saas Fee, 2017.
- [195] Y. Hotta, T. Susaki, and H. Y. Hwang. Polar discontinuity doping of the $\text{LaVO}_3/\text{SrTiO}_3$ interface. *Phys. Rev. Lett.*, 99:236805, Dec 2007.
- [196] Paolo Perna, Davide Maccariello, Milan Radovic, Umberto Scotti di Uccio, Ilaria Pallecchi, Marta Codda, Daniele Marré, Claudia Cantoni, Jaume Gazquez, Maria Varela, et al. Conducting interfaces between band insulating oxides: The $\text{LaGaO}_3/\text{SrTiO}_3$ heterostructure. *Applied Physics Letters*, 97(15):152111, 2010.

- [197] Emiliano Di Gennaro, Umberto Scotti di Uccio, Carmela Aruta, Claudia Cantoni, Alessandro Gadaleta, Andrew R. Lupini, Davide Maccariello, Daniele Marré, Ilaria Pallecchi, Domenico Paparo, Paolo Perna, Muhammad Riaz, and Fabio Miletto Granozio. Persistent photoconductivity in 2D electron gases at different oxide interfaces. *Advanced Optical Materials*, 1(11):834–843, 2013.
- [198] K Ueno, S Nakamura, H Shimotani, A Ohtomo, N Kimura, T Nojima, H Aoki, Y Iwasa, and M Kawasaki. Electric-field-induced superconductivity in an insulator. *Nature materials*, 7(11):855–858, 2008.
- [199] S. Thiel, G. Hammerl, A. Schmehl, C. W. Schneider, and J. Mannhart. Tunable quasi-two-dimensional electron gases in oxide heterostructures. *Science*, 313(5795):1942–1945, 2006.
- [200] Cheng Cen, S Thiel, G Hammerl, CW Schneider, KE Andersen, CS Hellberg, J Mannhart, and J Levy. Nanoscale control of an interfacial metal–insulator transition at room temperature. *Nature materials*, 7(4):298–302, 2008.
- [201] Zhiming Wang, S McKeown Walker, Anna Tamai, Y Wang, Z Ristic, Flavio Yair Bruno, Alberto De La Torre, Sara Riccò, NC Plumb, M Shi, et al. Tailoring the nature and strength of electron-phonon interactions in the SrTiO₃ (001) 2D electron liquid. *Nature materials*, 15(8):835–839, 2016.
- [202] Masahiro Yamamoto, Hiromichi Ohta, and Kunihiro Koumoto. Thermoelectric phase diagram in a CaTiO₃–SrTiO₃–BaTiO₃ system. *Applied physics letters*, 90(7):072101, 2007.
- [203] Saad Tariq, Afaq Ahmed, Saher Saad, and Samar Tariq. Structural, electronic and elastic properties of the cubic CaTiO₃ under pressure: A DFT study. *AIP Advances*, 5(7):077111, 2015.
- [204] H. F. Kay and P. C. Bailey. Structure and properties of CaTiO₃. *Acta Crystallographica*, 10(3):219–226, Mar 1957.
- [205] Martin R Castell. Scanning tunneling microscopy of reconstructions on the SrTiO₃ (001) surface. *Surface Science*, 505:1–13, 2002.
- [206] Natasha Erdman, Oliver Warschkow, Mark Asta, Kenneth R. Poeppelmeier, Donald E. Ellis, and Laurence D. Marks. Surface structures of SrTiO₃(001): A TiO₂-rich reconstruction with a c(4 × 2) unit cell. *Journal of the American Chemical Society*, 125(33):10050–10056, 2003. PMID: 12914468.
- [207] Katsuya Iwaya, Takeo Ohsawa, Ryota Shimizu, Tomihiro Hashizume, and Taro Hitosugi. Atomically resolved surface structure of SrTiO₃ (001) thin films grown in step-flow mode by pulsed laser deposition. *Applied physics express*, 3(7):075701, 2010.
- [208] Guo-zhen Zhu, Guillaume Radtke, and Gianluigi A Botton. Bonding and structure of a reconstructed (001) surface of SrTiO₃ from TEM. *Nature*, 490(7420):384–387, 2012.

Bibliography

- [209] M. Radovic, N. Lampis, F. Miletto Granozio, P. Perna, Z. Ristic, M. Salluzzo, C.M. Schlepütz, and U. Scotti di Uccio. Growth and characterization of stable SrO-terminated SrTiO₃ surfaces. *Applied Physics Letters*, 94:022901, 2009.
- [210] S.K. Sen, J. Riga, and J. Verbist. 2s and 2p x-ray photoelectron spectra of Ti⁴⁺ ion in TiO₂. *Chemical Physics Letters*, 39(3):560 – 564, 1976.
- [211] D. K. G. de Boer, C. Haas, and G. A. Sawatzky. Exciton satellites in photoelectron spectra. *Phys. Rev. B*, 29:4401–4419, Apr 1984.
- [212] A. E. Bocquet, T. Mizokawa, K. Morikawa, A. Fujimori, S. R. Barman, K. Maiti, D. D. Sarma, Y. Tokura, and M. Onoda. Electronic structure of early 3d-transition-metal oxides by analysis of the 2p core-level photoemission spectra. *Phys. Rev. B*, 53:1161–1170, Jan 1996.
- [213] A Bahadur and S Kumar Srivastava. Extrinsic and intrinsic plasmon effects in 2p_{1/2} x-ray photoemission satellites of scandium and titanium compounds. *Trakia Journal of Sciences*, 8(3):29–34, 2010.
- [214] M. W. Haverkort, Z. Hu, A. Tanaka, G. Ghiringhelli, H. Roth, M. Cwik, T. Lorenz, C. Schüßler-Langeheine, S. V. Streltsov, A. S. Mylnikova, V. I. Anisimov, C. de Nadai, N. B. Brookes, H. H. Hsieh, H.-J. Lin, C. T. Chen, T. Mizokawa, Y. Taguchi, Y. Tokura, D. I. Khomskii, and L. H. Tjeng. Determination of the orbital moment and crystal-field splitting in LaTiO₃. *Phys. Rev. Lett.*, 94:056401, Feb 2005.
- [215] D. Sando, A. Barthélémy, and M. Bibes. BiFeO₃ epitaxial thin films and devices: past, present and future. *Journal of Physics: Condensed Matter*, 26(47):473201, 2014.
- [216] M. Neupane, S.-Y. Xu, L. A. Wray, A. Petersen, R. Shankar, N. Alidoust, Chang Liu, A. Fedorov, H. Ji, J. M. Allred, Y. S. Hor, T.-R. Chang, H.-T. Jeng, H. Lin, A. Bansil, R. J. Cava, and M. Z. Hasan. Topological surface states and dirac point tuning in ternary topological insulators. *Phys. Rev. B*, 85:235406, Jun 2012.
- [217] T Eknapakul, PDC King, M Asakawa, P Buaphet, R-H He, S-K Mo, H Takagi, KM Shen, Félix Baumberger, T Sasagawa, et al. Electronic structure of a quasi-freestanding MoS₂ monolayer. *Nano letters*, 14(3):1312–1316, 2014.
- [218] Nasser Alidoust, Guang Bian, Su-Yang Xu, Raman Sankar, Madhab Neupane, Chang Liu, Ilya Belopolski, Dong-Xia Qu, Jonathan D Denlinger, Fang-Cheng Chou, et al. Observation of monolayer valence band spin-orbit effect and induced quantum well states in MoX₂. *Nature communications*, 5:4673, 2014.
- [219] Felix Bloch. Über die Quantenmechanik der Elektronen in Kristallgittern. *Zeitschrift für Physik*, 52(7):555–600, 1929.
- [220] Clarence Zener. A theory of the electric breakdown of solid dielectrics. *Proc. R. Soc. A*, 145(855), 1934.

-
- [221] L. Esaki and R. Tsu. Superlattice and negative differential conductivity in semiconductors. *IBM Journal of Research and Development*, 14(1):61–65, Jan 1970.
- [222] P Voisin, J Bleuse, C Bouche, S Gaillard, C Alibert, and A Regreny. Observation of the Wannier-Stark quantization in a semiconductor superlattice. *Physical Review Letters*, 61(14):1639, 1988.
- [223] G Von Plessen and P Thomas. Method for observing Bloch oscillations in the time domain. *Physical Review B*, 45(16):9185, 1992.
- [224] J Feldmann, K Leo, Jagdeep Shah, DAB Miller, JE Cunningham, T Meier, G Von Plessen, A Schulze, P Thomas, and S Schmitt-Rink. Optical investigation of Bloch oscillations in a semiconductor superlattice. *Physical Review B*, 46(11):7252, 1992.
- [225] Christian Waschke, Hartmut G. Roskos, Ralf Schwedler, Karl Leo, Heinrich Kurz, and Klaus Köhler. Coherent submillimeter-wave emission from Bloch oscillations in a semiconductor superlattice. *Phys. Rev. Lett.*, 70:3319–3322, May 1993.
- [226] Tobias Chris Rödel, Franck Fortuna, Shamashis Sengupta, Emmanouil Frantzeskakis, Patrick Le Fèvre, François Bertran, Bernard Mercey, Sylvia Matzen, Guillaume Agnus, Thomas Maroutian, Philippe Lecoeur, and Andrés Felipe Santander-Syro. Universal fabrication of 2D electron systems in functional oxides. *Advanced Materials*, 28(10):1976–1980, 2016.
- [227] Yosuke Urakami, Mizuki Yamato, and Yukio Watanabe. Surface conduction on poled BaTiO₃ single crystals in ultra high vacuum. *Ferroelectrics*, 346(1):32–36, 2007.
- [228] Jaita Paul, Takeshi Nishimatsu, Yoshiyuki Kawazoe, and Umesh V. Waghmare. Ferroelectric phase transitions in ultrathin films of BaTiO₃. *Phys. Rev. Lett.*, 99:077601, Aug 2007.
- [229] K. Jacobi, C. Astaldi, B. Frick, and P. Geng. Chemical and surface core-level shifts of barium studied by photoemission. *Phys. Rev. B*, 36:3079–3085, Aug 1987.
- [230] L. T. Hudson, R. L. Kurtz, S. W. Robey, D. Temple, and R. L. Stockbauer. Surface core-level shifts of barium observed in photoemission of vacuum-fractured BaTiO₃(100). *Phys. Rev. B*, 47:10832–10838, Apr 1993.
- [231] Meng-Qiu Cai, Ji-Cheng Liu, Guo-Wei Yang, Xin Tan, Yun-Lun Cao, Wang-Yu Hu, Ling-Ling Wang, and Yan-Guo Wang. Ab initio study of rumpled relaxation and core-level shift of barium titanate surface. *Surface Science*, 601(5):1345 – 1350, 2007.
- [232] J. E. Rault, J. Dionot, C. Mathieu, V. Feyer, C. M. Schneider, G. Geneste, and N. Barrett. Polarization sensitive surface band structure of doped BaTiO₃(001). *Phys. Rev. Lett.*, 111:127602, Sep 2013.
- [233] Claude Ederer and Nicola A Spaldin. Effect of epitaxial strain on the spontaneous polarization of thin film ferroelectrics. *Physical Review Letters*, 95(25):257601, 2005.

Bibliography

- [234] Peng Zhang, P Richard, T Qian, Y-M Xu, X Dai, and H Ding. A precise method for visualizing dispersive features in image plots. *Review of Scientific Instruments*, 82(4):043712, 2011.
- [235] Jiangpeng Chen, Ying Luo, Xin Ou, Guoliang Yuan, Yiping Wang, Ying Yang, Jiang Yin, and Zhiguo Liu. Upward ferroelectric self-polarization induced by compressive epitaxial strain in (001) BaTiO₃ films. *Journal of Applied Physics*, 113(20):204105, 2013.
- [236] Takashi Hayashi, Naoto Oji, and Hiroshi Maiwa. Film thickness dependence of dielectric properties of BaTiO₃ thin films prepared by sol-gel method. *Japanese journal of applied physics*, 33(9S):5277, 1994.
- [237] R.P. Feynman, R.B. Leighton, and M. Sands. *Feynman Lectures on Physics: Volume 2*. Addison-Wesley, 1964.
- [238] Kevin E Smith and Victor E Henrich. Resonant photoemission in Ti₂O₃ and V₂O₃: Hybridization and localization of cation 3d orbitals. *Physical Review B*, 38(14):9571, 1988.
- [239] Junguang Tao, Tim Luttrell, and Matthias Batzill. A two-dimensional phase of TiO₂ with a reduced bandgap. *Nature chemistry*, 3(4):296–300, 2011.
- [240] Ugo Fano. Effects of configuration interaction on intensities and phase shifts. *Physical Review*, 124(6):1866, 1961.
- [241] Ke-Jin Zhou, Milan Radovic, Justine Schlappa, Vladimir Strocov, Ruggero Frison, Joel Mesot, Luc Patthey, and Thorsten Schmitt. Localized and delocalized Ti 3d carriers in LaAlO₃/SrTiO₃ superlattices revealed by resonant inelastic x-ray scattering. *Phys. Rev. B*, 83:201402, May 2011.
- [242] Jorge Lobo-Checa, Fabian Meier, Jan Hugo Dil, Taichi Okuda, Martina Corso, Vladimir N. Petrov, Matthias Hengsberger, Luc Patthey, and Jürg Osterwalder. Robust spin polarization and spin textures on stepped Au(111) surfaces. *Physical Review Letters*, 104(18):187602, 05 2010.
- [243] Gertjan Koster, Boike L. Kropman, Guus J. H. M. Rijnders, Dave H. A. Blank, and Horst Rogalla. Quasi-ideal strontium titanate crystal surfaces through formation of strontium hydroxide. *Applied Physics Letters*, 73(20):2920–2922, 1998.
- [244] T. Ohnishi, K. Shibuya, M. Lippmaa, D. Kobayashi, H. Kumigashira, M. Oshima, and H. Koinuma. Preparation of thermally stable TiO₂-terminated SrTiO₃(100) substrate surfaces. *Applied Physics Letters*, 85(2):272–274, 2004.
- [245] Winfried Mönch. *Electronic properties of semiconductor interfaces*, volume 43. Springer Science & Business Media, 2013.
- [246] Anatoliy Evtukh, Hans Hartnagel, Oktay Yilmazoglu, Hidenori Mimura, and Dimitris Pavlidis. *Band Bending and Work Function*, pages 87–118. John Wiley & Sons, Ltd, 2015.

-
- [247] Masahito Mochizuki and Masatoshi Imada. Orbital physics in the perovskite Ti oxides. *New Journal of Physics*, 6(1):154, 2004.
- [248] Zhufeng Hou and Kiyoyuki Terakura. Defect states induced by oxygen vacancies in cubic SrTiO_3 : First-principles calculations. *Journal of the Physical Society of Japan*, 79(11):114704, 2010.
- [249] C. M. Yim, M. B. Watkins, M. J. Wolf, C. L. Pang, K. Hermansson, and G. Thornton. Engineering polarons at a metal oxide surface. *Phys. Rev. Lett.*, 117:116402, Sep 2016.
- [250] Anderson Janotti, Joel B Varley, Minseok Choi, and Chris G Van de Walle. Vacancies and small polarons in SrTiO_3 . *Physical Review B*, 90(8):085202, 2014.
- [251] S Nishikawa and S Kikuchi. Diffraction of cathode rays by mica. *Nature*, 121:1019–1020, 1928.
- [252] Jiang Peng, Wang Li-Li, Ning Yan-Xiao, Qi Yun, Ma Xu-Cun, Jia Jin-Feng, and Xue Qi-Kun. Two-step oxidation of $\text{Pb}(111)$ surfaces. *Chinese Physics Letters*, 26(1):016803, 2009.
- [253] BK Choudhury, KV Rao, and RNP Choudhury. Dielectric properties of SrTiO_3 single crystals subjected to high electric fields and later irradiated with x-rays or γ -rays. *Journal of Materials Science*, 24(10):3469–3474, 1989.
- [254] W Hofman, S Hoffmann, and Rainer Waser. Dopant influence on dielectric losses, leakage behaviour, and resistance degradation of SrTiO_3 thin films. *Thin solid films*, 305(1-2):66–73, 1997.
- [255] FM Pontes, EJH Lee, ER Leite, Elson Longo, and José Arana Varela. High dielectric constant of SrTiO_3 thin films prepared by chemical process. *Journal of materials science*, 35(19):4783–4787, 2000.
- [256] JP Hong, JS Kwak, CO Kim, SJ Park, JH Sok, and EH Lee. dielectric properties of pulsed-laser deposited SrTiO_3 films at microwave frequency ranges. *Journal of Applied Physics*, 88(6):3592–3595, 2000.
- [257] CWJ Beenakker. Search for Majorana fermions in superconductors. *Annu. Rev. Condens. Matter Phys.*, 4(1):113–136, 2013.
- [258] G. Hassnain Jaffari, Zahid Mehmood, Asad M. Iqbal, S. K. Hasanain, and S. Ismat Shah. Development of ferroelectric correlations in the quantum paraelectric and antiferrodistortive regimes in $\text{Ba}_x\text{Sr}_{1-x}\text{TiO}_3$ ($x < 0.10$). *Journal of Applied Physics*, 116(8):084101, 2014.
- [259] BQ Lv, S Muff, T Qian, ZD Song, SM Nie, N Xu, P Richard, CE Matt, NC Plumb, LX Zhao, et al. Observation of fermi-arc spin texture in TaAs. *Physical Review Letters*, 115(21):217601, 2015.

Bibliography

- [260] Juraj Krempaský, Stefan Muff, Federico Bisti, Mauro Fanciulli, Henrieta Volfová, Andreas P Weber, Nicolas Pilet, Peter Warnicke, Hubert Ebert, J Braun, F. Bertran, V. Volobuev, J. Minar, G. Springholz, J.H. Dil, and V.N. Srolov. Entanglement and manipulation of the magnetic and spin-orbit order in multiferroic Rashba semiconductors. *Nature communications*, 7:13071, 2016.

Stefan Muff

Curriculum Vitae

Länzeweid 7
6024 Hildisrieden
✉ muff.ste@gmail.ch
Date of birth: 04. March 1987
Nationality: Swiss

University Education

- 2013-2017 **Ph.D. in Physics**, *École Polytechnique Fédérale de Lausanne, EPFL*.
Ph.D. thesis title:
"Manipulation of the Two-Dimensional States at Titanates Surfaces studied by ARPES"
written at the Swiss Light Source (SLS), Paul Scherrer Institut (PSI) under the supervision
Prof. Dr. J. Hugo Dil
- 2011-2013 **Master of Science in Physics**, *University of Zurich, UZH*.
Subject: Solid state physics
Master thesis:
"Angle-Resolved Photoemission Spectroscopy of the Topological Insulator $\text{GeBi}_{4x}\text{Sb}_x\text{Te}_7$ "
written at the Swiss Light Source (SLS), Paul Scherrer Institut (PSI) under the supervision
of Prof. Dr. Jürg Osterwalder and Dr. J. Hugo Dil
- 2006-2011 **Bachelor of Science in Physics**, *University of Zurich, UZH*.
Minor subjects: Mathematics, Computational Science
Semester prize of the Faculty of Science for the Bachelor thesis:
"Kontaktwinkelmessung und Elektrochemie mit 0.1M HClO_4 auf h-BN/Rh(111) Nanomesh"
written under the supervision of Prof. Dr. Jürg Osterwalder and Prof. Dr. Thomas Greber

School Education

- 2000-2006 **Eidgenössische Matura**, *Kantonsschule Beromünster*.
1996-2000 **Primarschule**, *Primarschule Hildisrieden*.

Professional Experience

- 2013-2017 **Doctoral Assistant**, *École Polytechnique Fédérale de Lausanne*.
Spin Orbit Interaction Spectroscopy Group, Prof. Dr. J. Hugo Dil
- 2014-2017 **Teaching Assistant**, *École Polytechnique Fédérale de Lausanne*.
Physique Générale II for computer science, Prof. Dr. J. Hugo Dil
- 2013 **Research Assistant**, *University of Zurich*.
Surface physics group of Prof. Dr. Jürg Osterwalder
- 2008-2011 **Tutor**, *University of Zurich*.

Languages

- | | | |
|----------|-----------------|--------------------|
| German: | Level C2 | Mother tongue |
| English: | Level C1 | Advanced knowledge |
| French: | Level B1 | Basic Knowledge |

Publications

- 2017 S. Muff, M. Fanciulli, A.P. Weber, N. Pilet, Z. Ristic, Z. Wang, N.C. Plumb, M. Radovic and J.H. Dil.
Observation of a two-dimensional electron gas at CaTiO₃ film surfaces
in press at Applied Surface Science, doi.org/10.1016/j.apsusc.2017.05.229 (2017)
- M. Fanciulli, S. Muff, A.P. Weber and J.H. Dil.
Spin polarization in photoemission from the cuprate superconductor Bi₂Sr₂CaCu₂O_{8+δ}
Physical Review B, 95, 245125 (2017)
 - M. Kollár, L. Ćirić, J. H. Dil, A. Weber, S. Muff, H. M. Ronnow, B. Náfrádi, B. P. Monnier, J. S. Luterbacher, L. Forró and E. Horváth.
Clean, cleaved surfaces of the photovoltaic perovskite
Scientific Reports, 7, 695 (2017)
 - E. Razzoli, T. Jaouen, M.-L. Mottas, B. Hildebrand, G. Monney, A. Pisoni, S. Muff, M. Fanciulli, N. C. Plumb, V. A. Rogalev, V. N. Strocov, J. Mesot, M. Shi, J. H. Dil, H. Beck and P. Aebi
Selective Probing of Hidden Spin-Polarized States in Inversion-Symmetric Bulk
Physical Review Letters, 118, 086402 (2017)
 - M. Fanciulli, H. Volfova, S. Muff, J. Braun, H. Ebert, J. Minar, U. Heinzmann and J. H. Dil
Spin Polarization and Attosecond Time Delay in Photoemission from Spin Degenerate States of Solids
Physical Review Letters, 118, 067402 (2017)
- 2016 J. Krempaský, H. Volfová, S. Muff, N. Pilet, G. Landolt, M. Radović, M. Shi, D. Kriegner, V. Holý, J. Braun, H. Ebert, F. Bisti, V. A. Rogalev, V. N. Strocov, G. Springholz, J. Minár and J. H. Dil
Disentangling bulk and surface Rashba effects in ferroelectric α -GeTe
Physical Review B, 94, 205111 (2016)
- J. Krempaský, S. Muff, F. Bisti, M. Fanciulli, H. Volfova, A. P. Weber, N. Pilet, P. Warnicke, H. Ebert, J. Braun, F. Bertran, V. V. Volobuev, J. Minar, G. Springholz, J. H. Dil and V. N. Strocov
Entanglement and manipulation of the magnetic and spin-orbit order in multiferroic Rashba semiconductors
Nature Communications, 7, 13071 (2016)
 - S.-K. Mo, C. Hwang, Y. Zhang, M. Fanciulli, S. Muff, J. H. Dil, Z.-X. Shen and Z. Hussain
Spin-resolved photoemission study of epitaxially grown MoSe₂ and WSe₂ thin films
Journal Of Physics-Condensed Matter, 28, 454001 (2016)
 - S. F. L. Mertens, A. Hemmi, S. Muff, O. Gröning, S. De Feyter, J. Osterwalder and T. Greber
Switching stiction and adhesion of a liquid on a solid
Nature, 534, 676 (2016)

- R. Queiroz, G. Landolt, S. Muff, B. Slomski, T. Schmitt, V. N. Strocov, J. Mi, B. B. Iversen, P. Hofmann, J. Osterwalder, A. P. Schnyder and J. H. Dil
Sputtering-induced reemergence of the topological surface state in Bi_2Se_3
Phys. Rev. B, vol. 93, num. 16, p. 165409 (2016)
- 2015 B. Q. Lv, S. Muff, T. Qian, Z. D. Song, S. M. Nie, N. Xu, P. Richard, C. E. Matt, N. C. Plumb, L. X. Zhao, G. F. Chen, Z. Fang, X. Dai, J. H. Dil, J. Mesot, M. Shi, H. M. Weng, and H. Ding
Observation of Fermi-Arc Spin Texture in TaAs
Physical Review Letters, 115, 217601 (2015)
- C. Brand, H. Pfnür, G. Landolt, S. Muff, J.H. Dil, T. Das, C. Tegenkamp
Observation of correlated spin-orbit order in a strongly anisotropic quantum wire system
Nature Communications, 6, 8118 (2015)
 - F. Pielmeier, G. Landolt, B. Slomski, S. Muff, J. Berwanger, A. Eich, A. A. Khajetoorians, J. Wiebe, Z. S. Aliev, M. B. Babanly, R. Wiesendanger, J. Osterwalder, E. V. Chulkov, F. J. Giessibl and J. H. Dil,
Response of the topological surface state to surface disorder in TlBiSe_2
New Journal of Physics, 17, 023067 (2015)
 - G. Landolt, S. V. Ereemeev, O. E. Tereshchenko, S. Muff, K. A. Kokh, J. Osterwalder, E. V. Chulkov and J. H. Dil.
Direct measurement of the bulk spin structure of noncentrosymmetric BiTeCl
Physical Review B, 91, 081201(R) (2015)
- 2014 N. Xu, P.K. Biswas, J.H. Dil, R.S. Dhaka, G. Landolt, S. Muff, C.E. Matt, X. Shi, N.C. Plumb, M. Radovic, E. Pomjakushina, K. Conder, A. Amato, S.V. Borisenko, R. Yu, H.M. Weng, Z. Fang, X. Dai, J. Mesot, H. Ding and M. Shi,
Direct observation of the spin texture in SmB_6 as evidence of the topological Kondo insulator
Nature Communications, 5, 4566 (2014).
- G. Landolt, S. Schreyeck, S. V. Ereemeev, B. Slomski, S. Muff, J. Osterwalder, E. V. Chulkov, C. Gould, G. Karczewski, K. Brunner, H. Buhmann, L. W. Molenkamp, and J. H. Dil,
Spin Texture of Bi_2Se_3 Thin Films in the Quantum Tunneling Limit
Physical Review Letters, 112, 057601 (2014).
- 2013 S. Muff, F. von Rohr, G. Landolt, B. Slomski, A. Schilling, R.J. Cava, J. Osterwalder and J.H. Dil,
Separating the bulk and surface n- to p-type transition in the topological insulator $\text{GeBi}_{4-x}\text{Sb}_x\text{Te}_7$
Physical Review B, 88, 035407 (2013).
- B. Slomski, G. Landolt, S. Muff, F. Meier, J. Osterwalder and J. H. Dil,
Interband spin-orbit coupling between anti-parallel spin states in Pb quantum well states
New Journal of Physics, 15, 125031 (2013).

- G. Landolt, S. V Eremeev, O. E Tereshchenko, S. Muff, B. Slomski, K. A Kokh, M. Kobayashi, T. Schmitt, V. N Strocov, J. Osterwalder, E. V Chulkov and J. H. Dil, *Bulk and surface Rashba splitting in single termination BiTeCl* New Journal of Physics, 15, 085022 (2013).
- 2012 G. Landolt, S. V. Eremeev, Y. M. Koroteev, B. Slomski, S. Muff, T. Neupert, M. Kobayashi, V. N. Strocov, T. Schmitt, Z. S. Aliev, M. B. Babanly, I. R. Amiraslanov, E. V. Chulkov, J. Osterwalder, and J. H. Dil, *Disentanglement of Surface and Bulk Rashba Spin Splittings in Noncentrosymmetric BiTeI* Physical Review Letters, 109, 116403 (2012).

Public Presentations

- 2017 Oral Presentation at the DPG Annual Meeting, Dresden, March 2017
"Manipulation of two-dimensional states at the $XTiO_3$ surface ($X=Sr, Ba, Ca$)"
- 2016 Poster contribution at the ToCoTronics Fall School and Workshop, Wurzburg, October 2016
"Two-dimensional hole gas at ferroelectric $BaTiO_3$ film surfaces"
- Poster contribution at the ToCoTronics Fall School and Workshop, Wurzburg, October 2016
"Assessing topological protection in real space"
- Oral Presentation at ECOS32 32th European Conference on Surface Science, Grenoble, August/September 2016
"Two-dimensional hole gas at ferroelectric $BaTiO_3$ film surfaces"
- Poster contribution at ECOS32 32th European Conference on Surface Science, Grenoble, August/September 2016
"Assessing topological protection in real space"
- Oral Presentation at the SPS Annual Meeting, Lugano, August 2016
"Two-dimensional hole gas at ferroelectric $BaTiO_3$ film surfaces"
- Oral Presentation at the 39th VUVX conference *International Conference on Vacuum Ultraviolet and X-ray Physics*, Zurich, July 2016
"Two-dimensional hole gas at ferroelectric $BaTiO_3$ film surfaces"
- 2015 Poster contribution at the COR.S.O. 2015: *Summer school on new physics due to Spin-Orbit coupling in CORrelated electron systems*, Cargese, August 2015
"Metallic states at ferroelectric $BaTiO_3$ film surfaces"
- 2014 Oral Presentation at the SLS Symposium, Villigen (2014)
"Two dimensional electron gas at the surface of $BaTiO_3$ films"
- 2013 Oral Presentation at the Joint Users' Meeting at PSI (JUM@P'13), Villigen, (2013)
"Separating the bulk and surface n- to p-type transition in the topological insulator $GeBi_{4-x}Sb_xTe_7$ "

